Development of a Universal Spot Weld Model for Automotive FEM Crash Simulations

A thesis submitted in fulfilment of the requirements for the degree of Master of Engineering by research.

Khandoker Neamul Ahsan Noman
B. Sc. Eng. (Mech.)

School of Aerospace
Mechanical and Manufacturing Engineering
RMIT University

August 2007

Declaration

I certify that except where due acknowledgement has been made, the work is that of the author alone; the work has not been submitted previously, in whole or in part, to qualify for any other academic award; the content of the thesis is the result of work which has been carried out since the official commencement date of the approved research program; and, any editorial work, paid or unpaid, carried out by a third party is acknowledged.

Khandoker Neamul Ahsan Noman

27th August, 2007.

This work is
dedicated to my parents.

Hosneara Nilufar Nilu

&

Khandoker Hayat Uddin

Acknowledgements

I would like to gratefully acknowledge all those who rendered their support and contribution to this research work in both substance and spirit.

I am very much in debt to Dr. Monir Takla, my thesis senior supervisor, for his contribution and effective guidance through positive criticism at every step of my work and for extensive patience with continuous support for the completion of this thesis. I would like to take this opportunity to show my gratitude to him. I also gratefully acknowledge the generous support of Prof. Aleksandar Subic, Discipline Head, Mechanical and Automotive Engineering, RMIT University, my second supervisor, leading to the completion of this research project.

I would also like to thank Mr. Daniel Belton, Project Engineer, Holden Innovation, for his extensive support during the progress of this work and for the review of the thesis. I would also like to gratefully thank Dr. Thomas Ting, Business and Operations Manager / Projects Manager, VPAC (CFCP) for his untiring support for this work and for providing constructive thoughtful comments during the review of this thesis. I also gratefully acknowledge the financial support provided by the AUTOCRC for the completion of the research project.

A very sincere gratitude to Mr. Paul John Mignone, Application Engineer, SIMULIA Australia, for his extensive assistance in organizing the spot welding of the test samples. I am also very thankful to him for proof reading the manuscript of this thesis. I sincerely acknowledge the guidance provided by Mr. Joseph Kovacs of VPAC (CFCP) for introducing me to the HYPERMESH software.

I would also like to thank specially the staff members from the SAMME workshop in RMIT, Don Savvides, Trevor George and Peter Rosewarne for

their assistance in the procurement of the test materials and hardness testing. A very special and sincere gratitude to Mr. Peter Tkatchyk, of the RMIT Material Testing Laboratory, for his tireless assistance in developing the testing setup and conducting the experimental testings.

Last but not least; I would like to thank each and every member of my family for their continuous support and encouragement throughout the whole duration of my studies.

ABSTRACT

This thesis deals with the finite element simulation of spot welded joint in crash analysis. Spot welding is a very common joining process in the automotive industry. It is cost effective and it provides a very fast production rate of automotive body components. Despite this advantage, spot welds are very susceptible to various types of loading conditions. Therefore they are prone to failure, if not designed properly, during their service life time. Therefore it is very important to understand the behaviour of spot welds and their failure characteristics.

Generally, before the manufacturing stage, most of the automotive structural components are designed and tested in a virtual design environment. It is important to examine the crashworthiness of these body-in-white structures. To asses the crashworthiness of these structures they need to be represented correctly in virtual simulations, which necessitate the development of spot welded joint models to be included in crash analysis. Usually the models for the body-in-white structures are complicated and huge, which contains thousands of spot welded joints. Therefore a simple model for spot welded joints is desirable. Six different spot welded joint models were developed in this thesis to serve the above mentioned purpose. At the same time the simplicity issue of these developed spot weld models were also addressed, so that they can be integrated easily in a large assembly system, which consists of thousands of spot welded joints. Moreover for an effective modelling strategy, the computational costs incurred by the adopted spot weld models need also to be taken into consideration. Therefore the approach undertaken in this thesis was to study the characteristics of only one spot welded joint on a test coupon with the developed suitable spot weld nugget modelling configurations.

The performances of the developed spot weld nugget modelling configurations were validated using the results of the experimental testings. The experimental work in this thesis consists of two major parts; material testing and spot welded coupon testing. Material testing provided the mechanical properties of the material which were used in the development of the spot weld models. The experimental investigation with the spot welded test coupons presented a simple strategy to design a spot welded joint based on the desired mode of the joint failure. It identified the required dimensions of the test coupons to be used to study the characteristics of the spot welded joint. The characteristics of the spot welded joints from the experimental investigations were identified from the force displacement diagrams. These force displacement diagrams were used to validate the developed simple spot weld models for their load bearing capabilities. The experimental force displacement diagrams obtained from the spot welded test coupons also presented the insight of the real spot weld failure. During failure development, the degradation of the force displacement curve pointed out the loss of the load carrying capability of the joint. The failure mode observed in the experimental analysis showed that the material failure around the spot weld joint was the reason for the degradation of the force – displacement response.

Therefore a plasticity based damaged material failure model was implemented into the developed spot weld models to simulate the development of spot weld failure. The failure model used in this thesis was based on the state of stress and the equivalent strain. This strategy is different from the current trend of force based spot weld failure criterion, which effectively addressed the joint failure as reaching the elastic limit of the material. Moreover the force based criterion does not consider the post failure behaviour of the joint. The strategy adopted in this thesis addresses the post failure behaviour of the spot welded joint.

Table of Contents

Chapter – 5: Modelling Strategy

Chapter – 6: Finite Element Modelling of Spot Weld Joint

NOMENCLATURE

Chapter -1

H	Heat generated in Joules
I	Current flow in root mean square amperes
R	Electrical resistance in Ohms
T	Time of the welding process

Chapter - 2

D, d	Diameter of the spot weld nugget
T, t	Sheet thickness
w	Coupon width
S_y	Yield strength
N_c	Normal tensile strength of spot welded joint
S	Shear strength of the spot welded joint
H	Hardness value
P, F	Load
D_c	Critical damage variable
p	Accumulated equivalent plastic strain
σ_f	Rapture load in tension
τ_f	Shear rapture load
M	Bending moment
E	Young's Modulus

Chapter – 3

σ_o	Engineering stress
F	Load
A	Cross sectional area
e	Engineering strain
δ	Displacement
L	Length
σ_T	True Stress
ε	True strain
n	Strain hardening exponent
K	Strength modulus

Chapter – 4

d	Spot weld nugget diameter
t	Sheet thickness
w	Coupon width
S_y	Yield strength
H	Hardness value

Chapter – 5

K	Structural stiffness
R	Force residual
U	Displacement
c	Correction factor
I	Internal load
M	Mass
P	Applied external force
ε	Strain
Δt	Smallest time increment for stable analysis
L_e	Element characteristic length
C_d	Dilatational speed
λ	Lame's constant
ρ	Density of material
μ	Modulus of rigidity

Chapter – 6

ω_D	Material state variable
$\bar{\varepsilon}_D^{Pl}$	Accumulated plastic strain
η	Stress triaxial state
$\bar{\sigma}$	Undamaged stress tensor
σ	Stress tensor considering damage
G_f	Fracture energy dissipation
U	Displacement
σ_{ij}	Total state of stress
σ'_{ij}	Deviatory stress tensor
δ_{ij}	Kornecker delta
$\sigma_1, \sigma_2, \sigma_3$	Principal stresses
d	Damage variable
α	Exponential parameter

Chapter – 7

K	Shear stiffness
f	Dimensionless factor
G	Material shear modulus
t	Section thickness
$\bar{\varepsilon}_D^{Pl}$	Accumulated plastic strain
η	Stress triaxial state

LIST OF FIGURES

LIST OF TABLES

ACRONYMS

LS	Lap Shear Coupon
CP	Coach Peel coupon
UT	U Tension coupon
IRB	Individual Rigid Beam model
PMRB	Parallel Multiple Rigid Beams model
SEM	Solid Element Model
SC – 1	Spider Configuration - 1
SC – 2	Spider Configuration – 2
SC – 3	Spider Configuration – 3
TS	Transverse Shear effect
FS	Failure Strain
ED	Effective Displacement
TSF	Tensile shear force of the spot welded joint
RE	Relative error
EFV	Experimental force value
SFV	Simulation force value
IDS	Initial deformation stage
LWS	Load withstanding stage
FRS	Failure response stage

Chapter -1

Introduction

1.1 Overview of Thesis Structure

The objective of this thesis was to develop simple models to represent the spot weld joint for Finite Element Analysis (FEA). These spot weld models were studied for different loading conditions. A failure criterion was implemented in the developed finite element models of this study to predict the spot weld failure responses. The predictions obtained from these simple models were compared to the actual spot weld failure results. The actual spot weld failure results were obtained through the experimental studies. The structure of this thesis is as follows:

- **Chapter – 1: Introduction**

  This chapter provides a general overview of the spot welding process. It also discusses the necessary background information required for the proposed study.

- **Chapter – 2: Historical Background**

  This chapter presents the findings from the literature survey on spot weld failure characterisation. The modelling techniques presently used to represent the spot weld joints were also discussed in this chapter.

Thus it justifies the scope of current research. It also mentions the limitation of the present work.

- **Chapter – 3: Material property characterisation**

This chapter presents the experimental study undertaken for the identification of the sheet metal material properties, which were used for the development of the finite element models.

- **Chapter – 4: Experimental testing**

This chapter presents the experimental study on spot weld failure characteristics undertaken for the current research.

- **Chapter – 5: Modelling strategy**

This chapter discusses the modelling strategy taken for the simulation of the spot weld joint.

- **Chapter – 6: Finite element modelling of spot weld joint**

This chapter discusses the development of spot weld models for quasi static loading situations. It also presents the failure simulation of the developed simple spot weld models for crash loading situations. Different types of loading conditions were considered for the investigation.

- **Chapter – 7: Results and Discussion**

This chapter presents the discussion of results obtained from the developed spot weld finite element models.

- **Chapter – 8: Conclusion and recommendations**

This chapter presents the conclusion based on the present course of study. It also includes recommendations for future study.

1.2 Spot Welding Process

Spot welding is a resistance welding process. In spot welding two or more overlapping sheets of metal are joined at one or more locations via the local fusion of material. The local fusion is caused by the heat generation through work pieces that are held together under pressure by two electrodes. Spot welding is now the most widely used resistance welding process due to the fast rate of production. The production rate is fast because of the availability of semi automatic and automatic machines for the process. Moreover there is no requirement of adding the filler material as required by conventional arc welding, TIG or MIG welding process. Even during the manufacturing process, it facilitates a more general elimination of warping or distortion of parts and a high reliability and reproducibility are possible. Hence it was adopted as the most affordable joining technology in the automotive industry.

1.3 Spot welding Process factors

The general procedure for spot welding has been shown in the Figure 1.1.There are two major factors mainly incorporated in the resistance spot welding process:

a) The heat generation at the electrode to sheet metal contact area.
b) Pressure force applied by the electrode on the sheet metal.

The amount of generated heat follows the equation

$$H \propto I^2 RT \qquad (1.1)$$

Where:

H is the heat generated in joules

I is the current flow in root mean square amperes

R is the resistance in ohms

T is the time for the welding process

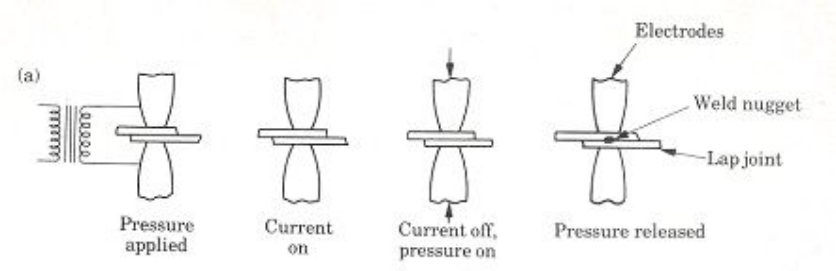

Fig 1.1 Sequence in the spot welding process after Kalpakjian (1992)

For controlling the temperature in the welding process, the magnitude and the timing of the welding current are regulated with all other factors kept constant. The resistance working in the welding process circuit has three components in general.

a) The resistance between the electrodes and the work pieces
b) The resistance in the electrodes and the work pieces individually
c) The resistance in the faying surfaces of the two work pieces.

The time is also an important factor here as seen from the above mentioned equation. By increasing the time factor heat generation will also increase. Generally, the total time involved in one welding cycle consists of the following parts.

a) Squeeze time – the duration between the initial electrode pressure and starting of the welding current
b) Welding time – the duration for the welding current flow

c) Hold time – the duration until the electrode pressure is removed to ensure joining of sheets after the last impulse of the welding cycle.
d) Off time - the interval between two consecutive spot welds cycle.

The electrode force or pressure also plays an important role in the welding process. The force brings the interfaces of the sheet metal into contact and is responsible for the contact resistance between the two sheets. During the welding process, this applied pressure through the electrodes ensures the sticking of the sheet metal parts. The magnitude and the timing of the pressure play a vital role for the formation of the weld nugget. If the pressure of the electrodes is too small then the two sheets and the electrodes will not contact properly. This will cause high contact resistance and may result in the surface burning or pitting the electrodes tips. If excessive pressure is applied during the hold time then softened metal may be expelled from the faying surface which will produce a nugget of smaller dimension. Another side effect is that the excessive pressure may cause larger indentations on the sheet surface.

If the surface conditions of the sheets at the faying sides are held constant and applied pressure is controlled, then the temperature in the welding process is regulated by the magnitude and duration of the welding current. Both direct current and alternating current are used in spot welding machines. The machine transformer converts the line power to low voltage and high amperage power. Most applications use single phase alternating current having the same frequency as the line power. The direct current applications are employed only for high amperage requirements. A typical current and pressure cycle for spot welding is shown in Figure1.2.

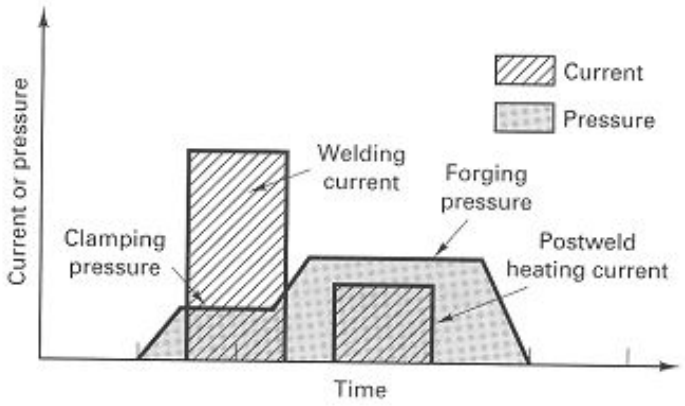

Fig 1.2 Typical current and pressure cycle for spot welding process after Degermo, Black and Kohser(1992)

1.4 Spot Weld Nugget Formation

The size of the spot weld nugget depends on the service conditions and various other attributes. Usually the surface of the spot welded sheet metal has the impression of indentation (caused by the electrodes) which may cause surface irregularities if electrode pressure is not controlled properly. As seen from Equation 1.1, current flow has a higher effect on heat generation in the welding process because of the second order parameter in the equation. Therefore it should also be very carefully controlled. When the current flows through the work pieces and the electrodes, the resistance against the current flow heated up the work piece locally. Due to this thermal load the work piece metal tries to expand in all possible directions except in the transverse direction of the sheet. The applied pressure through the electrodes restricts the metal flow in the transverse direction. So the heated metal usually expands radially in the plane of the sheets.

In general along the radial direction of one spot weld there are three distinct

regions.

a) the Base Metal (BM)
b) the Heat Affected Zone (HAZ)
c) the weld pool which becomes the Spot Weld Nugget (SWN) after the completion of the welding process.

The schematic representation of the various zones is shown in Figure 1.3.

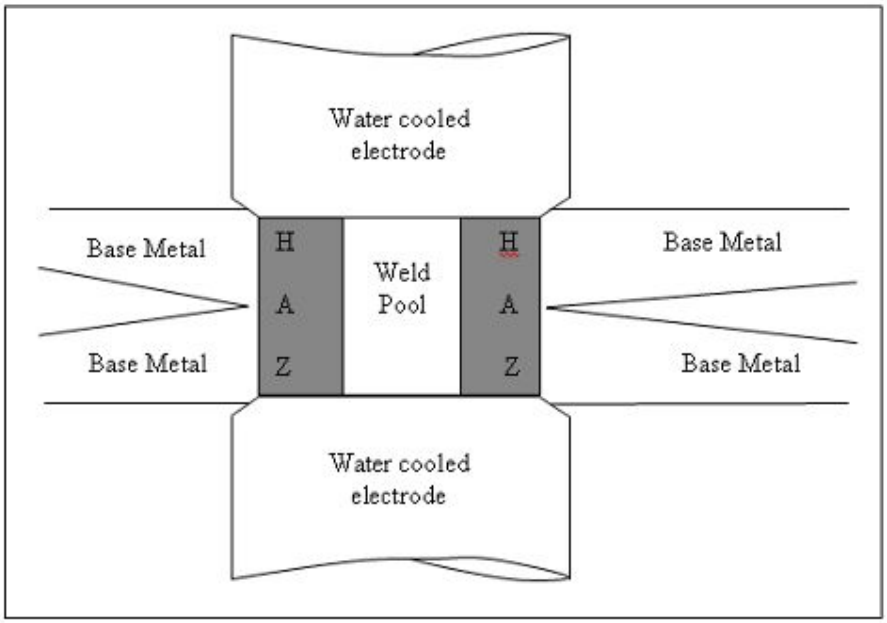

Fig1.3: Schematic cross section of spot welded sheet metal

Recently Darwish et al. (2000) critically examined the microstructure of spot welded low carbon steel. According to the study the key features of the spot welded joints from the metallurgical point of view are (as stated by the author of the paper) :

1) Fusion zone with a columnar dendritic structure.
2) Heat affected zone which shows a gradual transition from a coarse overheated structure through a normalized region to an original structure of unaffected base metal.
3) A narrow ferritic zone in the interface between the overheated and unaffected zones which is not always well defined.

These features are more concisely summarized in the following figure.

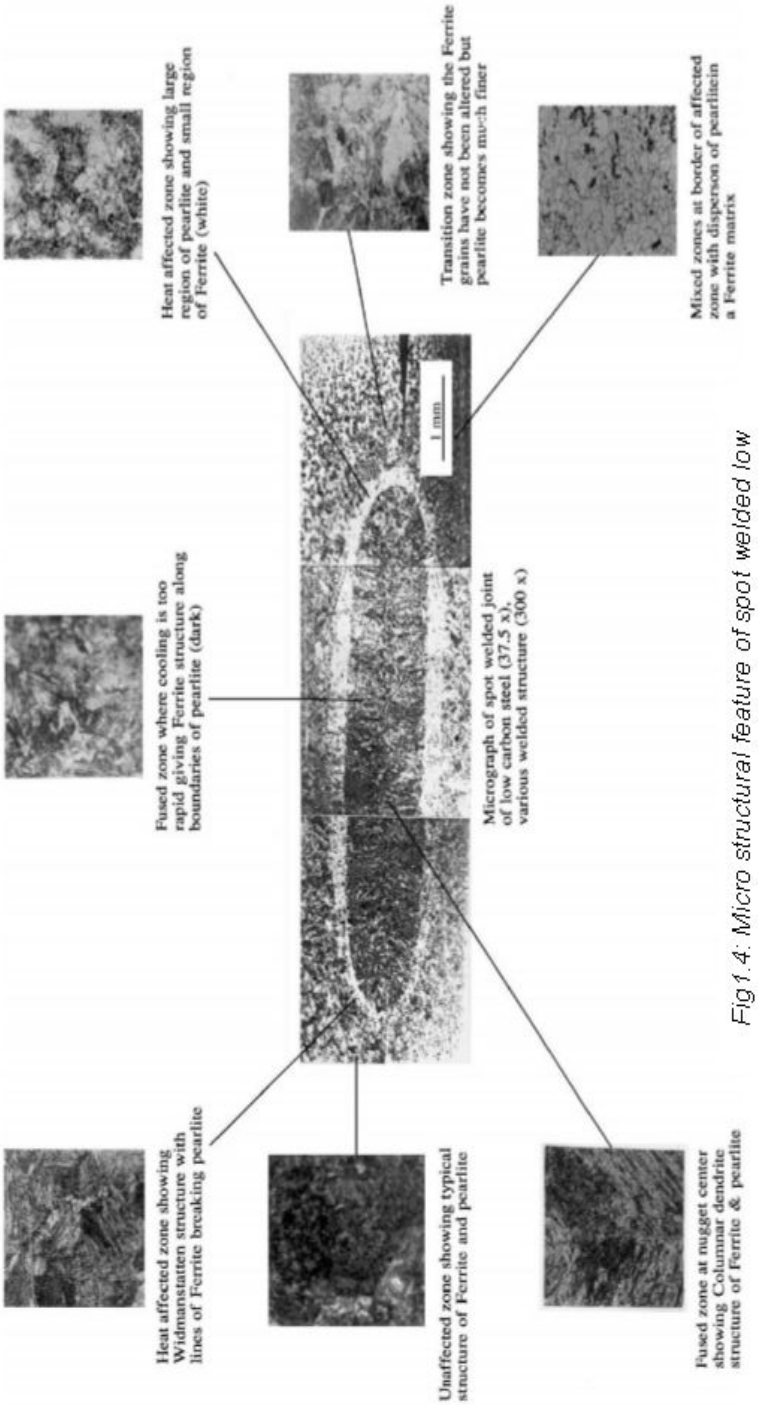

Fig 1.4: Micro structural feature of spot welded low carbon steel as presented by Darwish et al. (2000)

1.5 Quality of Spot Welds

The quality of the spot weld depends on many factors. It is a *"loosely defined term"* in literature (Zhou et. al. (2003)) because of the requirements at the service conditions. In a broad sense the quality of the spot weld can be estimated in

(a) Qualitative manner: The qualitative manner of spot weld quality identification can be described as flawless spot welds which do not have any manufacturing defects.

(b) Quantitative manner: The quantitative manner of spot weld quality identification can be described as the load bearing characteristics of the manufactured spot welds.

The quantitative identification of spot weld quality depends on the qualitative nature to some extent. Hence the spot welding process parameters play an important role for the quality assessment of the spot weld since they influence the nugget formation procedure during the manufacturing stage. According to Equation 1.1, for heat generation in the welding process, the current flow and the time for welding are the two most important parameters. A nominal amount of current is required to flow through the work piece for nominal period of time for the fusion to produce the weld nugget. Generally the shear strength of the weld may vary with the variation of the current flow and weld time during the welding process. The nature of the strength variations are given in the following Figure 1.5.

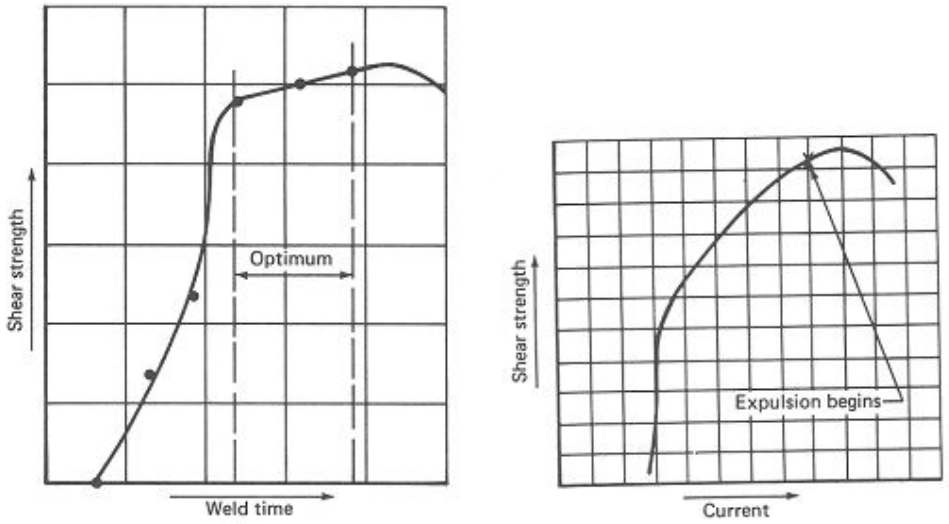

(a) (b)

Fig 1.5: Spot weld shear strength variation with weld time and applied current after AWS Welding Handbook (1980)

The most recent study of the effect of process parameters on spot welded joint characteristics was conducted by B. Bouyousfi et al. (2005). A statistical method based on a neural network was employed for this purpose for 304 L type austenitic stainless steel. The statistical model was verified by experiments with a cross tension coupon configuration. Due to utilization of the neural network approach the effect of the process parameters could be determined both individually and in a coupled manner. From the individual study it was shown that the welding force is the most influential factor on the yield strength of the spot welded cross tension sample, rather than the welding current intensity and welding duration (cycle) parameter. In case of the combined study for the welding force, welding current intensity and welding duration (cycle), the later two parameters seem to be insignificant for the strength prediction.

1.6 Necessity for quality spot weld models

Models are required to represent any physical system for mathematical analysis. The mathematical analysis can provide very insightful information about the physical systems if they are accurately represented in the analysis model. Body-in-white structures in the automotive industry contain thousands of spot welds. Generally before the manufacturing stage, most of the automotive components are designed and tested in a virtual design environment. For body-in-white structures an important parameter is its crashworthiness. To asses the crashworthiness of these kinds of structures they need to be represented correctly in virtual simulations. Hence it necessitates the actual representation of the spot welds for crash simulations.

A number of approaches can be found in the literature for the representation of the spot welds for finite element analysis. The merits and demerits of these current approaches are summarised in the next chapter. Hence the scope and the extent of this present study will also be identified in the next chapter.

Chapter -2

Historical Background

2.1 Overview

This chapter presents the current state of research for the spot weld behaviour studies found in the literature. Spot welded joint characteristics under mechanical loads were analysed by various researchers for different purposes. The aims of some of these researches were to identify the state of stress around the spot weld joint. Some of the studies were conducted to determine the load bearing capacity of a spot weld joint. Some research studied the mechanics of spot weld failure for different loading conditions. To capture the failure mechanism of the spot weld joint, different models were developed for analysing through the use of the finite element method. These models were tested for different loading situations. Moreover various spot weld failure criteria have been worked out using different parameters and they were implemented through different commercial finite element programs. Hence the historical background and the scope of the present work presented here are divided into the following sections:

2.2 Effect of spot weld failure
2.3 Spot weld failure mechanics
2.4 Spot weld load bearing characteristics
2.5 Spot weld models for stress analysis

2.2 Effect of Spot Weld Failure

Body-in-white structures in the automotive industry contain thousands of spot welds. Spot welds provide a very strong structural integrity among different parts of the automotive body. The manufacturing process of the spot welds requires a very high level of heat input into the sheet metal. Due to this high level of heat input the material characteristics of the respective locations of the spot welds can change significantly. For this particular reason an empirical formula was identified by Schneider and Jones (2004), for a structural effectiveness parameter for the crash response of spot welded top hat sections made from different materials. But crash response obtained from the FEA model for the top hat section could not identify the different structural effectiveness, due to the lack of defining the spot weld failure characteristics. Hence the requirement for a proper spot weld model definition in a FEM crash simulation should be emphasized. The folding pattern of the top hat section and spot weld failure and damage outline found in this study are given in the following Figure 2.1.

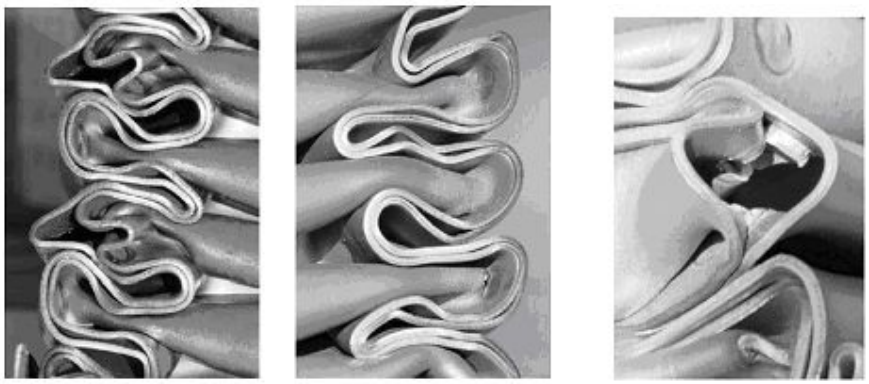

(a) (b) (c)

Fig2.1: Failure pattern of the spot welds in a top hat specimen after Schneider and Jones (2003, 2004) (a) Quasi – static crash with Mild Steel (MS) (b) Quasi – static crash with Interstitial-Free, Rephosphorized High Strength Steel (IFHS) (c) Dynamic crash with IFHS

2.3 Spot weld failure mechanics

To understand the failure mechanics of the spot weld, stress distribution around the spot weld joint was studied by various researchers. Zolotarev (1960) attempted to analyze the stress distribution around the spot weld nugget in a lap shear coupon (Figure 2.2). An analytical approach was adapted for this purpose. The area around the spot weld nugget was divided into four different regions and the stress distributions in those four regions were different from each other. These four regions were assumed to be acting as four big elements. These regions were divided according to their locations inside or outside the overlap area in the coupon. The calculation was based upon the assumption of elastic material properties, which were the same for all four regions. The stresses acting in a particular region were assumed to be constant for that region. Stresses acting in the perpendicular direction (along the thickness of the coupon) with the load were not taken into account in the analysis. So the analysis of the stress was handled as a plain stress model.

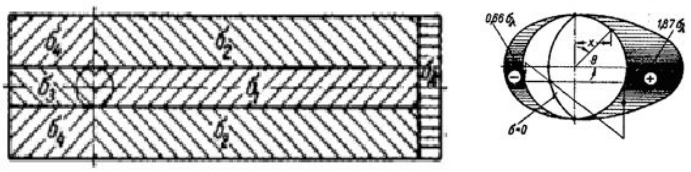

(a) (b)

Fig2.2: (a) Different regions for the analytical stress analysis on the lap shear sample considered by Zolotarev (1960)
(b) Distribution of stress around the spot weld nugget from the analytical solution by Zolotarev (1960)

Y. J. Chao (2003) has attempted similar type of investigation for spot weld failure. Chao assumed one dimensional state of stress in the direction of the applied load acting on the spot weld nugget. But the state of stress in the coupon was ignored in his work. The assumption for the lap shear coupon was extended in the cross tension coupon for the direct normal loading condition. The stress state assumed by Chao is given in Figure 2.3.

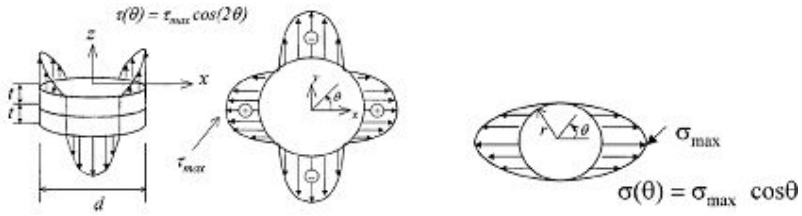

(a) (b)

Fig2.3: State of stress around the spot weld nugget assumed by Y. J. Chao (2003) (a) Cross tension coupon for normal loading condition (b) Lap shear coupon for the shear loading condition

VandenBossche (1977) had attempted to analyze the state of stress around the spot weld nugget to establish weldability criteria. A lap shear sample joint was used for the investigation. Two different failure modes for

the spot welded joint were considered for this study, namely the interfacial mode and the nugget pull out mode. The interfacial mode was designated to be the failure in the spot weld nugget. The nugget pull out mode was assumed for the failure occurrences near the heat affected zone on the sheet metal coupon. For the nugget pull out mode the analysis procedure involved the equilibrium study of the assumed state of stresses caused by the normal and shear loads acting around the nugget on the sheet metal coupon. For the interfacial failure the analysis was done from the point of view of the formation of a plastic hinge at the weld nugget. For both stress states, the equivalent stress was calculated using the distortion energy theory. To determine the transition among the failure modes, the critical nugget diameter - to - thickness ratio was determined utilising the inequality condition. The proposed critical weld diameter to thickness ratio from the analytical solution is given in Equation 2.1.

$$\left(\frac{d}{t}\right)_c = \left(1.5\frac{S_{yPM}\,w}{S_{yWM}\,t}\right)^{\frac{1}{2}} \qquad (2.1)$$

Later the derived analytical formula was verified through experimental investigation at quasi static rates. By utilizing some statistical analysis with the test results, the final form of the critical nugget diameter to the thickness ratio was proposed which is given in Equation 2.2.

$$\frac{d}{t} \le \left[\frac{0.54S_{yPM}}{1.54S_{yPM} + 572MPa}\left(\frac{w}{t}\right)\right]^{\frac{1}{2}} + 3.0 \qquad (2.2)$$

Where d is the weld diameter, t is the sheet thickness, w is the coupon width, S_{yPM} is the yield strength of the parent metal (base metal).

Later Nakano (2005) extended this study to investigate the strain rate effect on the failure of the spot welded joint. In this study the finite element simulation was undertaken along with the analytical approach. It was

reported that the failure mode of the spot weld joint was not affected for the account of the strain rate effect.

The experimental study of the failure mechanism of a single spot welded joint was undertaken extensively by Zuniga et al. (1997). They studied the weld failure in tensile shear and coach peel coupons made from zinc coated HSLA grade 50 steel with yield stress of 368Mpa and ultimate strength of 425Mpa. Experiments were carried out for overload conditions in quasi static state at stroke rate of 0.0508 mm / sec. Failure of the welds were detected through the force displacement curves obtained from these experimental results together with the optical and Scanning Electron Microscopic (SEM) images of the weld nugget. Most of the specimens for the tensile shear coupon and the coach peel coupon failed in the nugget pull out mode of failure (which can be referred to as the material failure). But the causes of the initiations of failure in these two cases were different. The reason of failure for the tensile shear specimens was due to localized necking near the boundary of the base metal and heat affected zone. However the nugget pull out failure in the coach peel specimen was initiated by micro void coalescence. The fractography study by SEM and optical microscope of the cross sectioned coach peel specimen presented in the paper reveals that the development of excessive blunting of the notch front in the heat affected region caused the micro void.

2.4 Spot weld Load bearing characteristics

The load bearing characteristics of the spot welded joints were studied by many researchers. The basic objectives of all of these researches were to predict the strength of the joints. These types of investigations were carried out mainly by experimental observations.

Julius Heuschkel (1952) studied the spot weld strength properties for steel with three types of loading conditions at quasi static loading rates. Different

coupons were used to ensure the loading modes. Experimental correlation between the geometric configurations and the load bearing capability were established. The specialty of these established correlations from this study were the inclusion of the carbon and manganese content of the stock metals. The correlation of the normal tensile strength proposed in this study is given in Equation 2.3.

$$N_c = TUD\left[\frac{a}{U-b} + c - \left(fC + gMn\right)\right] \tag{2.3}$$

Where N_c is the calculated normal tensile strength of weld in lb, T is sheet thickness in inch, U is prewelded steel strength in psi, D is the nugget diameter in inch, C is the number which is equal to the carbon content of the sheet, Mn is number which is equal to the manganese content of the sheet and a, b, c, f, g are constants relative to the thickness of the sheet metal. The shear strength of the spot weld studied here was expressed in the following form (Equation 2.4).

$$S = TUD\left[\alpha - \beta\left(C + {Mn}/{20}\right)\right] \tag{2.4}$$

Where S is the shear strength of the weld in lb, T is the sheet thickness in inch, U is the prewelded steel strength in psi, D is nugget diameter in inch, C is number which is equal to the carbon content of the sheet; Mn is number which is equal to the manganese content of the sheet and α, β are dimensionless constants for lap shear coupon in shear loading.

Recently Marya et al. (2006) conducted an in depth investigation for the load bearing characteristics of spot welded joints for dual phase steel material using the tensile shear coupon configuration. Differences in load bearing capability for the nugget pull out mode and interfacial mode of spot weld joint failure was addressed. The critical load for the transition in between these two failure modes was identified and was expressed in terms of maximum and minimum hardness values found in the spot welded region. The expression is given in Equation 2.5.

$$TSF_c = 831\left[0.53t^{3.22} + 8.48\left(\frac{H_{\max}}{H_{\min}}\right)^{-1.24}\right]^{1.68} \qquad (2.5)$$

Where TSF is the Tensile Shear Force, t is the thickness and H is for the hardness value. This expression is the most comprehensive of its kind due to the incorporation of the hardness values. Because the distribution of the hardness values represent the material states in the spot welded zone, which is dependent on the welding process parameters. The critical nugget diameter for the transition between failure modes was also presented in terms of the hardness value which is given in Equation 2.6.

$$d_c = 0.53t^{3.22} + 8.48\left(\frac{H_{\max}}{H_{\min}}\right)^{-1.24} \qquad (2.6)$$

This equation is similar in nature as the VandenBossche (1977) equation presented in the previous section. But the applicability of this equation becomes complicated due to the incorporation of the hardness value. Initially the critical weld nugget diameter may be calculated using this equation. But to achieve the desired nugget diameter, the welding process parameters have to be changed, eventually which will affect the initial hardness value.

B. Pollard (1974) investigated the spot welding characteristics of High Strength Low Alloyed (HSLA) steels for the application in the automotive industry. Tensile shear and cross tension tests were conducted for determination of the static strength and ductility. Pollard pointed out that the nugget-pull out failure only occurred with welds with the highest range of strength and later it was adopted as the desired mode of spot weld failure by Zhou(1999). The weld nugget pull out failure was caused due to ductile shearing through the thickness of the coupon either in the heat affected zone or base metal area as observed from the detached parts. This test was also extensively supported by Zuniga et al. (1997).

Thronton et al. (1996) studied the spot weld characteristics for non heat-treatable 5754 and heat-treatable 6111 and X613 aluminium alloys. For this study coach peel (for bending load) and tensile shear (for shear load) specimens were used and the performance of the spot welds were studied for static and fatigue loading cases. The following relationship (Equation 2.7) was proposed from the study of load bearing capacity of the spot weld in coach peel coupon.

$$P = (0.12t - a)d \qquad (2.7)$$

Here *P* is the load in KN, *t* is the sheet thickness in mm, *d* is the diameter of the spot weld in mm and *a* is constant whose numerical value depends on the failure mode of the spot weld model. For weld pull out failure the value of the constant "a" is 0.06 and for the interfacial failure 0.12. In case of the shear loading condition with the lap shear coupon, the relationship (Equation 2.8) for the nugget pull out failure was proposed as

$$P = 0.41d \qquad (2.8)$$

And for the interfacial failure this relationship (Equation 2.9) became

$$P = 1.4d - 5 \qquad (2.9)$$

From this study it was clear that the spot weld nugget diameter is the most critical parameter to determine the mode of failure for the spot welded joint. The drawback of the above mentioned expression is that it is a material independent expression since it did not consider any material property as a dependent variable. Hence these equations only express the weld characteristics for the aluminium alloys used in this investigation.

Birch et al. (2000) studied the structural joint systems for both the static and dynamic loading conditions. The spot welded joints considered for this study were made of mild steel material with yield stress of 160.9 Mpa, ultimate stress of 296 Mpa and engineering rupture strain of 30%. The geometric configuration of the coupons used for this study was a lap shear coupon. It was reported that the shape of the force displacement diagram

obtained from the tests and the mode of failure of the spot welded joint changes with the increase of the pull velocity. The force displacement response for the spot weld lap shear joint reported in this study is given in Figure 2.4. The peak load carried by the spot weld joints increased with the increment of the pull velocity. All of the joints failed around the nugget region of the joints. But different modes of failure were identified on the basis of the location of failure initiation and the final shape of the failed region around the spot weld nugget. Hence in this study only the nugget pull out mode of failure (Pollard (1974), Zuniga et al. (1997)) was addressed.

Zhang, Zhou and Hu (2001) attempted to study the spot weld failure behaviour under impact loading situations and tried to correlate the failure modes with the static loading failure conditions. The material used to make the coupon was DS steel with thickness of 1.0 mm. The nugget pull out and shear (interfacial) failure modes were observed in the test cases. For the optimum dimension determination study, nugget pull out mode was dominant in the narrow width specimens (width of 30, 36 and 40mm) while the interfacial failures were figured out in the wider specimens (width of 40 mm and 50 mm) with respect to a particular weld nugget diameter (manufactured with a particular welding schedule of 700lbs electrode force, 12 cycles welding time, 15 cycles holding time and 11.5 KA welding current), for impact loading situations tested with a pendulum type impact tester. A width of 50 mm was selected for this study as the samples with this dimension absorbed lowest level of energy. With these fixed dimensions (50 mm width and 200 mm length) the spot welded coupons were tested for quasi static and impact loading conditions. The spot weld nugget diameter was denoted according to the shape and tip diameters of electrodes used for the manufacturing. A brief summary of the reported results are provided in Figure 2.5. The similarity in the failure modes for impact and quasi static loading conditions were observed from these test results.

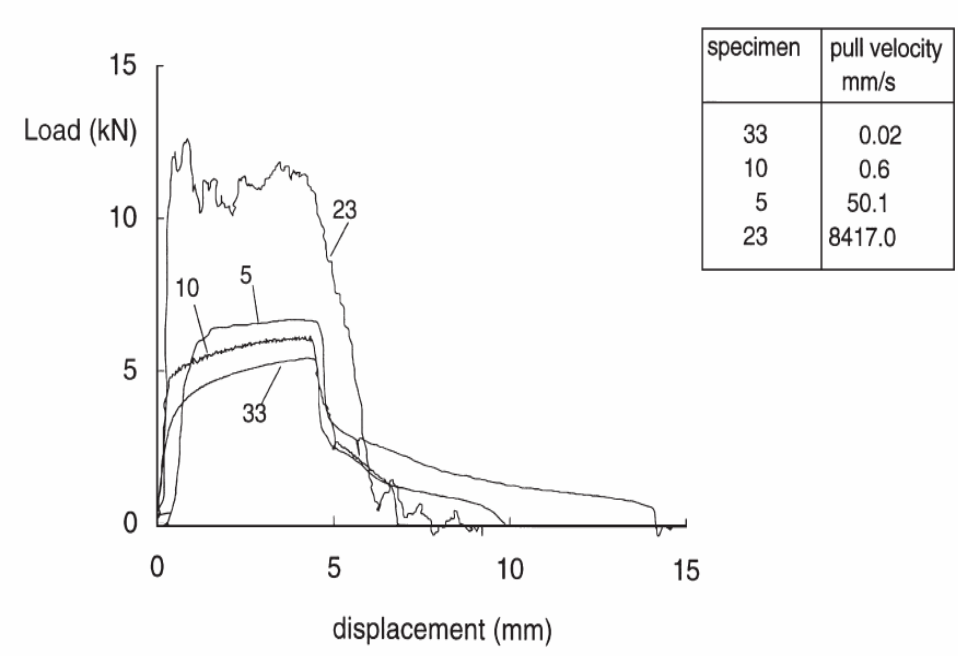

specimen	pull velocity mm/s
33	0.02
10	0.6
5	50.1
23	8417.0

(a)

Specimen	Failure Mode
33	Single Tearing Mode
10	Shear Plugging Mode
5	Single tearing Mode
23	Double Tearing Mode

(b)

Fig 2.4: Experimental results for spot welded lap shear coupons after Birch et al. (2000). (a)Load displacement characteristics for various loading rates (b) Failure modes at the respective pulling velocity

These results had clearly indicated that the quasi static tests for a spot welded lap shear configuration could point out the predictive qualitative responses for the impact loading condition if the proper geometric dimension is maintained.

Electrode	Impact tests		Tensile-shear tests			
	Energy (J)	Failure mode	Peak load (kN)	Maximum displacement (mm)	Energy (J)	Failure mode
$D = 4$ mm	9.39	Shear	5.12	1.06	4.25	Shear
$D = 6$ mm	142.06	Pull out	6.93	3.64	22.11	Pull out
$D = 8$ mm	153.85	Pull out	7.31	4.61	29.86	Pull out
Hot ring	162.82	Pull out	7.03	4.07	25.57	Shear
Cold ring	6.14	Shear	5.15	0.48	1.58	Shear
Rectangular—parameter	8.14	Shear	4.48	0.74	2.57	Shear
Rectangular—normal	8.20	Shear	5.19	1.01	4.40	Shear

(a)

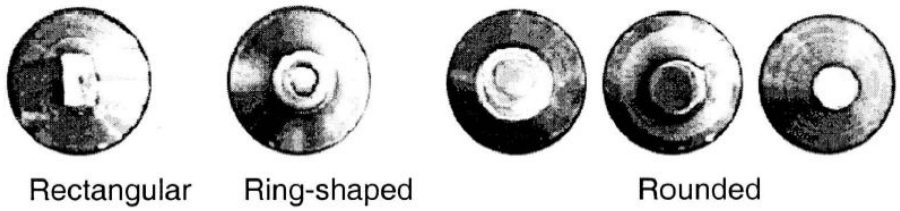

(b)

Fig 2.5: Comparative study of spot welded lap shear coupons for impact and quasi static loading condition after Zhang, Zhou and Hu (2001). (a) Summary of test results (b) Types of electrodes used in the study.

But no direct relationships between the test results of the two loading conditions were presented for this purpose.

Lin et al. (2004) studied the failure loads acting on the spot weld specimens under normal and shear loading conditions in impact situations. The impact situation on the spot welded coupon was imposed with the aid of a specially designed fixture. Two important features were observed from the obtained load displacement histories. The first was that the level of load bearing capability decreases with the increase of the loading angles. The second was that the displacement achieved by the test coupon at no load condition after the maximum load was dropped down, increased with the changing of the loading angle.

Ewing et al. (1982) had conducted research on spot weld responses for static and dynamic loading conditions. Three types of coupon

configurations were used in the study. Tensile shear coupon (for shear loading), Coach Peel coupon (for bending load) and Cross tension coupon (for tensile load) were used. For static loading a standard tensile testing machine was used. It was also used for impact testing in a gravity driven drop weight tester. From the test results it was concluded that the maximum loads increased with the test velocity for all test conditions. Another significant finding from the study was that there was no transition in failure modes (from interfacial failure to pull out failure) with the increment of test velocities for the range of velocities tested.

The above stated characteristics were generally found from the experimental investigations. The experimental results provided insight on the deformation patterns of spot weld joint but it was unable to investigate in depth states of stress during the deformation process. For this purpose many researchers employed the numerical simulation tools for the investigation.

2.5 Spot weld models for stress analysis

The spot weld joint was one of the prime interests for the stress analysts due its high level of geometric irregularities. Moreover the change of material properties (due to the welding process) near the joint also initiates irregular stress patterns.

Several finite element models were developed to investigate the stress patterns near the spot weld nugget. Fujimoto et al. (1982) developed 2D and 3D spot weld models to investigate the fatigue strength in terms of stress concentrations in the plane of loading. The model was tested for a lap shear coupon configuration. Two different types of 2D models were developed. The first 2D model was designated as the plane model. It was

developed with 3 node triangular elements with plane strain condition. The offset of the neutral planes of the lap plates were neglected in this finite element idealisation. All the shell elements were idealised on the same plane. In the overlap region the elements were defined doubly and the spot weld nugget was modelled as common elements for both coupons. The mesh used for this model is given in Figure 2.6. The results of the stress analysis from the 2D plane model were verified from the stress distribution values obtained from the middle layer of a single spot welded double lap shear coupon by the brittle coating technique.

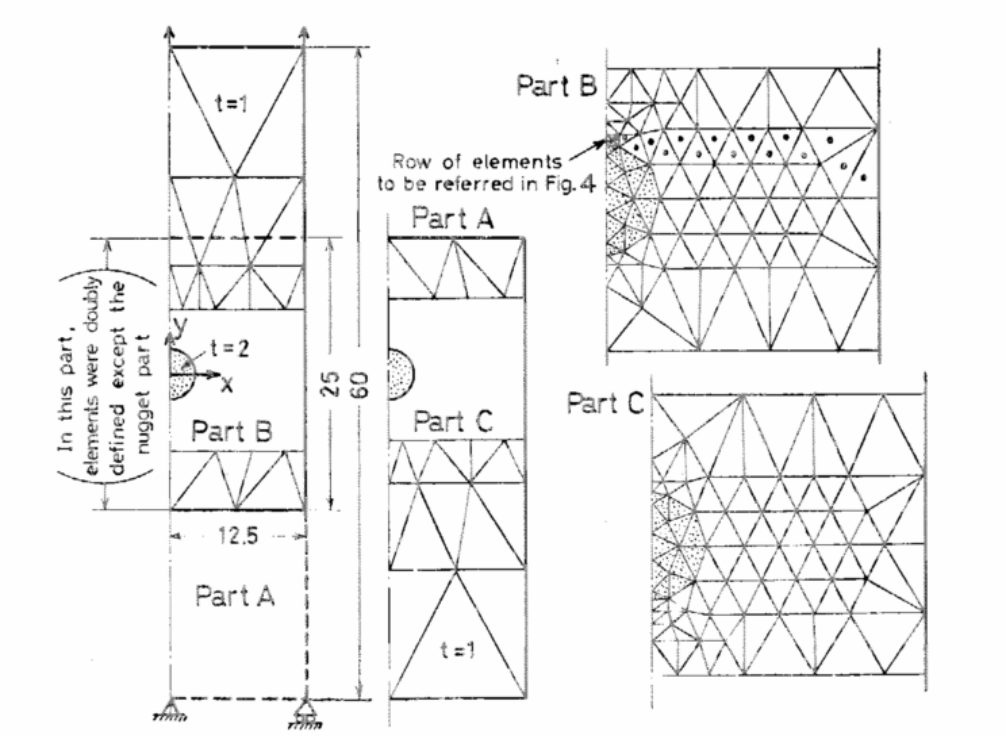

Fig 2.6: 2D finite element mesh with triangular elements for the “Plane model” proposed by Fujimoto et al. (1982)

The second 2D model was developed as a strip in plane strain condition and was referred to as the “Section model”. The section model was developed with the consideration of the offset distance between the two plates of the lap shear coupon configuration. The spot weld nugget was modelled with the aid of a boundary condition placed at a common node of

the two coupons. The results from the section model were verified by the results from a photo elastic test on spot welded epoxy resin plates. The mesh for the “Section model” and comparative results are presented in Figure 2.7.

The 3D model was developed with isoparametric hexahedron elements with 20 nodes per element. The FEM program “MARC” was utilized for the modelling purpose. The spot weld nugget and coupon area were modelled with similar type of elements. A symmetric condition was employed for the

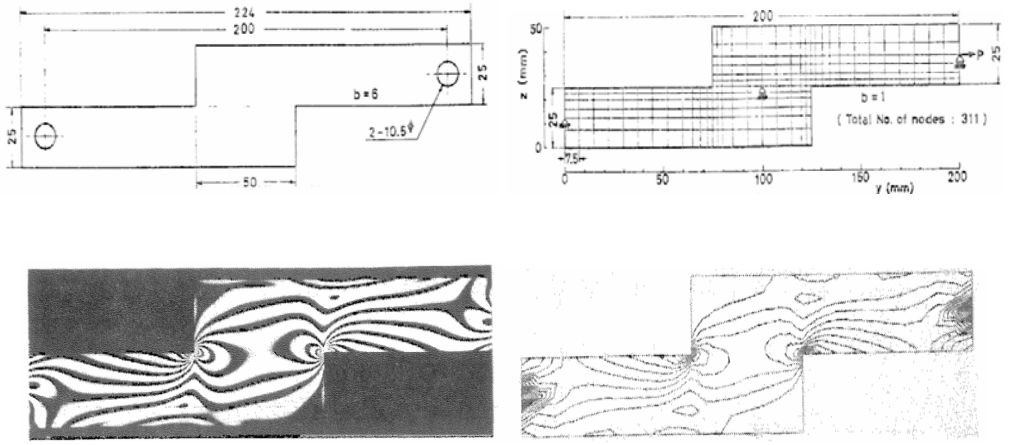

(a) (b)

Fig 2.7: 2D spot weld representation by the “Section model” proposed by Fujimoto et al. (1982). (a) Epoxy resin model and isochromatic lines from photo-elastic analysis (b) Finite element analysis mesh and contour plot of principal stress differences computed from the model

developed model. The material property used for the simulation was elastic and homogeneous for all the locations in the model. The mesh and results obtained from the 3D model are presented in Figure 2.8. The models were analysed for the static loading condition only. The results obtained from the 3D model were similar to the fringe patterns (isochromatic lines) obtained from the photo-elastic analysis.

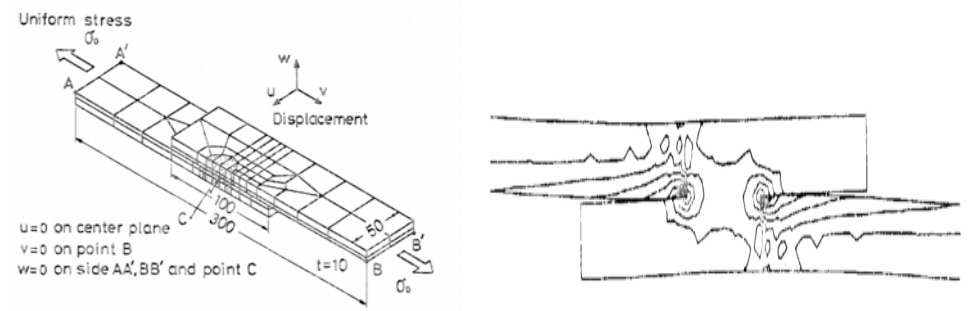

Fig 2.8: 3D spot weld model mesh proposed by Fujimoto et al. (1982).and contour plot of computed principal stress difference from the model.

The comparison between the predicted stress states from the 2D and 3D models were shown in the study. The results were agreeable in a qualitative manner for both the 2D and 3D models. For comparison purposes, the results were computed from both the 2D models by the superposition method. The predicted value from the 2D model was lower (nearly by 20% at a distance of 3 mm from the nugget) than the predicted value of the 3D models, which is shown in Figure 2.9 for the value of axial stress ratio ($\alpha_y = \frac{\sigma_y}{\sigma_0}$).

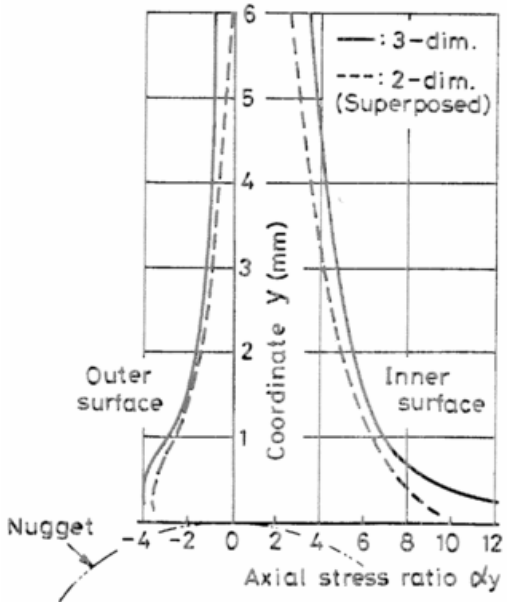

Fig 2.9: Comparison of axial stress ratio from 2D and 3D model after Fujimoto et al. (1982).

Other than this there are other 2D models introduced in the literature (Darwish et. al (2003, 2004)). 2D models are not accurate because they can not capture the deformation pattern for the spot welded joint. Hence to capture correct state of stress 3D models are required to represent the spot welds.

2.6 3D Elastic spot weld models

The 3D spot weld models are required to capture the actual deformation process of the joint system. Various researchers had developed the 3D models depending upon the requirements.

One of the earliest available finite element models of a spot weld joint was reported by Hahn et al. (1983). The spot weld model was built for the study of a single joint on a lap shear coupon with 1mm thickness. The diameter used for the spot weld nugget was 5 mm. The spot weld nugget and the coupon geometry were modelled separately. The mesh was designed in such a manner that the elements near the spot weld nugget were smaller in the overlap region than the elements in the free region. The designed mesh for the developed model is given in Figure 2.10.

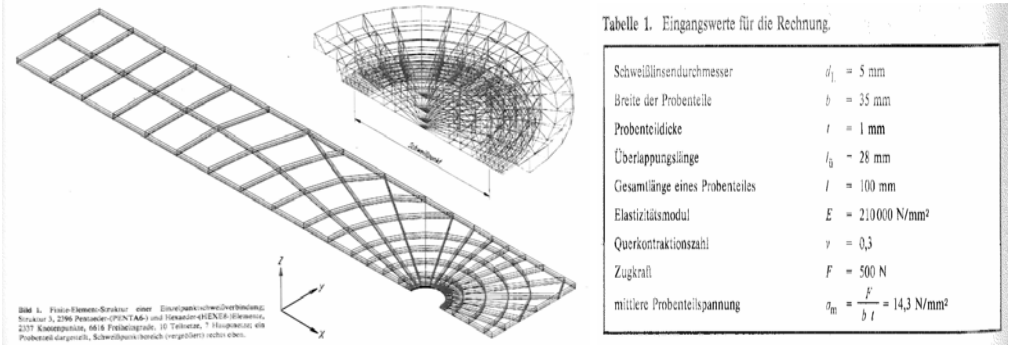

Tabelle 1. Eingangswerte für die Rechnung.

Schweißlinsendurchmesser	d_L	= 5 mm
Breite der Probenteile	b	= 35 mm
Probenteildicke	t	= 1 mm
Überlappungslänge	l_0	= 28 mm
Gesamtlänge eines Probenteiles	l	= 100 mm
Elastizitätsmodul	E	= 210000 N/mm²
Querkontraktionszahl	ν	= 0,3
Zugkraft	F	= 500 N
mittlere Probenteilspannung	σ_m	$= \frac{F}{b\,t}$ = 14,3 N/mm²

Fig 2.10: Mesh design and material property used by Hahn et al. (1983) for developing a spot weld model.

S Zhang (2001) has proposed a simplified spot weld model for stress intensity factor calculation near the weld nugget. The model was incorporated with the shell elements which represented the coupons to be joined. The spot weld nugget diameter was represented with a beam element with the representative dimensions. The beam element was joined to the shell elements with the aid of spoke patterns which transferred all the translation and one radial rotation degree of freedom. The material property used for the simulation (for both the beam element and the shell elements) was linear elastic. The model was tested for the shear loading condition on a tensile shear coupon and the results obtained from the simulation were satisfactory. But because of the uncoupled nature for all the degrees of freedom, this model might not be able to deliver all the force and moments to the joined sheet metal.

Deng et al. (2000) developed a spot weld model for the static loading condition using solid elements for both the sheet metal coupon and the weld nugget. The detailed model was developed with the utilisation of symmetric boundary conditions. Even though a detailed model was developed, homogeneous elastic material models were used for the simulation. It was argued that using elastic plastic material model for the simulation did not affect the stress ratios near the nugget. Thus elastic material definition for the spot weld model is sufficient to judge the qualitative nature obtained from the simulation. But using elastic material properties solely does not facilitate to obtain a proper force displacement response from the model for the overloading conditions.

Chen and Deng (2000) had attempted to judge the spot weld model performances using elastic material properties in the case of using shell and solid elements to represent the welded coupons. The spot weld was not modelled extensively and was assumed to be rigid when the coupon was modelled with shell elements. For the other model where the coupon was represented with solid elements, the spot weld nugget was similarly

represented with solid elements. It was suggested that the model with shell elements could predict reasonable results comparing to the model with solid elements and the effect of assuming the rigid nugget had negligible effect on the stress distribution results. This argument was further investigated by Xu and Deng (2004). They modelled the spot weld nugget with the solid elements and with different configurations of rigid beam elements. In this study the full spot weld model was used with a lap shear coupon configuration. A homogeneous elastic material property was used for the simulation. The results obtained from the developed models were compared with the results from a converged spot weld model using only solid elements for both the nugget and the coupons. The error was estimated between these two sets of simulation results using a simple formula utilizing the structural stiffness value. The key deficiency of this study is that all types of loading conditions were studied through only one geometric configuration (lap shear coupon) of the sheet metal. Moreover there was no contact definition reported for the developed models. For that reason the behavioural characteristics of the modelled spot weld nuggets do not project the actual response for the individual loading situations as it was intended to be. Further more the simple formula that had been used in the study for error estimation of the models is applicable only when the elastic material property for the material model is considered. Hence this approach has a deficiency in estimating spot weld model performances for overloading conditions.

From the above discussion it is clear that using a linear elastic material property may make the evaluation of the spot weld models easier. But it does not represent the real situation of the spot welded joint failure.

2.7 3D Elastic plastic spot weld models

Ahmed (2003) had attempted to discuss the effect of using plastic material properties to model the deformation around the spot weld nugget. The deformation patterns were obtained for the static loading condition. The coupon and the nugget both were represented by the 3D solid elements in this study. A lap shear coupon configuration was used for this study. The difference between the usages of elastic and elastic-plastic material properties for the nugget and the coupon region has been shown. From the stress pattern obtained from the simulation, it was shown that the failure mode of the spot weld joint depended on the nugget radius.

Westerberg (2002) has modelled the self piercing riveted joint for the crash situation on a Coach Peel type of coupon (for bending loading condition) and compared the performance of the developed riveted joint model with a spot weld model developed by Saleh (2002). Both the developed models were containing the same features except in the joint geometry. The sheet metal coupon and the joints were modelled with solid elements. The Johnson – Cook material model was used to represent metal plasticity. It was shown that the spot weld joint required more energy than the self piercing rivet joint due to excessive plastic deformation during failure. But the model performance study relating to the real situation was not conducted in this study.

Combescure et al. (2003), Langrand and Combescure (2004) had proposed a joint element model to represent a spot weld as a link between the two parts to be joined. The joint element model represented the spot weld with a single non linear spring element. The mechanical behaviour of this non linear spring was designed with elastic - plastic material properties. This homogenous elastic - plastic material property of the spring replaced the irregularity of the material properties in the actual spot welded region

.The developed model was tested with different coupon configurations for different loadings conditions.

The damage and failure of a spot weld connection in this study was modelled with a ductile failure model which was proposed by Lemaitre and Chaboche (1985). The damage was calculated by introducing a damage variable 'D' which was evaluated with the Young's modulus of the material and accumulated equivalent plastic strain (p) due to applied load. The material around the spot weld failed when a critical value D_c for the damage variable is reached. The evaluation of damage was defined according to Equation 2.10.

$$
\begin{aligned}
&E\left(D\right) = E\left(1-D\right)\\
&\dot{D} = 0, if\ ,\ \dot{p} = 0\\
&\dot{D} = 0, if\ ,\ p < p_s, or N_3 < 0\\
&\dot{D} = \frac{D_c}{p_u - p_s}\dot{p}, if\ ,\ \dot{p} \neq 0
\end{aligned}
\qquad (2.10)
$$

Where p denotes the accumulated equivalent plastic strain, D represents the damage variable, D_c represents the critical damage value when the material fails, E denotes the Young's modulus of the material and N represents the normal force acting in the designed joint element. The degradation of the material due to damage increment was simulated with a linear relationship with the accumulated equivalent plastic strain (p). Hence the developed model could predict the elastic plastic behaviour of the spot weld as compared with the experimental results. But the post failure response of the weld model was not captured properly in this study. The comparisons of the experimental and simulation results provided by the authors are given in the Figure 2.11.

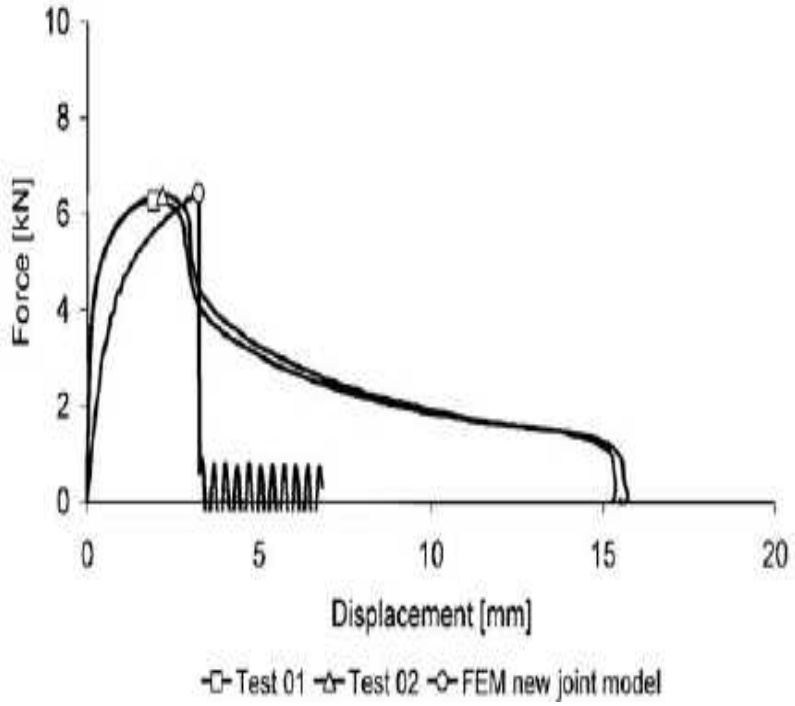
10
8
6
4
2
0
Force [kN]
0
5
10
15
20
Displacement [mm]
Test 01
Test 02
FEM new joint model

(a)

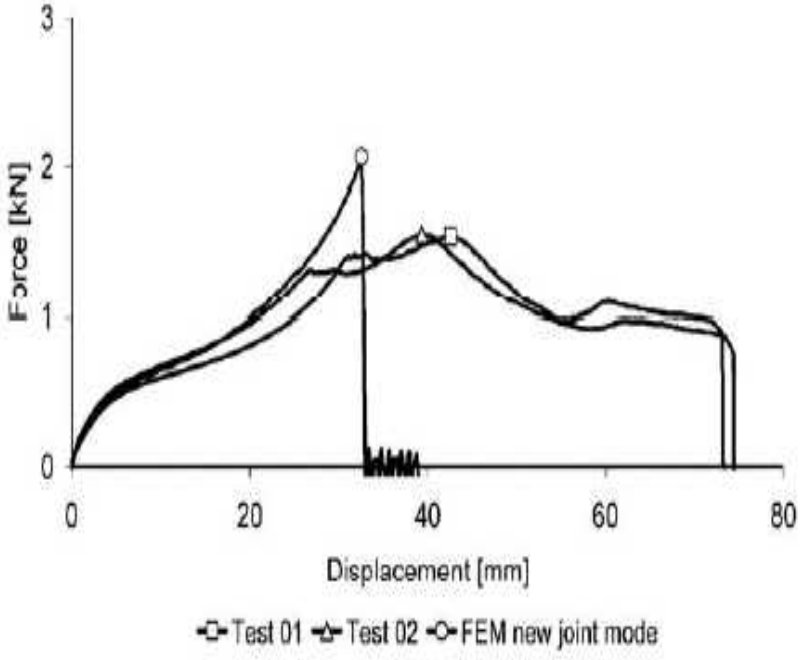
3
2
1
0
Force [kN]
0
20
40
60
80
Displacement [mm]
Test 01
Test 02
FEM new joint mode

(b)

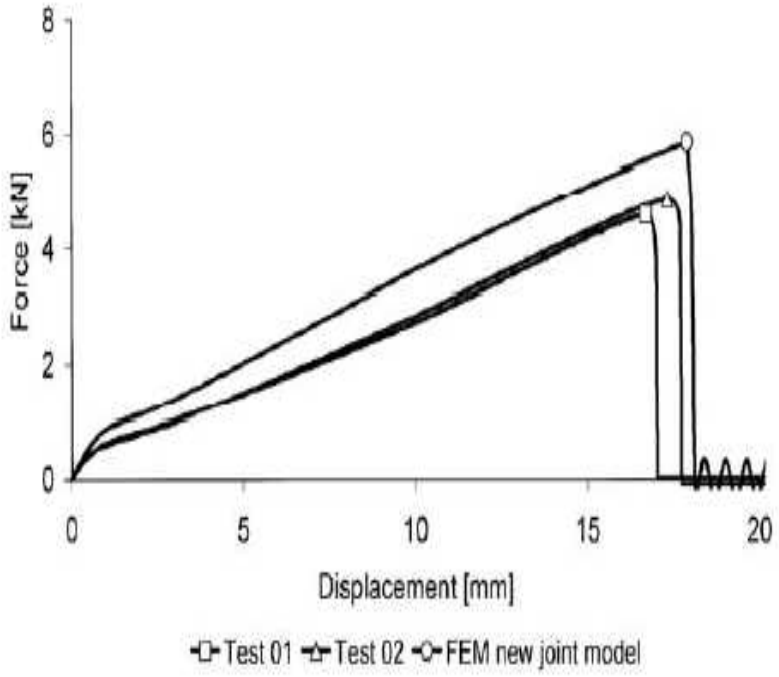

(c)

Fig 2.11: Comparison of the experimental and simulation results with the newly developed spot weld joint model after Langrand and Combescure (2004)
(a) Tensile shear coupon for shear loading condition.
(b) Coach peel coupon for tension loading condition.
(c) Cross tension coupon for bending loading condition

Robert N. Yancey (2004) has attempted to establish a spot weld model for the impact loading situation. The model configuration was designed only for a single spot weld on two inverted 'C' channel centres modelled with shell elements. The spot weld was modelled using a single weld element available within LS- DYNA which was entirely dependent on the mesh of the model. The mesh independent approach of modelling spot welds as a beam element was also investigated. Contact conditions were established for the shell elements of the c channel part with this beam element until the failure of the modelled spot weld had occurred. The post failure response of the spot weld joint model observed from the simulated results presented from this study were similar to those presented by Langrand and

Combescure (2004). The behaviour of the spot weld models was linear after the failure had occurred.

Allanki and Kumar (2005) have utilised one of the LS – DYNA keyword options to simulate the spot weld behaviour on a sheet metal coupon for the quasi - static state. The spot weld was modelled with a beam element in conjunction with the *CONTACT SPOTWELD key word. The failure of the spot weld was modelled with a stress based formulation depending on the notch stress value at the spot weld joint derived by Zhang (2004). The failure (maximum) load predicted by the model nearly matched the test data but the post failure degradation of the joint was not addressed in the study. The results presented in the study are given in the following Table 2.1 and Figure 2.12.

Thickness	**Test data** Lap Shear	Cross Tensile	**Simulation** Lap Shear	Cross Tensile	**Remark**
1-1	527±47 [447 612]	444±26 [403 481]	527	440	Testing and Fitting the values
1-0.8	440±49 [368 510]	437±27 [404 477]	412	425	Validation
1.25-1.25			636	485	Prediction
1.5-1.5			726	525	Prediction

Table 2.1: Results for the failure load of spot welded joint after Allanki and Kumar (2005)

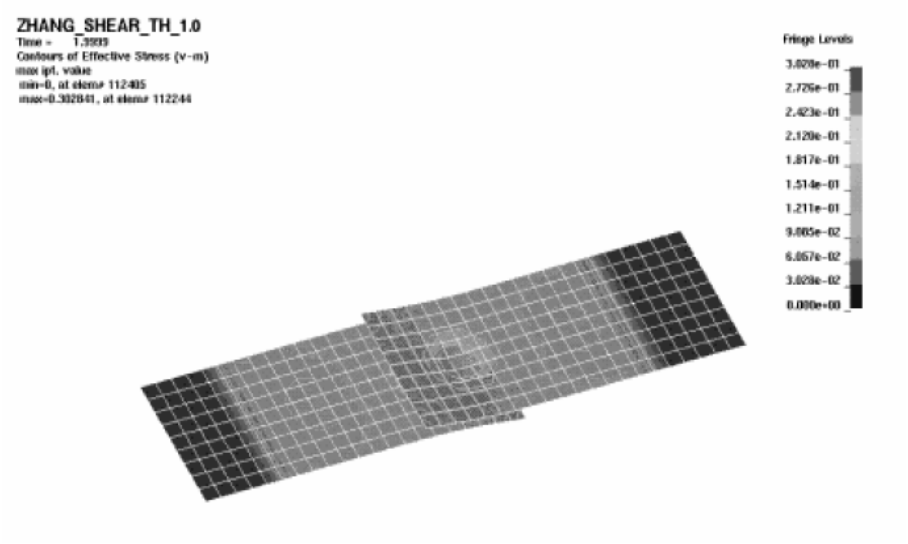

(a)

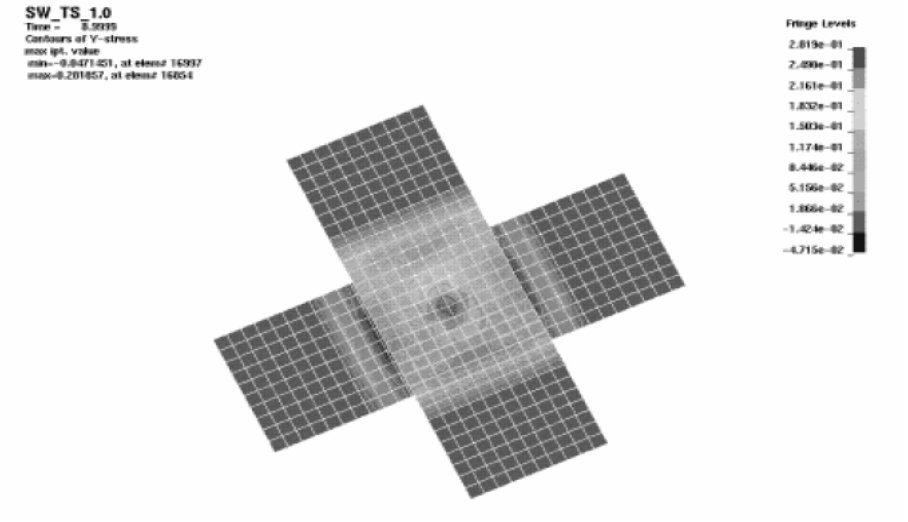

(b)

Fig 2.12: Contour plots of effective stresses (equivalent stress) after Allanki and Kumar (2005). (a) Lap shear coupon (b) Cross tension coupon

Cavalli et al. (2005) analysed the spot weld failure in a coupon from utilizing 3 – D cohesive elements at the interface of the spot weld nugget and the base metal. The spot weld nugget and the base metal were modelled using 3 – D solid elements. The failure criterion for the spot weld was utilized from a fracture mechanics point of view using traction separation laws. This

approach is well suited for the failure simulation but it does not represent the material degradation near the weld nugget boundary as had been reported from the experimental analysis by Zuniga et al. (1997).

Adib et al. (2004) has developed another spot weld model using 3D solid elements to study mechanical behaviour of the spot welded lap shear coupon under quasi - static tensile and compressive loading conditions. It was reported from this study that the joint connection with triple or multiple spot weld nuggets provides similar characteristics while the single spot weld nugget exhibited a complex deformation pattern. The failure location and failure propagation direction for multiple spot welded joint was identified in the study. But no failure criterion was implemented in this model.

Lee and Choi (2005) had attempted to model the spot weld failure for quasi - static states incorporating the Tvergaard yield criterion. The spot weld nugget and the coupon were modelled with solid elements only. The developed model was calibrated according to experimental results for spot weld overload failure in the quasi - static state. Then the model was forced to act according to that calibration.

Yoda et al. (2006) has developed a new rupture screening method for the spot welded automotive body sections. To predict the unknown parameters in the rapture detecting criterion, they had used two different spot weld models. They had developed a “detail model” by dividing the shell elements in the shape of a spider web to represent the spot weld nugget. The failure of the spot weld joint in this model was simulated based on the element strain. When the strain level reached a certain limiting value then the elements around the nugget were deleted. The other model “Spot beam model” was developed with a beam element to represent the spot weld nugget. The failure simulation of this model was attempted according to the following Equation 2.11.

$$\frac{F}{F_o} = 1$$
$$F = f(F_a, F_s)$$
$$F_o = g(\phi, t) \qquad (2.11)$$

F_a : axial force acting on spot beam element
F_s : shear force acting on spot beam element
F_o : a criterion derived from experiments
ϕ : loading angle
t : thickness of base sheet metal

But this model could not predict the failure of the spot weld connection properly. Hence they used the detailed model to identify the rapture load for the developed screening system. The load displacement history obtained from the developed spot weld models are presented in the following Figure 2.13.

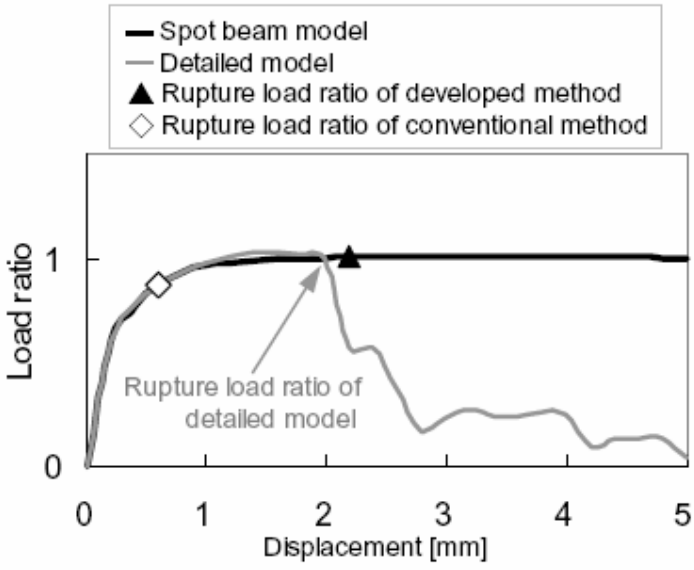

Fig 2.13: Load displacement history for lap shear coupon with thickness 0.8mm after Yoda et al. (2006)

The rupture loads obtained from the simulations (for lap shear, coach peel and U tension coupons) were used to predict the rupture risk depending on the stresses acting around the nugget according to the following rule.

$$R(\tau_{max}, \sigma_{max}) \equiv \left(\frac{\tau_{max}}{\tau_f}\right)^2 + \left(\frac{\sigma_{max}}{\sigma_f}\right)^2 \quad (2.12)$$

Where τ_f is the shear rupture load and σ_f is the rupture load in tension. But this formula is similar in nature with the condition used for simulating failure in “Spot beam model”. The proposed rule for calculating the rupture risk has got some inherent deficiency. Hence it was reported that for certain locations in a body structure this method under-predicted the number of spot weld joints that failed in a crash situation. P. Wung et al. (2000, 2001) had first proposed this type of formula based on the forces acting in the nugget. Discussion regarding Wung’s study is presented in section 2.11 of this chapter.

Wang et al. (2006) have used an arrangement of rigid beam elements around the circumference of the spot weld nugget to represent the joint connection. They have simulated the spot weld behavior for tensile and shear loading conditions. The force displacement response reported in this study is given in Figure 2.14. The Heat Affected Zone (HAZ) material properties around the spot weld connection along with the homogeneous base metal material property were used in the developed model. But the HAZ material properties (yield strength of the HAZ) were extracted by modifying the proposed equation (relating hardness values in HAZ) by Zuniga et al. (1995), which was extracted experimentally by thermal simulation for a particular material. So the extracted equation (even though it was modified artificially) might not be applicable for any different material other than the particular material of interest. This reason may have caused

the force deflection curve obtained from the simulation not to predict the characteristics similar to the experimental results. Two different types of characteristics were implemented within the developed model for simulation purposes in this study. The model with out any failure criterion was referred as “Model with out Failure” (MWOF). And model with the failure criterion was referred as “Model with Failure” (MWF). Four different cases were used from the point of view of used material properties (plastic range beyond the yield stress) for HAZ in the developed models. Case R0 refers the model response which used the material properties of the base metal only. Case R1 denotes the model which was developed with material properties for HAZ obtained by the method proposed by Lalam (as cited in Wang et al. 2006). Case R2 was developed on the basis of the proposed method by Rathbun et al. (2003) (as cited in Wang et al. 2006). For case R3 the material properties for the HAZ were developed with the averaged values of the other two methods. In case of R4 the yield strength of the HAZ material property was artificially made higher than the experimental value.

The failure criterion was incorporated for these different cases for different material property zones. For R1 and R3 cases the failure was defined in the base metal area. Whereas for the R2 and R4 cases the failure was defined in one of the HAZ layers which was adjacent next to the base metal area. The failure criterion used for the MWF models is based upon the maximum strain value attained by the MWOF model at the corresponding experimental failure displacement value. But the fact is that, this approach is actually referring to the simulation process of the material failure. Hence the failure parameter value should be obtained directly from the experimental tests of the material, not from the simulation with models without any failure criterion.

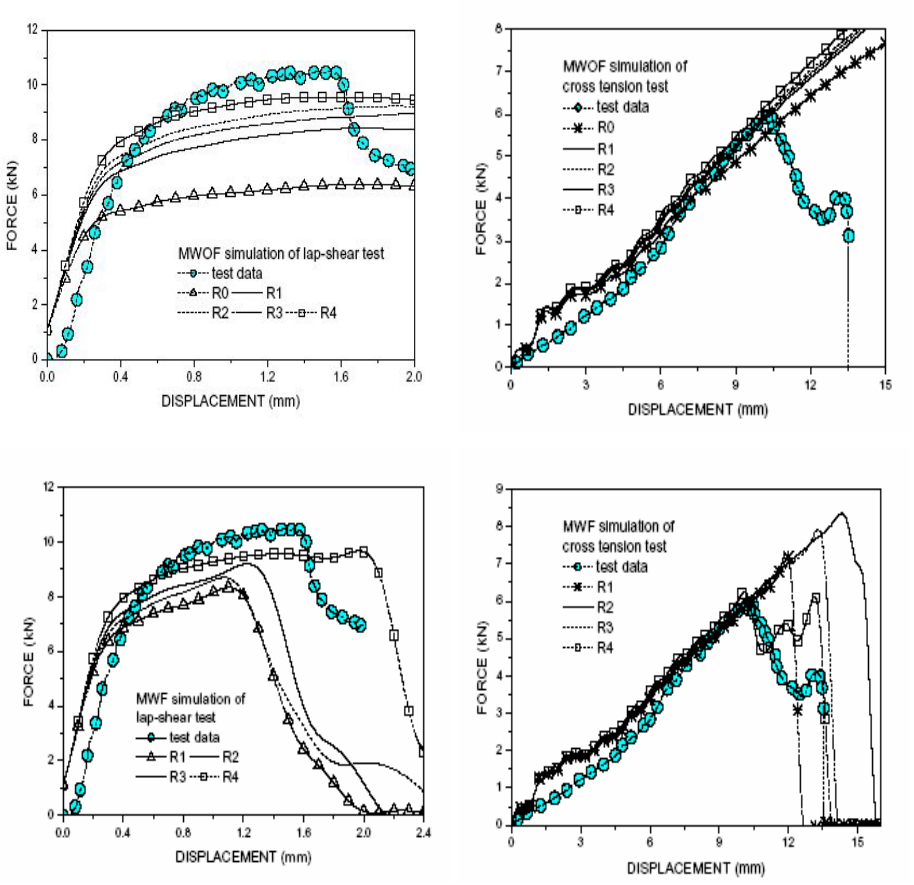

(a) (b)

Fig 2.14: Comparison of simulation result and experimental result for (a) lap shear coupon configuration and (b) cross tension coupon configuration after J. Wang et al. (2006)

2.8 Spot weld models for fatigue loading condition

Many researchers have attempted to model the spot weld joint for the fatigue loading condition. It is not the intention of this thesis to simulate the spot weld failure for the fatigue loading condition. But it might be advantageous to point out the characteristics of the spot weld models that have been used for this purpose. Hence in this section some of those spot weld modelling techniques and strategies used for durability analysis are discussed. It should be duly noted that the information presented here

excludes the discussion for different fatigue life prediction methodologies followed by these researchers.

Zilincik et al. (1998) had used similar spot model (arrangement of rigid beam elements) like J. Wang et al. (2006) to simulate the critical conditioned joint in an assembly of sheet metal parts which were definitive to be subjected to fatigue failure. The difference between these two models were J. Wang used 16 rigid beam elements along with heterogeneous heat affected zone material properties for the sheet metal coupon while Zilincik (1998) has used 9 rigid beams with homogeneous material properties for the sheet metal assembly system. Zilincik (1998) had utilized a quad dominated transition mesh to ensure that the internal loads are properly transferred between the meshed parts. Different types of loading conditions (static, dynamic and fatigue durability analysis) were considered for the developed model. It was reported that the model responded well for all the situations. But there were no failure criterion incorporated in this model for the static or dynamic loading situation.

Sheppard (1993) had developed different models for the spot weld connection to estimate the fatigue propagation life. She had proposed several arrangements of rigid beam elements along the circumference of the spot weld nugget diameter depending upon the output requirements, which also included the basic idea of the models used by Zilincik et al. (1998) and J. Wang et al. (2006). The nugget was also represented by the 3D solid elements and just a single rigid beam element. The solid nugget representation included a finite notch radius for the nugget which had increased the number of elements along the nugget diameter relative to the information sought from the simulation. The single rigid beam element model incorporated artificial stiffness by increasing the thickness of the shell elements at the connection point which was completely impractical.

Radaj (1990) has used solid elements to represent the spot weld model both on the test coupons and box type structures. This was done to obtain values of the stress parameters near the spot weld nugget boundary to be used to compute the stress intensity factors. The solid elements representing the weld nugget were attached to the shell elements which represented the coupons. In this model the solid elements were modelled with elastic material properties only. Further more geometric nonlinearity was not incorporated in this model. Hence it was unable to capture the actual deformation shape of the welded coupons.

Ni and Mahadevan (2003) reported the use of a similar type of spot weld model to predict the probabilistic fatigue crack growth analysis in T joint configuration. This model was developed by using MSC. / NASTRAN and MSC. / FATIGUE. Only elastic material properties were used in this model definition. The difference of this model with the previously developed model by Radaj (1990) is that the weld nugget was attached to solid elements which represented the T joint structure.

Rui et al. (1993) had attempted to estimate the fatigue life for a multi welded box type structure with a “Global-Local” approach. The far field stress distribution obtained from the simplest spot weld model in an assembly system with a bar element was utilized in conjunction with a detailed spot weld model with shell elements to predict the fatigue life. However the detailed spot weld model performance was not judged in this study. But that objective was accomplished by Dincer et al. (2006). Five different spot weld nugget representations were investigated in this study using a box profile with a torsional load applied at one end. The spot weld models considered for the study were the single rigid beam model, the single elastic beam model, the umbrella spot weld model, the nine point contact spot weld model and the weld element CWELD available in commercial finite element code MSC. / NASTRAN. It was reported that the nine point contact spot weld model had better performance in strain

prediction study. For the fatigue life study, the nine point contact model and the umbrella model had relatively better results than the other models. Here in this study all the model performances were judged using only elastic material properties. This might be sufficient for the fatigue life estimation study but is insufficient to consider the performances in other dynamic loading situations.

2.9 Spot weld models for NVH simulations

Liu (2000) had used a simple model to represent the spot weld connection in a sample cantilever beam structure used to analyse the vibration characteristics of welded structures. The spot weld was modelled as a coupled system and consisted of one translation and one rotation spring in this study. This model is very much similar as the common spot weld modelling trend (utilising single beam element) reported in Machine Design (1994). The combination of spring elements for a single spot weld joint has most likely been used to gain access to all six degrees of freedom at both the joining nodes.

Zhang (2005) had proposed a spot model to use with two non-matching shell element meshes. The model was developed because of the inherent disadvantage (inability to deliver the proper level of stresses for fatigue life prediction) of the CWELD spot weld element (in the commercial finite element code MSC. / NASTRAN). The developed spot weld model consisted of a central elastic beam element connected to the shell elements with rigid beam connections. This model was used to predict the natural frequency and mode of vibration and the results were verified with test results from simple coupon configurations. The model was also applied for fatigue life estimation and it was pointed out that this model could be a common spot weld model for both types of applications. The only remaining

sector to be emphasised to conduct study with this model is the crash situation.

Lardeur et al. (2000) attempted to analyse the spot weld modelling technique for vibration behaviour of automotive structures. As the basis for the comparison study the quality of modal bases and response to the frequency functions were chosen. The point-to-point connection and surface to surface connections were used as the modelling method of the spot weld joints. The representations of the developed models in this study are provided in the following Figure 2.15. It was reported that the surface based modelling of spot weld connections with a non coincident mesh were the better technique for this particular purpose. But all these models were developed based upon the linear approach which is quite reasonable for vibration analysis.

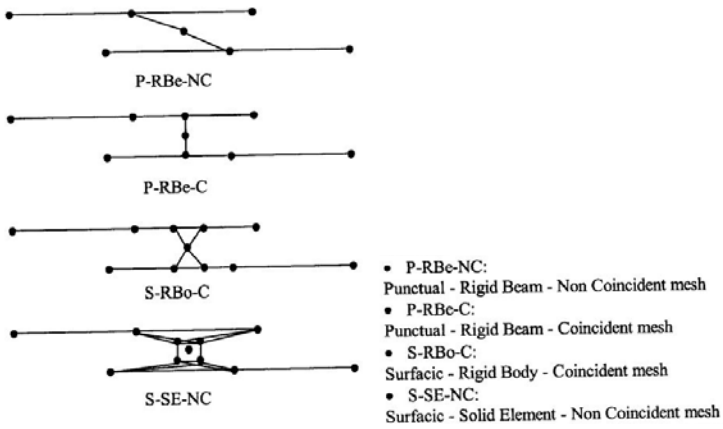

Fig 2.15: Models for vibration study after Lardeur (2000)

2.10 Spot weld model for Optimization simulations.

Many researchers had performed optimisation simulations on the spot welded automotive related structures for different purposes. Xian et al. (2006) had attempted to optimize the crashworthiness characteristics of the spot welded thin walled sections. To represent the spot welds, this study

had considered 16 different models. The variations of all these models were made by manipulating the common element sharing strategy, the common node adjustment technique or the placement of rigid beam or spring elements in different arrangements. No failure criterion was incorporated in any of the models. By comparing the data obtained from experimental analysis, it was reported that the rigid node spot weld model (where nodes of elements were defined as rigid) performed better in this analysis. This conclusion was based only on mean crushing force, but the separate performance study for the computational effort was not investigated.

Zhang and Taylor (2001) have used the umbrella model of the spot weld to maximize the stiffness value under fatigue life constraints. The umbrella model consisted of rigid beam elements to represent the weld nugget, which were attached to the shell elements that represented the sheet metal. It was reported that this model was successfully implemented in the optimisation scheme. The spot weld model and mesh design used in this study is given in Figure 2.16.

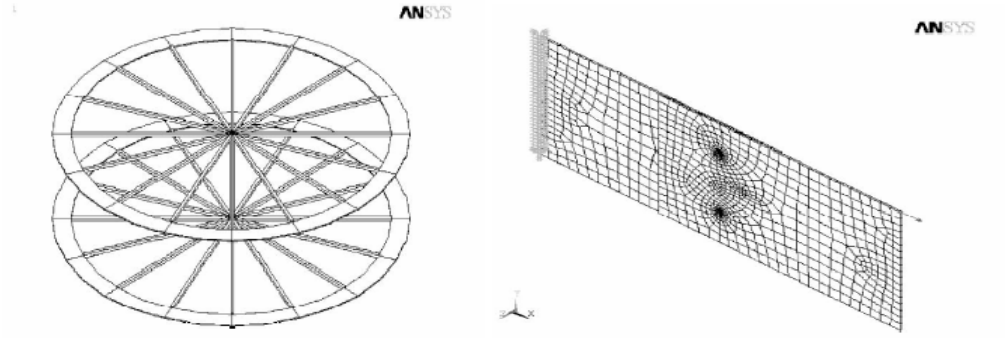

(a) (b)

Fig 2.16: Umbrella spot weld model and mesh design for tensile shear specimen after Y Zhang and D Taylor (2001)

2.11 Spot weld models for assembly systems

For the assembly systems there are couple of spot weld models that are reported to be widely used. The most common method to represent the spot weld joint is reported as the common node or coincident nodes of linear shell elements or bar elements (Y Rui et al. 1993, Machine Design 1994). A typical example was presented by Fermer et al. (1999) for the Volvo S80 Bi Fuel tank assembly system which is given in the following Figure 2.17. The spot welds were represented by CBAR elements (MSC. / NASTRAN code) in the virtual prototype of the fuel tank.

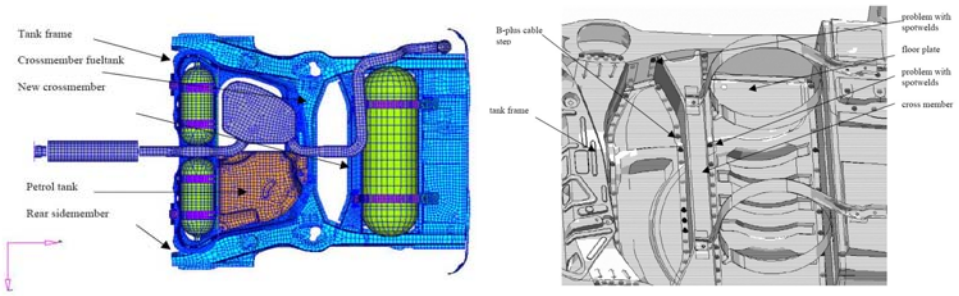

(a) (b)

Fig 2.17: Volvo S80 Bi Fuel tank assembly system after Fermer et al. (1999). (a) Mesh generated in the assembly system (b) Location of the spot welds.

Apart from all of these there is a couple of automatic spot weld models available in commercial finite element codes. Researchers and designers have used CWELD and ACM2 weld model or HEXA weld model available in commercial FEM code MSC. / NASTRAN. (Fang et al. (2000), Heiserer et al. (1999)). CWELD is designed as a shear flexible beam type element. The ACM2 or HEXA weld element is a solid element representing the spot weld nugget and attached to the sheet surface by rigid beam elements RBE3. It was reported by Pallmonela et al. (2004) that the ACM2 spot weld model performed slightly better than the CWELD model when used in the

natural frequency of vibration extraction from the spot welded double hat section. But the dimensions used to represent the spot weld by these two models in this study were different. The edge dimension for the ACM2 model used in this study was 3mm and the diameter for the CWELD element was 6 mm. It was suggested that the spot weld diameter did not have any influence on the failure of the spot weld for this kind of analysis. Moreover no report was found on the usages of these two spot weld models for dynamic crash analysis. In case of the dynamic crash loading it was observed from the experimental analysis that the spot weld failure modes depend on the diameter of the spot weld. (Y J Chao (2003)).

To simulate the spot weld failure in box type rail sections most of the researchers had employed the non linear finite element code LS – DYNA. Sawai et al. (2005) has concentrated on this particular section of spot weld failure modeling using LS – DYNA. Numerous types of keyword options available in LS – DYNA were used to represent the spot welds as beam and spring elements in the box type rail structure for static axial crash and dynamic crash simulations. Different connection strategies of these beam and spring elements (connected to element nodes, surface nodes etc.) were followed. A force based failure criteria was implemented with these models. Both the simplified force based failure criteria (consisting of only shear and normal force components) along with the complex (considering all the forces and moments in all the three directions) force based failure criteria were implemented. From the simulation results it was revealed that the spot weld model with the beam elements connected between the element nodes predicted relatively good results for the spot weld failure.

The force based failure criterion that was used by Sawai et al. (2005) was proposed by P. Wung et al. (2000, 2001). The failure rule was basically assumed from a combined fracture criterion. This assumption was verified by the experimental results obtained from simple spot welded sheet metal coupons. The form of the failure criteria is given in Equation 2.13.

$$\left(\frac{f_s}{F_s}\right)^{\alpha}+\left(\frac{m_b}{M_b}\right)^{\gamma}+\left(\frac{f_n}{F_n}\right)^{\mu}+\left(\frac{m_t}{M_t}\right)^{\beta}=1 \qquad (2.13)$$

where:

F_s = Failure load of spot weld in shear loading conditions

M_b = Failure bending moment for bending load conditions

M_t = Failure moment for in plane torsion load conditions

F_n = Failure loads of spot weld in tensile loading conditions.

f_s, fn, m_b, m_t = load carried by the spot weld model

α, β, μ, γ = Coefficients related to shear, torsion, normal or tensile and bending loading condition respectively. The values to all of these coefficients are 2.

Generally most of the failure criteria for engineering design are based upon the stress acting in the structural section. But in the case of a spot weld nugget, due to the geometric complexity and changes in material properties around the nugget, the stress field near the nugget is highly unpredictable. Hence the failure criterion forces acting on the nugget itself were used. One important point to be noted about the applicability of these relationships (as provided by Wung (2000, 2001)) is that they can be used as failure criterion until these forces become not proportional to the state of stresses. Hence this failure criterion defines failure of the spot welded joints within the elastic limit of analysis. Moreover this failure criterion does not address the behavioural characteristics of the joint once the failure is initiated. For simulating the crash behaviour of the joint, the post failure characteristics are important to predict the deformation pattern and level of absorbed energy. So for simulation this point should be addressed.

2.12 Scope of the present work

The present work will emphasize the realistic modelling of a single spot weld failure situation. At the same time this work will also consider the simplicity issue of the developed models, which is of critical interest if these models are to be incorporated in a large assembly system that contains thousands of spot welds. Six different models to represent the spot weld joint will be developed and presented in this study. Performance of these six models will be studied for their load bearing capability and for the failure simulations.

Generally the quality of spot welds is tested by destructive testing methods (Resistance Welding Committee, American Welding Society (AWS), (1956)). For these destructive tests, single spot welds on test coupons are used. Hence to compare and judge the performances of different developed models, configurations of simple test coupons for different loading conditions are used in this study. Similar test coupons are used for quasi static loading conditions and dynamic crash loading situations. Models were built with the similar dimensions as the experimental test coupons. For analysis purposes the commercial finite element code ABAQUS will be utilized. The spot weld models developed in this work will be evaluated with elastic plastic material properties and proper contact definition. The performances of the developed models for different loading conditions will be compared to identify a model which will be computationally cheap but accurate to simulate the failure of the joint.

It has been presented in the previous sections that the current state for the modelling of spot weld failures are lacking of addressing the post failure behaviour of a spot welded joint. Hence it will be attempted to simulate the post failure characteristics of a spot weld joint.

2.13 Limitations of the present work

The following points state the limitations of the current work:

- The variation of the spot weld manufacturing process parameters will not be considered in the present study.
- The residual stress resulting from the manufacturing process will not be considered in developing the spot weld models. Hence the developed models presented in this thesis are free of any previous distribution of residual stresses.
- The geometric irregularity of the spot weld nugget caused by indentation impression from the spot weld machine electrode tips will not be considered in this study.
- The developed models and their respective verifications are applied only to the designated material in this thesis. The results may vary if other materials are used.
- The developed models will predict only the nugget pull out type of failure for the spot weld joint as it is the desired mode of failure for the spot weld joint (Ewing (1982), Zuniga (1997)).
- The models presented and judged in this study were developed with homogenous material properties. That is the material property for the HAZ and the base metal is the same for all the models developed in this study. This gross assumption was made for the sake of simplicity in the developed models. It was already stated in section 2.12 that these models are developed with intention to be very simple, so that they might be incorporated in large assembly systems. Generally in large structural assemblies spot welds are modelled with a single rigid beam element (Machine Design (1994)). The rigid beam connects only two nodes on the different parts which are to be joined. The HAZ is completely ignored in those models. Hence one of the intentions of this study is to evaluate the achievable accuracy level with the most simple spot weld models

without the HAZ. Moreover, it has already been presented in section 2.7 that the most recent study on spot weld failure analysis by Wang et al. (2006) considered the HAZ properties with some assumptions which are scaled values of the base metal stress strain curve. There is no actual value for the material properties of the HAZ. The failure criterion was also implemented either in the base metal region or in the HAZ layer adjacent to the base metal area. The most successful model response presented in that study was obtained through case R4 as indicated in Figure 2.14. But in case R4 the yield stress of the HAZ material was artificially raised without any proper explanation, which eventually made the HAZ much stronger than the base metal. Therefore the strategy followed by Wang et al. (2006) is impractical and the HAZ material property is not included in the present study.

The material property used for the developed models in this thesis was extracted from the mechanical tests of the selected sheet metal. The mechanical testing procedure and the extraction procedure are presented in the next chapter.

Chapter 3

Material Property Characterisation

3.1 Overview

This chapter presents the methodology and the results for the experimental study undertaken to extract the material properties of the sheet metal used for the study of spot weld failure behaviours. The content of this chapter is presented according to the following subsections.

3.2 Material used for the study
3.3 Assumptions for material characterisation
3.4 Testing configuration for material characterisation
3.5 Specimen preparation for material characterisation
3.6 Data extraction for material characterisation
3.7 Flow curve construction
3.8 Results of material property characterisation experiments

3.2 Material used for the study

The material used for this study was a cold rolled formable CA3SN-G steel manufactured by “Blue Scope Steel Limited”. The sheet metal was provided with skin passed deep drawing properties and a general purpose surface finish. This sheet metal was produced according to the Australian standard AS/NZS 1595. Typically this sheet metal contained 0.04 – 0.06% of carbon. Other than carbon there are also some other particles present in the chemical composition of the steel used for manufacturing this sheet metal. The details of the chemical composition are provided in the Appendix - A. The yield

strength of CA3SN – G sheet steel is reported as 240 Mpa (maximum) by the manufacturer. Further more according to the manufacturer data sheet this general purpose sheet metal is typically used for unexposed drawn parts for automotive and appliance end applications. Hence this sheet metal was chosen to conduct the present study.

3.3 Assumptions for material characterisation

The first assumption in deriving the material parameters for this study, (as an input value in FEM simulations presented in next chapter) was the value of the modulus of elasticity of the chosen material. The value assumed for the chosen material was 200 GPA. The actual value for the chosen sheet metal was not derived from the experimental data due to the unavailability of a high precision extensiometer with automatic data recording facilities. The available extensiometer could not extract data within the elastic range of the chosen material with required precision. Moreover this value for modulus of elasticity is very common to any steel material for general purpose uses.

The second assumption was for the material model used in this study for the chosen sheet metal (CA3SN – G). It was assumed to be an isotropic material. The reason behind this assumption is primarily because there was no information provided in the manufacturer data sheet (Appendix - A) about the plastic strain ratio. Further more, the characteristics of a similar type of material (with modulus of elasticity of 200Gpa, yield strength of 245 Mpa and strain hardening exponent of 0.2) used by other researchers (Lee et al. (2006)) were reported to be of isotropic in nature. As an example the true stress true strain curve is provided in Figure - 3.1 after Lee et al. (2005).

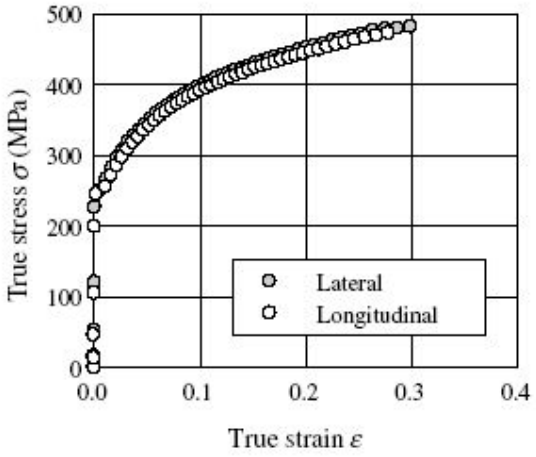

Fig3.1: The true stress – true strain curve in lateral and longitudinal direction after Lee et al. (2005)

3.4 Testing speed configuration for material characterisation

Material characterisations were carried out by uniaxial tensile tests. Material samples with specific dimensions according to an established standard were mounted in the universal tensile testing machine. For this purpose an Instron twin column table top type (Model Number 5569) universal testing machine with 50 KN load capacity was used. The testing machine had wedge shaped grip construction. The details of the machine specification are provided in the Appendix - B. For the strain reading, an extensiometer with computer interfaced data recording facility was utilized. The calibration details of the extensiometer are given in Appendix - C.

The prepared samples of the sheet metal were pulled apart to extract the material characterisation curve (true stress – true strain curve). Four different testing speed configurations were used for the testing purposes. One of the testing speed configurations was at the maximum speed limit of the tensile testing machine (500 mm/min). The other testing configurations were at reasonably slower speed limits (100 mm/min, 20 mm/min and 4 mm/min). The results (force - displacement curves) obtained from these tensile tests are presented in section 3.6 of this chapter (Figure 3.4).

3.5 Specimen preparation for the material characterisation

The specimens for the material characterisation tests were prepared according to the specifications provided by Standards Australia AS – 1391. This standard is technically similar to the international standard ISO 6892. The shape of the testing specimen was similar to a dog bone. The gauge length used for the tests was 50 mm. The grip sections at both the sides were 50 mm each. The thickness of the specimen was the same as the thickness chosen (1.19 mm) for the coupons to be used to prepare spot welded samples. The transition radius between the grip section and the gauge length was 12 mm. Three specimens were prepared for each type of testing speeds (500 mm/min, 100 mm/min, 20 mm/min and 4 mm/min). The detail dimensions of the prepared specimens used are provided in the Figure 3.2.

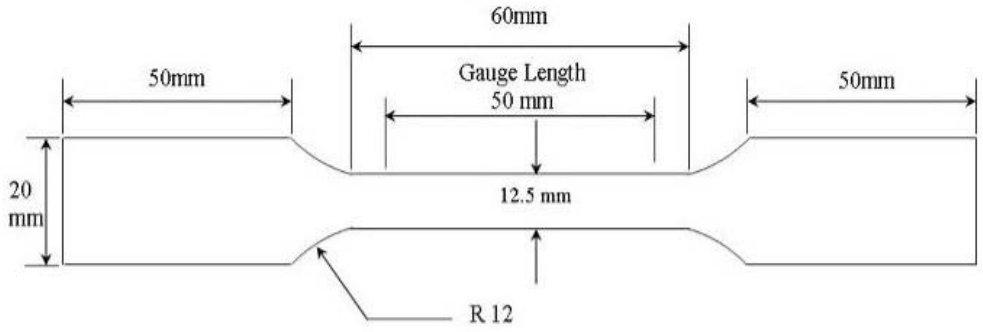

(a) Schematic figure of the test specimen

(b) Prepared tensile test specimens

Fig 3.2: Specimen dimensions for the tensile testing of sheet metal

3.6 Data extraction for material characterisation

From the uniaxial tensile tests performed in the universal tensile testing machine, the force data and the displacement data were recorded. The force data was obtained from the load cell reading which was mounted in the testing set up. The displacement data was recorded from the extensiometer reading which was attached along the gauge length of the specimens. The test setup is presented in Figure 3.3. The tests were repeated three times for every testing speed configuration (500 mm/min, 100 mm/min, 20 mm/min and 4 mm/min) and the average force displacement data for each case (speed configuration) was extracted from these responses. These experiments were displacement controlled experiments. So the averaged force values were considered for a particular displacement position. These averaged curves were used to construct the flow curve of the material which is discussed in section 3.7. The averaged force displacement responses are presented in Figure 3.4.

(a) (b)

Fig 3.3: The test setup for the material characterisation experiments

(a) Extensiometer setup for 500 mm / min tests

(b) Extensiometer setup for 4 mm / min tests

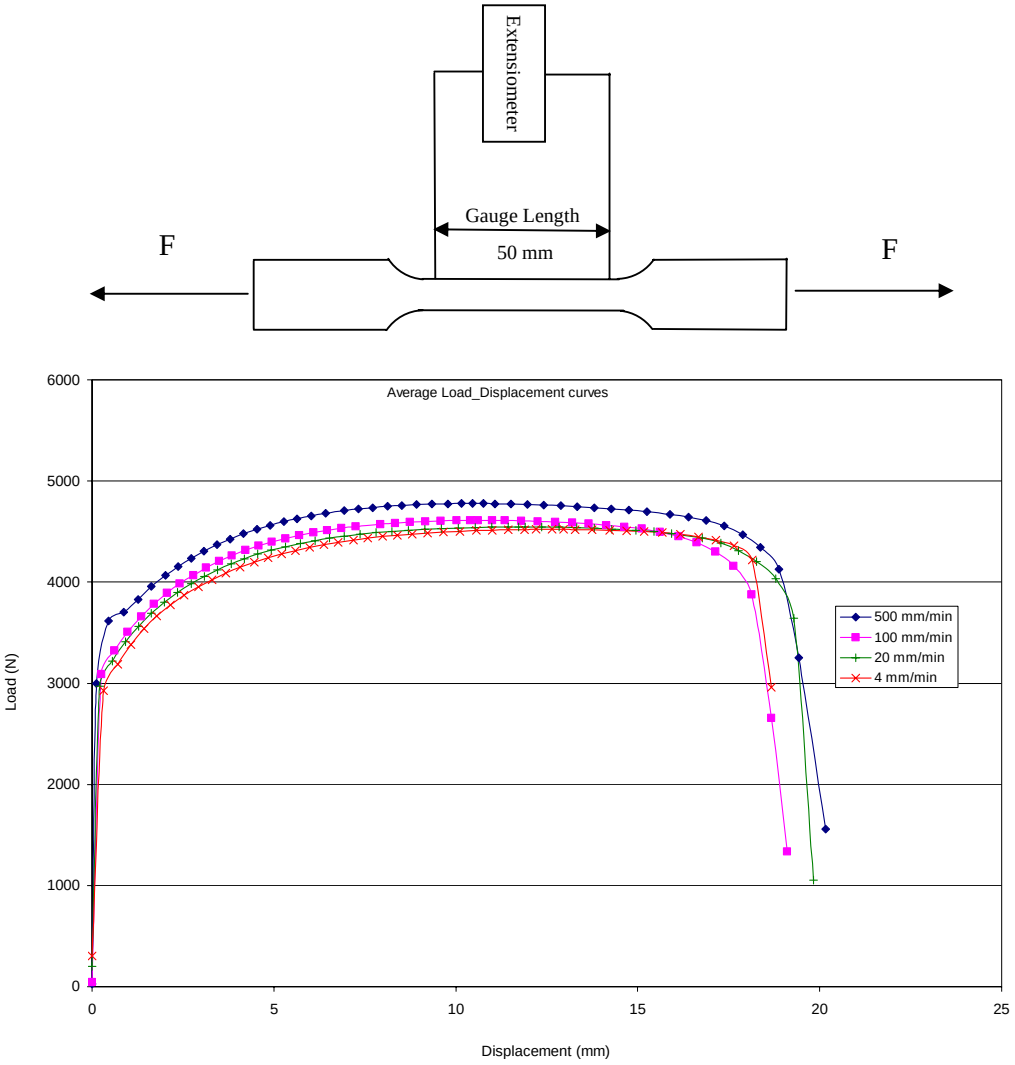

Fig 3.4: Force displacement curve of uniaxial tensile test of the sheet material

3.7 Flow curve construction

The flow curve was derived from the force displacement data obtained from the tensile testing of the chosen sheet material. The force-displacement data was converted into engineering stress and engineering strain values according to Equation 3.1 and Equation 3.2.

$$\sigma_e = \frac{F}{A_o} \qquad (3.1)$$

$$e = \frac{\delta}{L_o} \qquad (3.2)$$

Where σ_e and e are the engineering stress and the engineering strain respectively. A_0 is the initial cross sectional area of the specimen at gauge length section. L_0 is the initial gauge length.

The yield stress of the chosen material was determined by the classic approach of 0.2% offset method since the stress strain curve did not exhibit a precise point as a yield point. Here it should be noted that the slope of the offset curve was determined by assuming the modulus of elasticity as 200 GPA as it has been notified in the previous section (section 3.3). In Figure 3.5 the determining procedure of the location of the material yield point is shown.

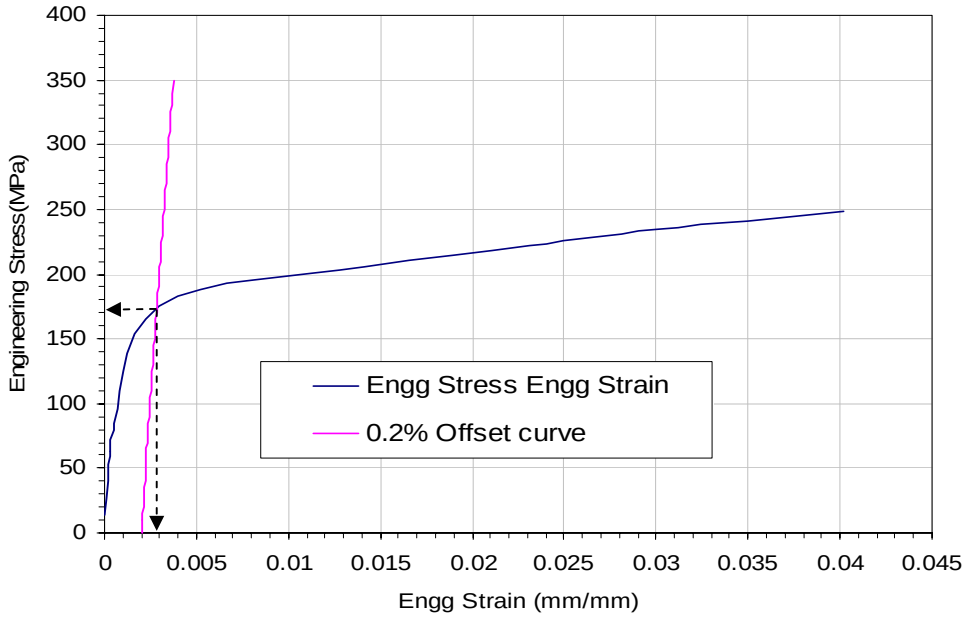

Fig 3.5: Schematic representation of yield stress determination by 0.2% offset curve.

After determining the yield stress locations for each test, the ultimate tensile strength point was determined from the maximum force location on the force displacement diagrams. Then the data points from the yield point to the

ultimate strength point of the engineering stress - engineering strain curves were separated to be converted into true stress true - strain curves. Data points were considered up to the ultimate strength point. This is because after this point the material failure process is initiated. The true stress data was obtained from the force data divided by the actual cross sectional area at that particular instance of loading condition. The exact cross sectional area was obtained by employing the condition of constant volume for the plastic deformation process of the material. The Equation 3.3 to Equation 3.7 were utilized to derive the true stress - true strain curve.

$$L_f = L_0 + \delta \qquad (3.3)$$

$$A_0 L_o = A_f L_f \qquad (3.4)$$

$$A_f = \frac{A_0 L_0}{L_f} \qquad (3.5)$$

$$\sigma_T = \frac{F}{A_f} \qquad (3.6)$$

$$\varepsilon = \ln\left(\frac{L_f}{L_0}\right) \qquad (3.7)$$

Where

$L_0 =$ Initial gauge length

$\delta =$ Displacement data obtained from extensiometer reading

$L_f =$ Actual gauge length of the specimen at a particular load $= L_0 + \delta$

$A_0 =$ Initial cross sectional area at the gauge length of the specimen

$A_f =$ Actual cross sectional area at the gauge length of the specimen at a particular load

$F =$ Force reading obtained from the load cell.

$\sigma_T =$ True stress

$\varepsilon =$ True strain

Now from the true strain value the elastic strain value and the plastic strain value were separated according to the Equation 3.8.

$$\varepsilon_{TPL} = \varepsilon_T - \frac{\sigma_T}{E} \qquad (3.8)$$

Where

$\varepsilon_{TPL} =$ True plastic strain

$\varepsilon_T =$ True strain

$\sigma_T =$ True stress

$E =$ Modulus of elasticity.

Now this true stress – true plastic strain values were used to fit for the parameters of the Ludwik's equation according to the form shown in Equation 3.9.

$$\sigma = \sigma_0 + K\varepsilon^n \qquad (3.9)$$

Where

$\sigma =$ Flow stress

$\sigma_o =$ Yield stress.

$K =$ Strength modulus

$\varepsilon =$ Flow Strain

n = Strength hardening coefficient.

3.8 Results of material property characterisation experiments

The equations of the flow curve obtained through the above mentioned procedure are as follows. The flow curves were constructed from the averaged force displacement curves presented in Figure 3.4. For 500 mm / min test the curve is

$$\sigma = 235.0 + 510.61\varepsilon^{0.1662} \qquad (3.10)$$

For the 100 mm / min test the equation is according to the following form.

$$\sigma = 220.0 + 515.38\varepsilon^{0.1901} \qquad (3.11)$$

For the 20 mm / min test the equation is according to the following form.

$$\sigma = 212.0 + 509.9\varepsilon^{0.1913} \qquad (3.12)$$

For the 4 mm / min test the equation is according to the following form.

$$\sigma = 209.0 + 517.55\varepsilon^{0.2045} \qquad (3.13)$$

All the curves are presented in the Figure 3.6.

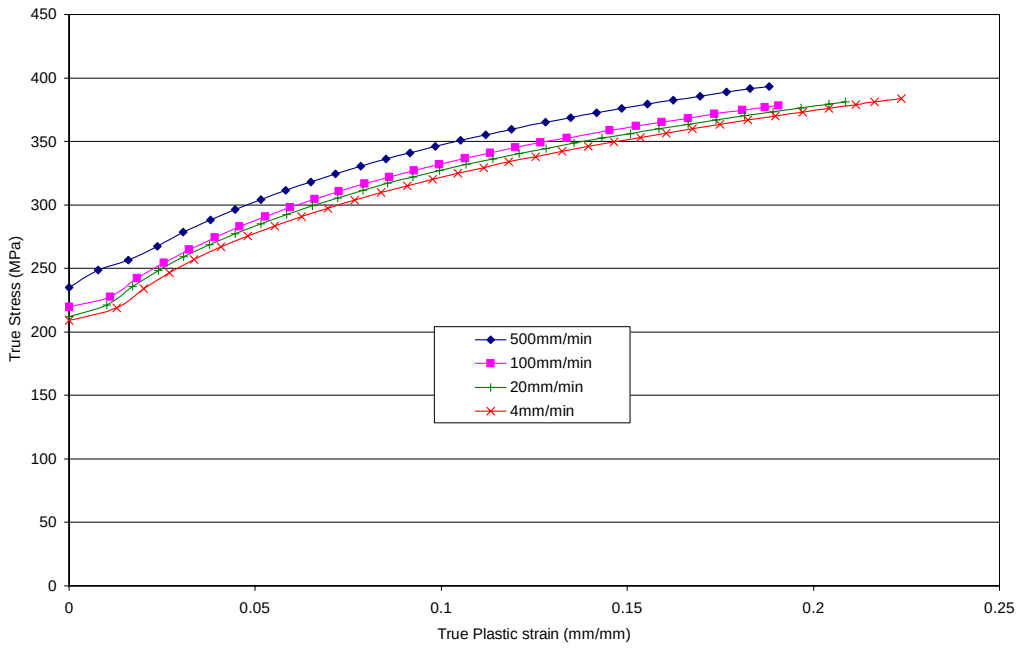

Fig 3.6: The true stress true strain curve for the material CA3SN – G

The results shown in the graph (Figure 3.6) had clearly depicted the influence of the changes of testing speed on the material characteristics. As the testing speed was increased the yield stress of the material had increased. Similarly the ultimate tensile strength point for the chosen material was reached earlier with the higher testing speed configuration. The summary of the obtained results from the flow curve characterisation experiments for all the testing speed configurations are given in Table 3.1.

Summary Topics	Testing Configuration			
	500 mm / min	100 mm / min	20 mm / min	4 mm / min
Yield Stress (Mpa)	235.0	220.0	212.0	209.0
Ultimate stress (Mpa)	325.3871	312.1102	308.8816	306.3556
% Elongation at Ultimate stress	20.93	21.23	23.43	25.3
Strain Hardening Exponent *n*	0.1662	0.1901	0.1913	0.2045
Strength Modulus *K*	510.61	515.38	509.9	517.55
Rate of extension (sec^{-1})	0.14	0.28	0.00561	0.00112

Table 3.1: Summary of the results obtained from different testing speeds for material characterisation experiments.

These material properties are going to be used for spot weld model development purposes described in chapter 6. The material properties extracted at 500 mm/min rate will be used to develop the spot weld models for dynamic loading situations with the explicit FEM code. Similarly the material properties extracted at 4 mm/min rate will be used to develop the spot weld models for quasi - static loading situations with the implicit FEM code. The spot welded coupons were prepared with the same sheet metal and were tested to extract the results which were needed to be used to validate the developed spot weld models. The testing procedure with the spot welded test coupons and results obtained from those experiments are presented in the next chapter.

Chapter 4

Experimental Testing

4.1 Overview

This chapter presents the methodology and the results of the experimental study undertaken to analyse the spot weld behaviour under different loading conditions According to the information provided by Wikipedia "*In the scientific method, an experiment (Latin: ex-+-periri, "of (or from) trying"), is a set of actions and observations, performed in the context of solving a particular problem or question, to support or falsify a hypothesis or research concerning phenomena. The experiment is a cornerstone in the empirical approach to acquiring deeper knowledge about the physical world."* Hence this chapter considers two different points of views for the present study.

- First it defines, justifies and provides conformation for different geometric dimensions used for the coupons to be spot welded for the study.
- Secondly it provides information to verify the performances of the FEM models which enable us to study the spot weld behaviour more rigorously.

The chapter is presented according to the following subsections.

4.2 Testing of Spot Welded Coupons

The testing of spot weld performance under different loading conditions can be conducted by using different coupon configurations. These coupon types are very common and had been used by various researchers for the experimental studies on the mechanical performance of single or multiple spot welds. In this study three different types of loading conditions are investigated. These loading conditions were chosen as these are very common loading conditions for automotive structures in crash situations. These different loading situations were generated through different coupon configurations. The changes in the coupon configurations according to the loading conditions are summarized in the Table 4.1 and shown in Figure 4.1. In this study the U tension coupon was used for the tensile loading condition.

Loading conditions	**Coupon types**
Shear Load	Tensile shear coupon
Tensile Load	Cross tension or U tension coupon
Bending load	Coach peel coupon

Table 4.1: Coupon type variation for different loading conditions.

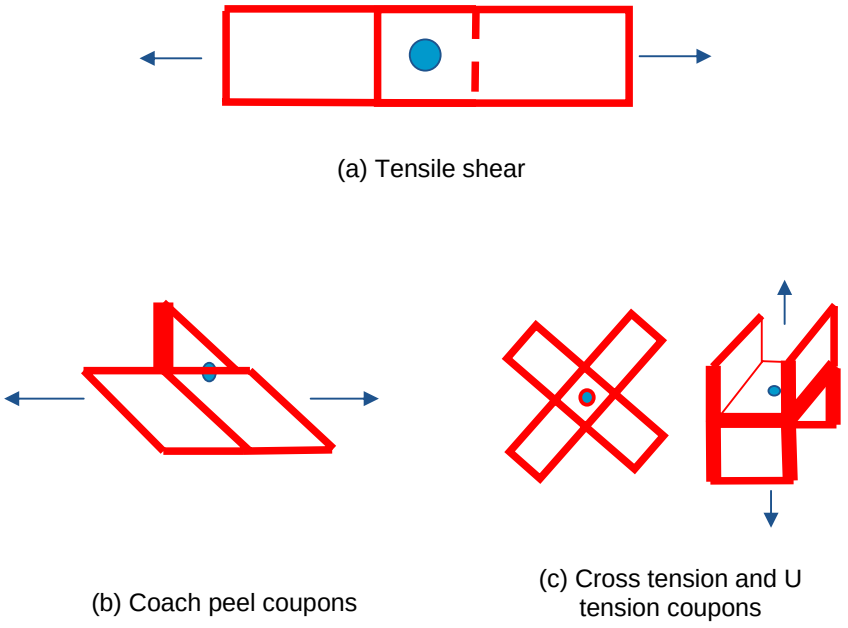

Fig 4.1: Different coupon configurations for different loading conditions.

Among all of these coupon types the tensile shear coupon is the most common for testing the spot weld strength. So the initial calculations for this study will be based upon the lap shear coupon configuration. Later the dimensions obtained from these calculations will be used for the other type of coupon configurations.

4.3 Failure Modes of the Spot Welds

The failure modes of the spot weld were discussed in details by various researchers. The possible locations of failure of the spot welded lap shear coupons were addressed in detail by Zhou et al. (1999). The failure locations and the schematics of the predictive characteristic curves for the respective cases are given in Figure 4.2.

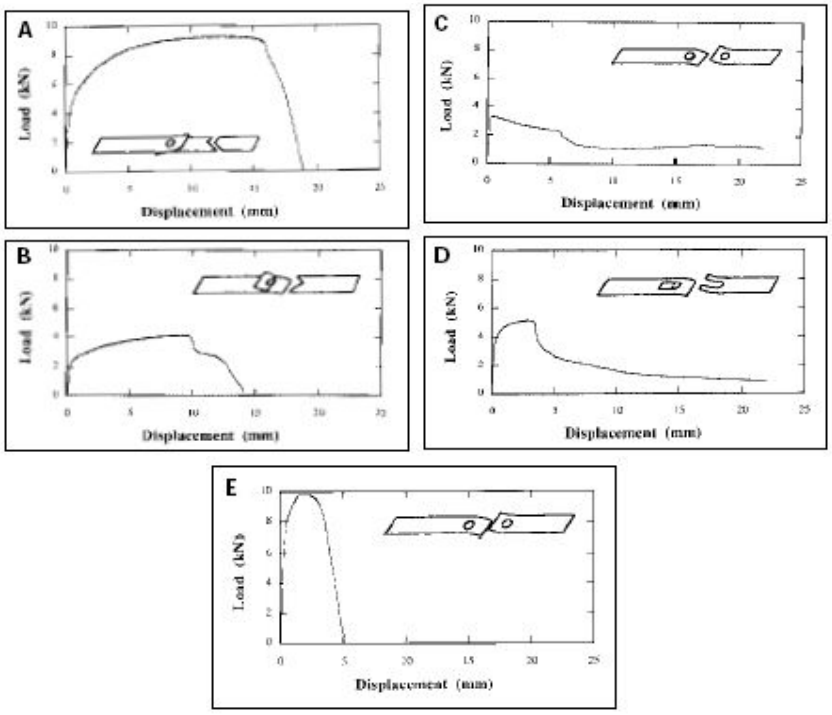

Fig 4.2: Schematic diagrams of failure locations of spot welded lap shear coupons after Zhou et. al (1999)

It can be readily observed from the above figures that the failure locations in Figure 4.2 (A) and 4.2(B) are in the base metal which is not close enough to the spot weld nugget location. Hence they are not the desired mode of spot weld failure. Narrow specimen sizes (length, width, overlap region) may cause these types of failure patterns.

From the other failure patterns (Figure 4.2 (C), 4.2 (D) and 4.2 (E)) it was concluded that these were the desired mode of failure as it causes local deformation to the spot welded region. Figure 4.2 (C) represents nugget pull out failure where the spot weld nugget gets out of the welded coupon. In this case when the nugget pulls out of the coupon, it leaves behind a circular impression of the failure on the coupon material. Figure 4.2 (D) represents

coupon failure near the nugget location where the material tears apart from the coupons. Figure 4.2(E) represents the interfacial failure where the coupons detach from each other at the interface of the spot weld joint without leaving any failure marks on the coupons.

As reported by Zhou et al. (1999) these types of desirable failure behaviours depend on the geometric dimensions of the spot welded coupons. By varying the spot weld nugget diameter (4 mm and 8 mm), width (19, 45 and 60 mm) and the thickness (0.8, 1.2, 1.5 mm) it was shown that most of the interfacial failure occurred in case of the smaller nugget diameter with the highest sheet thickness. Where as the nugget pull out failure occurred within a reasonable combination of the weld nugget diameter, thickness of the sheet metal and the width of the coupons. Further more Chao (2003) reported that for the nugget pull out failure the spot weld absorbs a higher amount of energy. Hence the nugget pull out failure was determined as the most desirable failure mode for the spot weld joints. These observations are also reported by the other researchers (Pollard (1974), Ewing (1982) and Birch et al. (2000)) for both the static and dynamic analysis. Similar types of failure pattern are also reported for other coupon configurations by various researchers (Schneider and Jones (2003), Lin et al. (2004)). The failure patterns reported by these researchers are provided in Figure 4.3. So to obtain reasonable experimental results for the verification of the finite element spot weld models, specific geometric dimensions should be established.

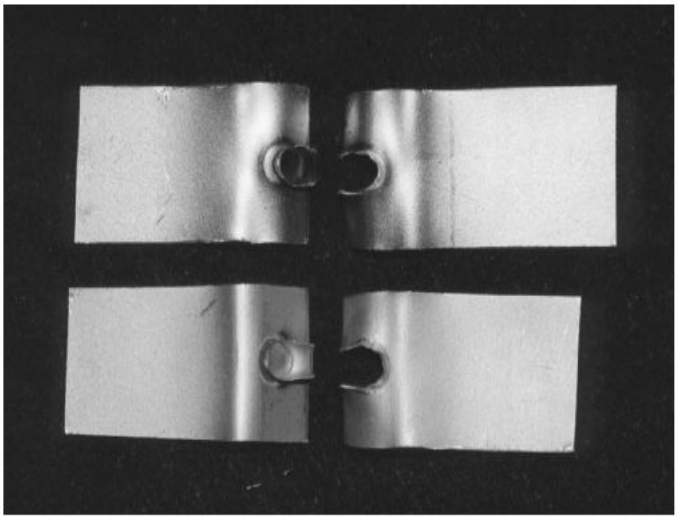

(a)

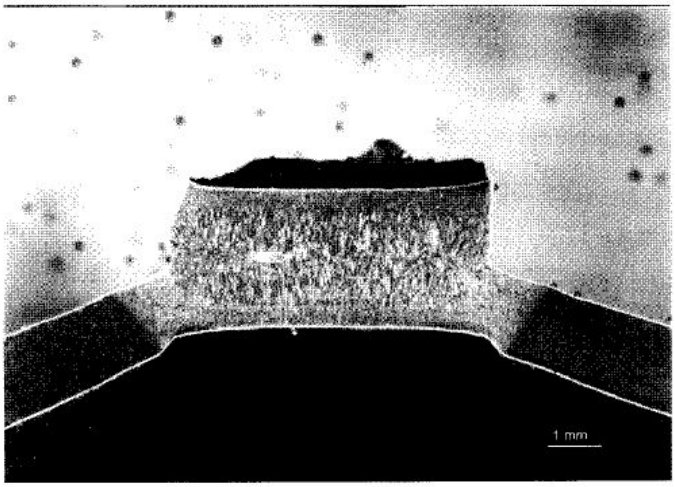

(b)

Fig 4.3: Failure configuration of spot welded coupons

(a) Spot welded Mild Steel (MS) and Interstitial-Free, rephosphorized High Strength steel (IFHS) coupons at quasi static rate after Schneider and Jones (2003)

(b) Sectioned micrograph of spot welded Mild Steel (MS) coupon tested for pure opening load condition at impact speed of 6.7 ms^{-1} after Lin et al. (2004)

4.4 Considerations for Geometric Dimension of the Coupons

The geometric dimensions of the spot welded test coupons that should be considered for the analysis are the thickness of the sheet metal, spot weld nugget diameter, width of the coupon, overlap region and the length of the coupon. In the following sub sections these points are discussed.

- **Choice of thickness**

The thickness of the sheet metal for making the coupons acts as an independent variable in case of the determination of the coupon dimensions. The spot weld nugget diameter depends on the thickness gauge of the sheet metal, which is presented in the next paragraph. The thickness of the sheet metal chosen for this study was 1.2 mm (averaged experimental value 1.19mm). The reason behind choosing this particular thickness gauge was because most of the spot weld nugget diameter - to - thickness expressions were derived and tested either for this particular thickness value, or this value was near the median value for the range of thickness dimension used.

- **Spot weld nugget diameter**

The most critical dimension to be determined for this study is the spot weld nugget diameter since it plays the vital role in determining the mode of failure of the welded joint. Several standards are set to determine the nugget dimension for a particular sheet metal thickness. Several researchers have also proposed mathematical equations for the calculation of a desired spot weld nugget diameter. Most of these standards and calculations were based upon the lap shear coupon configuration. Hence, the desired spot weld nugget diameter in this study is calculated for the lap shear coupon configuration and similar dimensions are used for all the other types of coupons.

Ewing et al. (1982) and Chao (2003) have reported such standards concisely. American Welding society (AWS), American National Standards Institute (ANSI) and Society of Automotive Engineers (SAE) jointly recommended the size of the spot weld nugget diameter for steel according to the following equation.

$$d = 4\sqrt{t} \tag{4.1}$$

where d and t are the nugget diameter and sheet thickness in mm respectively. Apart from the above mentioned equation, the following two equations are widely used in the industry for the minimum nugget diameter and nominal nugget diameter respectively.

$$d = 0.69\left(1.65t - 0.007\right)^{\frac{1}{2}} \tag{4.2}$$

$$d = 0.86\left(1.65t - 0.007\right)^{\frac{1}{2}} \tag{4.3}$$

where d and t are in inch respectively. All these formulas provide a general idea about the dimension but they can not distinguish between the failure modes of the spot weld nugget. VandenBossche (1977) first introduced such kind of formula to identify the nugget diameter in conjunction with the material property and coupon width value. The formula he proposed for transition weld diameter is given in the following form.

$$\frac{d}{t} = \left(0.54\frac{S_{YPM}}{1.54S_{YPM} + 572MPa}\frac{w}{t}\right)^{\frac{1}{2}} + 3.0 \tag{4.4}$$

where *d, w* and *t* are the nugget diameter, coupon width and sheet thickness in mm respectively. S_{YPM} is the yield stress of the base metal. Chao (2003) later proposed a very simple form of equation to predict the critical nugget diameter for the failure from the interfacial mode to nugget pull out mode. This

formula was verified with the test data for cold rolled mild steel with 1.18 mm thickness.

The critical nugget diameter proposed by Chao (2003) is

$$d_{cr} = 3.41t^{\frac{4}{3}} \tag{4.5}$$

where d and t are the nugget diameter and sheet thickness in mm.

Moreover Marya et al. (2006) has also proposed a relationship for the critical nugget dimension as follows.

$$d_c = 0.53t^{3.22} + 8.48\left(\frac{H_{\max}}{H_{\min}}\right)^{-1.24} \tag{4.6}$$

where t is the thickness of the sheet metal (in mm), H_{max} and H_{min} are the maximum and minimum hardness value of the spot weld joint area. But the use of this formula is omitted in this study due to the complexity of incorporating the spot weld manufacturing process parameter. This point has been explained in section 2.4 of the historical background chapter.

Using all of the above mentioned equations the preferred nugget diameter for the chosen material in this study is summarised in Table 4.2. The thickness value of the sheet metal used in calculating the diameter of the spot welds was 1.19 mm. This value was the average thickness found from the prepared sheet metal coupons subjected to experiments. The value of the yield stress used to calculate the nugget diameter from the VandenBossche equation (Equation 4.4) was 235 Mpa obtained from the uniaxial tensile test with the loading rate of 500 mm / min. Among all the calculated nugget diameter values, the maximum value (nugget dimension from the VandenBossche Equation 4.4) is the target dimension. This choice was made due to the conservative engineering practice.

Equation	Calculated Diameter (mm)
General equation (Equation 4.1)	4.36
Minimum Nugget Diameter Equation (Equation 4.2)	4.57
Nominal Nugget Diameter Equation (Equation 4.3)	5.79
Vandenbosche Equation (Equation 4.4)	6.05
Chao Equation (Equation 4.5)	4.3

Table 4.2: Summary of spot welds nugget diameter calculations.

- **Width of the coupon**

The width of the testing coupons is one of the most critical dimensions for spot welded samples (Zhou (1999, 2003)). It affects the strength prediction results severely. Zuniga et al. (1997) pointed out (shown in the following figure) that the coupons with reduced width size (19.05 mm) would absorb more energy than the adequate width size (38.1 mm) for the tensile shear coupon. Wung et al. (2001) has determined the critical width for the tensile shear coupon through experimental studies.

From the experimental force displacement curve they were able to show that the stability of the response curve was attained when the width of the specimen was over 35 mm, while all other dimensions were kept constant. Further more it has already been pointed out in section 2.4 that Zhang, Zhou and Hu (2001) had chosen 50 mm for the width dimension of the designed coupon for the impact loading situation as it absorbed the optimum amount of energy. So for the present analysis the widths of all the coupons were selected to greater than 35 mm. The details for the specific coupon configurations are given in Section 4.5.

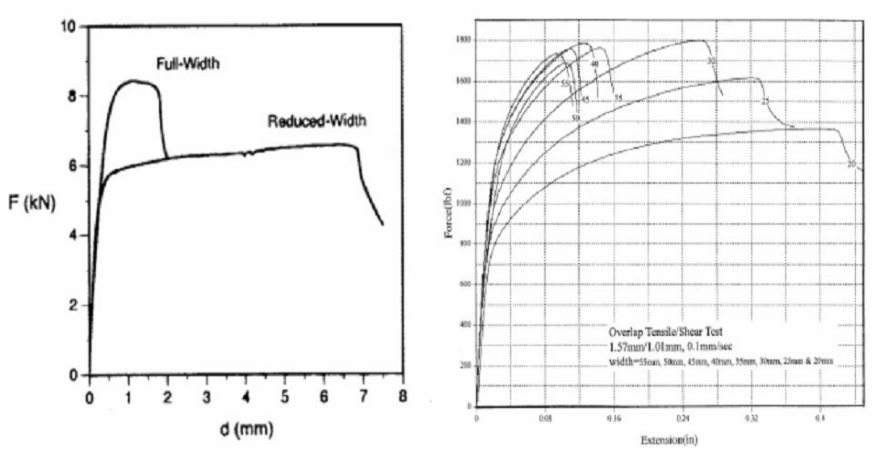

(a) (b)

Fig 4.4: Influence of tensile shear specimen width on strength of spot weld. (a) After Zuniga et al. (1997) (b) After Wung et al. (2001).

- **Length of the coupon**

The length of the coupon outside the overlap region (for lap shear coupon) does not play an important role on the spot weld failure mode. This is because outside the overlap region, the stress variation along the length direction does not change significantly. Various standards (ANSI, ISO, and AWS) have suggested different length dimensions for different gauges of sheet metal. Different researchers have used different values for the length dimensions. Zuniga et al. (1997) had used 85.7 mm for one coupon, Thronton et al. (1996) had used 113 mm in total for both the coupons including the overlap zone, Ewing et al. (1982) have used 127mm, Zhou et al. (2003) suggested the length to be 150 mm, Marya et al. (2006) had used 127 mm for only one coupon etc. just to name a few. In this study the dimension in length direction for the lap shear coupon was chosen to be 100 mm. The length wise dimensions for the other types of coupons (coach peel and U tension coupon) were at least 100 mm. For some cases the length was taken more than that to ensure better grip section for the experiments. The detail dimensions of the individual test coupons are provided in the next section.

4.5 Preparation of test coupons

The test coupons were prepared by shear blanking from a large piece of sheet metal. The bending and drilling operations were performed before making spot welds on the designed coupons. The purposes for different coupons were presented in section 4.2. The details of each of the test coupons are given as follows.

- **Lap shear coupon**

For the case of tensile shear loading conditions two different types of coupons were prepared. The basic dimensions for both the sets of coupons were 100 mm for length and width 38 mm. The overlap was selected to be equal to the width as it was recommended to be sufficient (Wung (2001)).

The differences in two types are due to the geometric configurations of the coupons. One set of coupons were made with out any back plate support. And the other types of coupons were made with the back plate of support. The dimensions for the back plate were chosen as 50 mm in length wise direction, width and thickness are the same as the original coupon dimensions (38 mm and 1.19 mm). This was done to investigate the effect of the loading condition on individual deformation patterns, i.e. bending deformation and shearing deformation. The back plates were joined by means of spot welding at the centre of their area. This spot weld joint will not affect the strength carrying capacity of the spot weld to be tested since the back plate spot weld joint was far away from the testing region of interest for this study. The differences in the configurations of the lap shear joint are clearly shown in Figure 4.5.

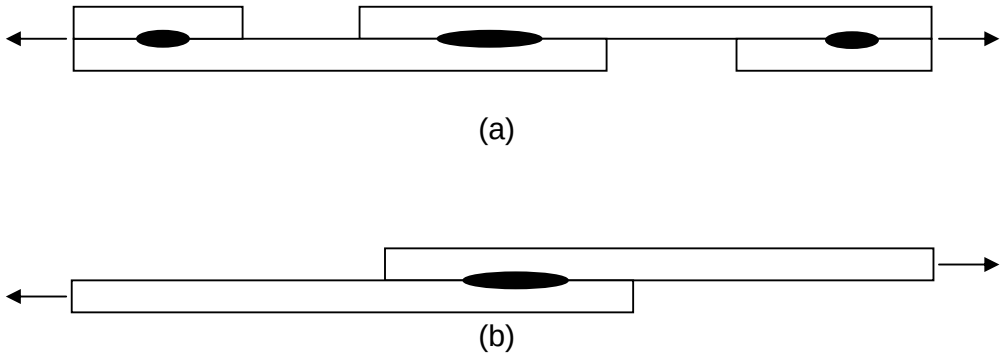

Fig 4.5: Different configurations for the lap shear coupon. (a) With back plate configuration (b) Without back plate configuration

- **Coach peel coupon**

The dimensions for the coach peel coupons were similar to that of the lap shear coupon. The length of the load arm of the coupon was 100 mm. The width was chosen as 38 mm. The overlap region was same as the width 38 mm. But as the over lap region was bent in 90^0. So the overall length of the coupon was extended than the lap shear coupon. The bent radius was 1/8 inch.

- **U - tension coupon**

The U – tension coupon was used to study the spot welds for the pure tension loading condition. The length for the U tension coupon was chosen as 50.8 mm for each side (load arm) and the width was chosen as 50.8 mm for the provision of better support. The bend radius was similar to that of the coach peel coupon 1/8 inch.

The summary of the prepared coupons are presented in Figure 4.6.

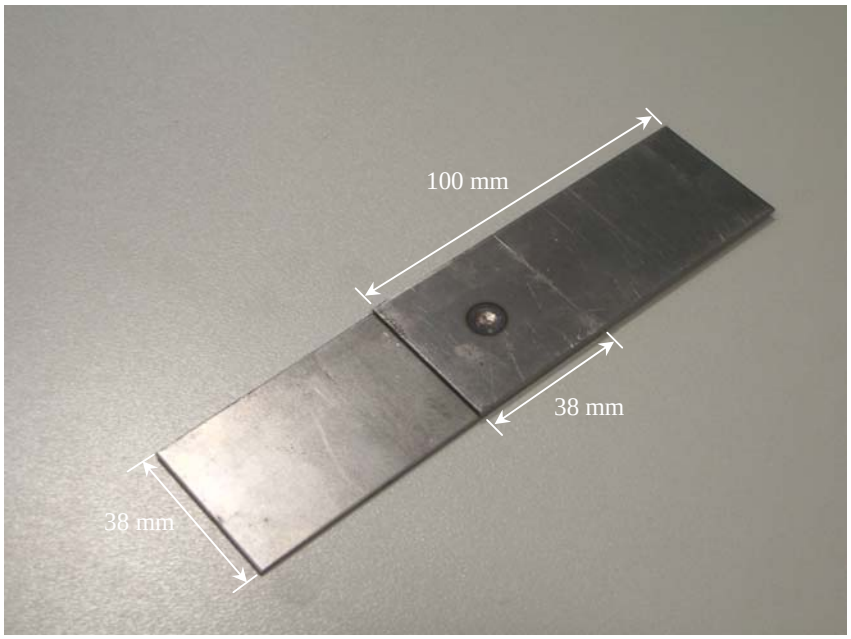

(a)

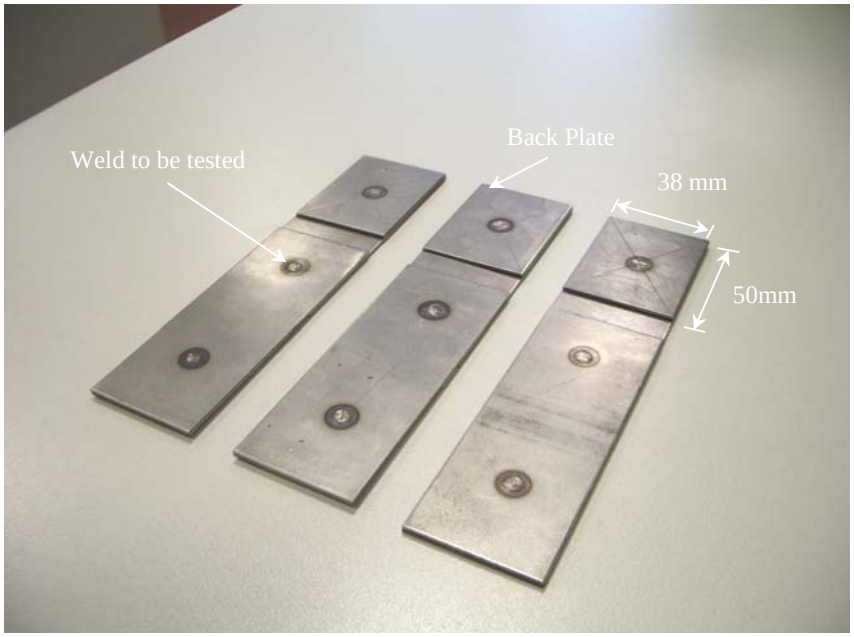

(b)

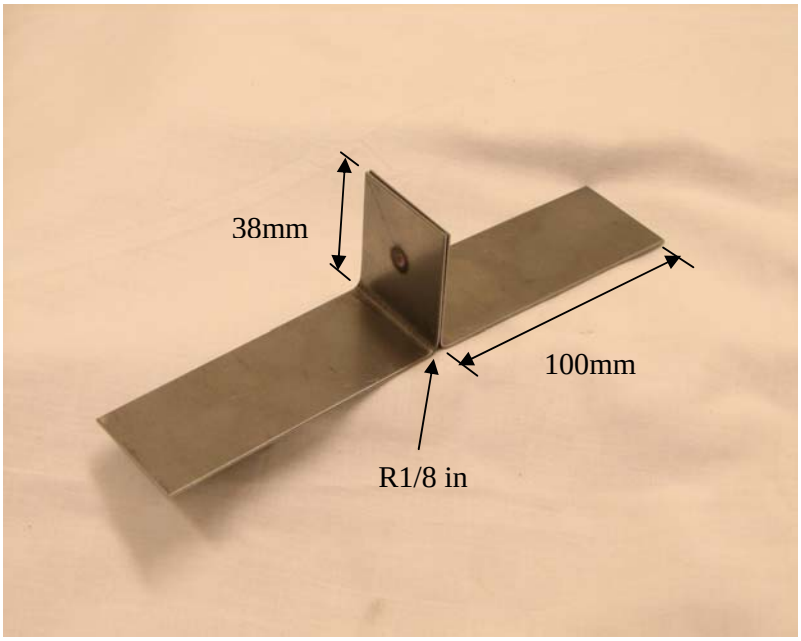

(c)

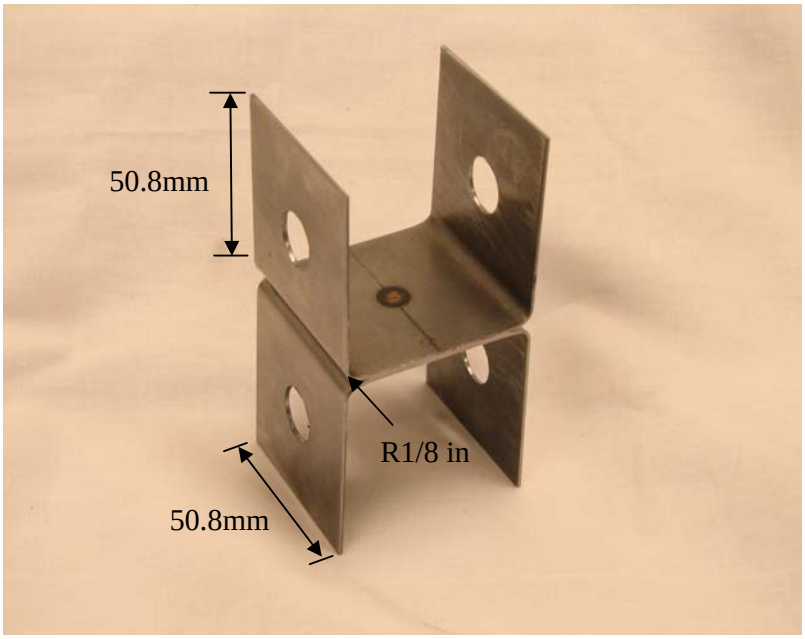

(d)

Fig 4.6: Prepared spot welded samples for the experiments (a) Tensile shear sample without the back plate (b) Tensile shear samples with back plate. (c) Coach peel sample (d) U – tension sample

4.6 Spot welding the coupons

For spot welding process a spot welding machine (Manufacturer: HERLESS, Norman Engineering), with rated configuration of 7.5KVA, 18 Amps, with a supply voltage of 415V – 50 Hz, control panel for the welding current, welding time and squeeze time controller was used. The welding electrodes were made of copper alloy with a conical shaped tip surface geometry. All the welding parameters were set to obtain a reasonably good spot weld nugget. It should be noted here that the weld lobe was not constructed in this study by varying the welding current and welding time during the spot welding process. The variation was performed to obtain the maximum possible weld nugget diameter that the spot welding machine can produce. Obviously the target was to attain the nugget diameter dimension as determined from the VandenBossche equation (Equation 4.4). The settings of parameters are given Table 4.3. This welding setting was used to produce all spot welded samples.

Welding Parameter	**Level indicated on the machine**
Welding current	Power level 5
Welding Time	Time cycle Long x 5 *
Squeeze time	Time cycle 7 *

** For the time cycle level 1 = 10 cycles and 50 cycle = 1 second*

Table 4.3: Settings for the welding parameters.

After performing the spot welding operation, the obtained spot weld nugget diameter was checked. This procedure is described in the next section.

4.7 Spot weld nugget dimension checking

The coupons were checked after spot welding them together to ensure the desirable nugget diameter was attained. The checking process was conducted by hardness testing on the surface of the spot welded specimen. During the welding process a large amount of heat is applied on the material, it undergoes severe changes in its micro structural format. So the hardness profile changes along the radial axis of the spot welded (nearly) circular nugget changes according to the applied heat. The three separate zones namely the spot welded nugget, the heat affected zones and the base metal are clearly identified in the following figure. These three zones have different levels of hardness values. So investigation of the hardness profile will definitely reveal the actual dimension of the spot weld nugget.

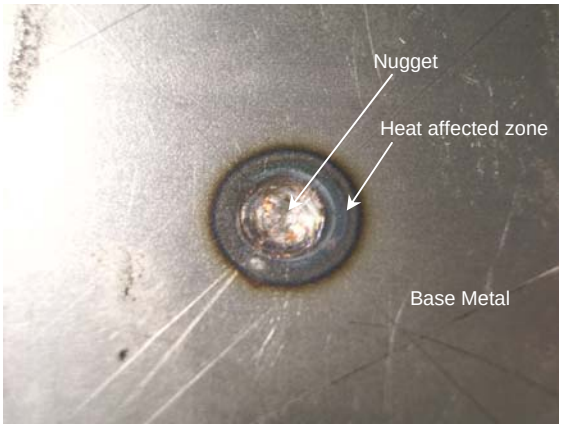

Fig 4.7: Different material zones around the spot weld

To conduct the hardness test a micro hardness testing machine (Future Tech Hardness Tester, Japan, and Model FV – 700 for Vickers hardness testing) was used. The detailed test setup for the hardness testing is presented in Appendix- D. Using the proper level of force the hardness value was measured in various directions around the spot weld nugget. The hardness values against the distance from the center point of the nugget were plotted. Hence the results obtained from these tests are given in Figure 4.8.

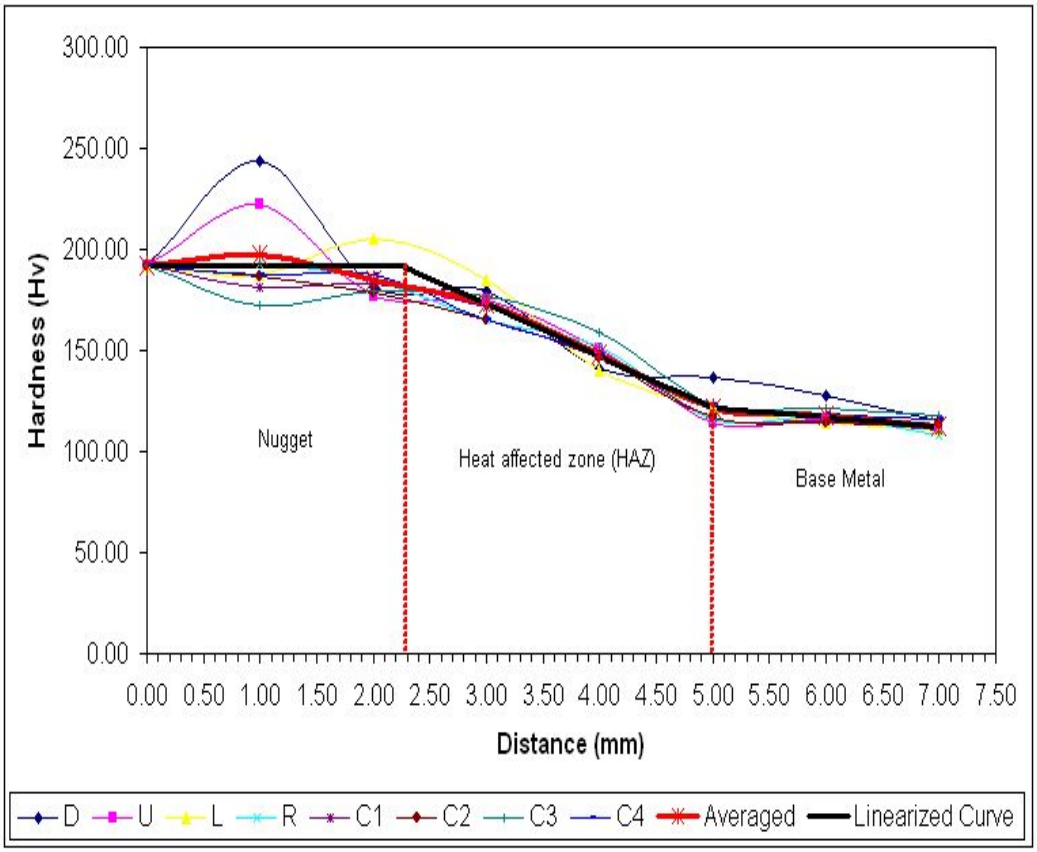

(a)

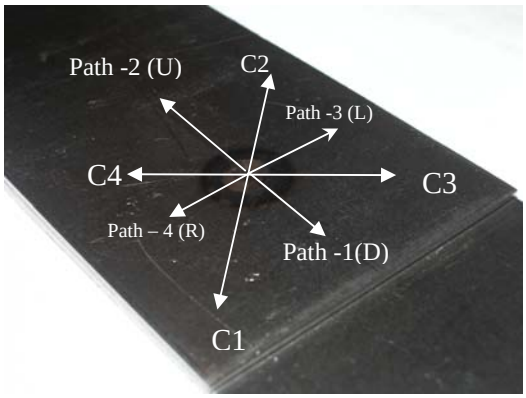

(b)

Fig 4.8: Hardness test results (a) Hardness distribution along the radial directions (b) Path directions used for the data collection

As seen from Figure 4.8 (a) the hardness distribution inside the nugget area in some of the cases are higher than the other. This may have resulted due to the imperfection of the welding electrode tip surface area, which in turn provided unequal pressure on the coupon surface. So the hardness distribution on the coupon surface in the welded nugget zone became different in different directions. From the collected data the average value was taken to linearize the hardness values in different zones. From the results presented, it is clear that the diameter dimension of the spot weld nugget is approximately 4.5 mm. This is the achievable nugget diameter dimension with the spot welding machine used to prepare the samples for this study. But this dimension is lower than the desired spot weld nugget diameter dimension calculated from the VandenBossche equation (Equation 4.4). However it is within the calculated nugget diameter range (General equation (Equation 4.1) and Chao equation (Equation 4.5)). So this dimension will be used for the modelling of the spot weld joint.

4.8 Testing set up for spot welded coupons

The spot welded coupons were tested in universal tensile testing machine. For each testing configuration 5 samples were tested. As a force transducer the load cell was mounted on the testing machine from which the applied load data was obtained for all the tests. Two different types of speed configurations were set for the testing of the coupons. These configurations (which were similar to those as used for the characterization of the material curves) were set to simulate the quasi static loading conditions and dynamic loading conditions. The chosen configurations are as follows.

- Configuration A: Test speed of 5 mm/min for quasi static condition.
- Configuration B: Test speed of 500 mm/min for dynamic loading condition.

These testing speed configurations were chosen because it was suggested by AWS (2005) (and approved by ANSI) to conduct the tests at the speed of 15 mm/min to minimize the effect of the pulling speed. It is noted here that the testing speed configuration chosen for the study of the dynamic loading condition, was not precisely within the dynamic speed range. Despite this fact, the speed was chosen to study the dynamic loading effect, due to the limitations of the testing speeds provided by the machine.

The results from the experimental testing are the force displacement graphs. The force data was collected from the load cell readings. The displacement data was recorded from the cross head displacement of the tensile testing machine. The deformations of the spot welded joints were concentrated around the joint location only. Outside of the joint location the deformation was negligible and can be considered as elastic deformation. These can be observed from the deformation patterns presented in section 4.9. Hence it is logical to obtain the displacement data from the testing machine cross head displacement.

The lap shear coupon and the coach peel coupons were gripped directly by the testing machine jaw. For the U tension coupons a testing set up was developed. The U tension coupon set up was designed in such a way that the spot weld nugget faces direct tensile load. The side plates were attached with the aid of nut, bolt and washer so that the coupons do not slip during the testing time. All these testing set ups are presented in Figure 4.9.

(a) (b)

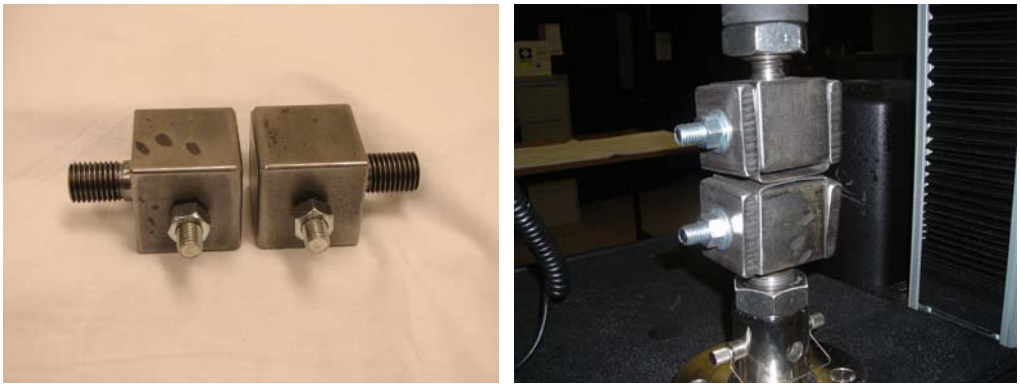

(c) (d)

Fig 4.9: Testing set ups for different coupon configurations.
(a) Lap shear coupons for shear loading condition (b) Coach peel coupon set up for bending load condition. (c) Jigs for U tension coupons. (d) U tension coupon set up.

4.9 Results obtained from the experiments

In this section the results obtained from the experiments are presented. The section is divided into the following sub headings.

- Deformation patterns of the spot welded joint
- Characteristic curve for the spot welded lap shear coupon
- Effect of different geometric configurations for the tensile shear coupons
- Effect of applied load rates

- **Deformation patterns of the spot welded joint**

The failure patterns for all the experiments for both the test configurations (at 5 mm / min and 500 mm/min) were critically observed. In spite of different loading rates, spot welds in all the test coupons failed in nugget pull out mode. In the following figure the deformation patterns for the failure of the spot welded coupons are shown. The snap shots were taken right after the complete failure of the spot weld joint has occurred while the coupons were still held by the testing machine jaw.

In Figure 4.10 the deformed pattern for the lap shear coupon used for the shear loading condition is shown. Deformation patterns for both the quasi - static load rate (5 mm / min) and dynamic load rate (500 mm / min) without the back plate configuration are given. The deformation pattern for the lap shear coupon with the back plate configuration, tested at 500 mm/min rate is also given in the figure. The deformation pattern shows that nugget came out of the joint system completely leaving a clear mark of degradation in the coupon material.

(a)

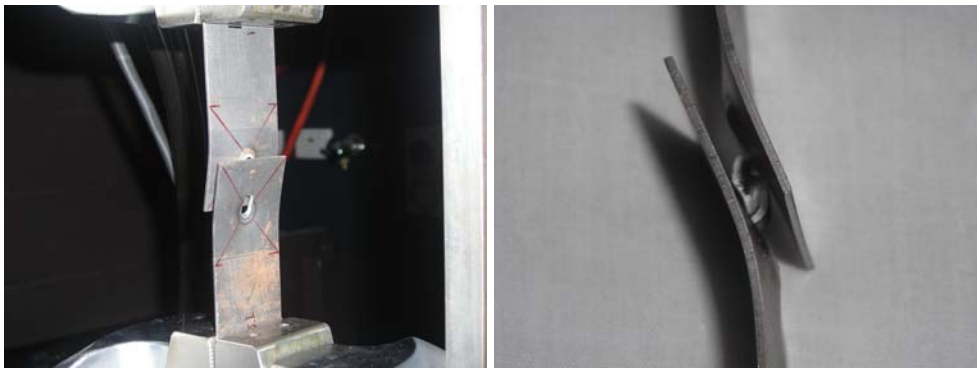

(b)

(c)

Fig 4.10: Failure patterns in the lap shear spot welded coupon

(a) Deformation directions without a back plate at rate of 5 mm/min

(b) Deformation directions without a back plate at rate of 500 mm/min

(c) Deformation directions with a back plate at rate of 500 mm/min

In figure 4.11 the deformation pattern for the coach peel coupons are presented. The applied load through the loading arm created a bending moment at the spot weld nugget. At first the applied load tried to turn the bent section of the designed coupon. Hence the failure always started around the spot weld nugget periphery near the loading arm and then propagated along the circumference of the weld nugget. The material coming out of the coupon clearly indicated the occurrence of the nugget pull out type of failure.

(a)

(b)

Fig 4.11: Deformation patterns for the bending load situation

(a) Coach peel coupon deformation pattern at rate of 5 mm / min

(b) Coach peel coupon deformation pattern at rate of 500 mm / min

In Figure 4.12 the deformation patterns for the U tension coupons are presented. The deformation pattern revealed that the deformation mechanism in the spot welded coupon initially started with the similar outline which was observed in the coach peel coupon. The applied load tried to turn the bent sections at both sides of the coupon. But as the level of the applied load increased, the jigs inside the coupon and the supporting plates outside the coupon prohibited the bending operation. It enforced the pure tensile load on the spot weld nugget. The deformation pattern ensured the type of failure to be of nugget pull out type failure in its nature.

(a)

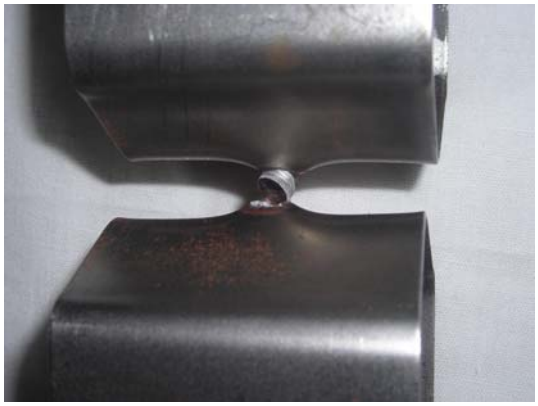

(b)

Fig 4.12: Failure of spot welded coupon for pure tensile loading condition

(a) Failure of the spot weld at loading rate of 5 mm / min.

(b) Failure of the spot weld at loading rate of 500 mm / min.

- **Characteristic curve for the spot welded joints**

The main results obtained from the above mentioned experiments are the force displacement diagrams. These force displacement diagrams represents the load bearing capabilities of the spot welded joints for different loading conditions. The force data was obtained through the load cell readings only. The displacement data was generated from the cross head displacements of the universal tensile testing machine.

The force displacement curves are presented in the following figures for each individual test specimen used in this study. Five specimens were used for each of the test cases. All of these experiments were displacement controlled tests. An averaged force displacement curve for a specific coupon configuration and specific loading rate was constructed from these five test specimens. For the averaged curve construction, the average force value for a certain displacement position was obtained in equal intervals. These averaged curves will be used for the validation purposes of the developed finite element models.

In figure 4.13 the force displacement data obtained for the lap shear coupon is presented. These experiments were performed at least five times for each of the cases. The individual result curve and the corresponding average curve are presented in the following Figure 4.13. The lap shear coupons were tested with and without the back plate attachment. The back plates had the similar thickness dimension as the coupon material. They were attached to the inner surface of both the coupons in lap shear configuration. The coupons with the back plate were only tested for the higher loading rate (500 mm /min). At the start of the test the force displacement response was linear in nature. In this initial stage the force level attained by the test coupons was nearly proportional to the applied displacement. As the applied displacement had increased, the force displacement relationship was no longer proportional until the failure process of the joint had been initiated. After the initiation of failure,

the joint started loosing its stiffness and the force displacement response had decreased. The material around the joint gradually lost the load bearing capability. This phenomenon can be observed from the negative slope of the force displacement curve until complete separation of the joint had occurred.

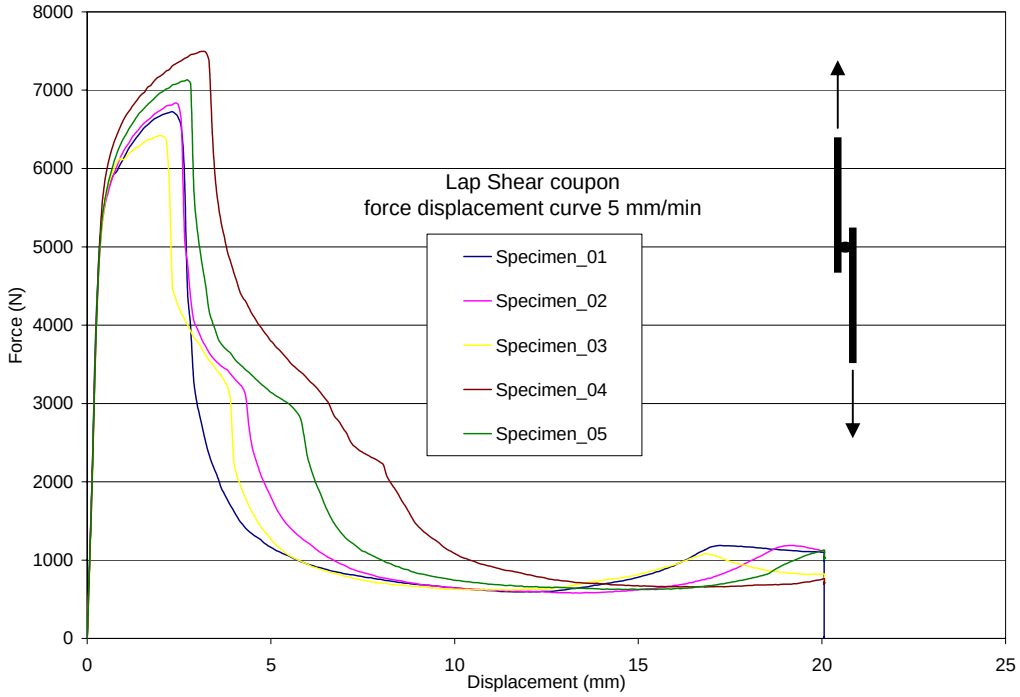

(a)

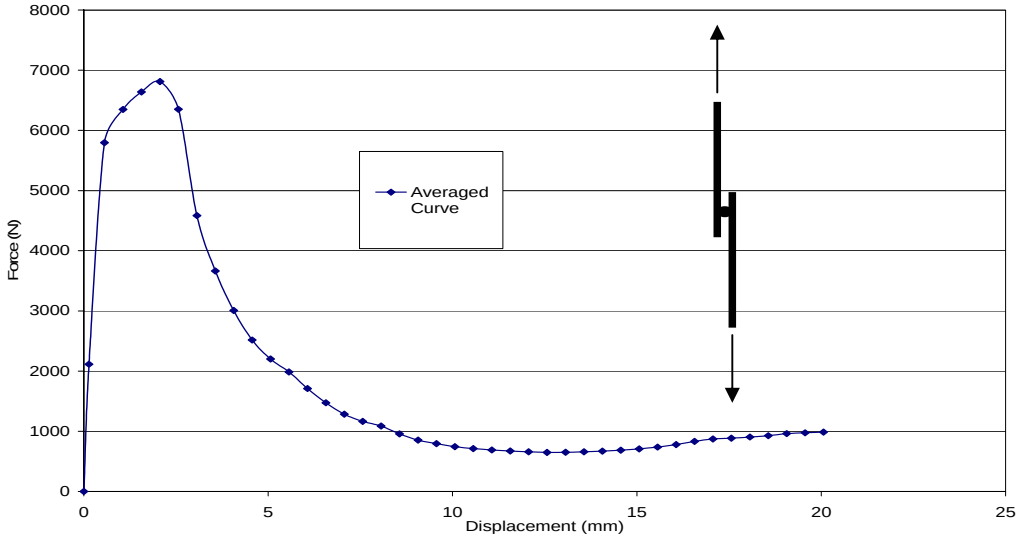

(b)

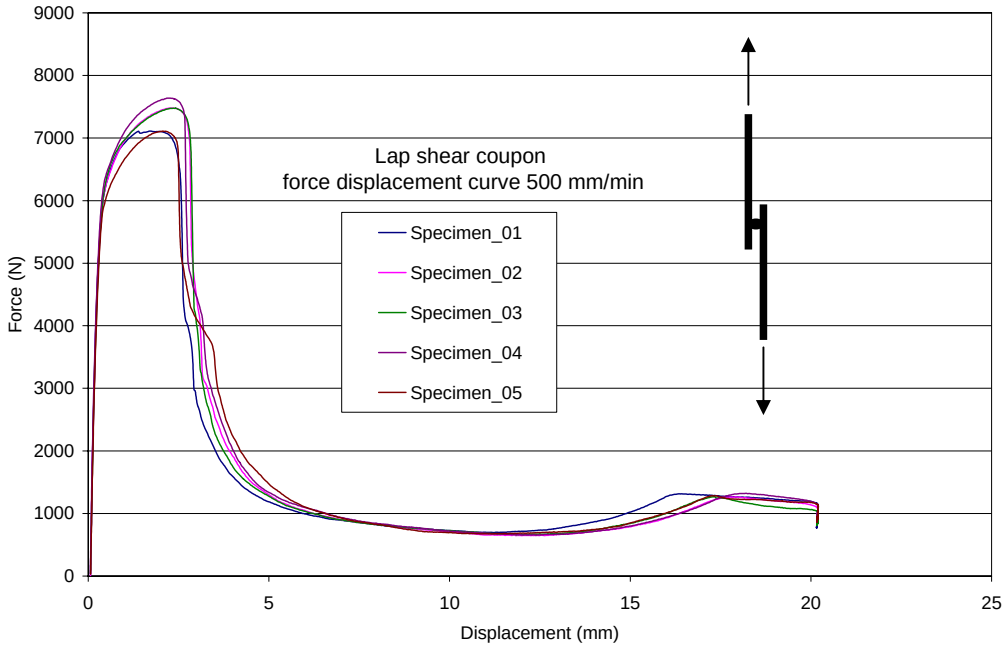
Lap shear coupon
force displacement curve 500 mm/min
Specimen_01
Specimen_02
Specimen_03
Specimen_04
Specimen_05
Force (N)
Displacement (mm)
0
1000
2000
3000
4000
5000
6000
7000
8000
9000
0
5
10
15
20
25

(c)

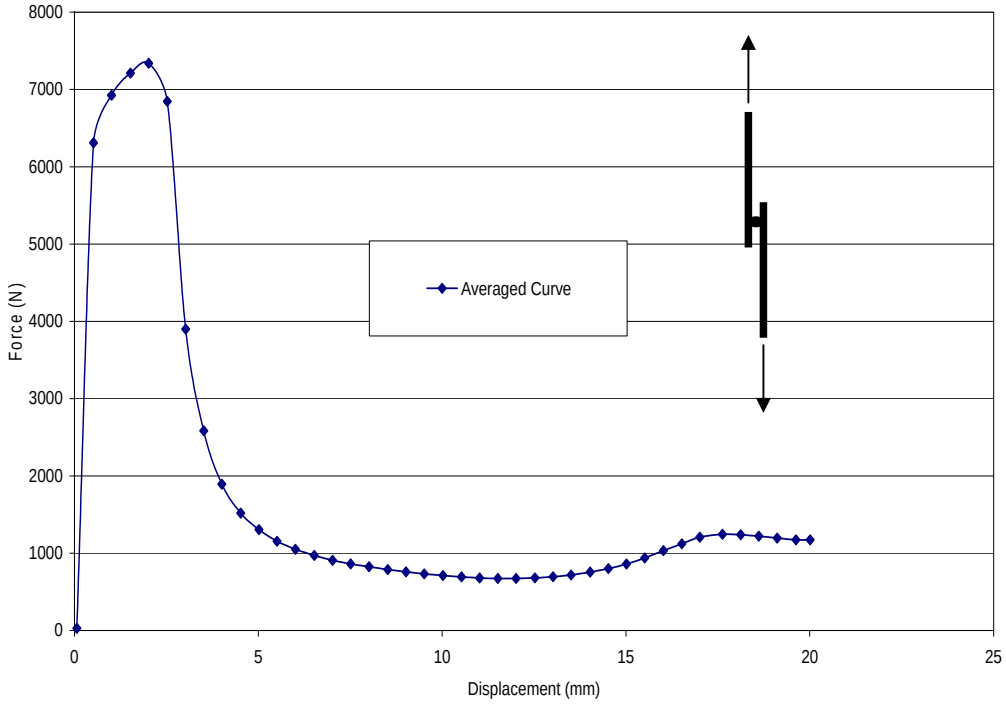
Averaged Curve
Force (N)
Displacement (mm)
0
1000
2000
3000
4000
5000
6000
7000
8000
0
5
10
15
20
25

(d)

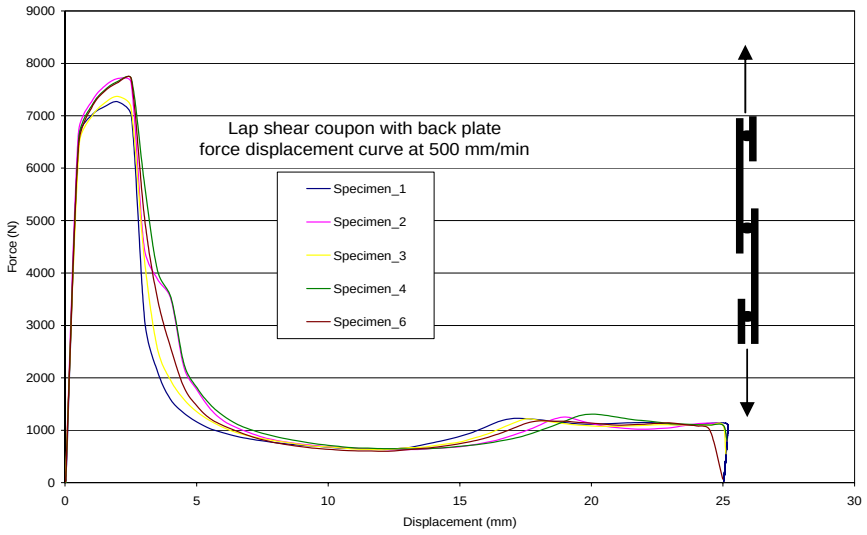

(e)

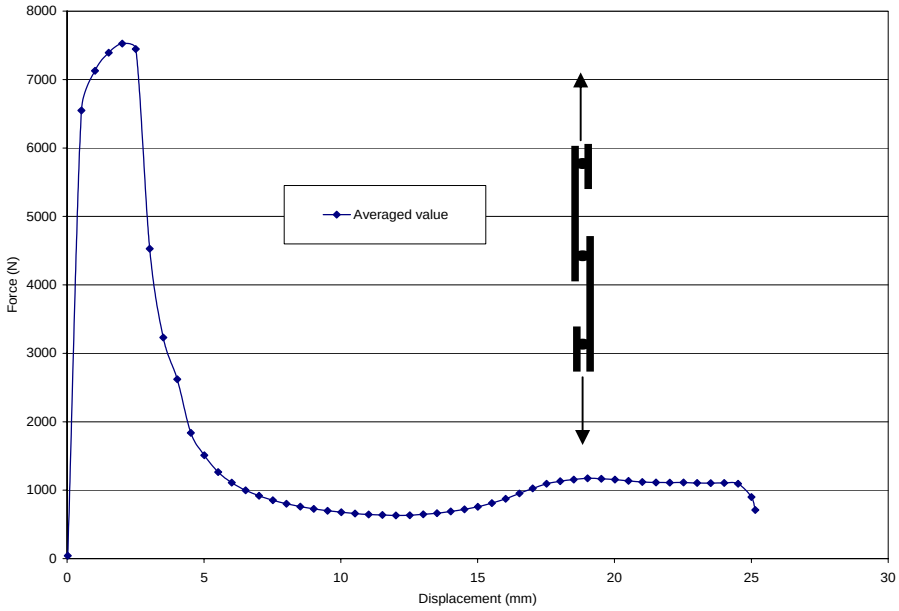

(f)

Fig 4.13: Force displacement response for the lap shear coupon. (a) Individual responses of the test specimens at loading rate of 5 mm / min. (b) Average response at the loading rate of 5 mm / min. (c) Individual responses of the test specimens at loading rate of 500 mm / min. (d) Average response at the loading rate of 500 mm / min. (e) Individual force displacement response for lap shear coupon with the back plate attachment at loading rate of 500 mm / min. (f)) Average force displacement response for lap shear coupon with the back plate attachment at loading rate of 500 mm / min.

In figure 4.14 the force displacement curves obtained for the coach peel coupons are presented. The lower test rate used here was 5 mm / min and the higher test rate was 500 mm /min. With the aid of the coach peel coupon spot weld failure at the bending load condition was studied. The force data was recorded through the load cell readings and the displacement data was recorded through the cross head displacement of the testing machine. The initial stage of force displacement response for the coach peel coupon was not proportional like the lap shear coupon. This is due to the fact that the applied load attempted to straighten the bent section of the coupon first. Hence the bending moment was imposed on the spot weld nugget. Due to this bending moment the spot weld joint could resist a comparatively lower level of load for the bending load condition than the shear loading condition tested with the lap shear coupon. Due to the failure of the joint the force displacement response goes down after it reaches the peak load. But from the experimental data, two different peak values could be observed in case of a few specimens of coach peel coupons. This is because of the failure process of the spot weld joint and the coupon configuration.

The failure around the spot weld nugget starts from the loading arm side and it propagates around the nugget circumference. When the failure initiated the force displacement response drops down from the peak value. But then support for sustaining the applied load was obtained from the free end side of the coupon configuration. Hence the force displacement response went up to another peak value. When the failure propagation around the spot weld nugget was nearly completed, the support from the free end was withdrawn automatically due to the deformation pattern for the applied load. Therefore the level of the force displacement response went down. Hence the first peak value should be considered as the failure load for the coach peel coupon configuration.

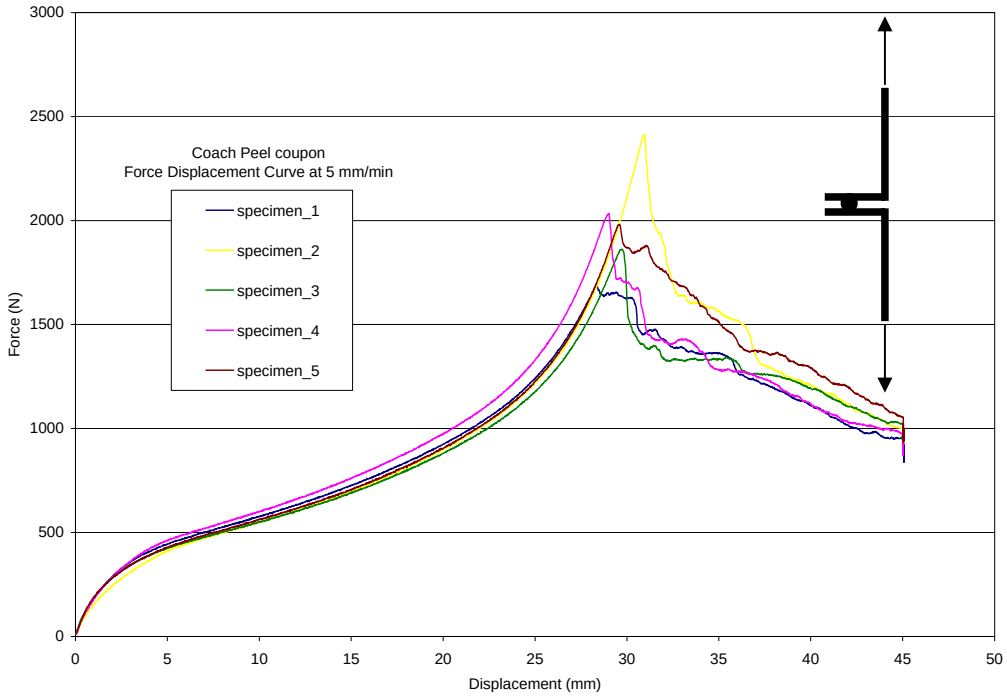
Coach Peel coupon
Force Displacement Curve at 5 mm/min
specimen_1
specimen_2
specimen_3
specimen_4
specimen_5
Force (N)
Displacement (mm)
0
500
1000
1500
2000
2500
3000
0
5
10
15
20
25
30
35
40
45
50

(a)

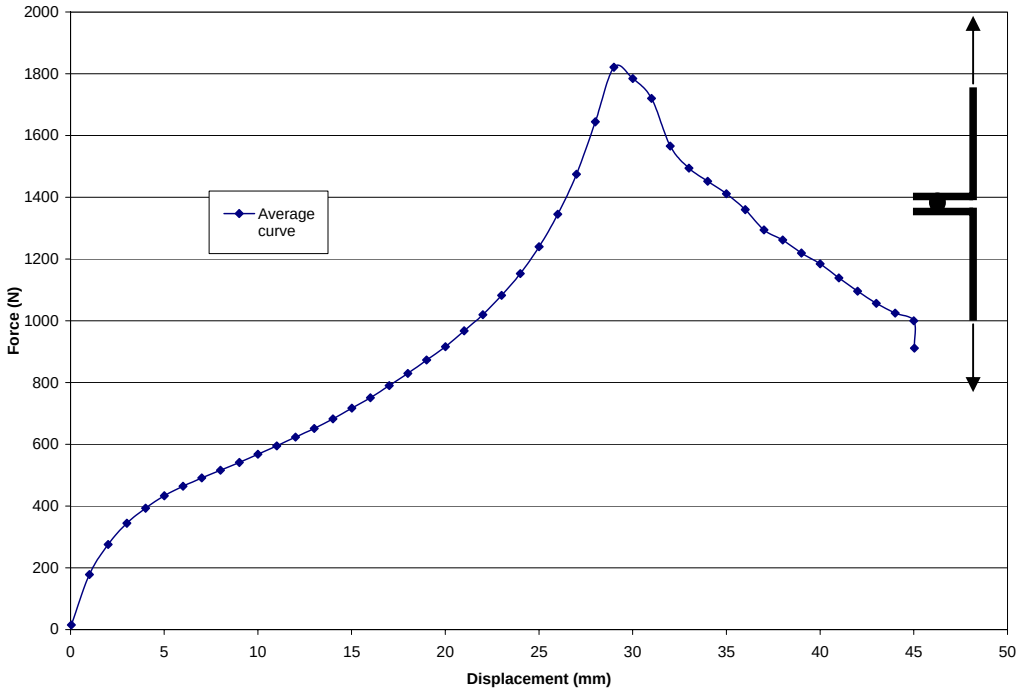
Average curve
Force (N)
Displacement (mm)
0
200
400
600
800
1000
1200
1400
1600
1800
2000
0
5
10
15
20
25
30
35
40
45
50

(b)

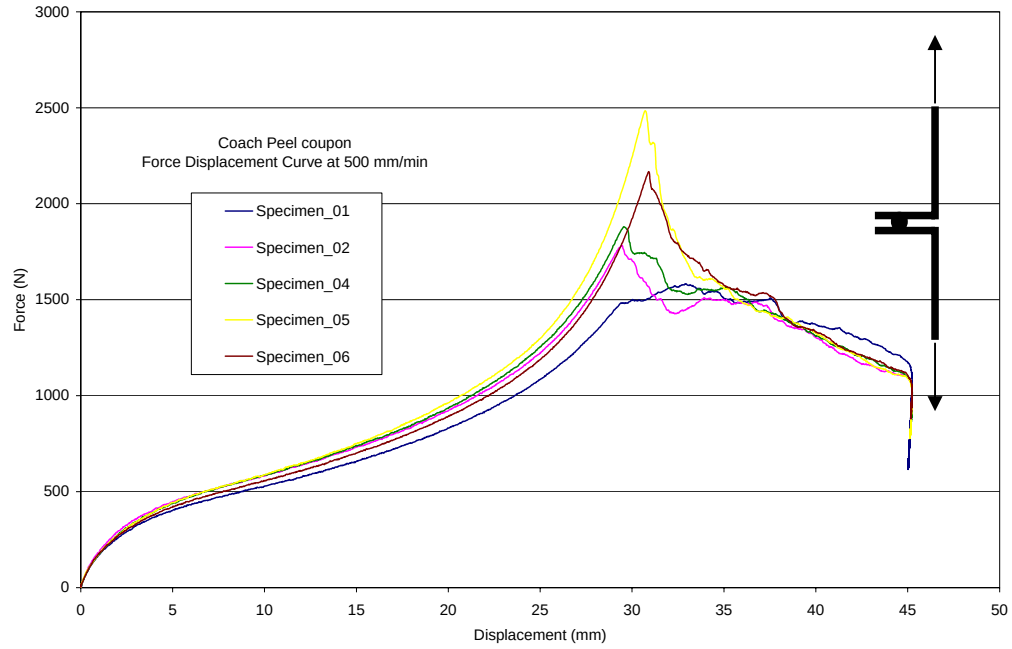

(c)

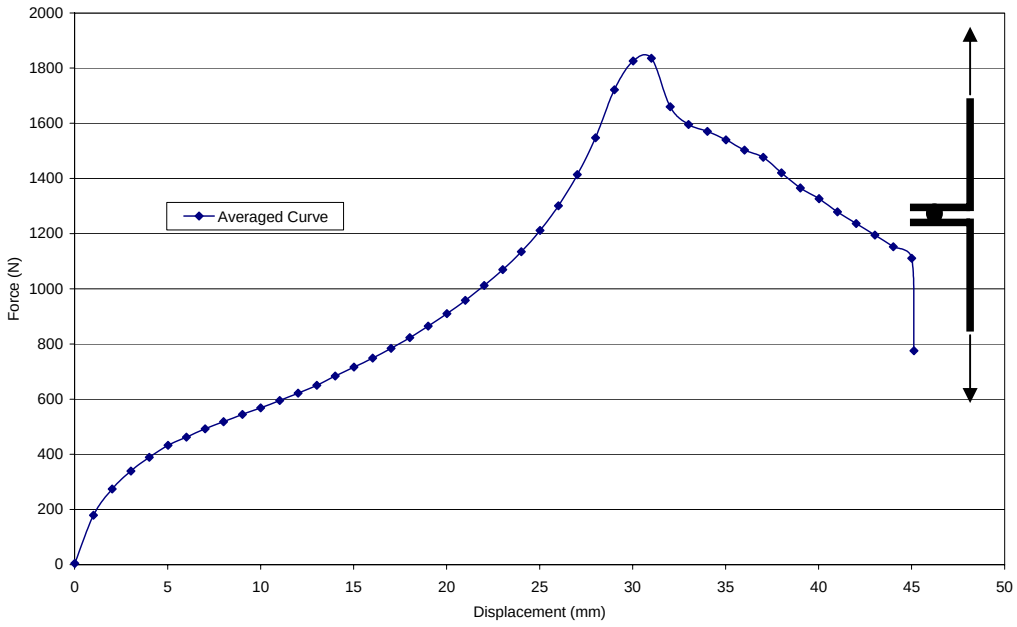

(d)

Fig 4.14: Force displacement response for the coach peel coupon. (a) Individual responses of the test specimens at loading rate of 5 mm / min. (b) Average response at the loading rate of 5 mm / min. (c) Individual responses of the test specimens at loading rate of 500 mm / min. (d) Average response at the loading rate of 500 mm / min.

Spot welded coupons were tested for the tensile loading condition with the U tension coupon. The configuration for the U tension coupon was similar to the double coach peel coupons from two sides. Hence the force displacement response initially showed some bending like behaviour. The initial bending deformation at the spot welded plane can be observed from Figure 4.15. But that bending deformation was stopped by the square insert and the attached plates of the testing set up. The insert ensured that the load acting on the spot weld nugget was a pure tensile load. The test specimens were preloaded with a 100 N force to prevent the unavoidable initial slippage of the set up. This is observed from the initial readings of the force displacement curves. The individual and the averaged force displacement plots are presented in the Figure 4.15.

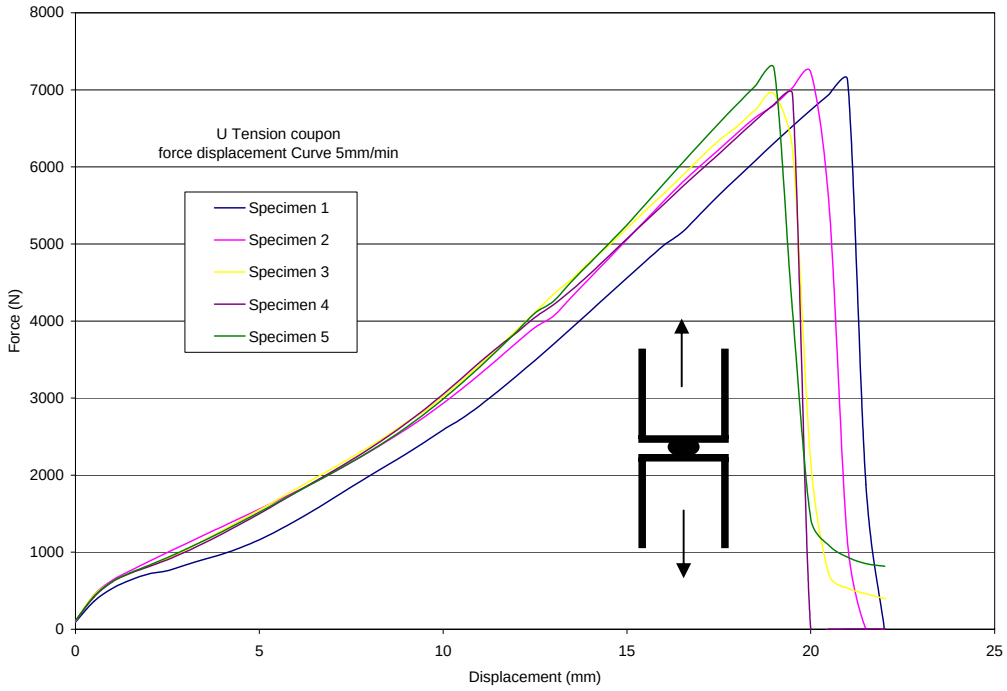

(a)

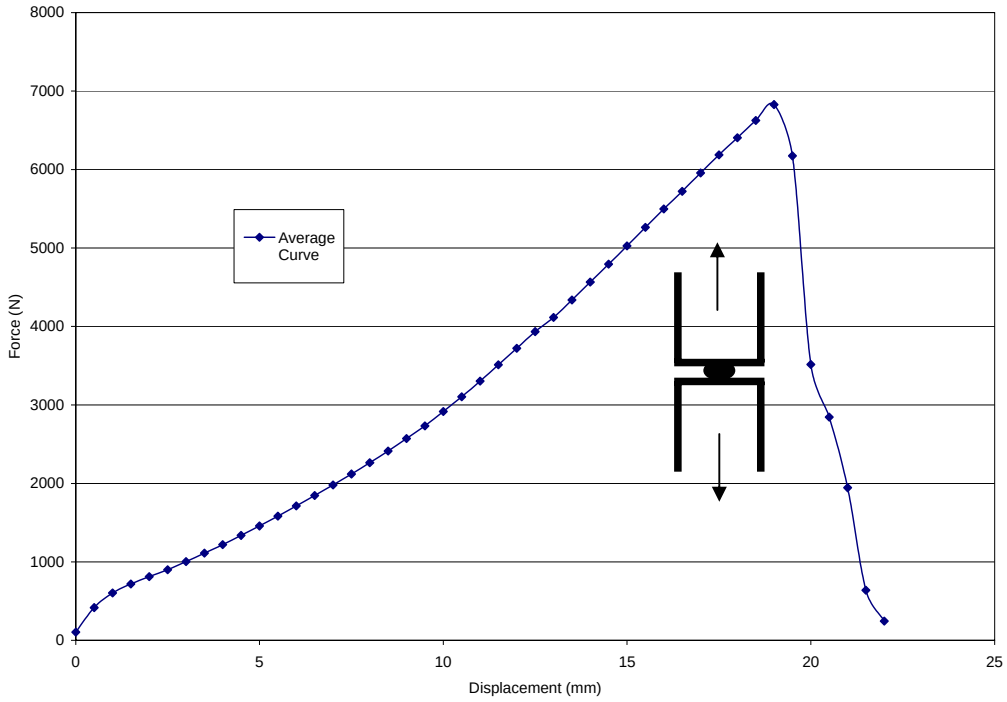
8000
7000
6000
5000
4000
3000
2000
1000
0
Force (N)
0
5
10
15
20
25
Displacement (mm)
Average Curve

(b)

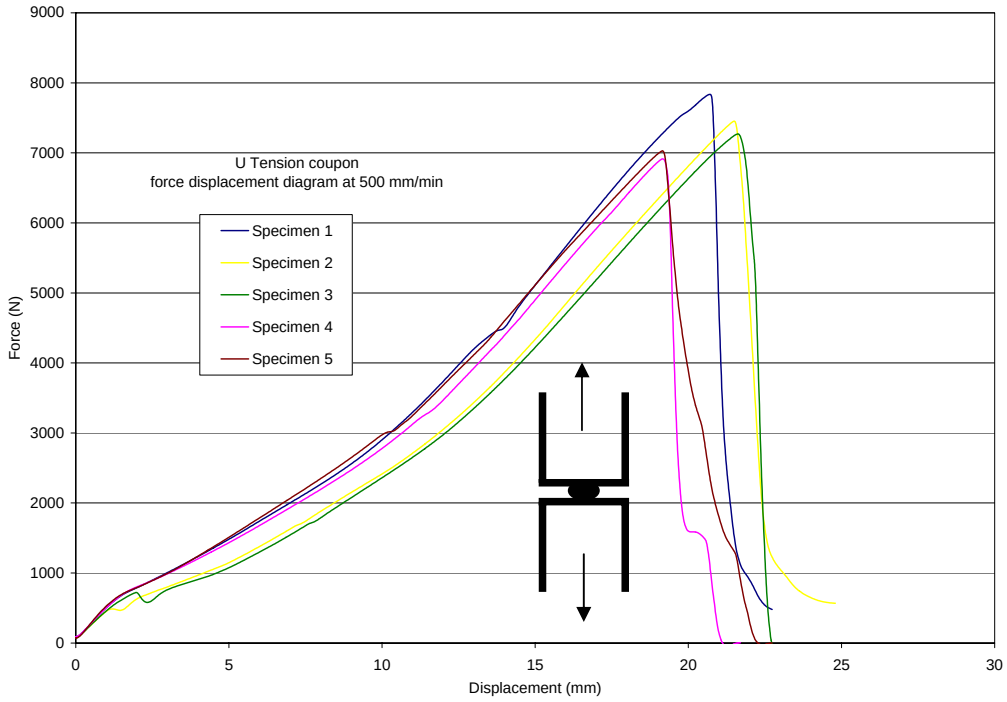
9000
8000
7000
6000
5000
4000
3000
2000
1000
0
Force (N)
0
5
10
15
20
25
30
Displacement (mm)
U Tension coupon
force displacement diagram at 500 mm/min
Specimen 1
Specimen 2
Specimen 3
Specimen 4
Specimen 5

(c)

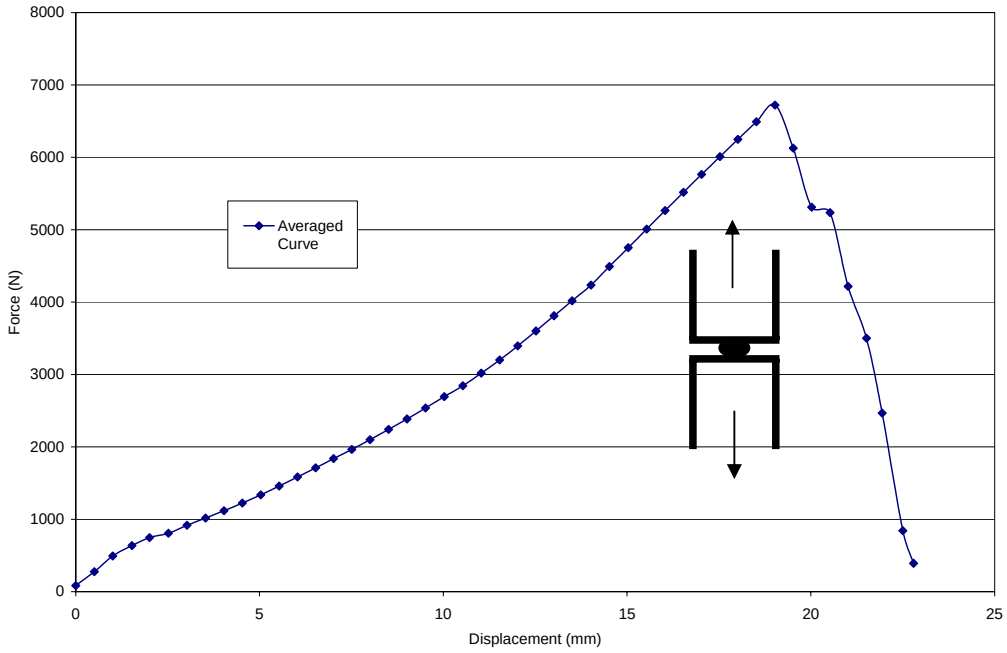

(d)

Fig 4.15: Force displacement response for the U-tension coupon. (a) Individual responses of the test specimens at loading rate of 5 mm / min. (b) Average response at the loading rate of 5 mm / min. (c) Individual responses of the test specimens at loading rate of 500 mm / min. (d) Average response at the loading rate of 500 mm / min.

- **Effect of different geometric configurations for the tensile shear coupons**

It was mentioned earlier that two different types of coupons were manufactured according to the geometric configurations. They were coupons with back plates and coupons without back plates. The coupons with the back plates were tested at only velocity of 500 mm/min. Hence in this section, results obtained from 500 mm/min tests for the coupons with or with out back plates are discussed. In the following figure the average experimental results for the lap shear coupons with and without the back plate are compared.

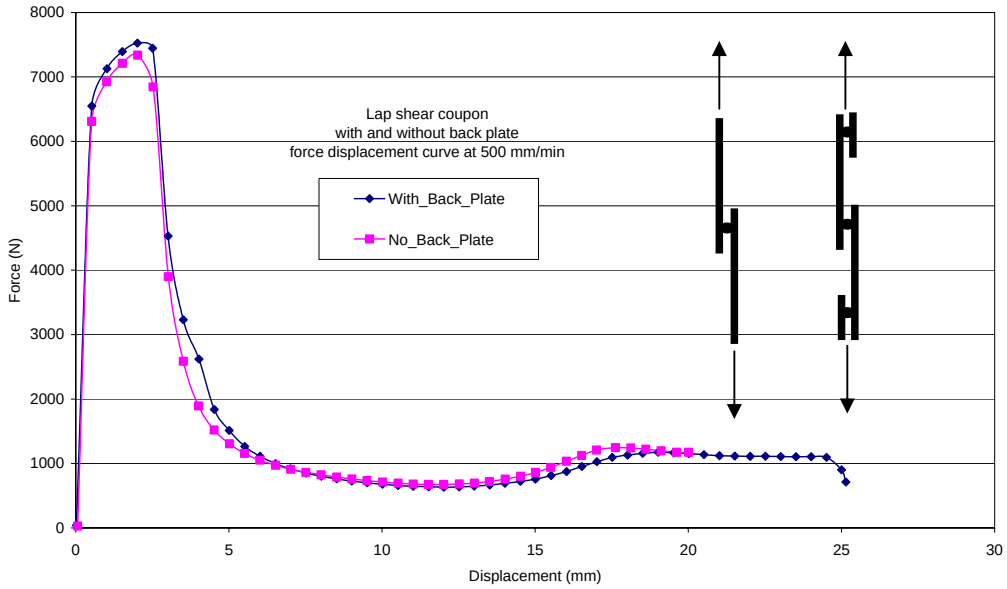

Fig 4.16: Comparison of force displacement curves for lap shear coupon with and without the back plate configuration at the loading rate of 500 mm /min.

From the results it can be seen that the coupon with the back plates is predicting a higher load carrying capacity, and at same time it is showing more stiffness than the test coupons without the attached back plates. This is because of the presence of the back plate, load which is applied at the end of the coupon, can not subdivide itself into a bending load and shear load state. Hence there was no bending deformation observed in the transverse direction. Attachment of the back plate ensured the pure shear loading on the spot welded nugget.

- **Effect of applied load rates**

It has been pointed out earlier that two different load rates were applied for every set of tests. The chosen configurations were as follows.

- Configuration A: Test speed of 5 mm/min for quasi static condition.
- Configuration B: Test speed of 500 mm/min for dynamic loading condition.

The average results from both the test configurations for all types of coupons are presented in Figure 4.17.

From these presented graphs it can be seen that generally for the higher loading rate the test specimens had shown more rigid characteristics. This feature is very much clear for the shear loading condition. Moreover it can also be understood that for the higher loading rates the test specimens generally absorbed more energy than the lower loading rates.

However for the tensile loading condition (with U tension coupon) this feature is not observed from the force displacement response. But the force displacement responses for both the loading rates in U tension coupon showed a similar trend and the maximum force values are very close to each other.

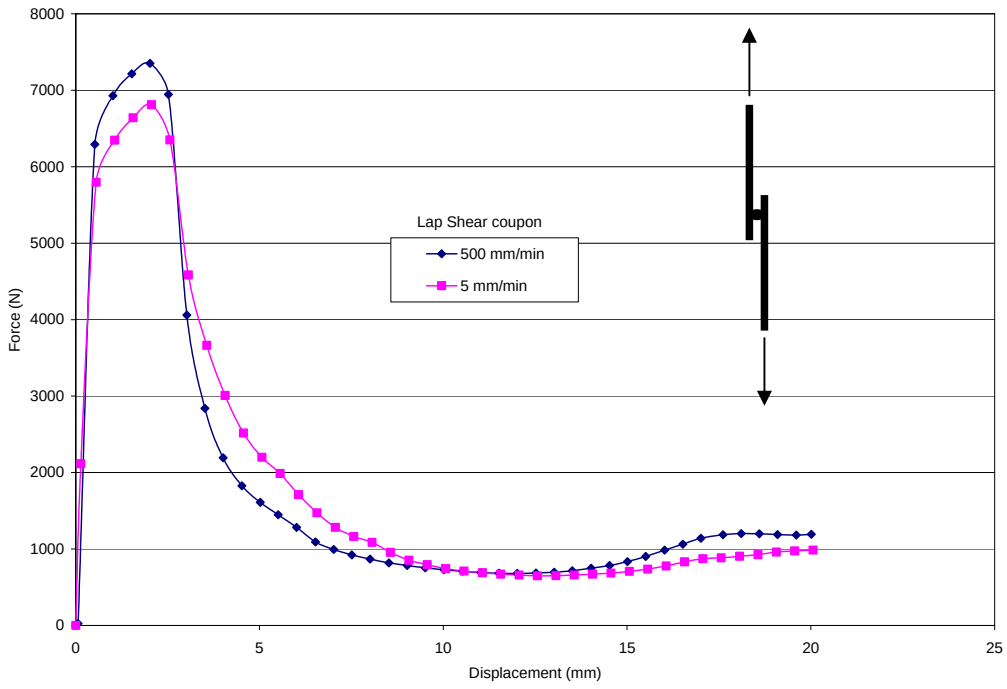

(a)

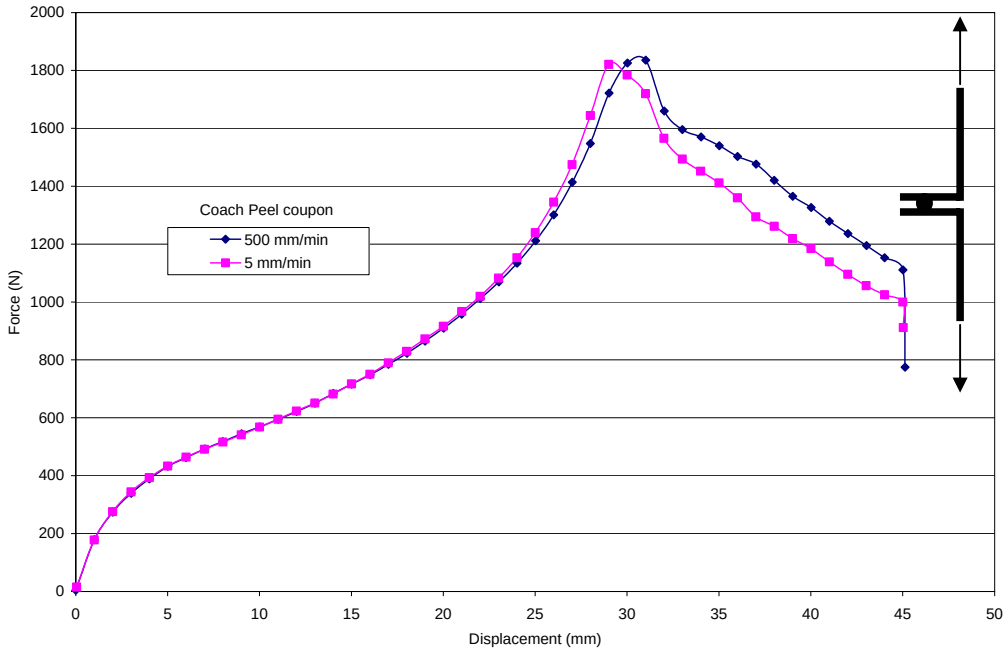

(b)

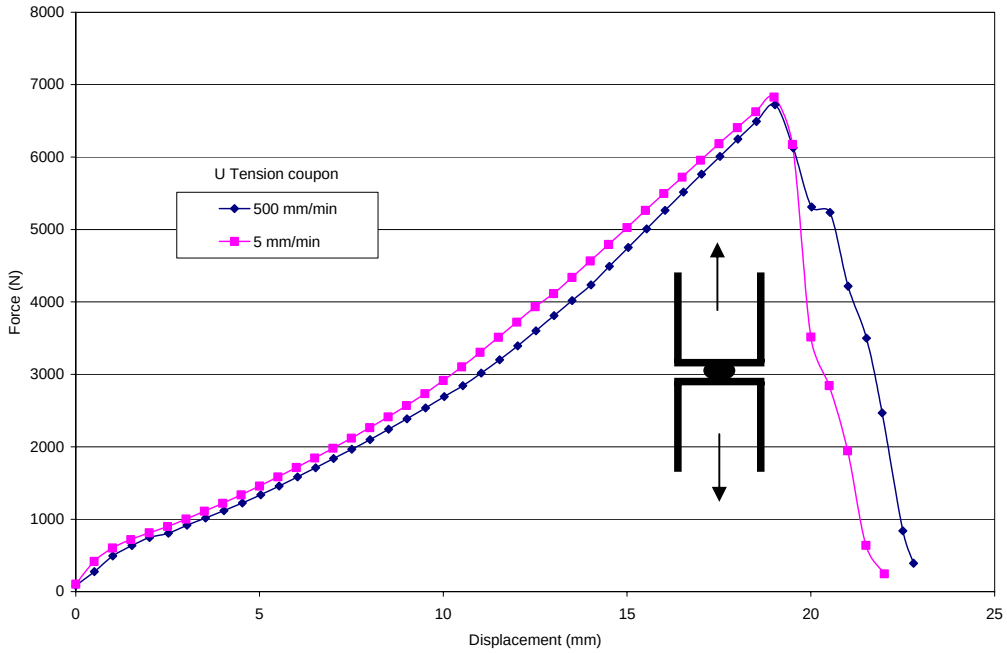

(c)

Fig 4.17: Comparison of applied load rates

(a) Graph for shear loading condition with lap shear coupons

(b) Graph for bending loading condition with Coach Peel coupons

(c) Graph for tensile loading condition with U-tension coupons

The results from the lower loading rates will be compared with the simulation results obtained from the implicit finite element code. These results will be denoted as the results for the quasi - static condition. While the test results from the higher loading rates will be compared with the simulation results from the explicit dynamic finite element code. These results will be denoted as the results for the dynamic loading condition. It should be noted here that effectively the loading rates chosen for the experimental analysis were all within in the quasi - static range due to the limited capability of the testing machine. The loading rates were chosen according to near the lowest and the highest loading rates available from the testing machine for each coupon configurations. As such the comparatively higher loading rate is denoted as the dynamic loading situation. Similarly finite element models are developed for quasi static and dynamic loading situation and compared with these test results. The modelling strategies followed for the development of these models are described in the next chapter.

Modelling Strategy

5.1 Overview

This chapter presents the modelling strategy followed in this thesis to develop the finite element models for the spot weld joint. The spot welded test coupons were modelled in full dimensions to accurately simulate the failure occurrences for different loading conditions. Different commercial softwares were used for the model development purpose. A detailed description of the combined interaction of those commercial softwares at the model development stage is provided in this chapter. The modelling approach followed in this thesis is described in this chapter according to the following sections.

5.2 Model development process

To model the spot weld joint the commercial finite element code ABAQUS was used. Many non-linear capabilities available in this commercial code were utilized to simulate the joint failure process. To represent the spot weld joint, six different models were developed which will be thoroughly discussed in the next chapter. They were modelled in simple test coupons to evaluate the different model performances. The development process of the models is elaborated in the following flow diagram.

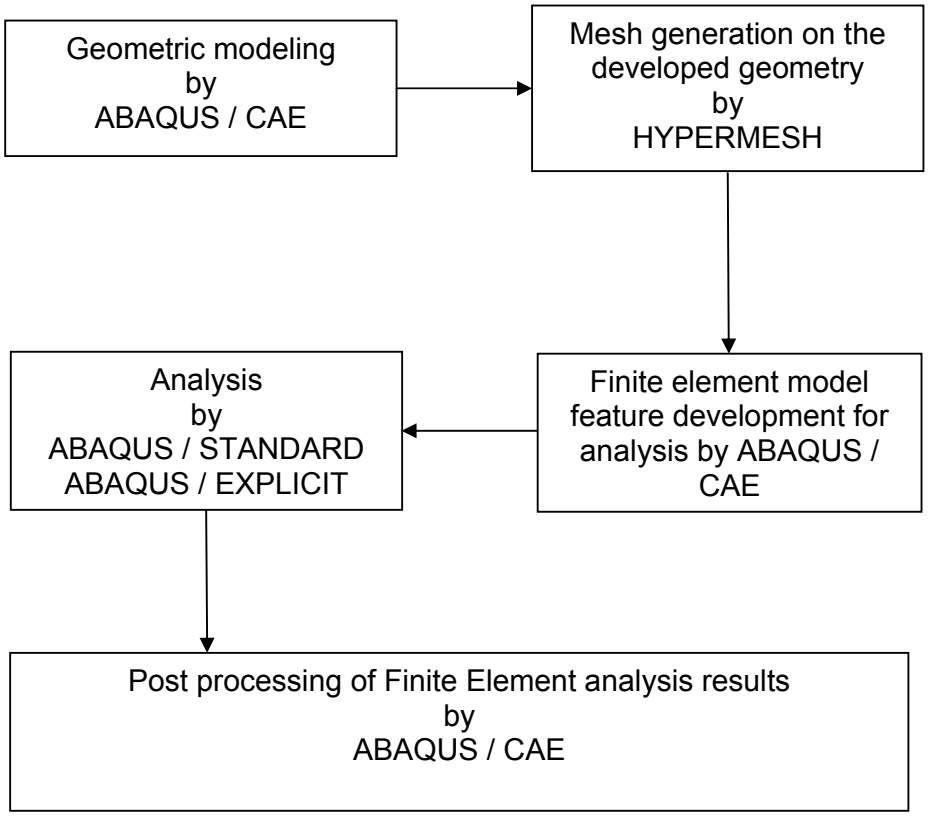

Chart 5.1: Model development process for simulating the spot weld joint

The geometry of the coupons was developed using ABAQUS / CAE. The material property definition, contact definition, boundary conditions and loading conditions were all developed in the CAE environment. The developed model was exported to the special mesh generating pre-processor HYPERMESH. The meshing for the entire model was generated

through HYPERMESH. Only quadrilateral shaped elements were used in the developed models. The mesh generated by HYPERMESH was then imported back to the ABAQUS /CAE environment. Other features required for the finite element study were added to the model and were then submitted to ABAQUS / STANDARD or ABAQUS / EXPLICIT for the analysis.

5.3 Meshing strategy

The developed models in this study were three dimensional shell models of the spot weld joints. It was essential to model the joint with the correct stiffness value. At the same time it was also required to simulate the occurrence of failure at the joint location accurately to compare the performance of the different models. Hence the stress distribution around the spot weld nugget should be correctly predicted by the developed models which largely depend on the proper meshing characteristics.

In this study linear shell elements were used to model the sheet metal coupons. Generally linear shell elements are chosen to perform failure analysis in automotive structures due to the reason that they provide homogenous pressure distribution for the contact definition. Only quadrilateral shaped elements were used for the simulations. In this study the spot weld nugget region was assumed to be having a circular cross sectional area. Hence the quadrilateral elements were arranged along the circumference of the nugget region to represent the exact diameter dimension measured in the experiments. The geometric features of the test coupon used for testing the models performances were very simple in configuration. The overlap region near the nugget boundary was identified as the critical area of the coupons. This is due to the reason that the stress concentration which initiates the failure of the spot weld joint in the test coupon was located at that particular region. Outside that overlap area in each type of coupons were of less importance for not having any high stress concentration zone. Hence the mesh size outside the overlap zone should not be of critical importance.

5.4 Mesh characteristics

The meshing of the test coupon geometry was performed by the specialized pre-processor HYPERMESH. It was mentioned in the previous section that the meshing around the spot weld nugget within the overlap region is the most important part. The geometric features of the overlap region were similar for all the coupon configurations. Hence the mesh characteristics around the nugget region will be studied only for the lap shear coupon. Similar type of meshing around the nugget region will be used for other test coupon configurations. Moreover as the stress distribution inside the spot weld nugget is not considered important (for nugget pull out failure simulation) in this study, elements inside the nugget region will not be considered in the mesh characteristics study.

It was identified in the previous section that three dimensional linear quadrilateral shaped shell elements will be used in this study to represent the coupon. Five different mesh configurations around the spot weld nugget were studied to identify the most suitable mesh. As linear elements were used to represent the coupon, it is an approximation for these types of elements to represent a circular dimension of the spot weld nugget as a linear path due to their linear interpolation scheme. Hence the number of elements along the circumferential direction of the spot weld nugget is very important. The five different meshes studied in this thesis were based upon mainly the number of elements around the spot weld nugget.

- Mesh – A consisted of 8 elements around the nugget.
- Mesh – B was with 16 elements around the nugget.
- Mesh – C consisted of 32 elements around the spot weld nugget.
- Mesh – D consisted of 32 elements around the spot weld nugget.
- Mesh – E consisted of 32 elements around the spot weld nugget.

The number of elements in the length and the width directions did not vary for the first two mesh types. But for the rest of the three designs (Mesh C, D and E), a finer mesh with more elements both in the width and length

directions were used. All the five different mesh types are provided in the following Figure 5.1.

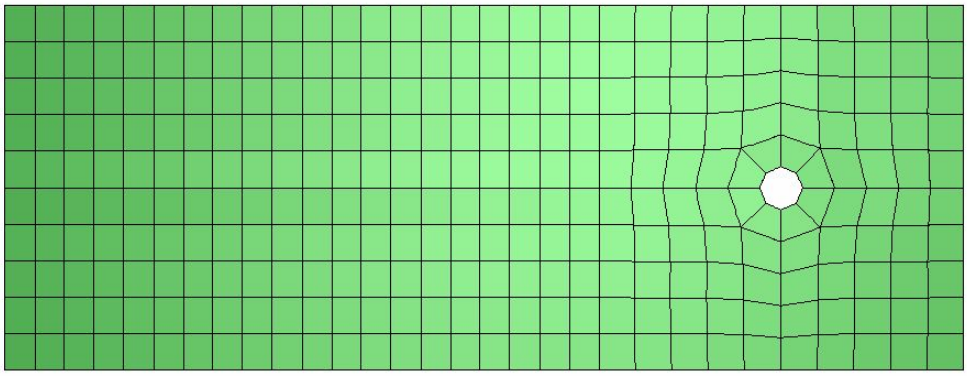

(a) Mesh – A with 8 elements around the spot weld nugget

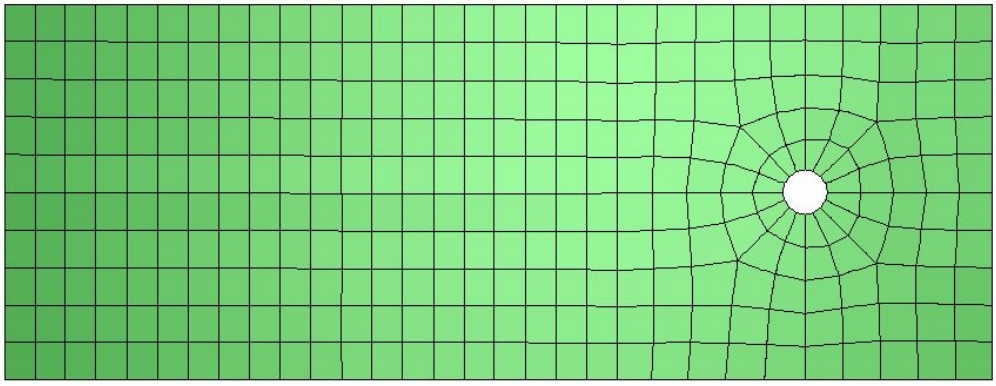

(b) Mesh – B with 16 elements around the spot weld nugget

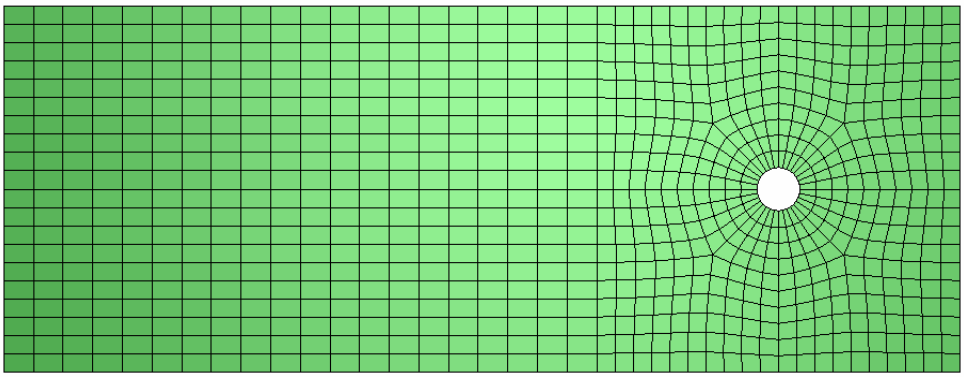

(c) Mesh – C with 32 elements around the spot weld nugget

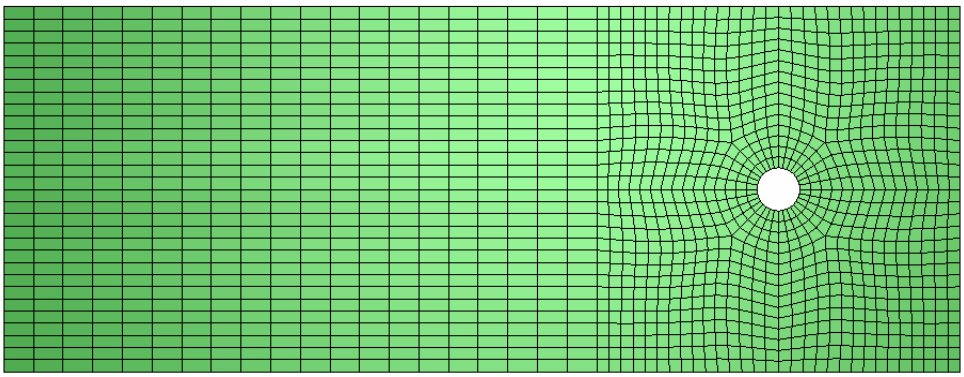

(d) Mesh – D with 32 elements around the spot weld nugget

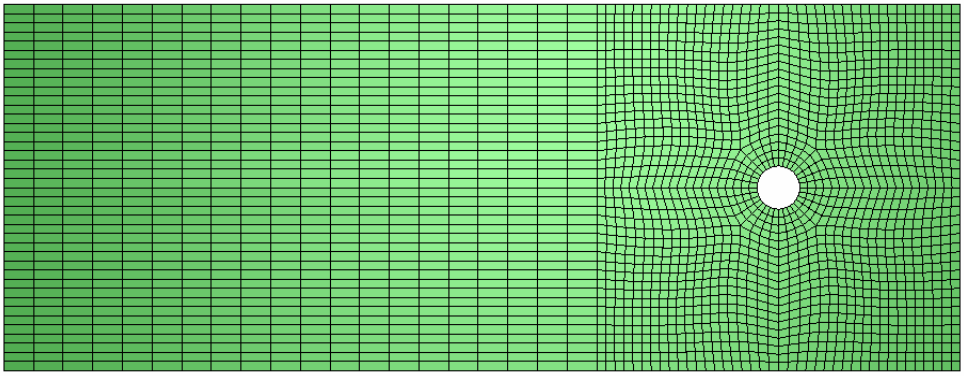

(e) Mesh – E with 32 elements around the spot weld nugget

Fig5.1: Different mesh design around the spot weld nugget region with 3D linear shell elements.

These generated meshes were checked according to the default criteria in HYPERMESH. As the test coupons were having a basic and simple geometry the checking criteria were very limited. The main criteria used to check the element quality were minimum and maximum angles in the quadrilateral elements, aspect ratio and the value of minimum jacobian. The aspect ratio is defined as the ratio of the longest side to the smallest side of the generated elements. The jacobian is a measure of the quality of an element in comparison to the ideal element shape. The set values (default in HYPERMESH) used for checking the quality are provided in the following Table 5.1.

Criteria	value
Minimum angle in an element	$< 45^0$
Maximum angle in an element	$> 135^0$
Minimum Jacobian	< 0.7
Aspect ratio	> 5.0

Table5.1: Mesh quality checking criteria

The values of the different parameters for the three meshes shown in the previous Figure 5.1 are summarized in the following Table 5.2.

Criteria	Minimum Angle (among all undeformed elements)	Maximum Angle (among all undeformed elements)	Minimum Jacobian (Undeformed Shape)	Maximum Aspect Ratio (Undeformed Shape)
Mesh – A with 8 elements around the nugget	64.72^0	112.50^0	0.59	2.54
Mesh – B with 16 elements around the nugget	62.88^0	108.93^0	0.55	4.53
Mesh - C with 32 elements around the nugget	67.92^0	103.05^0	0.7	4.25
Mesh - D with 32 elements around the nugget	66.84^0	106.89^0	0.78	2.66
Mesh - E with 32 elements around the nugget	61.26^0	111.60^0	0.79	3.26

Table 5.2: Characteristics parameters for different meshes

5.5 Convergence analysis and mesh choice

The mesh used for the simulation of spot weld joint failure was chosen according to the values of the characteristic parameters presented in the previous section. Only linear elements will be used in all the simulations discussed in this thesis. Hence the minimum angles of the generated elements should be higher than 45^0 and the maximum angle of the elements should be less than 135^0. These values should be maintained to obtain good results from the FEA analysis. Because the stress distribution values at the integration point of an element in displacement based finite element analysis are obtained from the interpolation of the computed displacement values at the element nodes. Apart form the element angle criteria the minimum jacobian value also plays an important role for obtaining good results from finite element analysis. Because jacobian is an element quality measurement index with respect to the ideal shaped element which is having 90^0 angles at every corner. The value of jacobian for the ideal element is 1.00. So the mesh which contains elements with maximum jacobian value closest to 1.00 will be the better than the others.

The chosen mesh configuration will be used for simulating the spot weld joint failure for both the static and dynamic loading conditions. The choice of a particular mesh will be based on the following categories.

- Maximum value for the minimum element angle parameter.
- Minimum value for the maximum element angle parameter.
- Maximum value for the minimum jacobian parameter of the elements.

Depending on the minimum element angle values and maximum element angle value, the Mesh – C can be chosen. But on the basis of the minimum jacobian parameter the Mesh – E can be chosen. But in case of Mesh – C and Mesh – E the element characteristic length would be very small

because of the high aspect ratio value. This will reduce the stability limit criterion for the explicit dynamic analysis procedure by nearly 50%. So if Mesh – C or Mesh - E (32 elements around the nugget) is chosen then in case of dynamic explicit analysis it will increase the computational cost by choosing smaller increment size in comparison to Mesh – B or Mesh – A (16 elements or 8 elements around the nugget). Moreover for static analysis which is an implicit analysis procedure followed by ABAQUS / STANDARD, Mesh – C, D and E (32 elements around the nugget) will require a higher computational cost and a higher data storage capacity for containing higher numbers of degrees of freedom in comparison to Mesh - A (8 elements around the nugget) and Mesh – B (16 elements around the nugget).

So it is very important to choose a proper mesh design for a reasonable analysis stability as well as the computational cost. The chosen mesh design should be replicated for all the coupon configurations used for different loading conditions used in this study. To choose a particular design, a mesh convergence study for the designed mesh configurations (Mesh – A, B, C, D and E) was performed with one of the spot weld models. The Spider Configuration – 3 (SC – 3) model was chosen for this purpose because this was one of the spot weld models which represented a complete rigid spot weld nugget. A detailed description of this model is provided in section 6.4 of chapter 6. The ABAQUS / STANDARD code was used for this convergence study among the designed mesh. The reference result for the study was the experimental force displacement diagram obtained at 5 mm/min rate and presented previously in chapter 4. The convergence results (force displacement diagrams) for the model were compared with the averaged experimental results. All the three coupon configurations (Lap Shear, Coach Peel and U - Tension) were considered for this convergence study. The comparative force displacement diagrams are given in the following Figure 5.2.

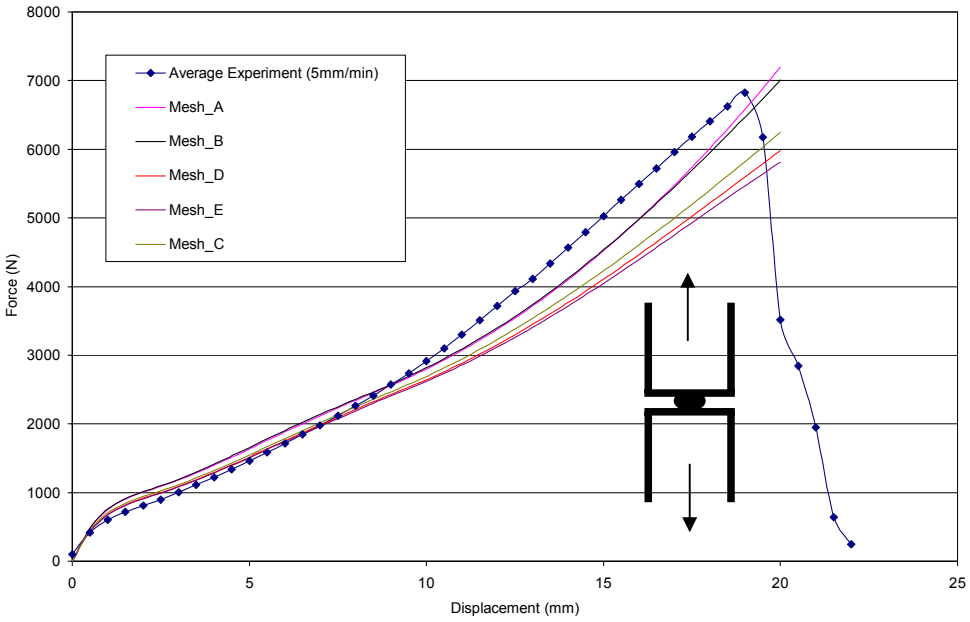
Average Experiment (5mm/min)
Mesh_A
Mesh_B
Mesh_D
Mesh_E
Mesh_C
Force (N)
Displacement (mm)
0
1000
2000
3000
4000
5000
6000
7000
8000
0
5
10
15
20
25

(a)

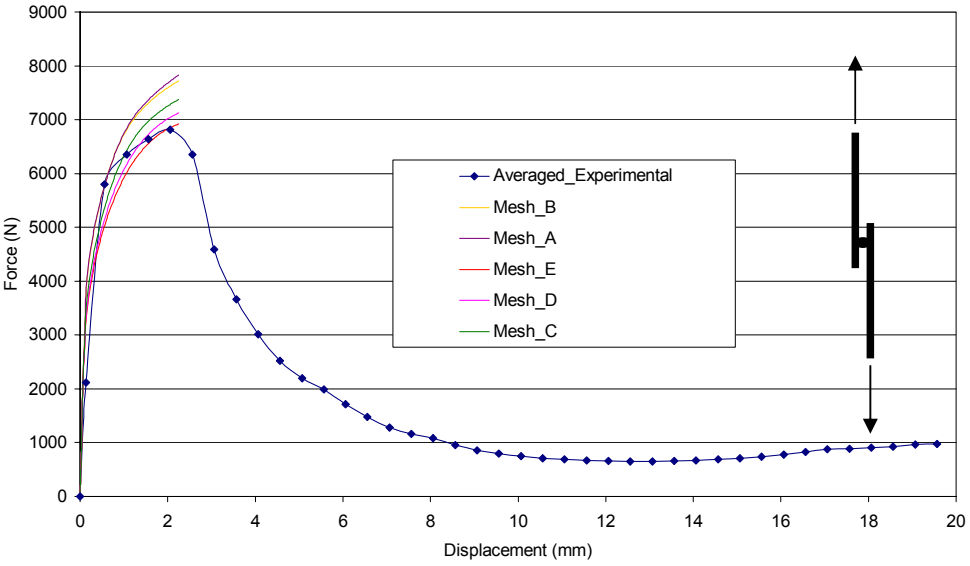
Averaged_Experimental
Mesh_B
Mesh_A
Mesh_E
Mesh_D
Mesh_C
Force (N)
Displacement (mm)
0
1000
2000
3000
4000
5000
6000
7000
8000
9000
0
2
4
6
8
10
12
14
16
18
20

(b)

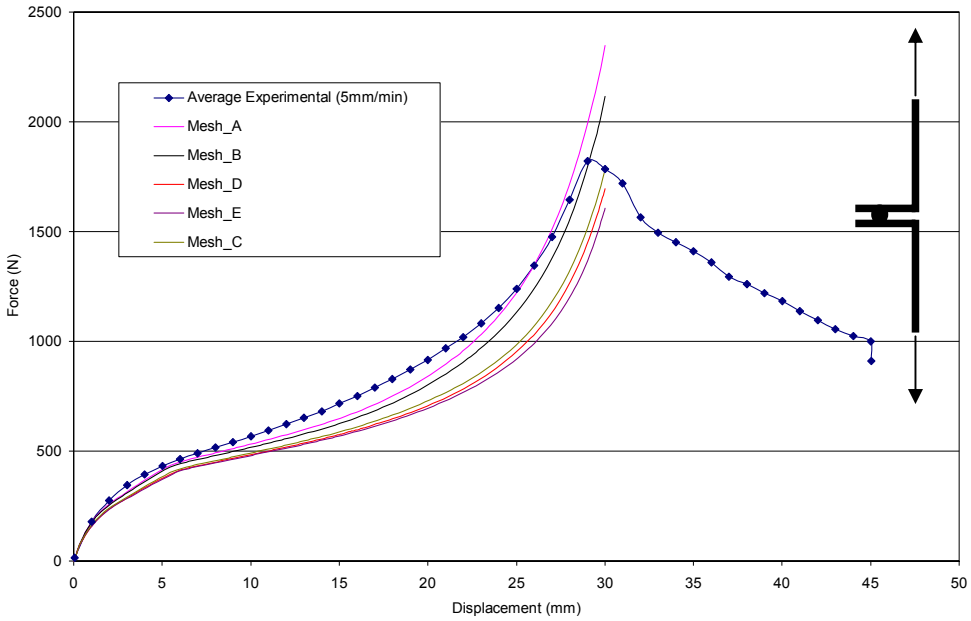

(c)

Fig 5.2: Mesh convergence study force displacement diagrams. (a) U Tension coupon results for tensile loading condition (b) Lap Shear coupon results for shear loading condition (c) Coach Peel coupon results for bending loading condition.

It can be seen from these presented curves that as the number of elements increased in the analysis, the force displacement response had decreased. The decreasing trend could also be observed for all the loading conditions intended to be studied in this thesis with different coupon configurations. But for different loading conditions a different mesh design provided a better correlation.

It is impractical to design the mesh with different configurations around the same spot weld model for different loading conditions. Hence it was intended to identify a specific mesh configuration to be used for all the loading situations. A relative error study is proposed to be conducted with these force displacement responses. For this purpose the maximum force values attained by the spot weld joints (as observed from the presented

averaged experimental curves) for the different loading conditions were utilized. All the experiments conducted in this thesis were displacement controlled experiments. Similarly the models in the simulations were also loaded by displacement. Therefore the comparison of the force values attained by the model in different loading situations, the displacement values for which the maximum forces were attained in the experiments for different loading situations were pivoted. For this pivoted displacement value the force values attained by the spot weld model with different mesh designs were used to calculate the relative error using the following Equation 5.1

$$\% RE = [(EFV \sim SFV) / EFV] \times 100 \qquad (5.1)$$

where RE = Relative Error

EFV = Experimental Force Value

SFV = Simulation Force Value

These experimental force values, the simulation force values and relative error for different loading cases are given in the following Table 5.3. The average error values presented in the table is the arithmetic average of all the relative errors in the considered loading situations.

It was evident from these relative error studies that Mesh – A had a better performance in the tensile loading situation. Mesh – B a had better performance for the bending loading situation and Mesh – C was better for the shear loading situation. But on the basis of the average error values Mesh – B had the best performance among the designed mesh configurations. Hence Mesh – B (16 elements around the nugget) configuration was chosen and replicated for all other types of coupon configurations. The finite element analysis procedures which were responsible for the selected mesh are briefly described in the following sections.

Mesh Configurations	Loading situations	Maximum experimental force (N)	Simulation force value (N)	Relative error (%)	Averaged relative error
Mesh - A	U Tension	6827.86	6604.94	3.26	9.21
	Lap Shear	6810.8	7684.74	12.8	
	Coach Peel	1820.96	2031.77	11.58	
Mesh - B	U Tension	6827.86	6488.44	4.97	5.69
	Lap Shear	6810.8	7596.06	11.5	
	Coach Peel	1820.96	1831.7	0.59	
Mesh - C	U Tension	6827.86	5837.12	14.51	12.04
	Lap Shear	6810.8	7257.7	6.55	
	Coach Peel	1820.96	1546.9	15.05	
Mesh - D	U Tension	6827.86	5614.2	17.78	13.97
	Lap Shear	6810.8	7019.5	3.05	
	Coach Peel	1820.96	1437.25	21.07	
Mesh - E	U Tension	6827.86	5482.35	19.71	14.96
	Lap Shear	6810.8	6830.05	0.28	
	Coach Peel	1820.96	1367.94	24.88	

Table 5.3: Relative error study for different mesh configurations

5.6 Analysis Techniques

The quasi static loading situation was simulated using ABAQUS / STANDARD code. The dynamic situation is simulated using ABAQUS / EXPLICIT code. The working principles of these two codes are described in details in the documentation accompanying them. A very brief idea of the working principle of these two codes is described in the following sections.

5.7 Quasi static analysis with ABAQUS / STANDARD

ABAQUS / STANDARD performs computation on implicit analysis procedures. For the implicit analysis procedure the stiffness matrix is formed for the developed model at the beginning of the analysis. This stiffness matrix remains the same throughout the analysis for every increment if geometric nonlinearity is not incorporated in the calculation. But if geometric nonlinearity is included in the analysis then this stiffness matrix is updated at the start of every increment based upon the geometric configuration, and the material state of the model at the end of the immediate previous increment. The displacement and rotation values at every node of the model for every degree of freedom are obtained by inverting the stiffness matrix and multiplying it with the force vector which is obtained from the applied forces and boundary conditions in the model. Lower Upper triangular matrix decomposition (LU Decomposition) method is used by ABAQUS / STANDARD to invert the stiffness matrix. Newton-Raphson method is used to obtain the nonlinear response for the model at each increment. A brief description of the Newton's method is provided in the following section.

5.8 Nonlinear response from ABAQUS / STANDARD

Newton-Raphson method is used to solve the nonlinear equilibrium equations in the iterations involved in an increment. The complete solution

is obtained as a series of increments. During each increment a number of iterations are involved to obtain an equilibrium state of stresses along with the correct modelling of history dependent effects. In the following Figure 5.3 a sample load displacement history diagram is presented to explain the working principle of the Newton-Raphson method.

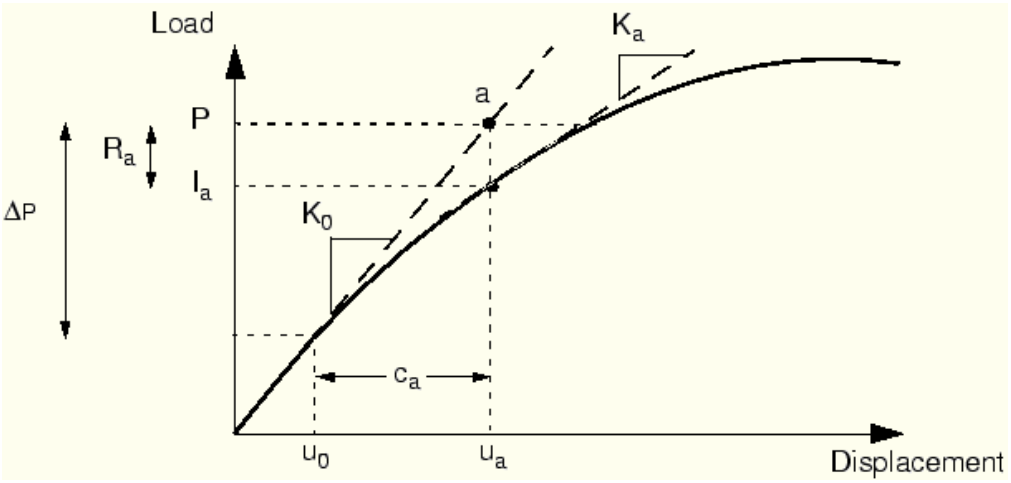

Fig 5.3: Load displacement history diagram for the iteration in an increment according to Newton-Raphson method (ABAQUS DOCUMENTATION, 2005).

In the above figure K_o is the initial structural stiffness which is based upon the configuration of the structure at the initial displacement u_O. ΔP denotes the small increase in load value in an increment. ABAQUS / STANDARD uses u_O and ΔP to calculate the displacement correlation factor c_a for the structure in the first increment. Then the value of c_a is used to update the structural configuration up to u_a. The new stiffness matrix for the model K_a is then formed at the stage of u_a. The new internal load level I_a is then calculated in the updated configuration and the force residual R_a in the updated configuration is also calculated according to the following equation.

$$R_a = P - I_a \qquad (5.2)$$

In the above mentioned equation P denotes the applied load on the structure in that particular increment. If R_a is equal to zero for every degree

of freedom then point “a” lies on the load displacement curve and it is considered that the structure is in equilibrium. R_a is provided with a tolerance value of 0.5% of the force acting in the structure averaged over time. The largest force residual value among all degrees of freedom in the models is compared with the tolerance limit. If R_a is less than the tolerance value then it is considered as a converged solution for that increment. If R_a is greater than the tolerance limit then ABAQUS / STANDARD tries to bring the internal and external forces into the balance.

Before accepting the converged results ABAQUS / STANDARD also checks the calculated displacement correction factor c_a. It is checked against the total incremental displacement $\Delta u = u_a - u_0$. If c_a is greater than 1% of the incremental displacement then ABAQUS / STANDARD performs the second iteration.

The 2nd iteration is performed using the stiffness K_a which was calculated at the end of the immediate last iteration and the force residual R_a to compute another displacement correction factor c_b which will bring the structural system close to equilibrium. The iteration process described in the previous paragraph is repeated again and again until the force residual tolerance limit is satisfied. The number of iterations required to find a converged solution for a particular increment depends on the level of nonlinearity involved in the problem formulation. By default if a converged solution for a problem is not found in 16 iterations then ABAQUS / STANDARD abandons the increment size and cut back the size to 25% of the previous value. This cut back option is allowed by the code for a maximum of 5 times in an increment before stopping the analysis.

If two consecutive chosen increment size converges in less than 5 iterations then ABAQUS / STANDARD automatically increases the increment size by 50%. But the Newton-Raphson method has a finite range of convergence which affects the size of the increments. If large increments are considered, then it can prevent any solution from being obtained due to

the reason that, the initial state is too far away from the desired equilibrium state that is being sought. Moreover if the increment size is too big then it will affect the computational efficiency because of the requirements of more iterations to attain the equilibrium state. So it is very much logical for an algorithmic restriction to be implemented in the solution procedure. For the study of the quasi - static state, automatic incrementation was adopted. For the automatic incrementation scheme the first increment is required to be suggested. Thereafter ABAQUS / STANDARD automatically adjusts the increment sizes to solve the nonlinear problems efficiently.

5.9 Dynamic simulation with ABAQUS / EXPLICIT

ABAQUS / EXPLICIT performs calculations according to the explicit dynamic principles. The explicit code is generally used for high speed dynamic events. Complex contact formulations and material degradation or failure can easily be incorporated in explicit code. Implicit code can also be used for simulating a dynamic event. But in that case the contact formulations and material degradation might cause high level of convergence difficulties in implicit procedures due to the restriction of increment limit which has been discussed in the previous section.

The calculation procedure for the explicit dynamic principle is completely different from the implicit procedure. In the explicit procedure the stiffness matrix is not formulated at all. The calculations are performed in such a manner that the state of stress in elements at the end of an increment is based completely on the nodal values of accelerations, velocities and displacements at the beginning of that specific increment. The increment size for explicit method is very small. The total computation generally completes on the order of 10,000 to 1,000,000 increments but the computation cost per increment is very small. This is due to the fact that there is no stiffness matrix formation for the calculation procedure. Hence there is no simultaneous equation to be solved. So no matrix inversion procedure is required for the explicit calculations. Furthermore for the same reason in comparison to the implicit procedure for the similar type of

simulation conditions, huge data storage capacity is not required for the explicit dynamic code.

The working principle of the explicit dynamic procedure is illustrated by an example in the following Figure 5.4. Let us say that the dynamic load P is being applied to a structure which is having the following mesh arrangement. The load is applied at node A of the element 1.

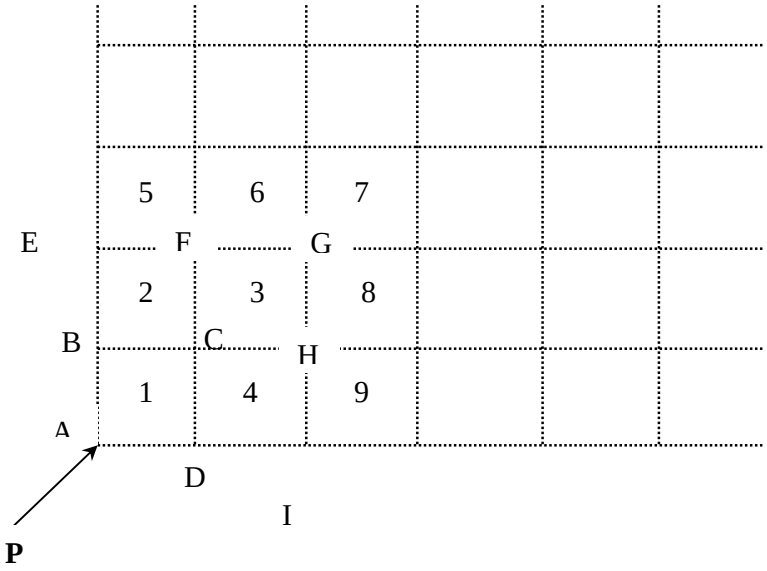

Fig 5.4: Sample loading condition and mesh configuration for explanation of the working principle of explicit dynamic code.

As a result of the applied force the node A of element 1 faces acceleration which has to satisfy the dynamic equilibrium condition. It should be noted here that in dynamic explicit procedure in the first increment, only the element facing the force undergoes the deformation process. The rest of the elements in the mesh do not face the force in the first increment. The stress wave starts to propagate from the element that is under the force. The acceleration of this stress wave has to satisfy the dynamic equilibrium equation. The dynamic equilibrium equation used in the explicit procedure is as follows.

$$Mu'' = P - I \qquad (5.3)$$

where M is the mass of the element, P is the external applied force, I is the internal force acting on the nodes of the element and u'' is the acceleration. The acceleration of the stress wave over the time period is calculated according to the following equation.

$$u''_{(t)} = \left(M\right)^{-1}\left(P - I\right)_{(t)} \qquad (5.4)$$

It is assumed that this acceleration value is constant over the span of the increment. So the size of increment remains very small. The acceleration value is then integrated to obtain the velocity and displacement values. ABAQUS / EXPLICIT incorporates the central difference formula for the integration procedure. Then the strain value is calculated from the displacement values and the total strain acting in an element is calculated according to the following expression.

$$\varepsilon_{Total} = \varepsilon_0 + \varepsilon_1 \qquad (5.5)$$

where the total strain ε_{Total} is expressed as a summation of the initial strain ε_0 and the incremental strain ε_1 as result of the applied force. Then the total strain ε_{Total} is employed to calculate the stress σ in the element 1 by using the material constitutive definition. This stress delivers the forces on the other nodes (B, C and D) of the element 1.

At the end of the first increment forces acting on the nodes B, C and D of element 1 are known. Hence the stress σ acting in the first element (element 1) transmits the internal forces in the neighbouring elements (2, 3 and 4) at the node B, C and D which are associated with the element 1. Due to this internal force, stress formulated in the elements 2, 3 and 4 are calculated utilizing the dynamic equilibrium condition according to the procedure described previously. So the forces acting on the element nodes (E, F, G, H and I) and stresses acting in the elements (2, 3 and 4) surrounding element 1 is known at the end of the second increment. Similarly this process of analysis continues with the increase of increments until it reaches the desired total time for the complete analysis. The complete procedure can be described according to the following Chart 5.2.

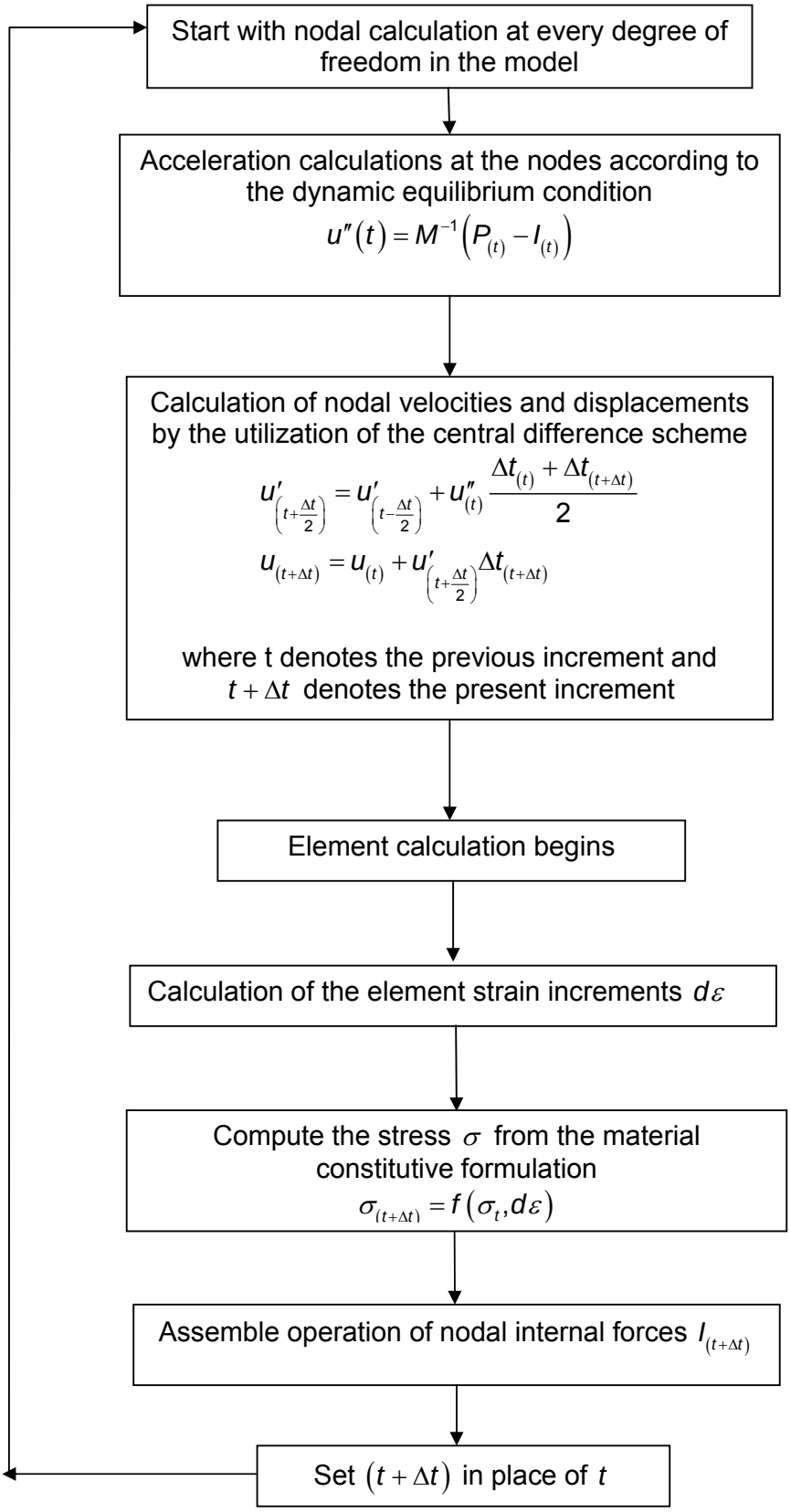

Chart 5.2: Explicit analysis procedure

5.10 Stability Limit for Explicit Analysis

The calculation procedure for ABAQUS / EXPLICIT advances through increments of real time Δt , which is based on the state of the model at the beginning of that particular increment. The stability limit for an explicit analysis is defined as the transit time required by the dialatational wave to cross the distance defined by the characteristic element length. Hence the mathematical expression for the stability limit is composed of element length L^e and the dialatational wave speed of the material c_d.

$$\Delta t = \frac{L^e}{c_d} \qquad (5.6)$$

In the above expression the dialatational speed is defined as

$$C_d = \sqrt{\frac{\lambda + 2\mu}{\rho}} \qquad (5.7)$$

where

λ = Lame's constant

ρ = Density of the material

μ = Modulus of rigidity

Hence the mesh size and the material property used for dynamic analysis affect the explicit calculation procedure effectively.

5.11 Summary

In this chapter the modelling strategy followed for the development of spot weld joint was described. A definite mesh configuration with 16 elements arranged around the spot weld nugget (Mesh – B) was chosen for all types of coupon geometry. This choice was made on the basis of the element quality study and the working principle of the implicit and explicit finite element codes. The explicit code will be used to simulate the occurrence of failure in spot welded joints in dynamic loading situations. The implicit code will be used to simulate the load bearing capability of different spot weld models in the quasi - static loading conditions. The descriptions of these models are provided in the next chapter.

Chapter 6

Finite Element Modelling Of Spot Weld Joint

6.1 Overview

In this chapter the modelling strategy for a single spot weld on different coupon configurations is described. The reasons behind choosing the development strategy are also briefly provided. The validation procedure of the developed models from the experimental data is also shown. After the models are validated the response obtained from the different models are discussed. A suitable failure criterion is incorporated in the developed spot weld models. Hence the chapter is organized according to the following sections.

6.2 Model description
6.3 Assumptions for the modelling the spot weld joints
6.4 Spot weld models
6.5 Material property
6.6 Element choice
6.7 Boundary condition and loading condition
6.8 Nonlinearity in the model
6.9 Spot weld FEM models for quasi static simulation
6.10 Spot weld failure features
6.11 Characteristic definition of the spot weld failure
6.12 Failure criterion for the spot weld joint models
6.13 Mechanism of the failure criterion
6.14 Determination and calibration of the failure criterion
6.15 Spot weld failure simulation

6.2 Model Description

For the simulation of spot weld behaviour under different loads, a full model of the test coupons were developed. The geometric dimensions used for the full models were identical to the dimensions used for manufacturing the test coupons and the spot weld nugget. These dimensions were provided in Figure 4.6 of chapter 4. The spot weld nugget dimension was modelled as 4.5 mm as this dimension was conformed from the hardness distribution around the spot weld joint and was reported in section 4.7.

It is noted here that all the types of coupons used in this study, had a geometrically symmetric shape. The loading faced by the spot weld nugget was also symmetric. The deformation pattern with respect to the loading directions was also symmetric as has been observed for the experimental deformation pattern. Therefore only half of the model could have been modelled utilizing symmetric boundary conditions. But that was not done because the intention of this modelling study was to get the full response from the spot weld model. Further more these models will be studied under dynamic loading situations where the failure location would be clearly identified. Therefore the full spot weld FEM model was built in this study.

6.3 Assumptions for modelling spot weld behaviour

There were two different assumptions while modelling the spot weld behaviour. These two assumptions can be described from two different points of view. One of them is from the material behaviour perspective. The other one is in regards to the model development.

The first assumption has already been introduced in the previous chapters. The material model used here for the chosen sheet metal was with the isotropic formulation. The isotropic material behaviour was such that it

behaved similarly both in tension and compression loading conditions. Another assumption about the material properties used in these models is that they have been modelled as homogeneous material. That is the material property for the heat affected zones were not considered for the developed models. Reasons to exclude the heat affected zone material properties were provided in section 2.13 (Limitations of the present work) of chapter 2.

The second assumption is about the choice of elements for modelling the spot weld nugget. This assumption was made possible due to of the findings reported by Wung et al. (2000. 2001). According to this report the spot weld nugget in a tensile shear coupon does not face any metallurgical changes after the failure has occurred. The metallurgical structure remains the same before and after the tests. So this finding provided the basis to assume that the nugget (for detail modelling purposes) can be modelled with rigid elements. The only exception was the solid nugget model in which case the nugget was modelled with solid elements with the same material property as the coupon sheet metal.

6.4 Spot weld models

With the assumption stated in the previous section six different spot weld models were built for in this study. The spot weld nugget in the models was represented by a circular area with a diameter of 4.5 mm. In all the models this circular area was modelled with 16 elements. For the solid element model, the circumference on the cylindrical surface of the solid body was meshed with 16 elements and in the thickness direction it contained 8 elements. In all the cases the rigid beams in the models were used to constrain the motion for all 6 degrees of freedom. The proposed spot weld models are as follows

- Individual Rigid Beam Model (IRB)
- Parallel Multiple Rigid Beams Model (PMRB)

- Solid Element Model (SEM)
- Spider Configuration – 1 (SC – 1)
- Spider Configuration – 2 (SC – 2)
- Spider Configuration – 3 (SC – 3)

It should be noted here that same mesh was used for building all the models. The detail descriptions of the developed models are provided below.

Individual Rigid Beam Model (IRB)

Individual rigid beam model is the simplest of all the spot weld models. It is currently the most widely used spot weld model incorporated in body in white structure models in industrial design (Machine design, 1994). The spot weld nugget is represented by a single rigid beam connection. The connection is made to one point on both the coupons. It should be noted here that as this model is represented by a point to point connection. The configuration of the model is shown in Figure 6.1.

Parallel Multiple Rigid Beams Model (PMRB)

Parallel multiple rigid beams model is a modification of the IRB model. Here in this model the spot weld nugget diameter is represented physically. The spot weld nugget is represented by several rigid beam elements connecting both the coupons along the circumference of the nugget diameter. For this study there were 16 rigid elements along the circumference of the spot weld nugget. The elements inside the nugget region are represented by shell elements and all of these shell elements were having the same material property. The configuration of the model is shown in Figure 6.1.

Solid Element Model (SEM)

The solid element model represents the spot weld nugget with three dimensional solid elements. The solid elements were joined to the shell elements (which represented the coupon sheet metal) with rigid beams. The configuration of the model is shown in Figure 6.1.

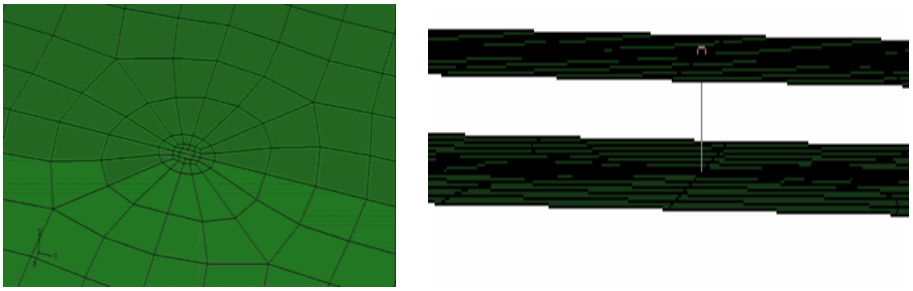

Top view Side view

(a) Individual Rigid Beam Model (IRB)

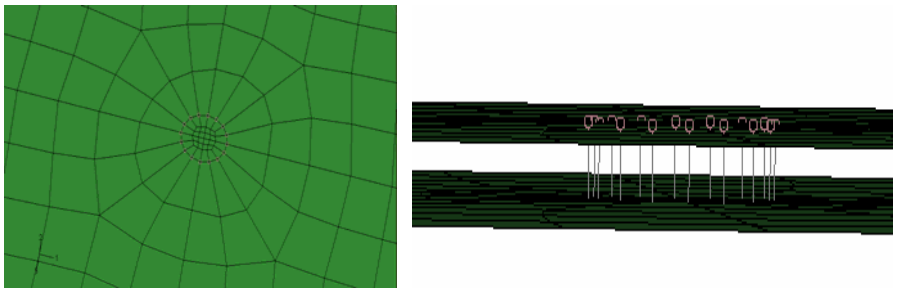

Top view Side View

(b) Parallel Multiple Rigid Beams Model (PMRB)

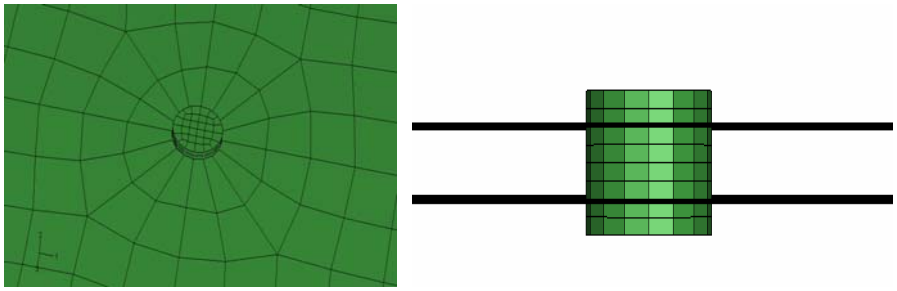

Top view Side View

(c) Solid Element Model (SEM)

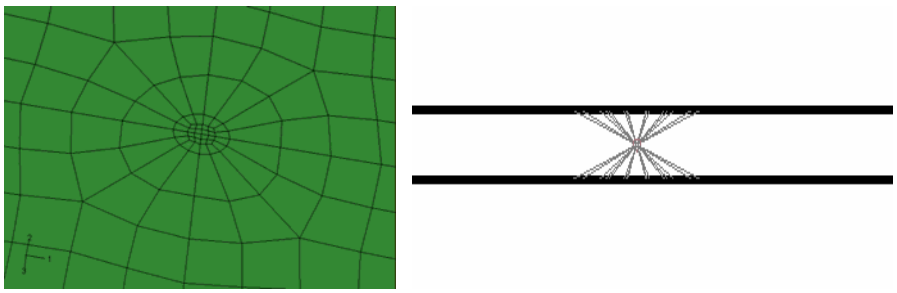

Top view Side View

(d) Spider Configuration – 1 (SC – 1)

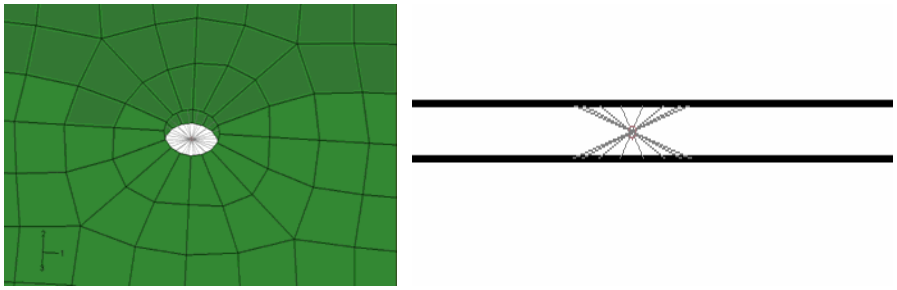

Top View Side View

(e) Spider Configuration – 2 (SC – 2)

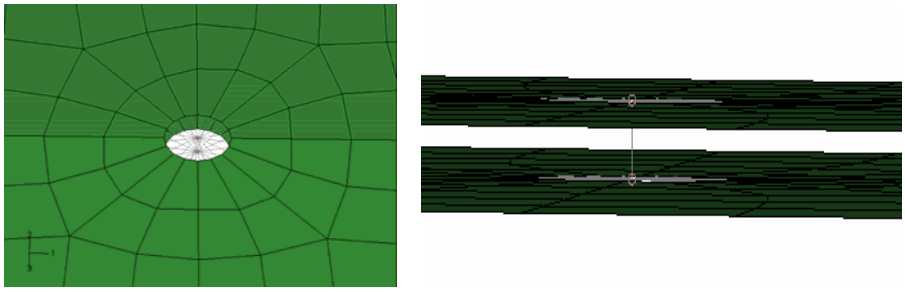

Top View Side view

(f) Spider Configuration – 3 (SC – 3)

Fig 6.1: Diagrams of different configurations of spot weld models.

Spider Configuration – 1 (SC – 1)

In Spider configuration - 1 model the spot weld nugget diameter is also represented by shell elements. But these shell elements representing the nugget diameter are rigid elements. The coupons in this model are connected with a certain spider orientation. The configuration of the model is shown in Figure 6.1.

Spider Configuration – 2 (SC – 2)

The 'spider configuration – 2' model for representing the spot weld joint is another variation of the spider configuration - 1 model. Both the sheets are connected in this model by means of spider patterns. The nugget diameter of the spot weld joint is represented by a hollow space in this model. The configuration of the model is shown in Figure 6.1.

Spider Configuration – 3 (SC – 3)

The spot weld nugget in this model is represented as a rigid beam element. The connection of the rigid beam element to the shell elements of the coupon is established by providing spider pattern at both the ends of the rigid beam elements. This model is called as Spider configuration – 3 model. The configuration of the model is shown in Figure 6.1.

6.5 Material property

As mentioned in the previous sections that the material model used in this analysis were assumed to be isotropic in nature with similar behaviour in tension and compression loading condition. Further more only one material property was used for the simulation. The material properties (used for quasi static simulations with ABAQUS/STANDARD) were extracted from the

uniaxial tensile test of the base metal with the loading rate of 4 mm/min. The material properties used in the simulation are as follows.

- Modulus of elasticity 200GPa.
- Poisson's ration 0.3
- Yield stress 209 Mpa
- Ultimate Tensile strength 325.38 Mpa.

The true stress true strain curve of the used material is given in Figure 6.2.

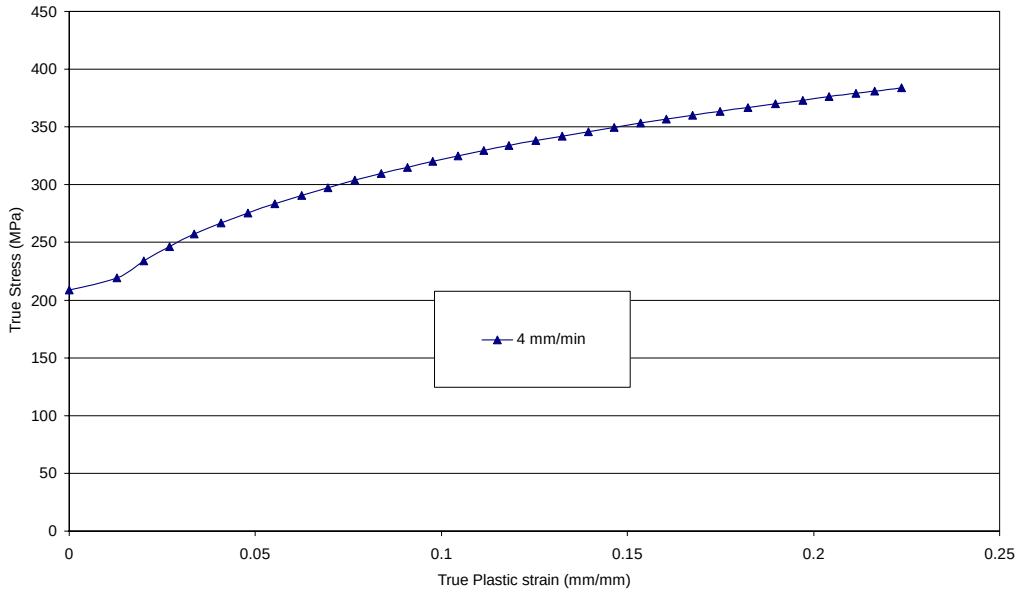

Fig 6.2: True stress true strain curve used for the quasi static simulation obtained at 4 mm/min.

6.6 Element choice

The mesh used for the analysis is presented in Figure 6.3. The presented mesh is only for the lap shear coupon. A similar mesh configuration was used for the all other coupon configurations. The element arrangement near the spot weld nugget was the same for all the coupons and loading conditions. The mesh arrangements for all the coupons can be observed from figure 6.4. The coupons were modelled with shell elements because the thickness to length ratio for the chosen dimension was very low. The nugget was modelled with rigid elements and solid elements. The reason for the choice of rigid

elements for representing the nugget was explained in the previous sections (6.3, 6.4). The solid elements were chosen to represent the nugget to check whether these brick elements could provide sufficient stiffness to the whole model.

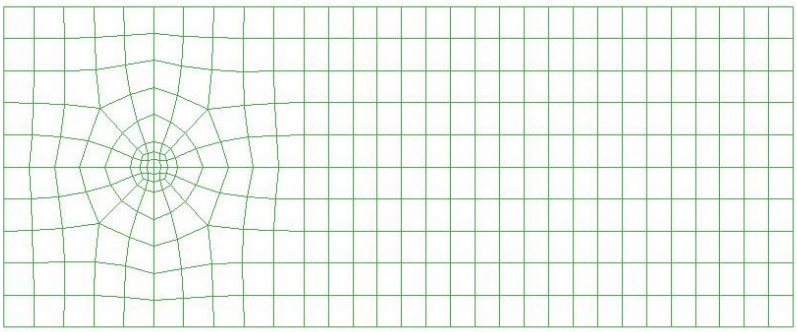

Fig 6.3: Meshing of the structure used in the study.

Generally linear elements are chosen to perform failure analyses due to the reason that they provide homogenous pressure distribution for contact definitions. Hence linear elements were chosen to perform all the simulations presented in this thesis. The choice for the shell elements were S4R and for the solid element was C3D8R. These two types of elements were linear elements in nature. Further more the shell element S4R is reduced integration element. The location for the integration point in this element is at only one location – at the centroid of the element. Hence it would be helpful to face the hourglass control situation. Moreover, due to limited number of integration points, reduced disk space would be required to store the results obtained from the simulation.

6.7 Boundary condition and loading condition

The boundary conditions were imposed on the model to simulate the actual gripping situations of the tests which were conducted for different coupon configurations. At one end of the coupons, encastered boundary conditions were imposed to restrict all the degrees of freedom. On the other end boundary conditions were applied to restrict the motion in the transverse direction of the applied load direction. Moreover to constrain the rotation of the rotational degree of freedom at the loading end, rotational motion was

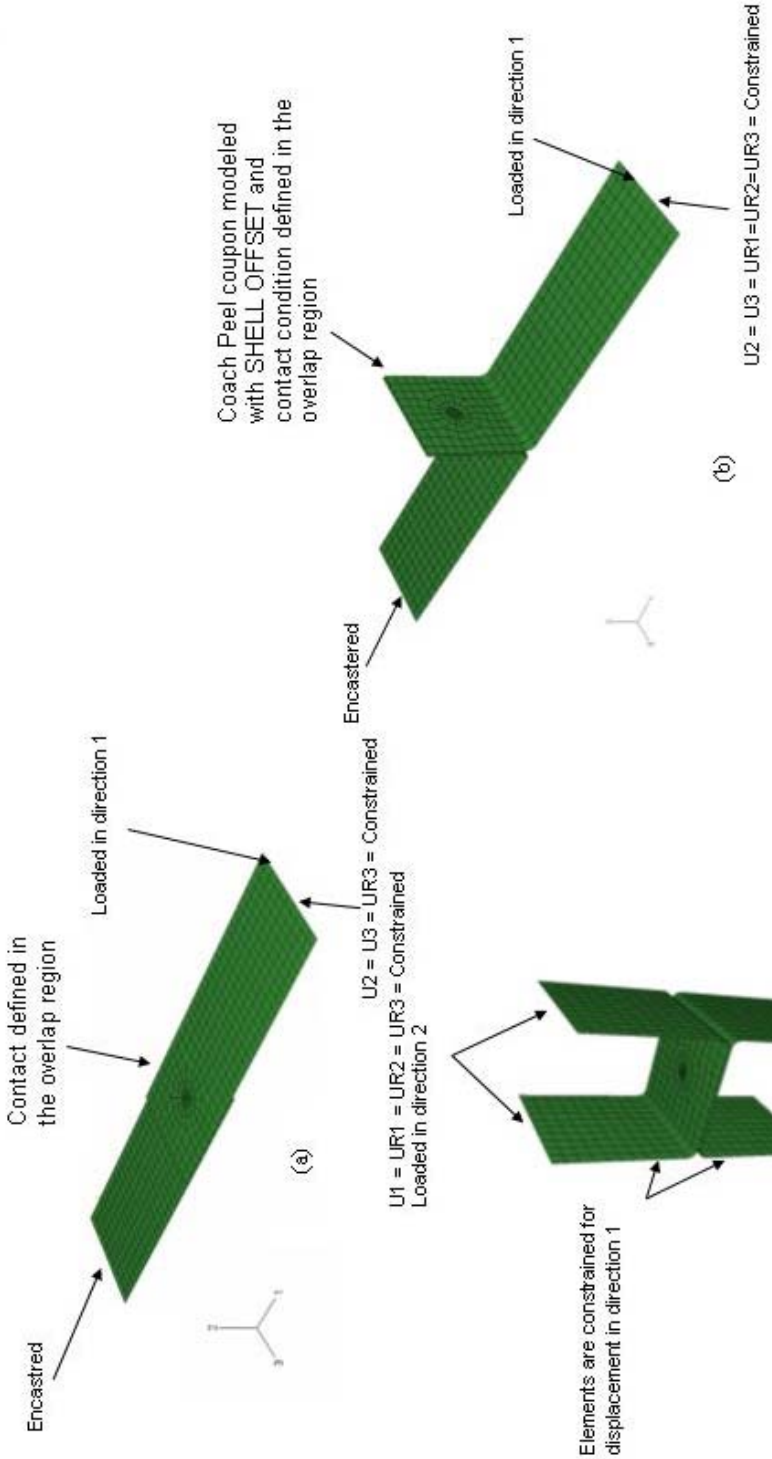

Fig 6.4 Loading and boundary conditions for different coupon configurations (a) Lap shear for shear loading condition. (b) Coach peel coupon for bending load condition. (c) U tension coupon for tensile load condition

restricted for the lap shear and coach peel coupon. In Figure 6.4 the summary of the applied loadings and boundary conditions are provided.

For the U tension coupon all of the rotational degrees of freedom were constrained to simulate the gripping of the test coupons. Moreover a couple of elements in the loading arm section were having constraints in one displacement degrees of freedom (direction 1) to ensure the setting of the test fixture which was shown in Figure 4.9 (d).

6.8 Nonlinearity in the model

There were three different kinds of nonlinearity involved in the model described in the previous sections. These nonlinearities are

- Material nonlinearity
- Geometric nonlinearity
- Nonlinearity at the boundaries.

The material nonlinearity was described in the material property section (Section 6.5) of this chapter. The geometric nonlinearity was incorporated to consider the updated geometric information at every increment of the analysis. So all the simulations presented in this study are large deformation analysis. The large deformation analysis captured the bending deformation of the spot welded coupons in all the directions.

The nonlinearity due to the change of geometric boundary lines was included in the model through contact definition. The general metal to metal friction coefficient value was incorporated in defining the contact. The coefficient of friction was defined as 0.15 with finite sliding formulation. For better establishment of the contact in case of the Coach Peel coupon, the sheet metal coupon was modelled with the “SHELL OFFSET” option.

6.9 Spot Weld FEM models for quasi static simulation

The spot weld models were analysed for the quasi - static loading condition with the implicit code ABAQUS/Standard. Before interpretation of the results obtained from the finite element analysis, it is required to understand that the developed models are providing proper results. Hence the developed models need to be validated. For validation purposes, the experimental results obtained and presented in previous chapter (chapter 4) are utilised. The experimental response curve used for the validation purpose is showing the averaged values obtained from experiments. The averaged values of forces from the experimental testing were obtained at certain displacement positions because all the experiments were displacement controlled tests. Similarly the force displacement responses were recorded from every model presented in this study. Then the force displacement curves obtained from the developed models are compared with the force displacement curve from the experiment. The complete process of the comparison scheme is presented in Chart – 6.1.

The force was measured by load cell in the experimental analysis. For the simulation the force was calculated at the point of load application. In experiments the displacement data was recorded from the tensile testing machine cross head displacement. In case of the simulation the displacement data was captured from the same location of the models. The resulting force displacement diagram obtained from the above stated procedure is presented in Figure 6.5.

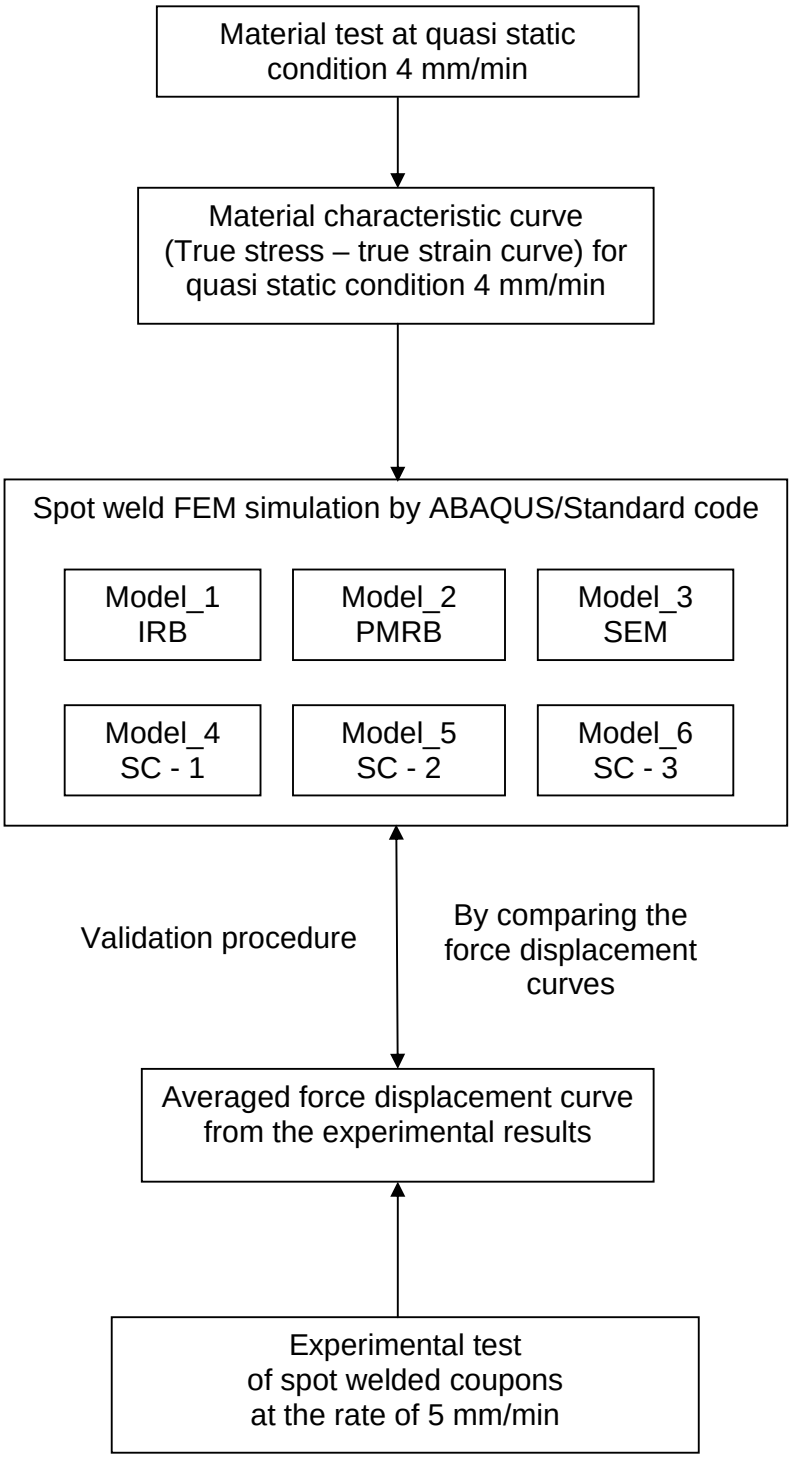

Chart 6.1: Validation procedure for the developed spot weld models at quasi static loading condition

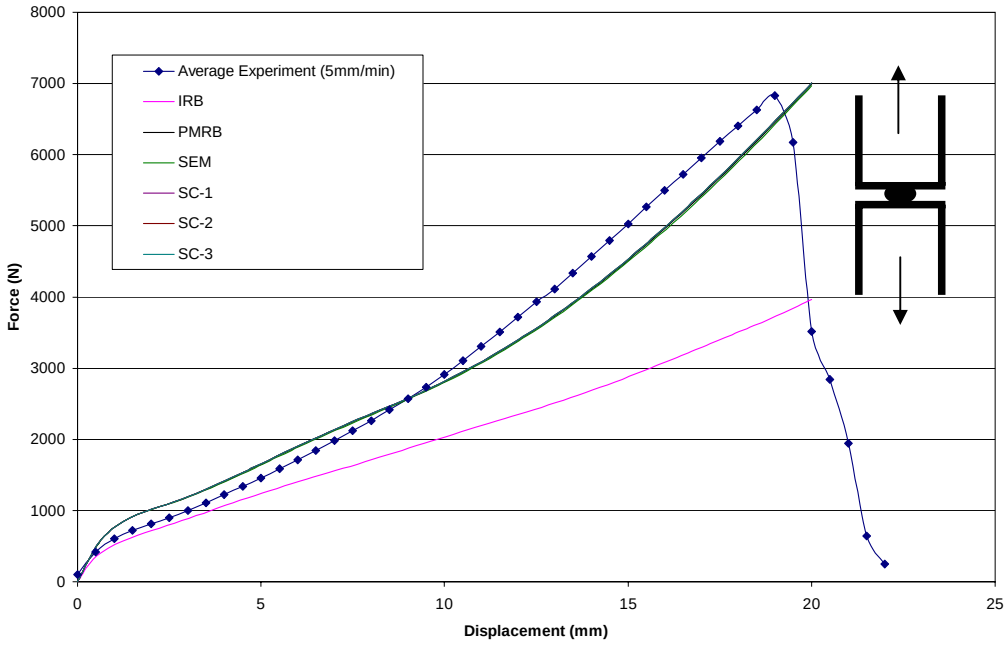
8000
7000
6000
5000
4000
3000
2000
1000
0
Force (N)
0
5
10
15
20
25
Displacement (mm)
Average Experiment (5mm/min)
IRB
PMRB
SEM
SC-1
SC-2
SC-3

(a)

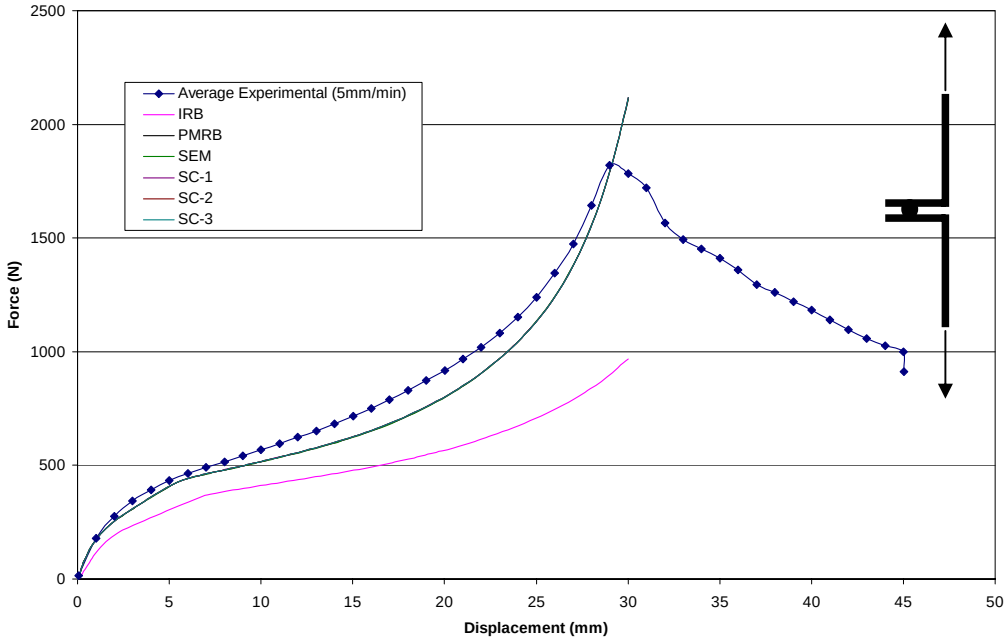
2500
2000
1500
1000
500
0
Force (N)
0
5
10
15
20
25
30
35
40
45
50
Displacement (mm)
Average Experimental (5mm/min)
IRB
PMRB
SEM
SC-1
SC-2
SC-3

(b)

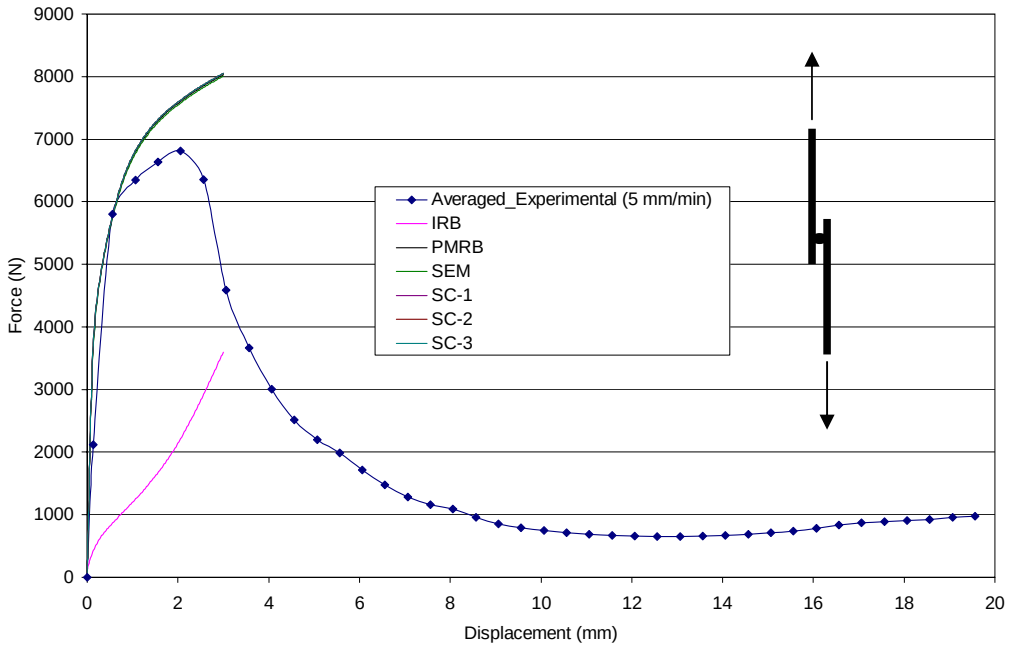

(c)

Fig 6.5: Force displacement response obtained from experiments and simulation. (a) U tension coupon (b) Coach-peel coupon (c) Lap Shear Coupon

From the figure it can be observed that the force displacement response curves obtained from most of the developed models nearly matches with the experimental curve. Hence the responses of five different models are verified. Apart from all of these the only exception was the curve obtained from the Individual rigid beam (IRB) model in all the loading conditions. Response from the Individual rigid beam model shows that it collapses at a very early period of its loading stage. This is because the individual rigid beam model does not represent the proper joint connection for the spot welds. The reasons behind these responses are discussed in the next chapter. The models responses (force displacement curve) in case of the lap shear coupon used for testing the developed models in the shear loading condition, over predicted than the averaged experimental results. The reason behind this over prediction will also be discussed in the next chapter.

At some stages the force displacement curves obtained from the FEM models (for U Tension and Coach Peel coupon) under predict the response. At highest loading stage they over predict the experimental response. The reasons behind the under prediction and over prediction will be discussed in Chapter - 7.

The experimental curve clearly shows failure of the spot welded joint by decreasing the response after the peak load was attained. But the responses from the developed FEM models could not project similar response characteristics except for the IRB model which collapsed earlier. It was due to the absence of any failure characteristics in these developed models. This failure prediction needs to be investigated and is presented in the next section. As the force displacement response from the IRB model collapsed earlier, the failure criterion need not to be incorporated in the IRB spot weld model.

6.10 Spot weld failure features

The general failure patterns for the spot welded joints have been clearly pointed out by Zhou (1999, 2000), which was supported later by other researchers (Schneider et al. (2003), Lin (2004)). Based on their findings it will be attempted to simulate only the nugget pull out failure mode for the spot welded joints. Experimental conditions which prevail the nugget pull out failure pattern were elaborately discussed in chapter 4. Similar conditions will be used to simulate the spot weld failure situation.

The failure patterns of the spot welded test coupons have been presented in section 4.9. In all the test cases the failure had occurred around the spot weld joint nugget. Similar failure patterns were reported by other researchers (Zhou (1999, 2003), Zuniga et al. (1997), Lin (2004), Schneider et al. (2003)). In these cases the spot weld nugget came out of the coupon material

completely. The spot weld nugget acted as an individual body itself. The separation pattern of the spot weld nugget was as such that it left behind a clear mark (hole) in the welded test coupons.

6.11 Characteristic definition of the spot weld failure

The characteristic definition of the spot weld joint failure that will be used in this study is recognized from a macroscopic point of view. This definition does not consider specific causes of the failure for different loading conditions. The idea behind this is to identify a general predictable qualitative failure definition for all the loading conditions which can be used for denoting the failure of the developed models from the simulations. Hence the characteristic failure definition is pointed out from the response curve (force displacement curve) observed from the experiments with the spot welded coupons.

The failure of the spot weld joints in this study is identified from the force displacement curve as the response shows the loss of load bearing capability of the joint. The load bearing capability of the joint decreases as the joint starts loosing its integrity. Hence the failure point on the force displacement curve is identified when response from the force displacement curves goes down.

6.12 Failure criterion for the spot weld joint models

It has been identified in chapter 4 that the spot weld nugget acts as an individual identity in the failure of the test coupon joint. The material of the test coupons was pulled out of the joint area leaving a clear mark on the test coupons (figure 4.9). Hence the failure condition for the spot weld joint is defined as a material failure model. The failure of the material could be discussed from three points of view. These are as follows.

(a) Yielding of the material
(b) Initiation of plastic instability of the material
(c) Complete separation of material

The material failure model considered here is not the yield stress of the material. This is because the material does not loose its load bearing capability at the yield stress. The plastic deformation starts after the yield stress is reached. The loss of the load bearing ability of the material starts at the initiation of the plastic instability of the material. It is identified as the maximum load bearing point of the material itself (Ultimate tensile strength of the material from the uni axial tensile test data). The material completely looses the load bearing capability when the complete separation of the material occurs. This phenomenon can be clearly pointed out from the force displacement curve as the response goes straight down at this point. These ideas regarding the failure criterion are explained as follows.

The failure criterion in the developed spot weld models will be implemented through explicit finite element code ABAQUS/Explicit. The general outline of the material failure model to be used for the simulation of spot weld failure can be described using the following Figure – 6.6. A general material constitutive relation curve (stress – strain curve) for metal is used for this purpose. Three distinct regions are identified from the presented stress – strain curve. The linear elastic region is denoted by a-b. The plastic region for the material law is pointed by the region b – c. The region c – d' denotes the undamaged material response. But if damage is defined in the model then the material constitutive relation follows the region denoted by c – d. The region c – d is shows the degradation of the load bearing capability of the material. This region is controlled by the evolution of the degradation of the material stiffness. As the material stiffness is degraded beyond point c on the stress strain curve, it is known as the failure initiation criterion. In the next section explanation for this criterion is presented.

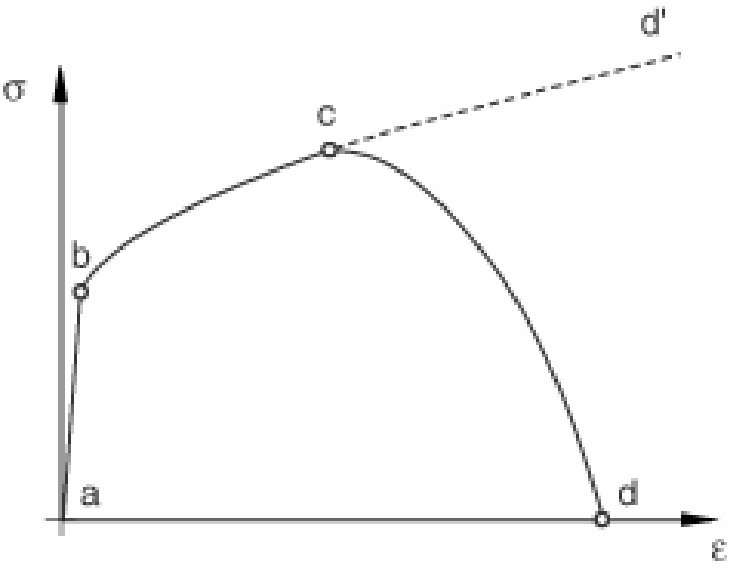

Fig 6.6: General stress – strain curve for metal (ABAQUS DOCUMENTATION, 2005).

6.13 Mechanism of the failure criterion

The failure criterion used in this study is based upon the state of stress and the failure strain. The mechanism of the material failure criterion follows the similar three distinctive regions as stated in the previous section. The material failure model used here is a ductile type of material failure model. The elastic (range a – b in figure 6.6) and the plastic range (range b – c in figure 6.6) are defined through the material property definition in the model development process. The location of the damage initiation criterion (point c in figure 6.6) is introduced through the ductile damage model.

The ductile damage model was implemented in the developed spot weld models through the usages of the keyword *DAMAGE INITIATION in the ABAQUS / EXPLICIT code. The failure model calculates the equivalent plastic strain $\bar{\varepsilon}_{pl}^{D}\left(\eta, \bar{\varepsilon}^{pl}\right)$ at the failure point as a function of stress triaxial state $\left(\eta\right)$ and equivalent plastic strain $\left(\bar{\varepsilon}^{pl}\right)$. The value of the material state

variable ω_D is dependent on the calculated equivalent plastic strain and it changes with the increment of the plastic deformation. For each increment in the analysis, the increment increase for ω_D is calculated according to the following equation.

$$\Delta\omega_D = \frac{\Delta\bar{\varepsilon}^{Pl}}{\bar{\varepsilon}_D^{Pl}\left(\eta, \dot{\bar{\varepsilon}}^{Pl}\right)} \geq 0 \qquad (6.1)$$

The failure of material is initiated when the following law is satisfied by the value of the material state variable.

$$\omega_D = \int \frac{d\bar{\varepsilon}^{Pl}}{\bar{\varepsilon}_D^{Pl}\left(\eta, \dot{\bar{\varepsilon}}^{Pl}\right)} = 1 \qquad (6.2)$$

Once the material failure criterion is met the decrement of the material stiffness begins. The damage evolution law clarifies the rate of degradation of the material stiffness. The damage evolution law is implemented in the developed models through *DAMAGE EVOLUTION keyword. For the ductile damage model the material stiffness was modelled with a scalar damage equation. At any given time of the analysis after the damage criterion is satisfied the stress tensor for the current material property is calculated according to the following equation.

$$\sigma = (1 - D)\bar{\sigma} \qquad (6.3)$$

where $\bar{\sigma}$ = effective or undamaged stress tensor computed in the current increment.

σ = stress tensor considering the damage of the material

and D = overall damage variable.

The use of the above mentioned equation is described using the Figure 6.7. This figure is an elaborative form of the Figure 6.6.

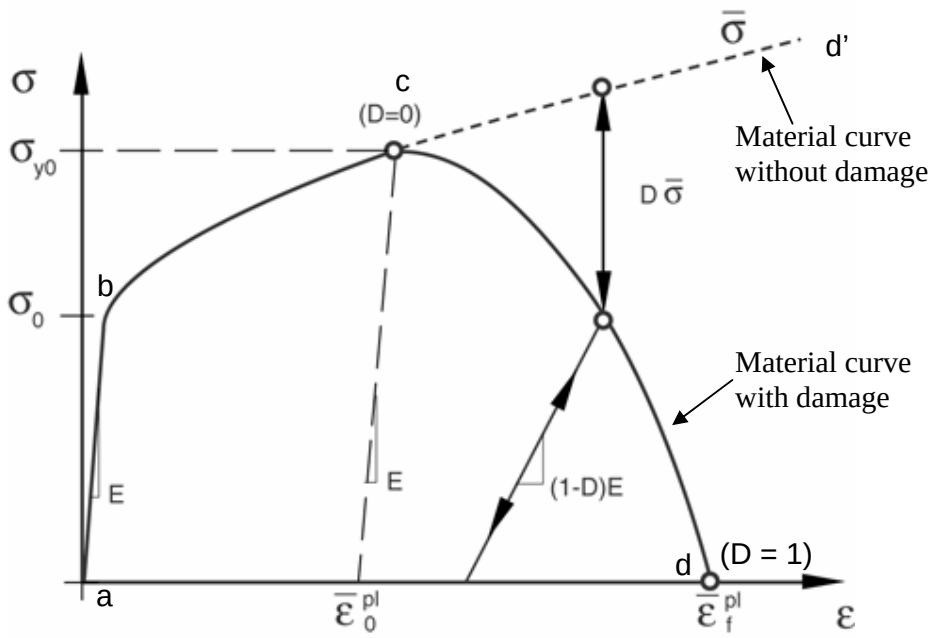

Fig 6.7: Ductile material stress strain response for the implemented damage evolution law (ABAQUS DOCUMENTATION, 2005).

The stress strain values at different points on the curve (a, b, c, d) are shown in the figure at their respective locations. The elastic plastic material property (region a – c) was defined as isotropic material model with power hardening (Ludwik's equation) definition. When the damage criterion is satisfied according to the rule presented in equation 7.2 the failure is initiated in the model. This is shown as point c. The σ_{y0} is the state of stress at this point and $\bar{\varepsilon}_0^{pl}$ is the equivalent plastic strain during the initiation of damage. As the analysis goes on this damage variable D defines two different processes. These processes are

(a) Softening of the failure stress defined at point c in Figure 6.7.
(b) Degradation of elasticity of the material.

At point c (on set of the initiation of damage) the value for the damage variable D is zero. When the load carrying capability of the material is completely lost then the value of D becomes one. At this point $\bar{\varepsilon}_f^{pl}$ is the equivalent plastic strain at complete failure.

The parameter $\bar{\varepsilon}_f^{pl}$ is identified in terms of equivalent plastic displacement $\bar{u}_{pl}$ or fracture energy dissipation G_f, which is required to open a unit area of crack. According to this approach, the softening response after damage initiation is modelled by a stress-displacement response rather than a stress-strain response of the material. The implementation of this stress-displacement concept in a finite element model requires the definition of a characteristic length, L associated with an integration point. The fracture energy is then given as

$$G_f = \int_{\bar{\varepsilon}_0^{Pl}}^{\bar{\varepsilon}_f^{Pl}} L\sigma_y \dot{\bar{\varepsilon}}^{Pl} = \int_0^{\bar{u}_f^{Pl}} \sigma_y \dot{\bar{u}}^{Pl} \qquad (6.4)$$

This expression introduces the definition of the equivalent plastic displacement, $\bar{u}^{Pl}$, as the fracture work conjugate of the yield stress after the onset of damage (work per unit area of the crack). The characteristic length (L) definition is based on the element type and geometry used in the model. For shell elements it depends on the square root of the integration point area. This definition of the characteristic length was used in this analysis approach because the direction in which fracture would occur was not known in advance.

In this study the damage propagation will be incorporated on the basis of the plastic displacement required by an element before the complete failure (separation of material) had occurred. During the analysis at every increment

the overall damage variable D will be calculated according to Equation 6.1 and 6.2. The elements which reach the specified plastic displacement and (thus the equivalent plastic strain value of $\overline{\varepsilon}_f^{pl}$) will be having the damage variable (D) value as 1.0, are deleted from the analysis. Deleting the failing elements refers that these failing elements would no longer would be able to contribute in the analysis procedure. There will be no stiffness for these failed elements. But these elements will have connection to their adjacent elements which may not completely fail. Therefore the stress distribution in these failed elements would be zero. Thus the failure would be identified in the developed models.

6.14 Determination and calibration of the failure criterion

The failure model to be used for the failure simulation of the spot weld joints is a material failure model (complete separation of the material). This has been discussed in the earlier sections of this chapter. Hence the input values for the failure criterion should be determined from the material property test results. The failure parameters will be extracted and calibrated from the simulation of the material tests. Uniaxial tensile test were conducted for this purpose. Test results were presented and discussed in chapter – 3. Similar tensile test models were developed for the determination and calibration of the failure parameters.

The developed tensile test model had the exact same dimensions as the physical test specimens as had been presented in Figure 3.2. But the bent radius section (Figure 6.8 (a)) in the transition area of the actual tensile test specimen was replaced by a straight section. This assumption was made due to the reason that the bent radius dimension would not affect the simulation results effectively, because of using only one row of element along that area. The S4R elements were used to develop the tensile test model because the same element type was used to simulate the spot welded coupon models. The details of the tensile test model is provided in Figure 6.8.

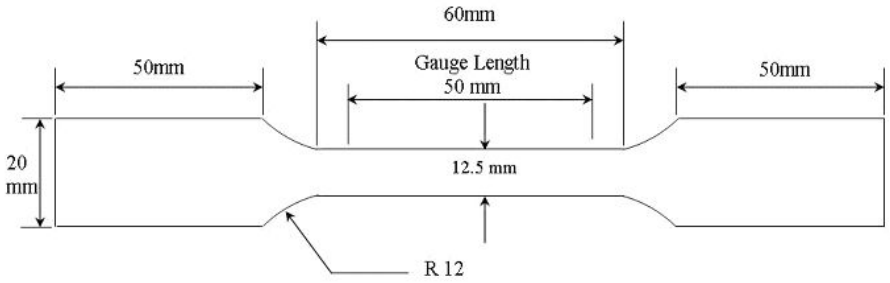

(a)

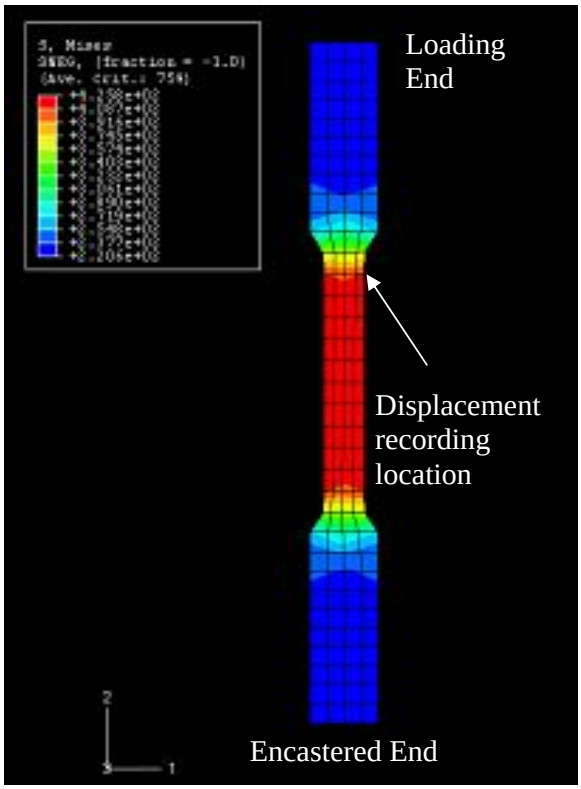

(b)

Fig 6.8: Configuration of the tensile test model for determining and calibrating the failure properties. (a) Physical dimension of the test specimens (b) Tensile test simulation result with out the failure criterion.

The material property (Figure 6.9 (b)) used for the tensile test models were extracted at the testing speed of 500 mm/min. The averaged force displacement curve from which this material property was derived is given in Figure 6.9 (a). This curve will be used for the validation of the tensile test models with the *DAMAGE INITIATION and *DAMAGE EVOLUTION keywords.

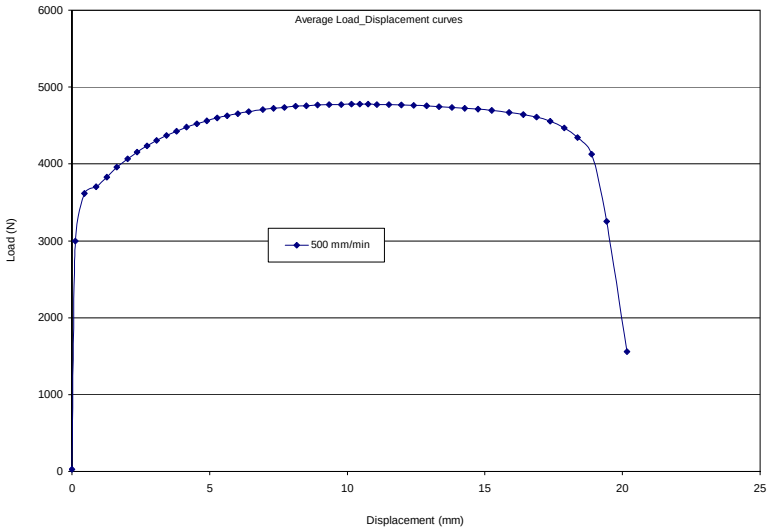

(a)

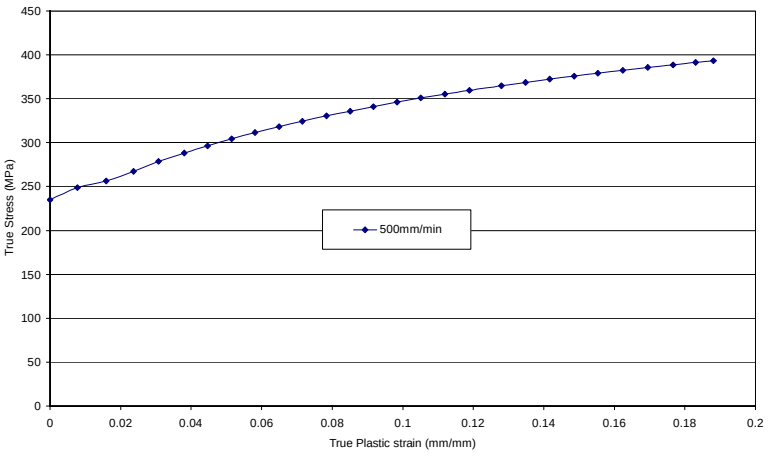

(b)

Fig 6.9: Material property curve used for the tensile test simulation
(a) Force displacement curve (b) True stress true strain curve.

The failure of material was defined through equivalent plastic strain which eventually was the function of state of stress in the material. The state of stress was identified through the stress triaxial state. The stress triaxial state is defined as a ratio of pressure stress and Mises equivalent stress.

$$\text{Stress triaxial state} = \eta = -\frac{p}{q}$$

where p = the pressure stress

q = Mises equivalent stress.

Generally any total state of stress acting in the material can be expressed in terms of the hydrostatic stress and stress deviator. The total stress tensor of any state can be divided in these two parts. The decomposition in these two parts can be expressed in tensor notation according to the following equation.

$$\sigma_{ij} = \sigma'_{ij} + \tfrac{1}{3}\delta_{ij}\sigma_{kk} \qquad (6.5)$$

where

σ_{ij} = Total state of stress

σ'_{ij} = Deviatory Stress tensor

$\tfrac{1}{3}\delta_{ij}\sigma_{kk}$ = Hydrostatic stress component.

$$\delta_{ij} = \text{Kornecker delta} = \begin{vmatrix} 1 & 0 & 0 \\ 0 & 1 & 0 \\ 0 & 0 & 1 \end{vmatrix} = \begin{cases} 1 & i = j \\ 0 & i \neq j \end{cases}$$

The deviatory stress component is responsible for the plastic deformation of the material. Hydrostatic stress component causes the volumetric change of

the material. This hydrostatic stress component is defined as the pressure stress in the failure definition and will be calculated for the uniaxial tensile test. The material stress state for a uniaxial tensile test is elaborated in Figure 6.10. The stress tensor for the total state of stress is also given in the figure. The pressure stress calculated for the uniaxial tensile condition is as follows.

$$\tfrac{1}{3}\delta_{ij}\sigma_{kk} = \frac{\sigma_x + 0 + 0}{3} = \frac{1}{3}\sigma_x \qquad (6.6)$$

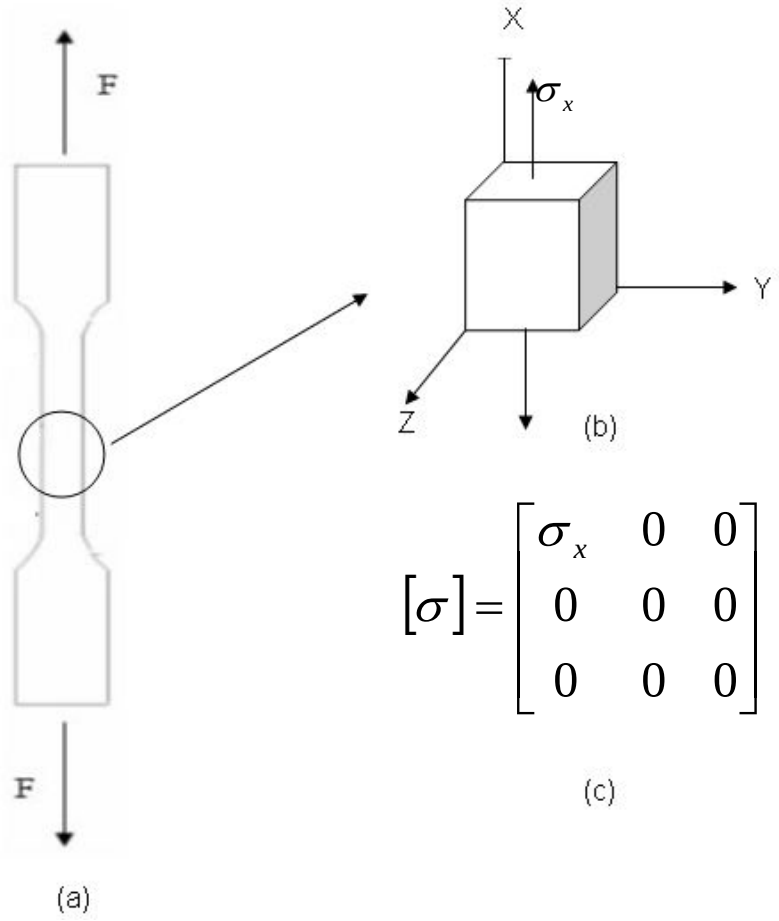

Fig 6.10: Total state of stress for uniaxial tensile test. (a) Uniaxial tensile test configuration. (b) Stress acting in the middle region of the test specimen (c) State of stress matrix for the tensile test

The Mises equivalent stress can be calculated from the equation below.

$$\sigma_{eq} = \frac{1}{\sqrt{2}}\sqrt{(\sigma_1 - \sigma_2)^2 + (\sigma_2 - \sigma_3)^2 + (\sigma_3 - \sigma_1)^2} \qquad (6.7)$$

In the above stated equation $\sigma_1, \sigma_2, \sigma_3$ are the principal stresses in direction x, y, z respectively. As stress state in uniaxial tensile test has no shear component $\sigma_1 = \sigma_x$ and $\sigma_2, \sigma_3 = 0$. Therefore the equivalent Mises stress for the material testing state is as follows.

$$\sigma_{eq} = \sigma_x \qquad (6.8)$$

Hence the value to be used for the stress triaxial parameter is $\eta = 0.33$. It should be noted here that the negative sign in the definition of the stress triaxial parameter would be cancelled out due to the pressure stress state.

The failure initiation is defined at the maximum load bearing point on the force displacement curve (Figure 6.9(a)). The failure initiation equivalent plastic strain $\bar{\varepsilon}_{pl}^{D}\left(\eta, \bar{\varepsilon}^{pl}\right)$ would be determined from the corresponding displacement value of the maximum load bearing point using the following equations.

$$L_f = L_0 + \delta \qquad (6.9)$$

$$A_0 L_o = A_f L_f \qquad (6.10)$$

$$A_f = \frac{A_0 L_0}{L_f} \qquad (6.11)$$

$$\sigma_T = \frac{F}{A_f} \qquad (6.12)$$

$$\varepsilon_x = \ln\left(\frac{L_f}{L_0}\right) \qquad (6.13)$$

In case of the uniaxial tensile test

$$\varepsilon_{eq} = \varepsilon_x \qquad (6.14)$$

So the failure initiation equivalent plastic strain would be

$$\bar{\varepsilon}^{pl} = \varepsilon_x - \frac{\sigma_T}{E} = \ln\left(\frac{L_f}{L_o}\right) - \frac{\sigma_T}{E} \qquad (6.15)$$

The value of failure initiation plastic strain $\bar{\varepsilon}^{Pl}$ is determined in this procedure from the uni axial tensile test data at 500 mm/min rate was 0.19. To point out the damage propagation (to identify ε_f^{pl}) after the initiation of failure, the equivalent plastic displacement data was incorporated into the model through the exponential format. The equivalent plastic displacement was utilized according to the following exponential equation.

$$d = \frac{1 - e^{-\alpha\left(\bar{u}_{Pl} / \bar{u}_f^{Pl}\right)}}{1 - e^{-\alpha}} \qquad (6.16)$$

where d is the damage variable, α is the exponential parameter, $\bar{u}_f^{Pl}$ is the plastic displacement before complete failure or the deletion of the elements from the analysis and $\bar{u}_{Pl}$ is the plastic displacement of the elements at different increments during the analysis. The data used for the damage propagation simulation is given in Figure 6.11.

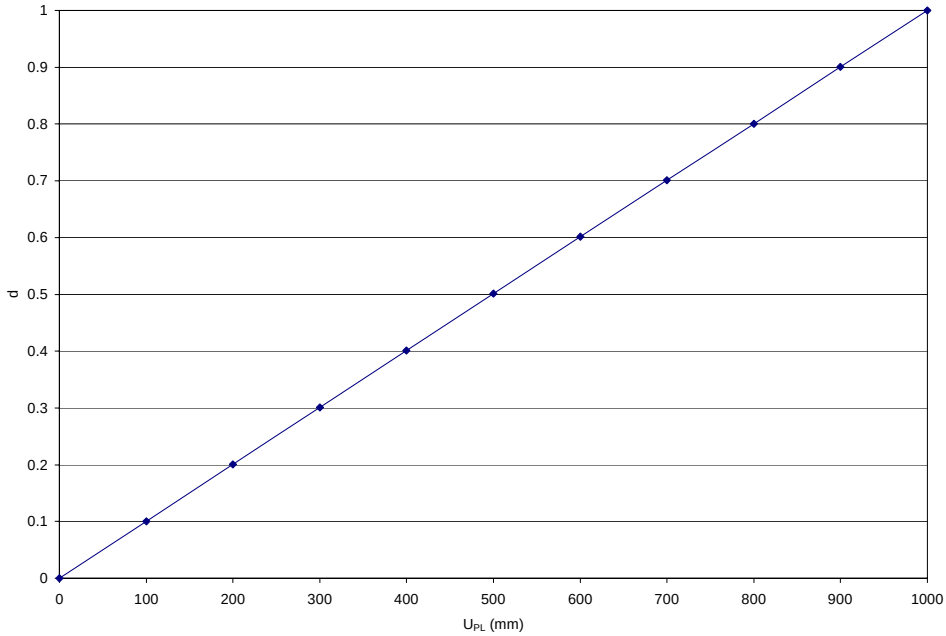

Fig 6.11: Damage propagation data for the tensile test simulation

As it can be seen from the Figure 6.11 that the elements were given 1000 mm of plastic displacement before the complete failure (separation of material) had occurred. But this value of plastic displacement was not practical at all. Hence no elements were deleted from the analysis using the above stated values (Figure 6.11 and 6.12). Therefore the damage parameter (d) value was controlled in such a manner that the elements were having an effective plastic displacement of 2.3 mm before they were deleted from the analysis to simulate the separation of the material (complete failure). The effect of this controlled simulation can be identified from the force displacement curve obtained from the uni axial tensile test simulation. The result from the tensile test simulation is provided in Figure 6.12. The experimental force displacement curve obtained at the rate of 500 mm/min is used for comparison purposes. The failure data used for the tensile test simulation will be incorporated in the developed spot weld models. This is presented in the next section.

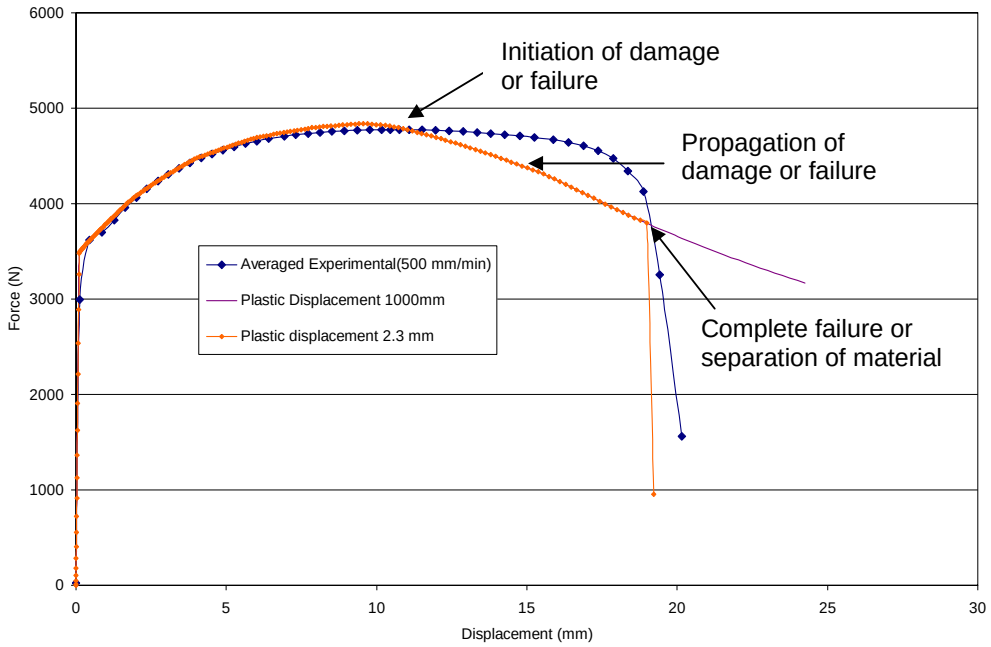

(a)

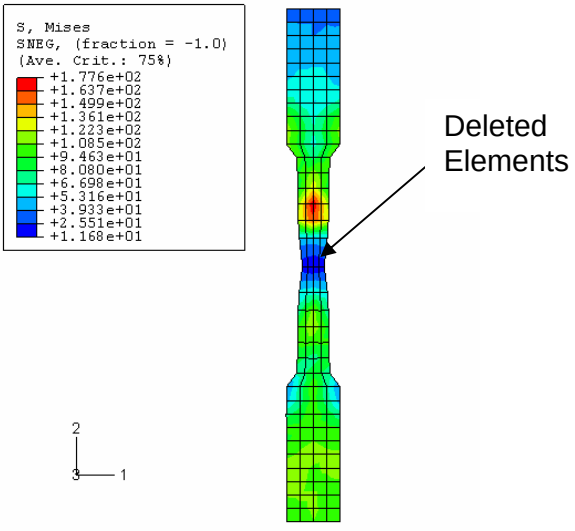

(b)

Fig 6.12: Results from the tensile test simulation with the failure or damage initiation and propagation criterion (a) Force displacement response (b) Location of the deleted elements with effective plastic displacement of 2.3 mm.

6.15 Spot weld failure simulation

The spot weld models with the failure criterion were developed with the assumption that failure would occur in the base metal region. Hence the failure criterion described in the above section was derived and verified from the base metal material property extraction experiments and simulation.

Commercial finite element code ABAQUS / EXPLICIT was used to implement the failure criterion for the dynamic loading condition. S4R elements (same element types that were used for the quasi static simulations with ABAQUS / STANDARD) were used for these models. The reasons behind using these elements were already introduced in section 6.6. When these elements in the developed models reach the specified strain value $\bar{\varepsilon}_{pl}^{D}\left(\eta, \bar{\varepsilon}^{pl}\right)$ (which indicates the respective state of stress at that particular strain level) the elements will be immediately deleted. This strategy was chosen due to the occurrence of the complete separation of metals as observed from the experimental analysis and verified through the simulation of the uni axial tensile test.

The spot weld models considered for failure simulation were the same as the models presented in section 6.4. The IRB model was not considered for the failure simulation due to the fact that this model had collapsed in the early stage of the applied load. This fact was presented in the force displacement graphs of the spot weld joint simulation for quasi static loading conditions (Figure 6.5).The models were loaded through application of acceleration and the boundary conditions for failure simulations were the same as presented in Figure 6.4. The lap shear coupon with the back plate configuration (Figure 4.5 and 4.6) was simulated by offsetting the load application points by half of the sheet metal coupon thickness.

The material property used in this analysis was assumed to be isotropic in nature. The material model for the spot weld joint failure simulation had similar characteristics for both the tensile and compressive loading conditions.

Further more only one material property (base metal) was used for the simulation. The material properties were extracted from the uniaxial tensile test of the base metal with the loading rate of 500 mm/min. The true stress true strain diagram of the used material property was presented in Figure 6.9 (b). The summary of material properties used in the simulation is as follows.

- Modulus of elasticity 200GPa.
- Poisson's ration 0.3
- Yield stress 235 Mpa
- Ultimate Tensile strength 325.39 Mpa

Here only one spot weld model (except the IRB model) was used to verify the failure simulation responses for different loading conditions. Because other than the IRB model, all other developed models provided the similar type of force displacement responses for the quasi static loading situations (Figure 6.5). For this purpose The Spider Configuration – 3 model was chosen because it provided a complete rigid nugget and was also used for the mesh convergence study (presented in chapter 5). The complete modelling and verification strategy for the failure simulation is given in Chart 6.2.

The force displacement graph from the failure simulations are presented in Figure 6.13. The force and the displacement were recorded from the developed models at the point of load application. It can be clearly seen from the presented graphs that with the incorporated failure criterion the spot weld models did not fail for any of the simulated loading conditions. The reasons behind this non failure and the required modifications of these models are presented and discussed in the next chapter.

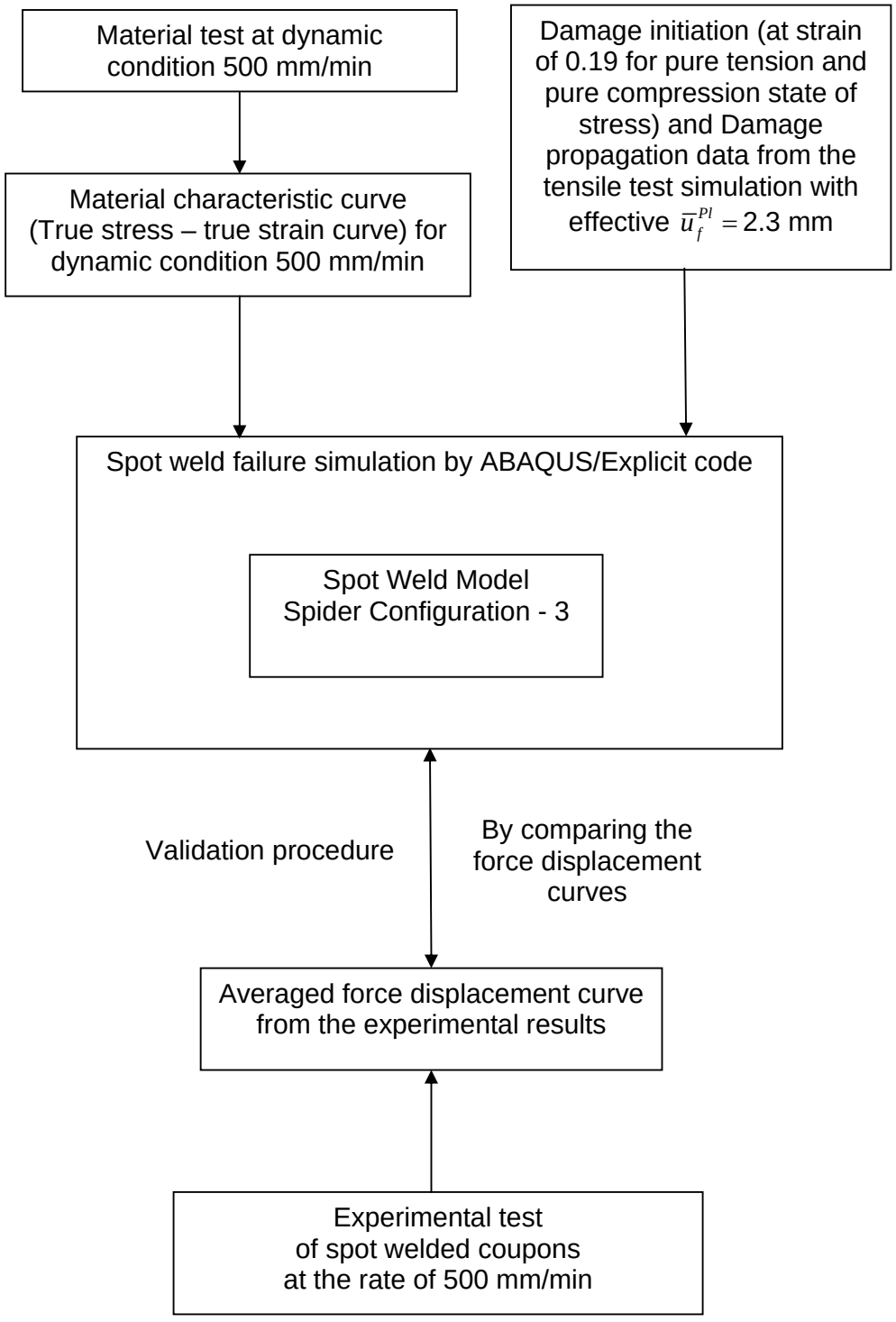

Chart 6.2: Validation procedure for the developed spot weld models for failure simulation

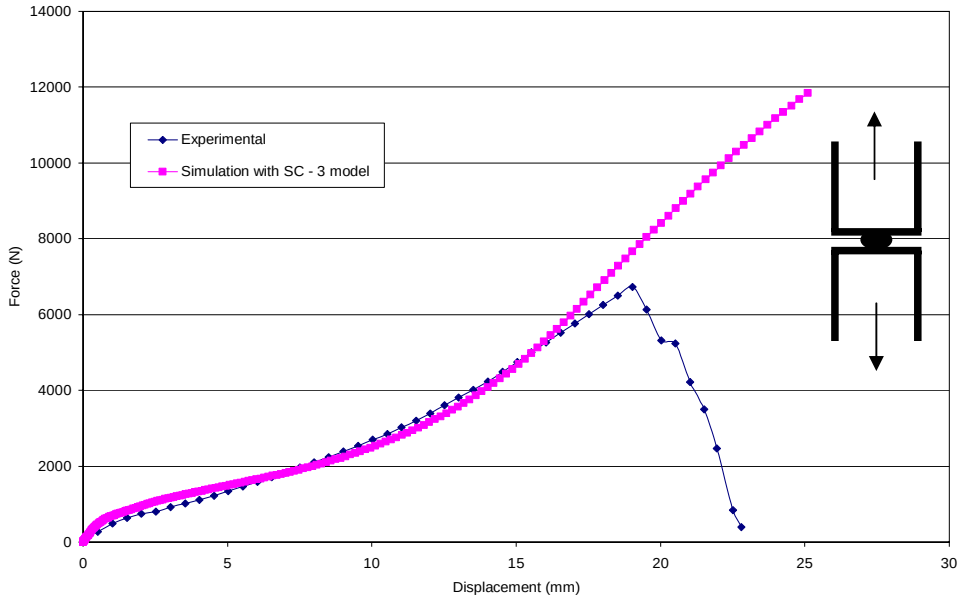
14000
12000
10000
8000
6000
4000
2000
0
Force (N)
0
5
10
15
20
25
30
Displacement (mm)
Experimental
Simulation with SC - 3 model

(a)

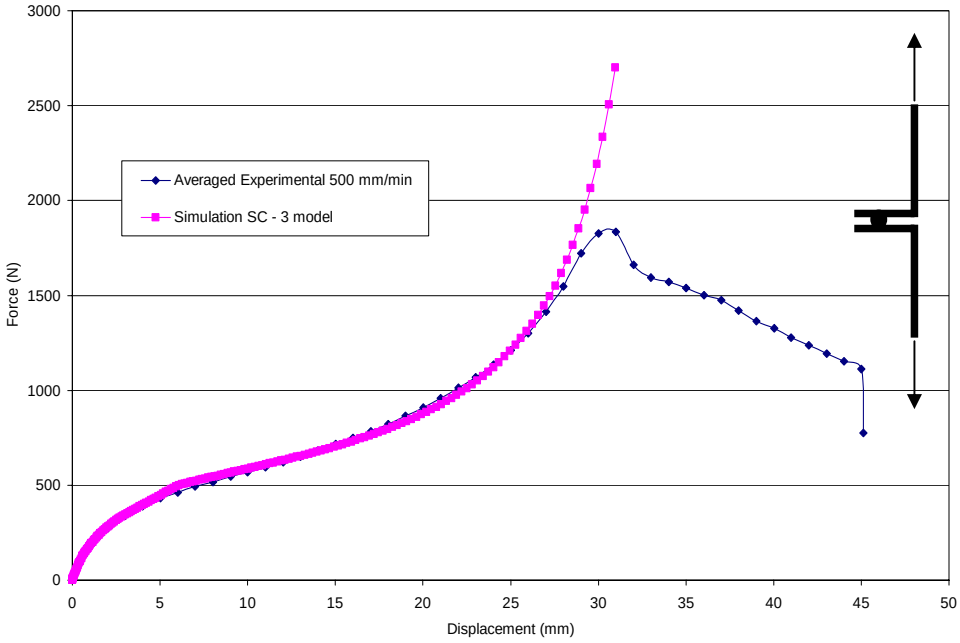
3000
2500
2000
1500
1000
500
0
Force (N)
0
5
10
15
20
25
30
35
40
45
50
Displacement (mm)
Averaged Experimental 500 mm/min
Simulation SC - 3 model

(b)

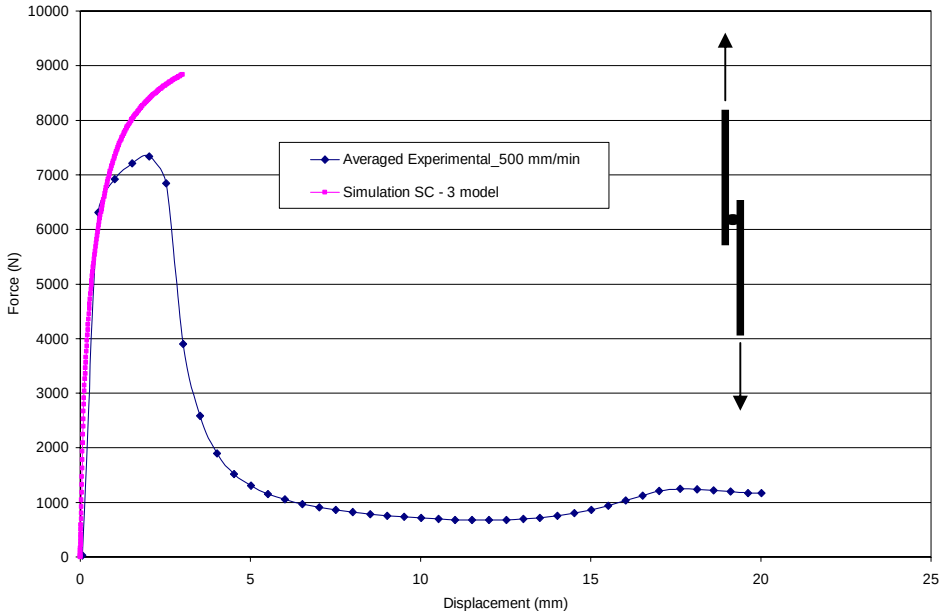

(c)

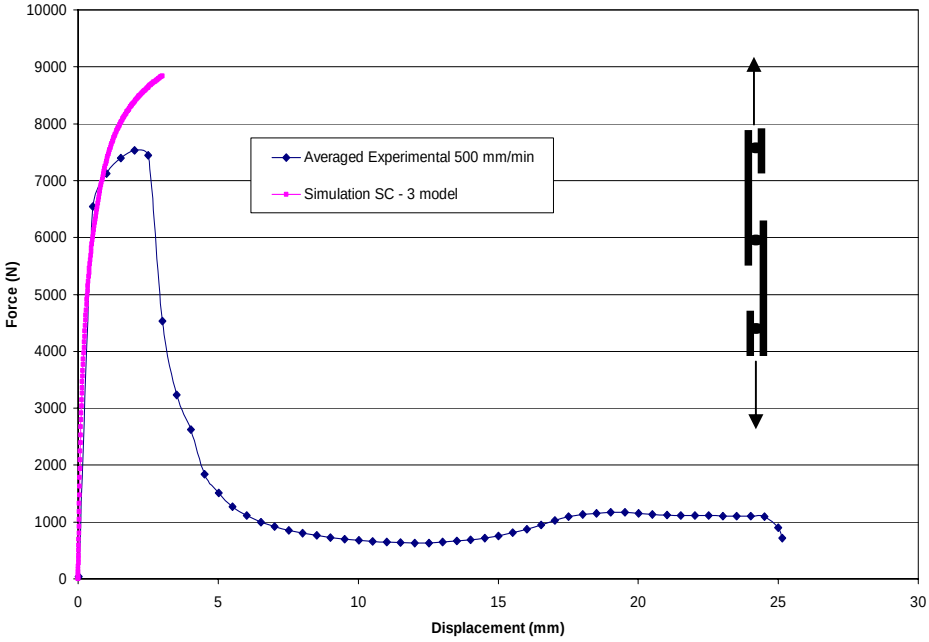

(d)

Fig 6.13: Spot weld joint failure simulation (with the failure criterion used for the simulation of the uni axial tensile test) results for Spider Configuration – 3 (SC-3) model. (a) U Tension coupon used for tensile loading condition (b) Coach Peel coupon used for tensile loading condition (c) Lap Shear coupon without back plate used for shear loading condition (d) Lap Shear coupon with back plate used for shear loading condition

Chapter - 7

Results and Discussion

7.1 Overview

This thesis deals with the realistic modelling of the spot weld joints. The intension was to identify the most suitable model to represent the spot weld joint. The suitability was evaluated from two points of view.

(a) The level of accuracy attained by the spot weld models compared to experimental results.
(b) The simplicity of the models so that they can be repeatedly reproduced many times for a large assembly system.

To make the developed models simple certain assumptions were made. The limitations of this work regarding these considerations were stated in chapter 2 and were discussed in chapter 6. The levels of accuracy achieved by the developed models were validated with respect to the experimental results presented in chapter 4.

In this chapter the results obtained from FEA studies for the spot weld behaviour regarding load bearing characteristics as well as failure of the joint obtained from the FEA study will be presented and discussed in detail. The observations from the FEA study will also be critically analysed. The behaviour of different developed models with the implemented failure criterion will also

be thoroughly discussed. Hence the developed spot weld models will be validated to asses their accuracy level. Moreover the computational performance of the different models will also be compared. Hence a suitable model for representing the spot weld joint will be identified. The chapter is organized according to the following sections.

7.2 Load bearing characteristics of the spot weld joint model
7.3 Transverse shear effect for the spot weld joint model.
7.4 Including failure criterion in spot weld models
7.5 Stress distribution around the spot weld joint models.
7.6 Performance study of the developed models.

7.2 Load bearing characteristics of the spot weld joint models

The load bearing characteristics of the spot weld joint is generally evaluated using force displacement responses, because it comprehensively shows the level of force a spot weld joint can withstand. The force displacement response curves obtained from the quasi-static analysis by the ABAQUS/Standard code is presented here in the following Figure 7.1, 7.2 and 7.3. All of these experiments were conducted as displacement controlled experiments. The average experimental curves used here for comparison purposes were obtained with the displacement application rate of 5 mm/min.

As observed from these graphs, the trends of the force displacement responses are different for different coupon configurations. These are mainly due to the different types of the loading generated in each of the different coupon configurations. Moreover the force displacement curves (for a particular coupon configuration) change slopes at different stages of the

applied displacement. Hence in general the force displacement responses can be divided into three distinctive stages.

a) Initial Deformation Stage (IDS).
b) Load Withstanding Stage (LWS).
c) Failure Response Stage (FRS).

All these three stages are distinctively marked in the presented force displacement graphs. The initial deformation stage is identified at the starting of the applied load. The deformations in the models take place in all of the elements (adjacent, near and far from the spot weld nugget location) during this Initial Deformation Stage (IDS).

The Load Withstanding Stage (LWS) is denoted as when the large deformation in the model is concentrated around the spot weld joint only. The characteristic trend of the LWS depends on the type of loading situation faced by the spot weld joint. The maximum load that a spot weld joint can withstand is attained in this stage as it can be observed from the averaged experimental curves.

The Failure Response Stage (FRS) starts after the spot weld joint has attained the maximum force level. The spot weld joint looses its load bearing capability during the FRS. The force value decreases with the increase of the applied displacement in this stage. This is the post failure characteristic response of the spot weld joint models. These post failure characteristics are discussed in section 7.4. Spot weld model force displacement response at the other two stages are discussed below.

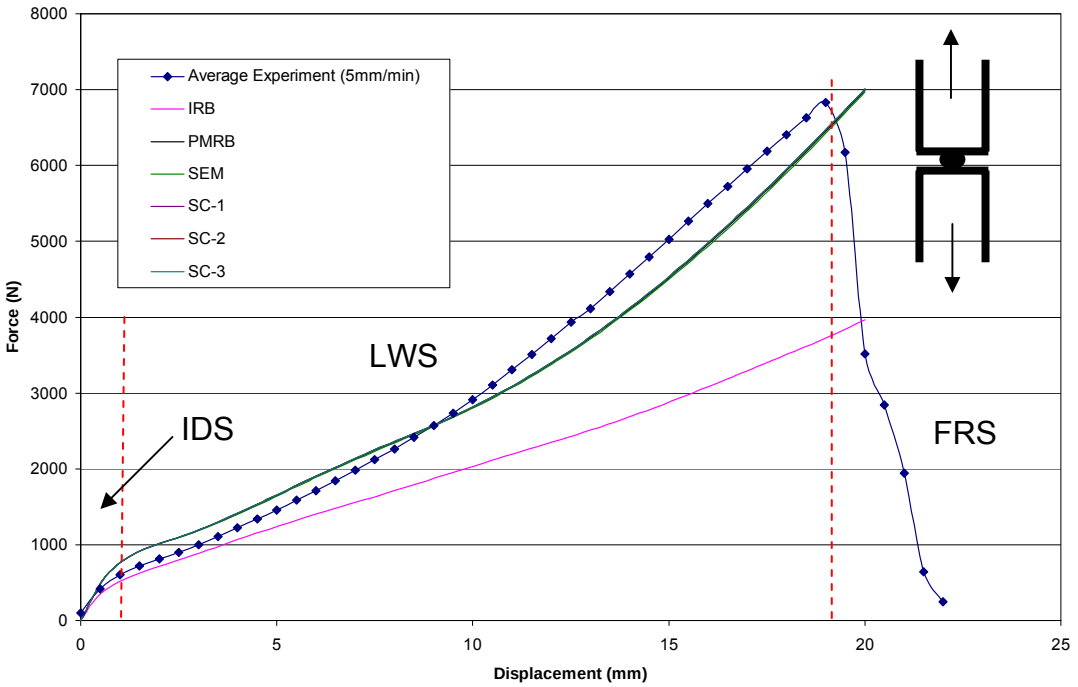

Fig 7.1: Force displacement response of the developed spot weld models for the tensile loading condition with the U Tension coupon

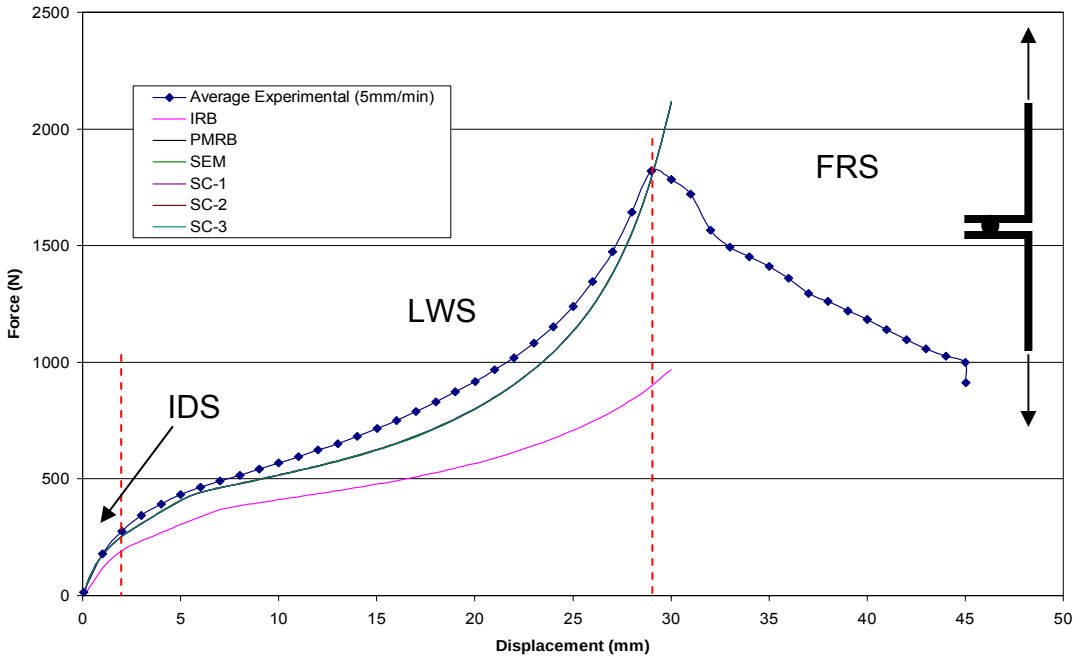

Fig 7.2: Force displacement response of the developed spot weld models for the bending loading condition with the Coach Peel coupon

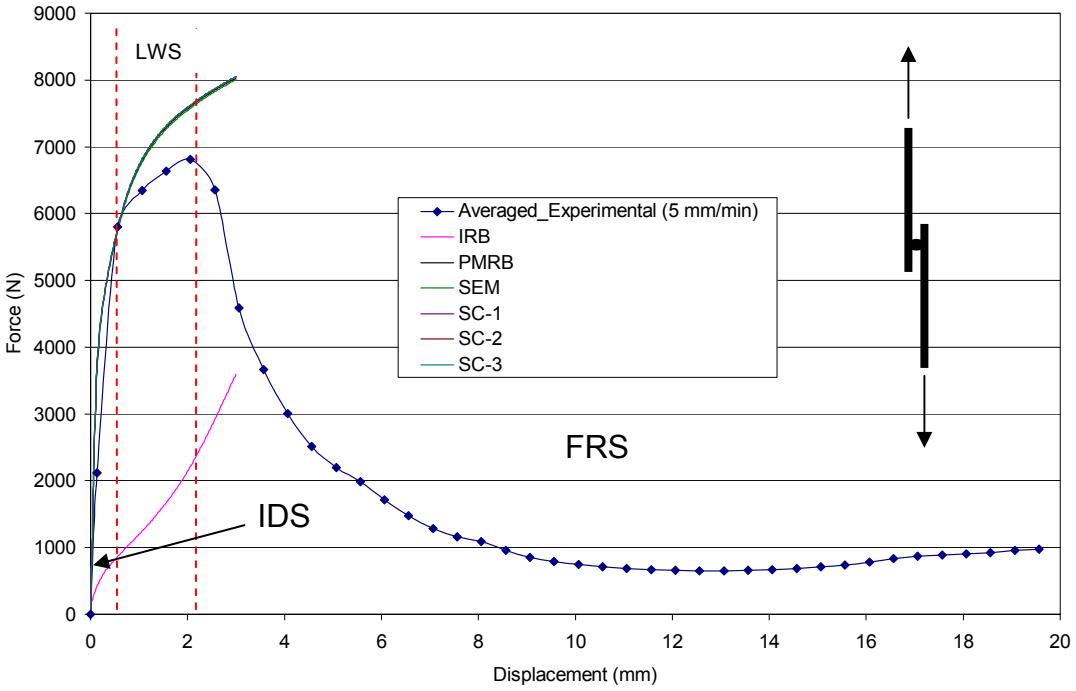

Fig 7.3: Force displacement response of the developed spot weld models for the shear loading condition with the Lap Shear coupon with out the back plate

The force displacement responses at the LWS stage are different for different coupon configurations. For the lap shear coupon configuration (Figure 7.3) the rate of increment for the force value is relatively lower than the immediate previous stage. This indicates that the stress is concentrated around the spot weld nugget joint at this stage. This issue can be more clearly observed from the stress distribution results presented in section 7.5. The force response from the developed spot weld models in the LWS stage is much higher than the averaged experimental results. This was because of the mesh configuration chosen for the simulation of the lap shear joint configuration. The fact was presented in Table 5.3 of chapter 5. This mesh was chosen because this mesh configuration provided the overall better performances. The

difference between the experimental force data and the simulation force data (except the IRB model) at the same applied displacement location (for maximum force location) was about 11.5%. This difference was huge because of the large amount of deformation around only one spot weld model. But if the spot weld models were considered for a very large assembly system then this 11.5% would be much lower because of the relatively smaller individual deformation around each of the spot weld models.

On the other hand for the U tension coupon and the coach peel coupon (Figure 7.1 and 7.2) the increment trend of the force level in LWS is quite similar. It gradually increased to reach for the maximum load bearing point. But the force displacement responses from the developed models under predict the spot weld joint characteristics in these two coupon types. The assumptions regarding the proper material properties in the model may cause this deviation in the results. The changes in material properties for the Heat Affected Zones (HAZ) were ignored in the model development process. Even though from the presented graphs it can be clearly seen that the developed five models (Parallel Multiple Rigid Beams, Spider Configuration - 1, Spider Configuration - 2, Spider Configuration - 3 and Solid Element Model) are behaving closely according to the expected outcome of the experimental investigations. The force displacement responses from these developed models are better than the existing results in literature which are reported most recently (Figure 2.14, after J. Wang et al. (2006), case R0).

But the force displacement responses obtained in case of the individual rigid beam (IRB) model were different than the other models for all the coupon configurations. Due to its simplicity this type of model is widely used to represent the spot weld connection in a very large assembly of different components (Machine Design, 1994). But while testing its behaviour on a

coupon configuration, the IRB model showed an early collapse situation. The reason behind this kind of early collapse response (caused by the local buckling) is due to the way of making the connection between the top sheet and the bottom sheet of the test coupon configurations. For the IRB model the connection was made from one point to another point only. Hence this connection actually did not represent the diameter of the actual spot weld. So it did not represent the actual stiffness of a single spot weld as observed from the experimental force displacement response. Further more from the modelling point of view, to represent the spot weld itself; the rigid connection was established from only one point to another point. Therefore in this particular model (IRB) not many of the elements (from the top sheet and from the bottom sheet) were involved to provide enough stiffness to the whole model. This means that the force displacement response from the IRB model could not follow the average experimental force displacement curve in any of the above described different stages (IDS, LWS and FRS). As an early collapse situation was shown in all the loading cases in this study, the failure criterion used for the failure simulations of the spot weld joints, need not to be incorporated in the IRB model.

At the initial deformation stage (IDS) the force displacement response from the other five models (Parallel Multiple Rigid Beams, Spider Configuration - 1, Spider Configuration - 2, Spider Configuration - 3 and Solid Element Model) followed the similar trend as the average experimental curves. But there are deviations in the results from the developed models especially for the lap shear coupon. To remove these deviations the transverse shear effect was included in these models and it is discussed in the next section.

7.3 Transverse shear effect for the spot weld joint model

The transverse shear effect is a stiffness defined in response to pure transverse shear strain in the shell elements. The assumed theoretical state of stress in the lap shear coupon was presented in Figure 2.3 of chapter 2. To incorporate these states of stresses into the shell elements the transverse shear effect was defined. This investigation was carried out for the lap shear coupon configuration (without the back plate configuration) only.

The transverse shear stiffness for a shear flexible shell element was defined as

$$\bar{K}^{ts}_{\alpha\beta} = fK^{ts}_{\alpha\beta} \qquad (7.1)$$

Where

$\bar{K}^{ts}_{\alpha\beta}$ are the components of the section shear stiffness (α, β=1,2….are the default surface direction for the shell elements)

f is the dimensionless factor that is used to prevent the shear stiffness becoming too large in the thin shell elements.

$K^{ts}_{\alpha\beta}$ is the actual shear stiffness of the section which is defined by the user.

Now for a homogeneous shell made of a linear, orthotropic elastic material, where the element local 1 direction is the strong material direction, the transverse shear stiffness is defined as:

$$K_{11} = \frac{5}{6} G_{13} t$$
$$K_{22} = \frac{5}{6} G_{23} t \qquad (7.2)$$
$$K_{12} = 0.0$$

Where G = material shear modulus

t = section thickness.

But the material that has been used in this study was modelled as an isotropic material.

For an isotropic material model, the values for the transverse shear become as follows:

$$K_{11} = K_{22} = \frac{5}{6} Gt \qquad (7.3)$$

Therefore for the chosen material described in chapter 3 the shear stiffness value was around 74000 N/mm.

After incorporating this value the following force displacement diagrams (Figure 7.4) were obtained. For the study of this transverse shear effect only one spot weld model (Spider configurations -3) was used. This was done because the force displacement responses from the other five spot weld models (except the IRB model) were quite similar to this model. For the actual transverse shear value of 74000 N/mm the force displacement response remained unchanged. This is because the transverse shear stiffness is defined as a linear format and only effective in the elastic range of the initial stiffness definition. Hence the transverse shear stiffness changes the initial deformation stage (IDS) response for the spot weld model slightly. If the transverse shear

value is reduced significantly to obtain the effect in the plastic range of the analysis, then the changing effect could be observed in these force displacement curves. The LWS responses of the force displacement curves were deviated accordingly. Considering the force displacement responses in IDS and LWS the value for the transverse shear was chosen as 1000 N /mm. This value will be incorporated for all the spot weld models in lap shear coupon configurations with and without the back plate.

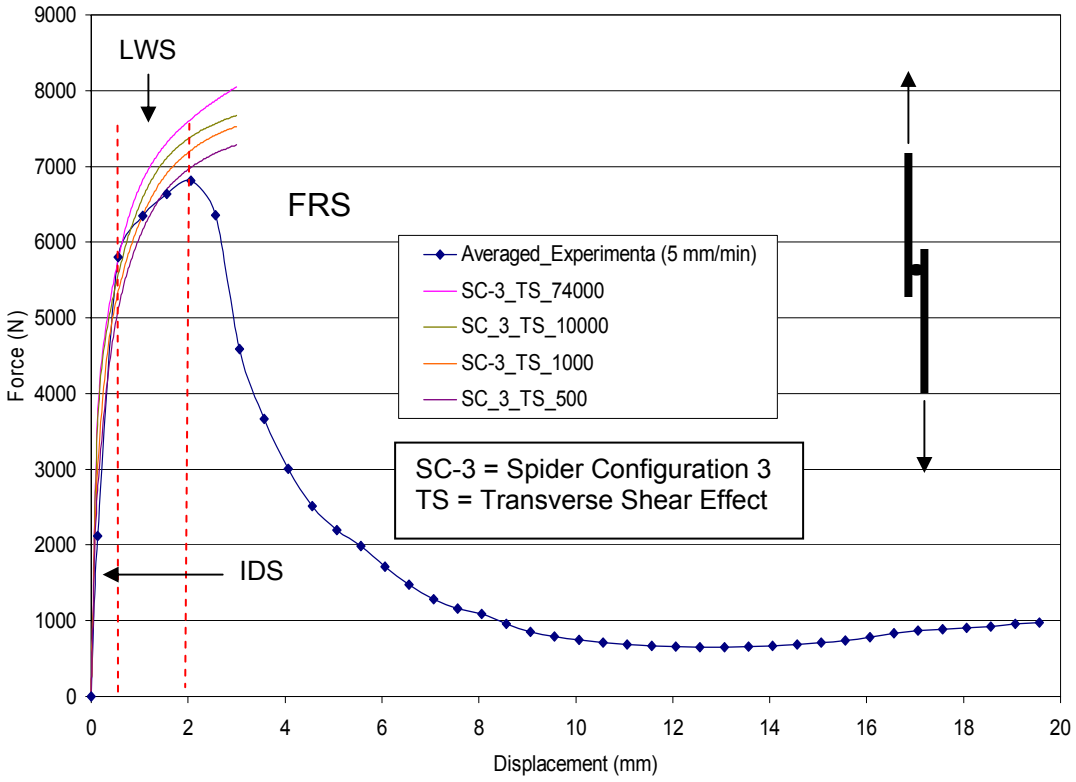

Fig 7.4: Force displacement response for the spot weld model with the transverse shear effect in lap shear coupon configuration without the back plate.

7.4 Including failure criterion in spot weld models

The load bearing characteristics for the failure simulations of the spot weld joints were implemented through the ABAQUS / Explicit code. The failure simulation in this study addressed the material separation type of failure. A strain based criterion along with the state of stress was used as a material failure criterion. At first, the failure criterion was implemented in the simulation of the uni axial tensile test to validate the failure criterion for the material separation conditions. For the uni axial tensile test simulation the plastic strain at failure initiation was 0.19 with an effective plastic displacement of 2.3 mm (Figure – 6.13, Chapter 6) before the element deletion to represent the complete material separation situation. Then this similar failure condition was included in the spot weld joint models (for both the tensile and compressive state of stresses) in the tensile, bending and shear loading conditions. But the exact failure criterion for the uni axial tensile test could not initiate failure for the spot weld models. Hence the force displacement responses presented in Figure 6.14 did not show the loss of the load bearing capability of the spot weld joints. The reason behind this was because the state of stresses and the strain around the spot weld joint location were different in different locations and all the state of stresses around the spot weld joint model nugget were not represented properly in the definition of the failure criterion. This was obvious due to the difficulty to generate a proper material failure condition with the simple uni axial tensile test data only.

So the material failure criterion for the spot welded joints needed further calibration. The calibration was performed with respect to two material failure parameters.

a) The material failure initiation plastic strain $\bar{\varepsilon}_{pl}^{D}\left(\eta, \bar{\varepsilon}^{pl}\right)$

b) The controlled effective plastic displacement $\bar{u}_{f}^{Pl}$

The value for the material failure initiation plastic strain $\bar{\varepsilon}_{pl}^{D}\left(\eta, \bar{\varepsilon}^{pl}\right)$ was calibrated irrespective of the state of stress η value. That is the value for η remained same as before (η =0.33 for both tension and compression).The state of stresses was not considered for the calibration because of two reasons.

(i) First the state of stress around the spot weld joint nugget changes in every direction at every increment of the analysis. So it is pointless to extract the state of stresses at a certain location and at certain stage of the analysis and then use it for the failure criterion. Moreover this approach does not represent the actual material separation characteristics as it is not related to the material testing results.

(ii) Second if the failure criterion is to be related to the material testing results, then it has to be related only with the results of the uni axial tensile tests due to unavailability of other material testing facilities. Now there is only one state of stress in the case of the uni axial tensile test which was described in section 6.14.

Therefore the state of the stress variable can not be utilized for the calibration procedure. The controlled effective plastic displacement $\bar{u}_{f}^{Pl}$ (described in section 6.14) before the deletion of the elements was utilized for the further calibration. The spot weld model Spider Configuration – 3 (SC - 3) was used for this purpose. The tensile loading condition for the spot welded joint (with U Tension coupon) was considered because it is the most common loading condition. The results of the calibration procedure are presented in the following Figure 7.5.

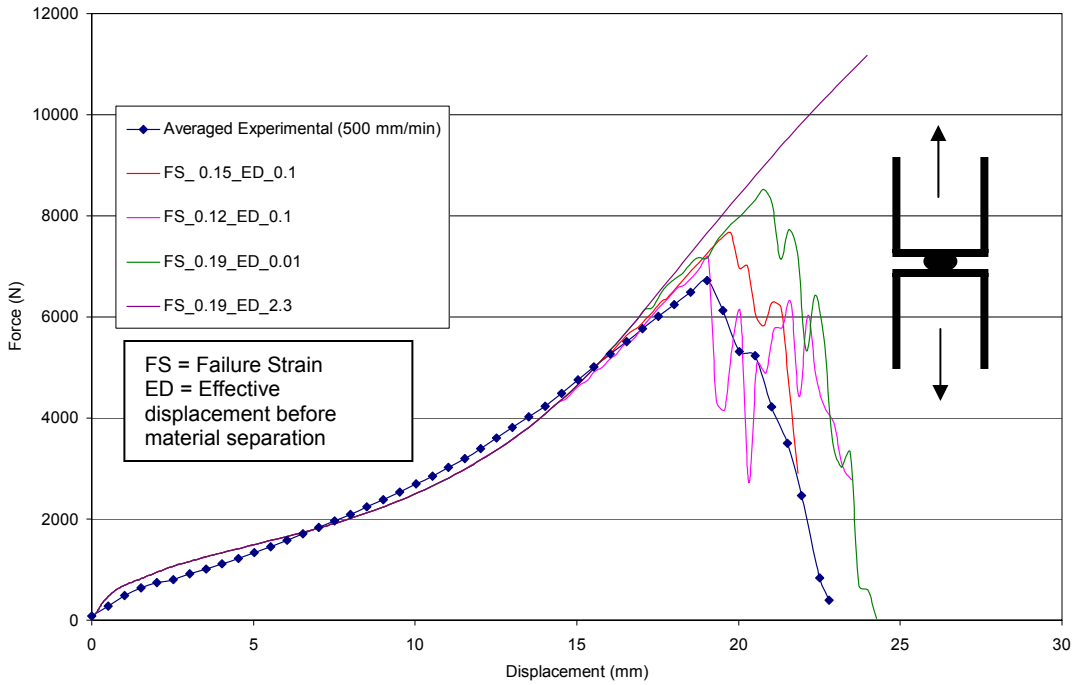

Fig 7.5: Failure parameter calibration results for spot weld joint with the U – Tension coupon

It could be observed from the presented force displacement curves that as the failure strain decreased along with the effective plastic displacement before the deletion of the elements from the analysis, the response moved closer to the averaged experimental results. Following this approach from the failure calibration curve the failure strain was chosen as 0.15 and the effective plastic displacement before the complete material separation occurred was chosen as 0.1 mm. These values were incorporated into the other spot weld models for the U tension coupon configuration. The results are given in the following Figure 7.6.

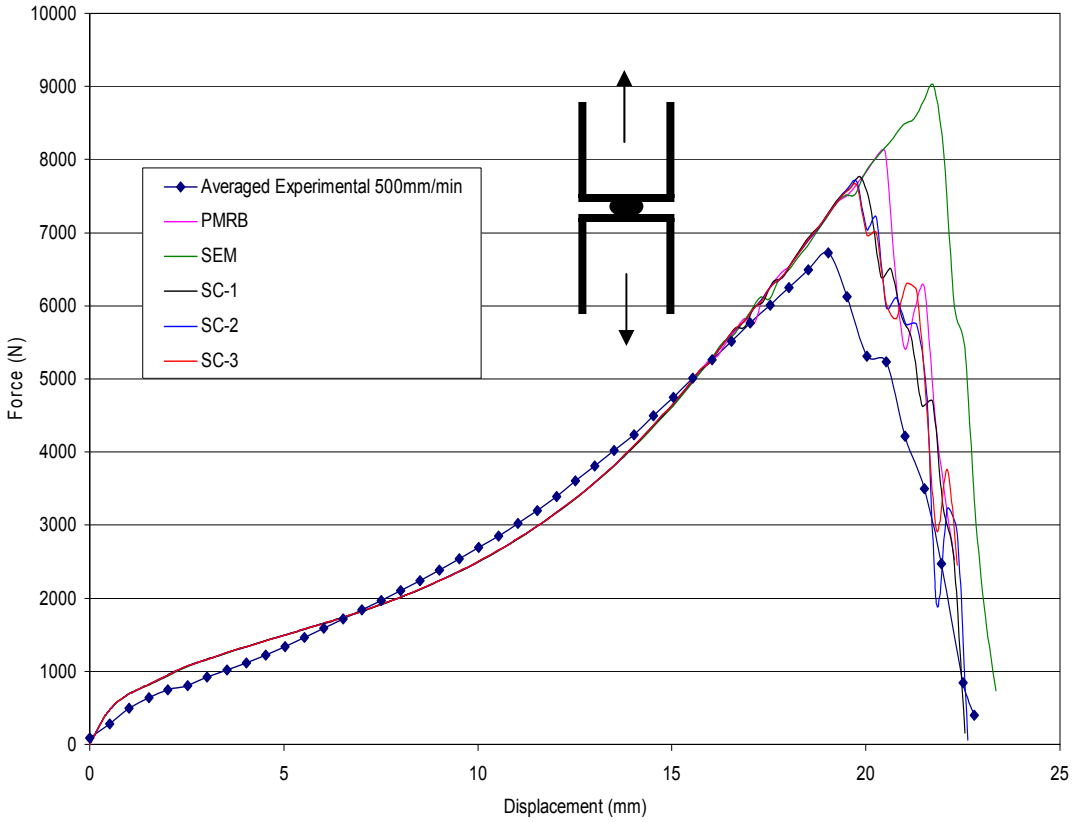

Fig 7.6: Failure simulation results for different spot weld joint models.

From the presented figure 7.6 it can be observed that the models with the Spider Configurations provided coMparatively better results than the other models. The Solid Element Model (SEM) provided higher force and the higher displacement value at the failure of the joint model. The Parallel Multiple Rigid Beams (PMRB) model provided a little less response than the SEM model. These two models provided a relatively rigid response than the spider configuration models. Considering the failure force displacement response it can be decided that the Spider Configuration models had a better performance for the failure simulation in the tensile loading condition. To identify a specific spider configuration model the computational performances of these models need to be considered and are presented in section 7.6.

The failure criterion obtained from the uni axial tensile test simulation and the calibrated failure criterions were also included in the lap shear coupon (with and without the back plate configurations) and the coach peel coupon configurations. The transverse shear effect was included in the simulations for the lap shear coupon configurations. The value for the transverse shear was chosen as 1000 N/mm. The reasons for choosing this particular value were described in the previous section 7.3. The Spider Configuration - 3 spot weld nugget model was used for this purpose. The reason behind this was because SC-3 model was used for the calibration of the failure criterion and most of the other developed spot weld models (except the IRB model) showed the similar response for the quasi static simulations. The resulting force displacement responses are presented in the Figure 7.7, 7.8 and 7.9.

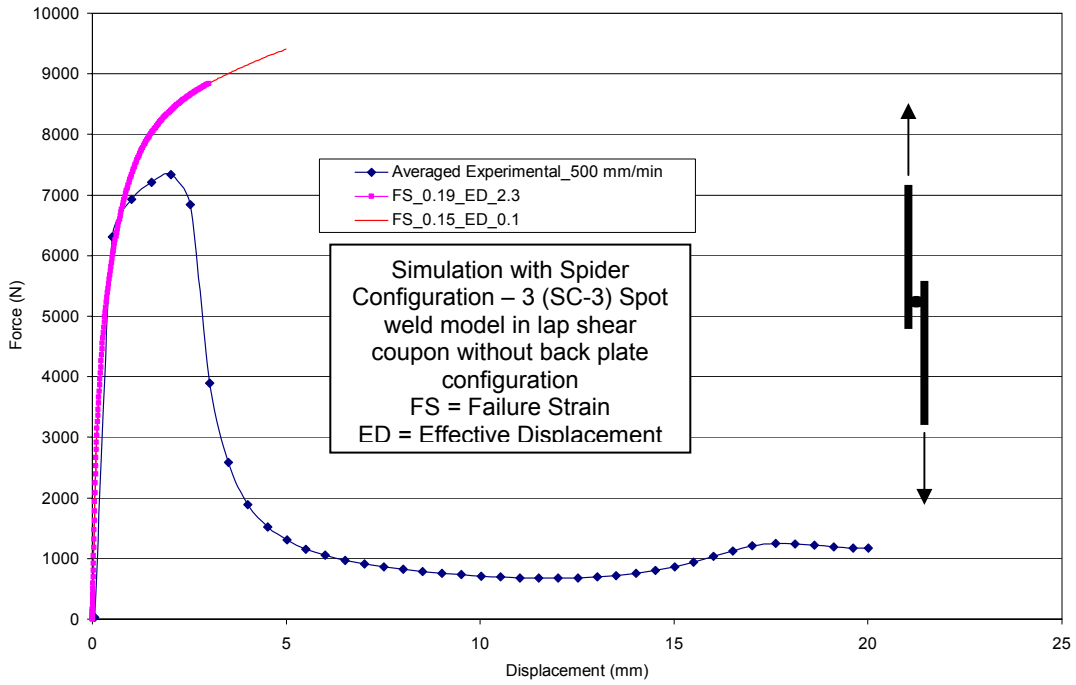

Fig 7.7: Force displacement response for spot weld model SC-3 with the failure criterion for the lap shear coupon without the back plate configurations

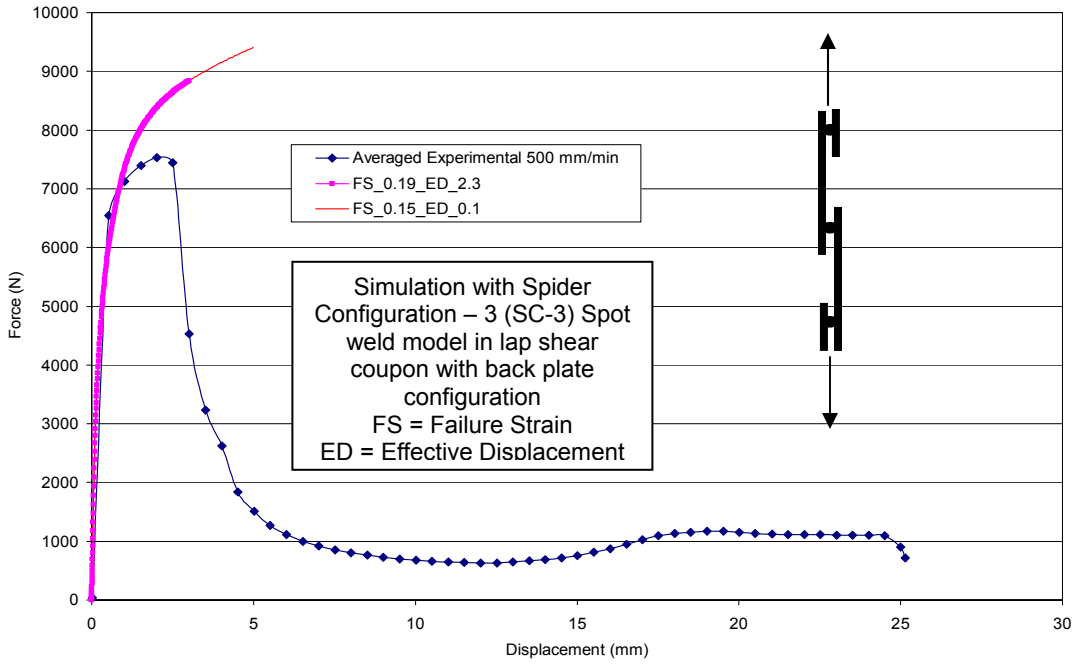

Fig 7.8: Force displacement response for spot weld model SC-3 with the failure criterion for the lap shear coupon with the back plate configurations

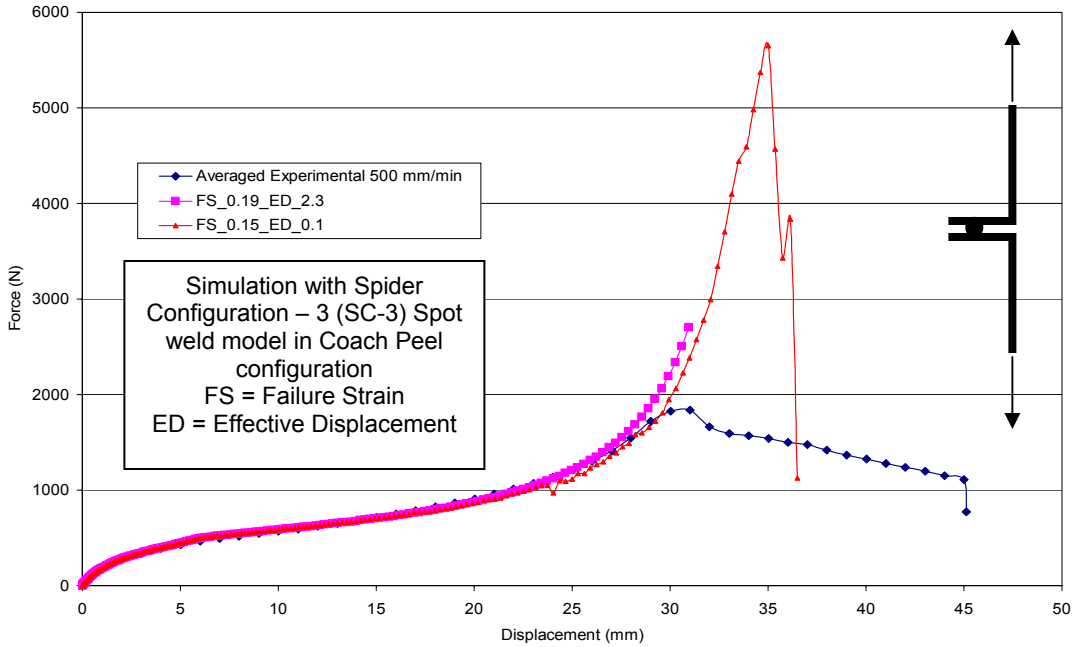

Fig 7.9: Force displacement response for spot weld model SC-3 with the failure criterion for the Coach Peel coupon configurations

It can be seen from the presented graphs that the calibrated failure model did not cause the failure in the spot weld models in lap shear coupon configurations with and without the back plate. In the case of the Coach Peel coupon configuration the failure model did cause the intended failure but the force value was too high from where the response (force displacement) actually dropped down. The probable reason behind this behaviour was that the failure criterion used in these simulations was lacking the definition for the other states of stresses which might initiate the failure around the spot weld nugget in lap shear and the coach peel coupon. For the coach peel coupon after the failure initiation, the propagation of the failure was not observed as well.

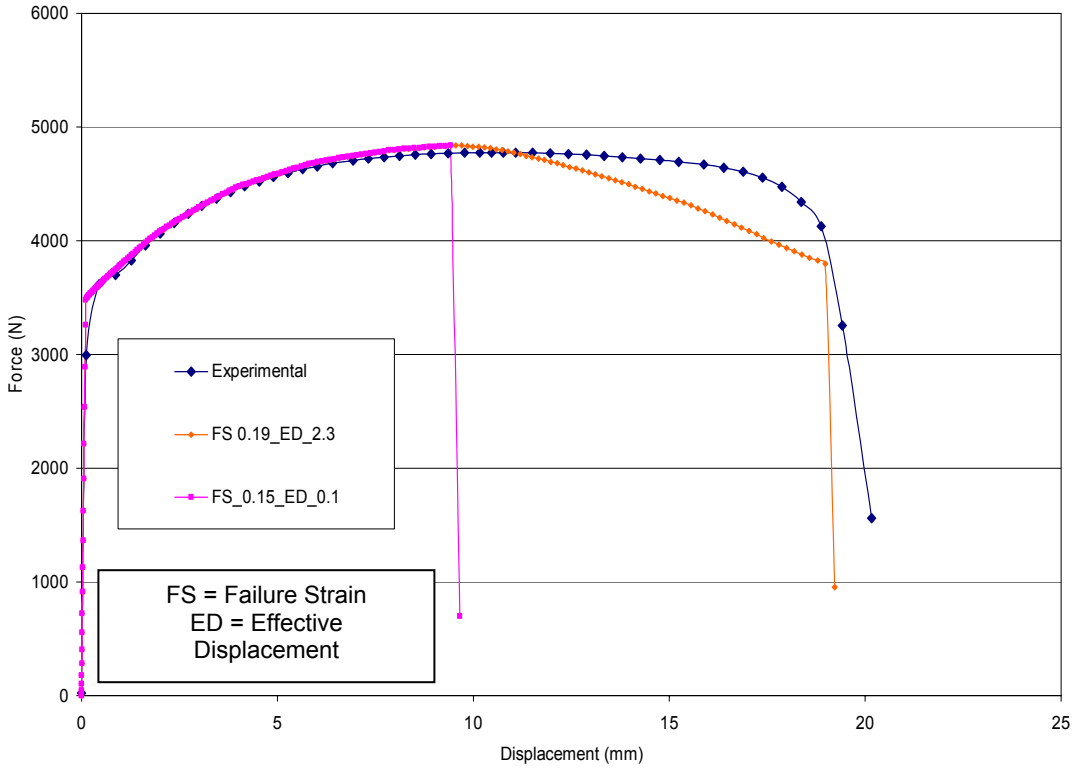

Fig 7.10: Force displacement response for uni axial tensile test with the calibrated failure criterion.

The failure propagation in the spot weld model in the coach peel coupon was like brittle failure rather than a ductile failure as could be seen from the averaged experimental graph. Now it is pointless to have different failure initiation and propagation characteristics for the ductile type of failure of the same material. So different types of material test data was required to get better results for the spot weld failure initiation and propagation simulations in the lap shear and the coach peel coupon. Probable required material tests are provided in the recommendation section of the next chapter. As this failure criterion did not work properly with SC-3 model it was useless to implement the same failure criterion for the other developed spot weld models in lap shear and coach peel coupons.

If the same calibrated failure criterion for the U – Tension coupon configuration was to be implemented back in the simple uni axial tensile test simulation (previously presented in Section 6.14) then it could be observed that the force displacement response (Figure 7.10) dropped down immediately after the failure initiation point was reached. This indicated that there was not much failure propagation characteristics involved in the failure of the spot weld joint in the U tension coupon for the tensile loading condition. It was also evident from the averaged experimental force displacement curve presented in Figure 7.6 which had a sharp fall down after the maximum force was attained by the test specimens.

7.5 Stress distribution around the spot weld joint models

In the following figures the distribution of Von Mises equivalent stress and the distribution of equivalent plastic strain in different coupon configurations obtained for different nugget assumptions in the quasi - static analysis (by ABAQUS/ Standard code) and failure analysis (by ABAQUS/ Explicit code) are provided.

From these particular contour plots for the quasi - static analysis the effects of the various nugget assumptions become very clear. The stress is concentrated around the spot weld nugget which particularly denotes the Load withstanding stage (LWS) of the force displacement curve, which was discussed in the previous sections. For the Solid Element Model and the Parallel Multiple Rigid Beams model the equivalent stress distribution can be found inside the nugget as well as out side the nugget region. But as for the assumption of the rigid nugget (Spider Configuration – 1, Spider Configuration – 2 and Spider Configuration – 3 model) the stress distribution could be observed only out side the nugget region. For the IRB model the stress was found to be concentrated only inside the joint area. In this model the stress and the strain distribution were confined within the centre of the nugget area only. Therefore the elements which are at that region faced extreme distortion. The Individual Rigid Beam model behaved in this way because this connection configuration could not provide enough stiffness to the whole model. This means that the extreme deformation at the centre of the joint could not spread through the other elements. As the distribution of the stresses around the spot weld nugget in the IRB model was not significant, this model was not suitable to predict the failure responses.

The equivalent stress and equivalent strain distribution for the failure simulations are provided only for the U tension coupon. From the equivalent stress and equivalent strain distribution of the failure simulations, the failed elements could be identified in the developed models. The failed elements around the spot weld joints are having about zero equivalent stress and the highest equivalent strain value. This is obvious because these elements were deleted (no longer affects the stiffness value of the model) from the analysis once the included failure criterion was satisfied. But at the same time they maintained the connections to the adjacent elements. It is important to point out that only the shell elements around the spot weld nugget in the Solid Element Model (SEM) failed. However, no sign of failure was observed in the solid nugget at all.

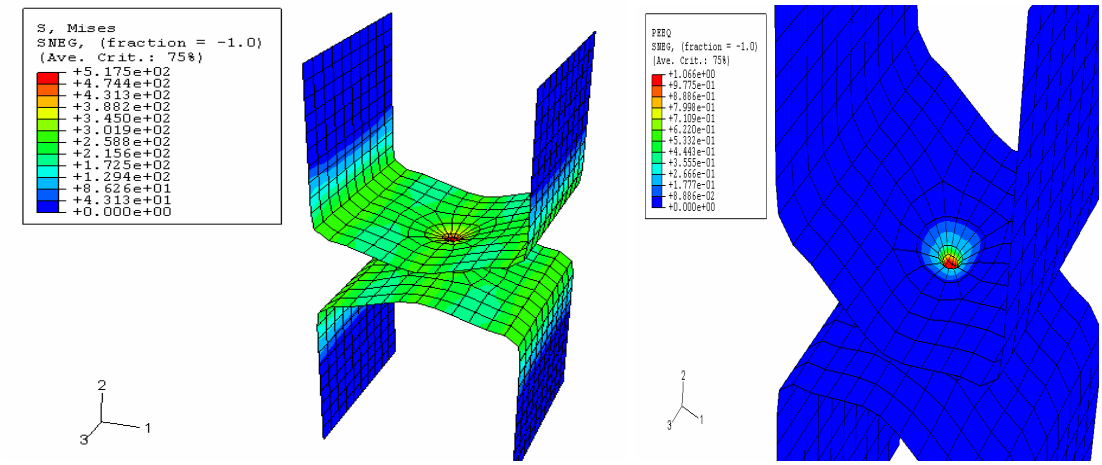

(a) **(b)**

Fig 7.11: U Tension coupon with Individual Rigid Beam Model (IRB) for quasi static loading condition analysed with ABAQUS / Standard.

(a) Mises equivalent stress distribution (Mpa) (b) Equivalent Strain distribution.

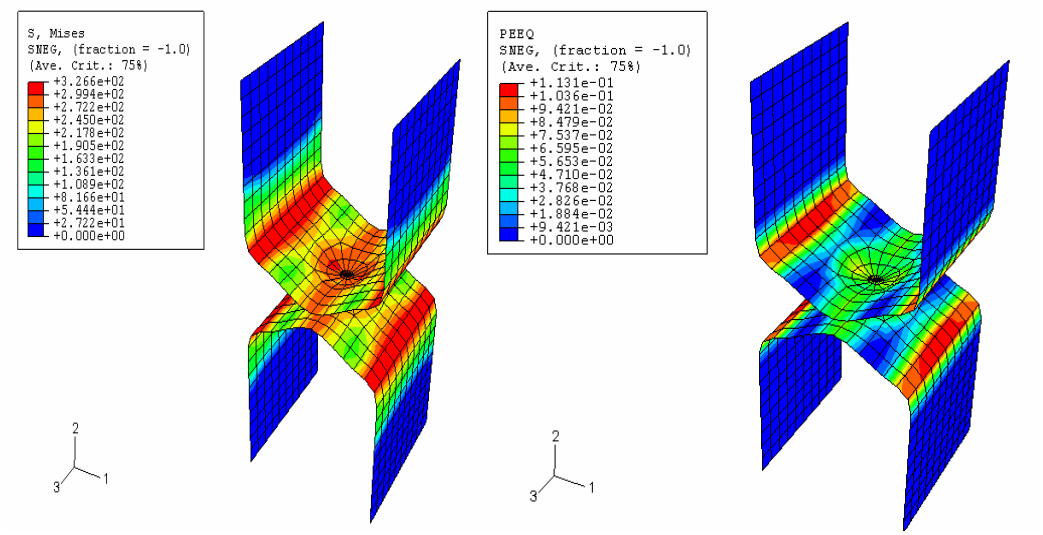

(a) (b)

Fig 7.12: U Tension coupon with Parallel Multiple Rigid Beams Model (PMRB) for quasi static loading condition analysed with ABAQUS / Standard.

(a) Mises equivalent stress distribution (Mpa) (b) Equivalent Strain distribution

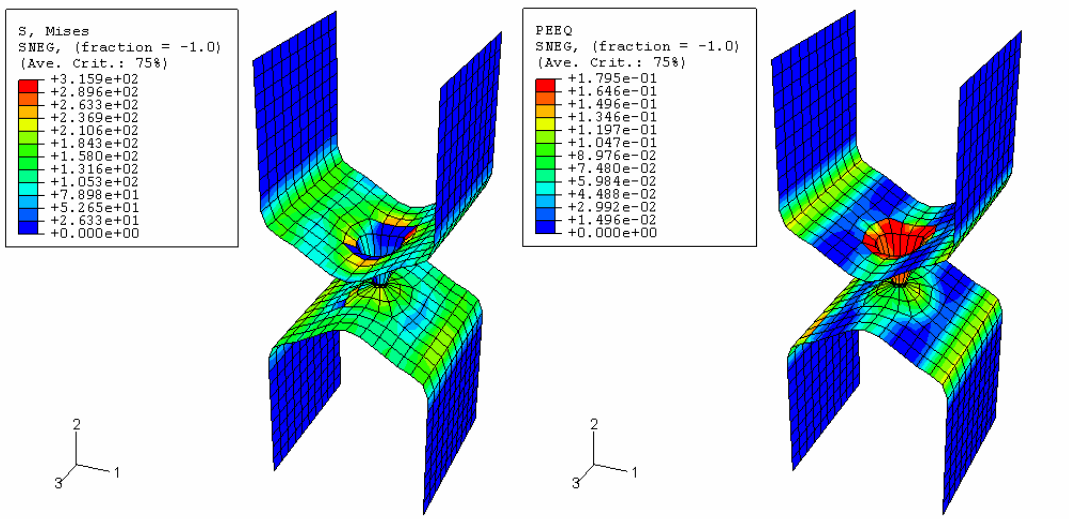

(a) (b)

Fig 7.13: U Tension coupon with Parallel Multiple Rigid Beams Model (PMRB) for failure loading condition analysed with ABAQUS / Explicit.

(a) Mises equivalent stress distribution (Mpa) (b) Equivalent Strain distribution

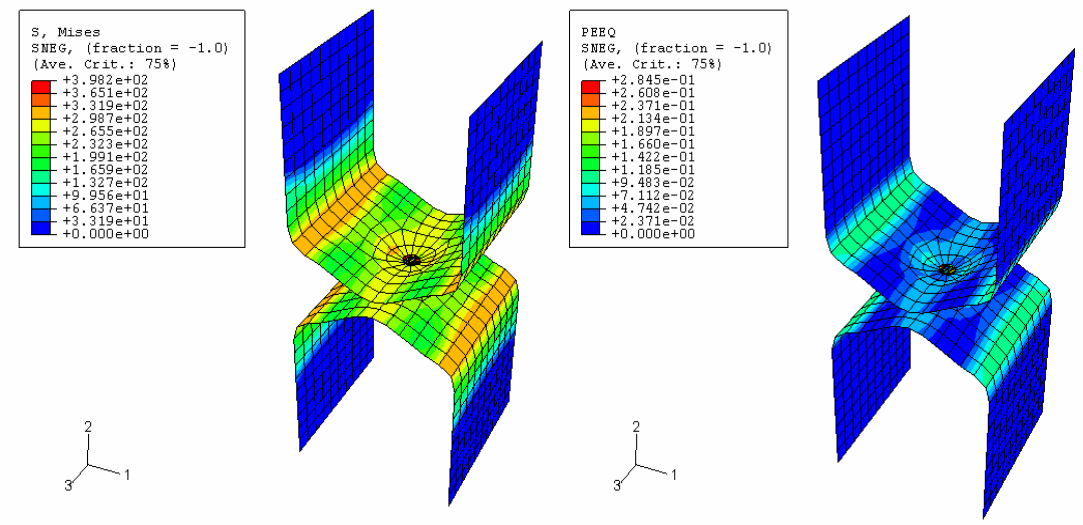

(a) (b)

Fig 7.14: U Tension coupon with Solid Element Model (SEM) model for quasi static loading condition analysed with ABAQUS / Standard.

(a) Mises equivalent stress distribution (Mpa) (b) Equivalent Strain distribution

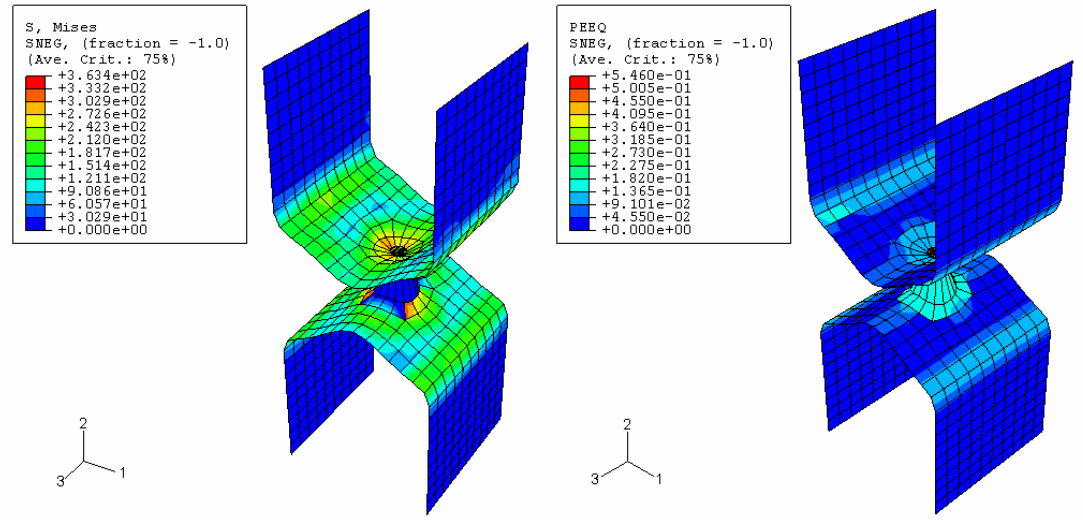

(a) (b)

Fig 7.15: U Tension coupon with Solid Element Model (SEM) model for failure loading condition analysed with ABAQUS / Explicit.

(a) Mises equivalent stress distribution (Mpa) (b) Equivalent Strain distribution

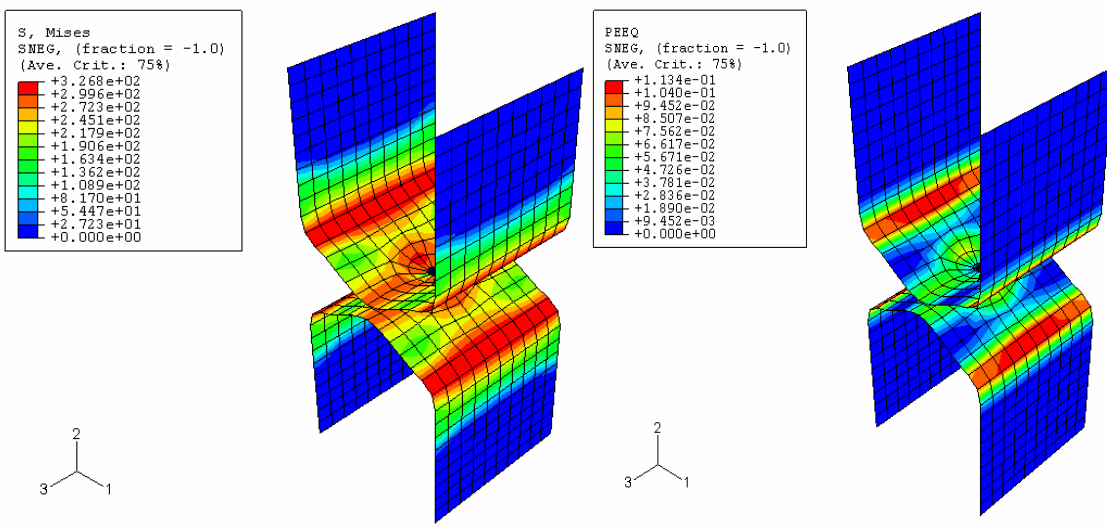

(a) (b)

Fig 7.16: U Tension coupon with Spider Configuration – 1 (SC-1) model for quasi static loading condition analysed with ABAQUS / Standard.

(a) Mises equivalent stress distribution (Mpa) (b) Equivalent Strain distribution

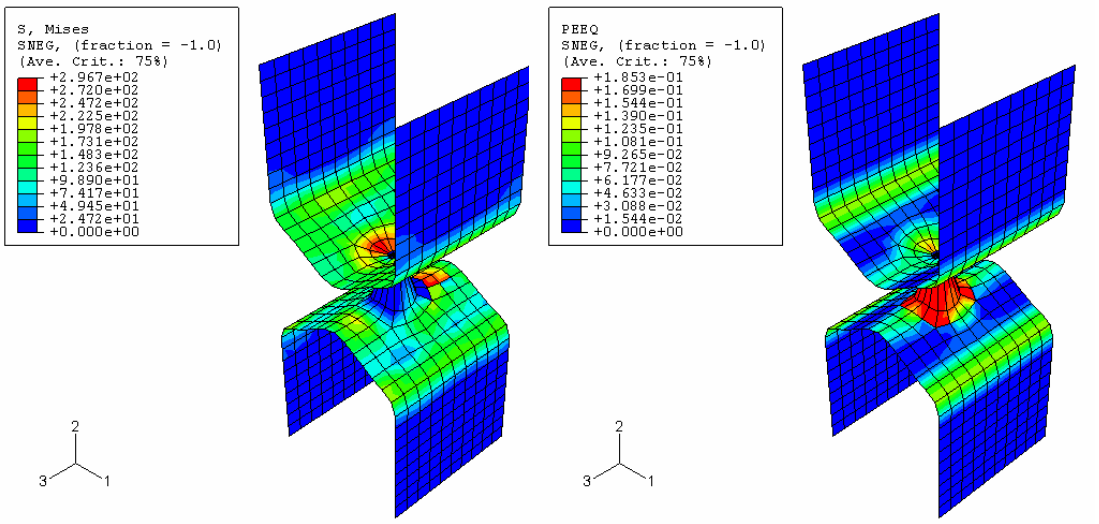

(a) (b)

Fig 7.17: U Tension coupon with Spider Configuration – 1 (SC-1) model for failure loading condition analysed with ABAQUS / Explicit.

(a) Mises equivalent stress distribution (Mpa) (b) Equivalent Strain distribution

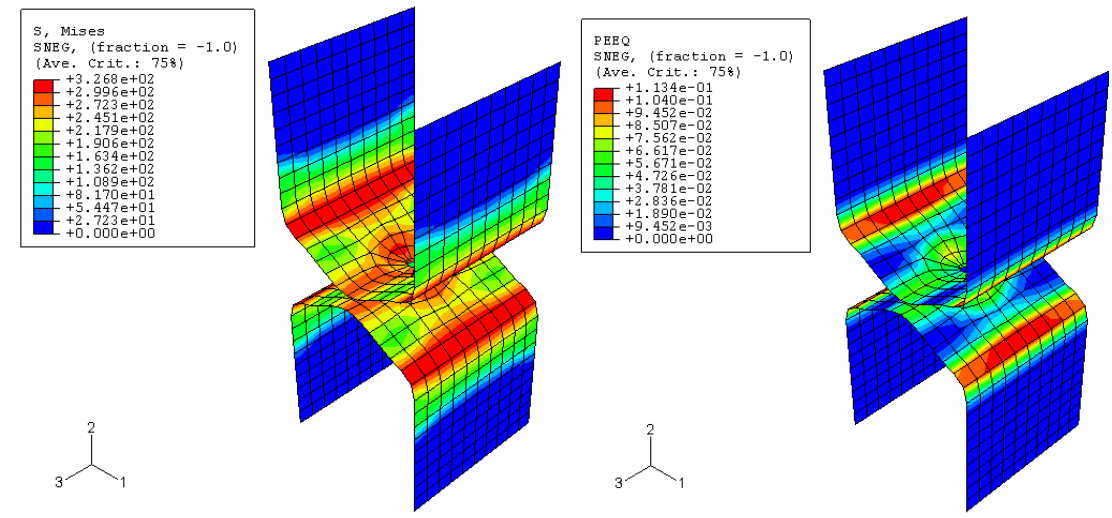

(a) (b)

Fig 7.18: U Tension coupon with Spider Configuration – 2 (SC-2) model for quasi static loading condition analysed with ABAQUS / Standard.

(a) Mises equivalent stress distribution (Mpa) (b) Equivalent Strain distribution

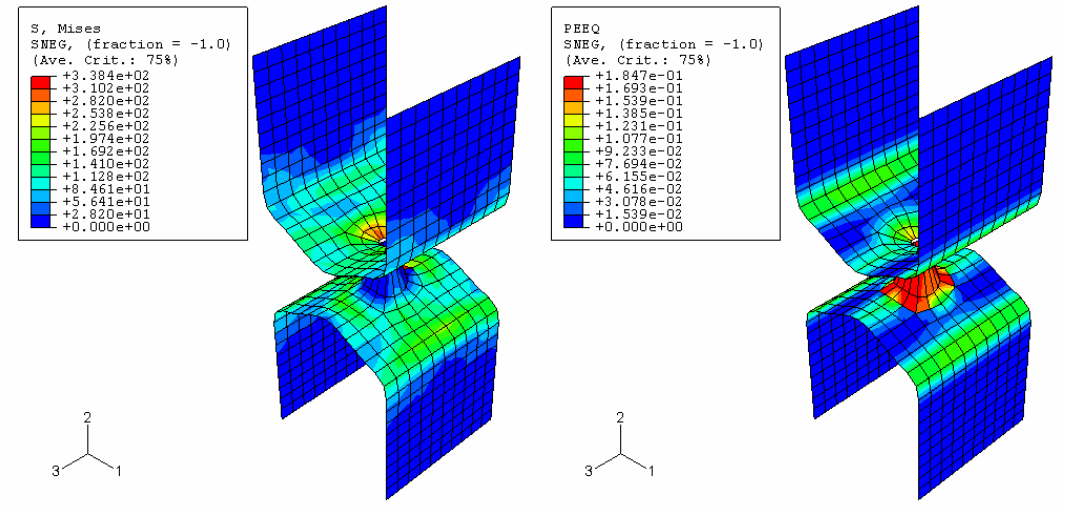

(a) (b)

Fig 7.19: U Tension coupon with Spider Configuration – 2 (SC-2) model for failure loading condition analysed with ABAQUS / Explicit.

(a) Mises equivalent stress distribution (Mpa) (b) Equivalent Strain distribution

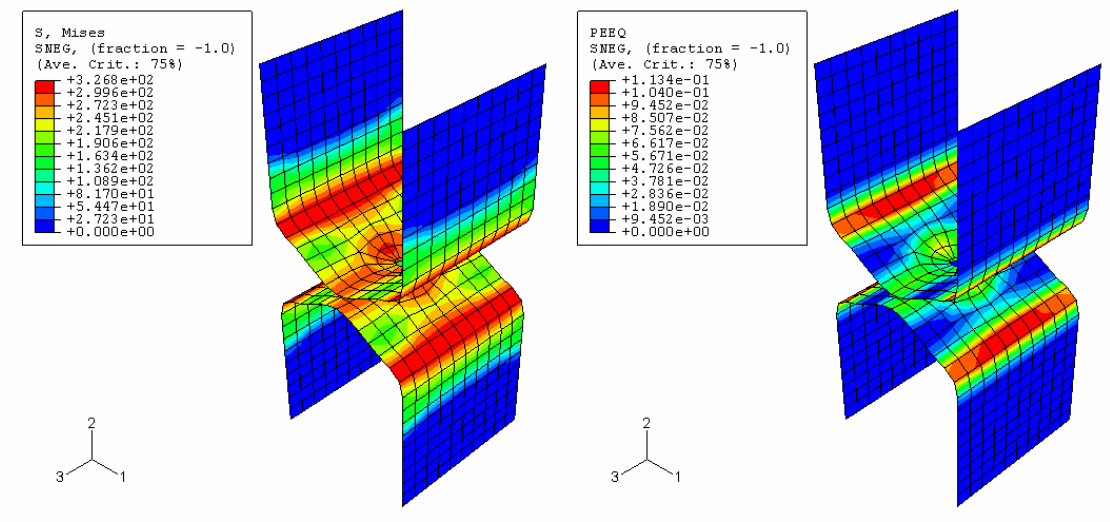

(a) (b)

Fig 7.20: U Tension coupon with Spider Configuration – 3 (SC-3) model for quasi static loading condition analysed with ABAQUS / Standard.

(a) Mises equivalent stress distribution (Mpa) (b) Equivalent Strain distribution

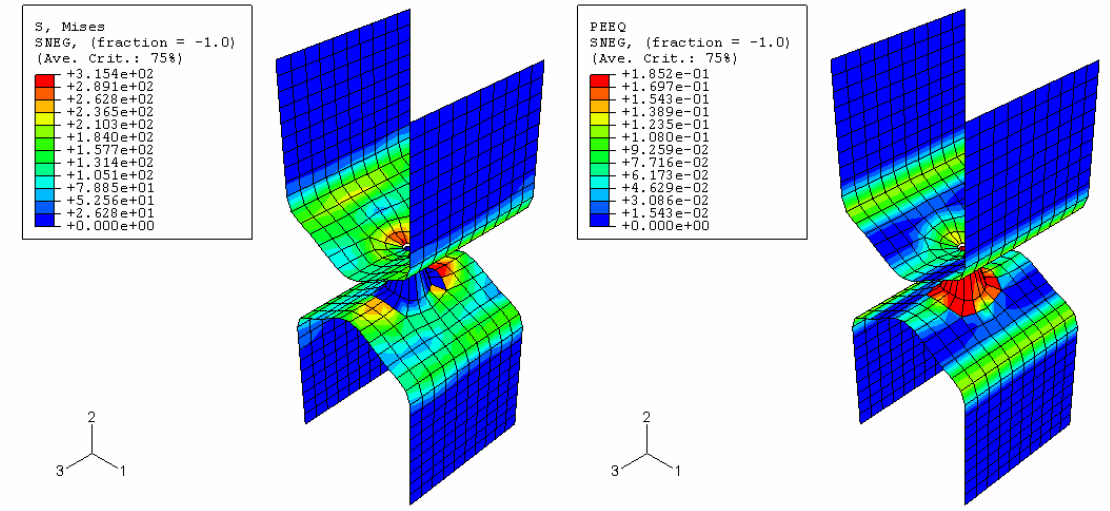

(a) (b)

Fig 7.21: U Tension coupon with Spider Configuration – 3 (SC-3) model for failure loading condition analysed with ABAQUS / Explicit.

(a) Mises equivalent stress distribution (Mpa) (b) Equivalent Strain distribution

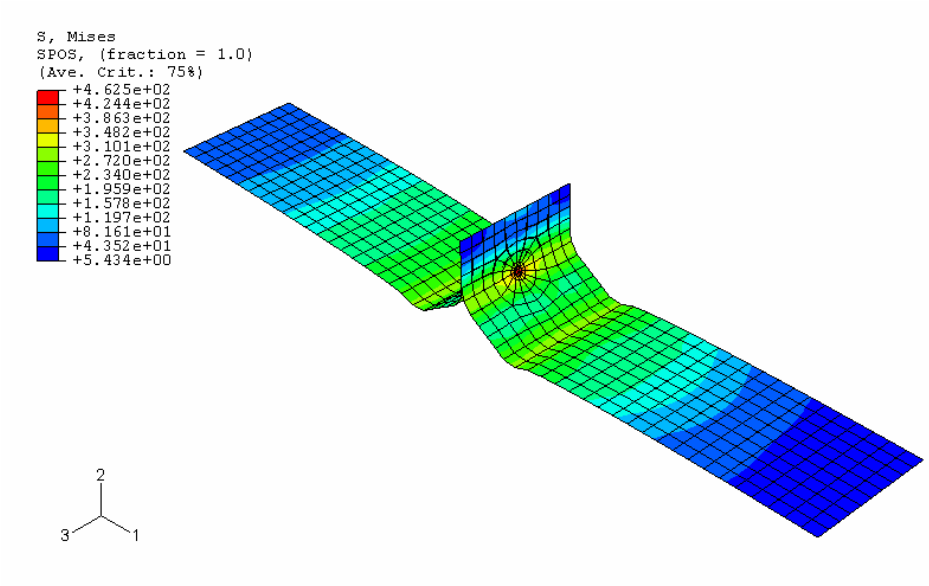

(a)

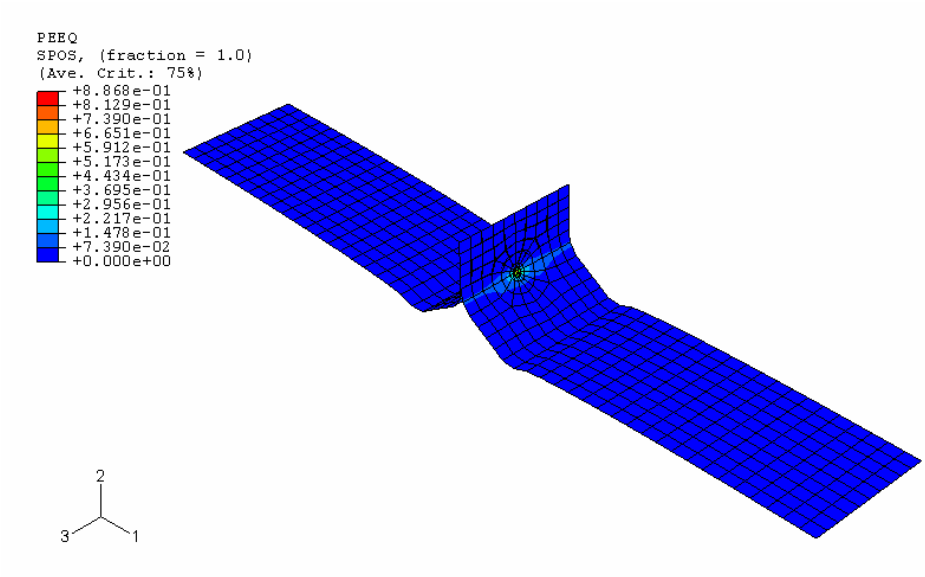

(b)

Fig 7.22: Coach Peel coupon with Individual Rigid Beam (IRB) model for quasi static loading condition analysed with ABAQUS / Standard.

(a) Mises equivalent stress distribution (Mpa) (b) Equivalent Strain distribution

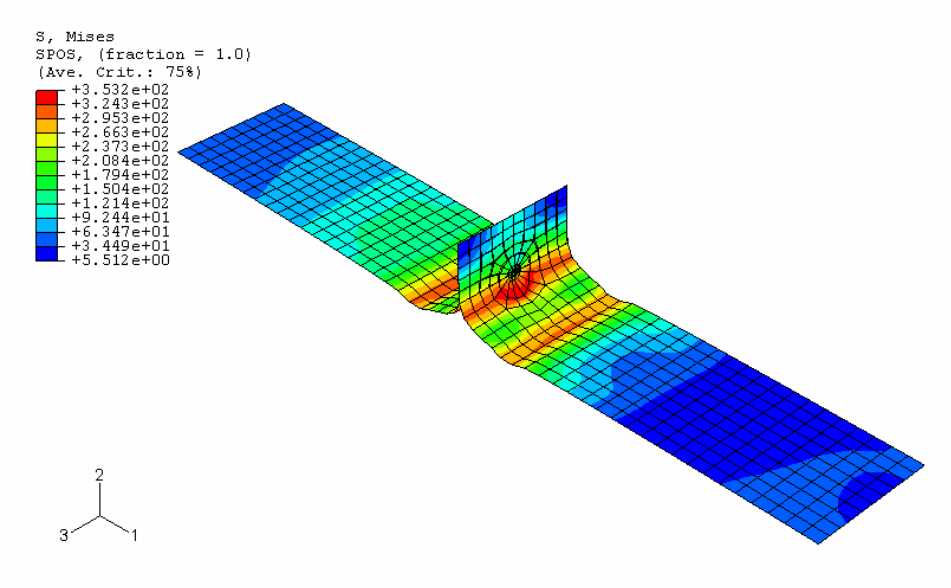

(a)

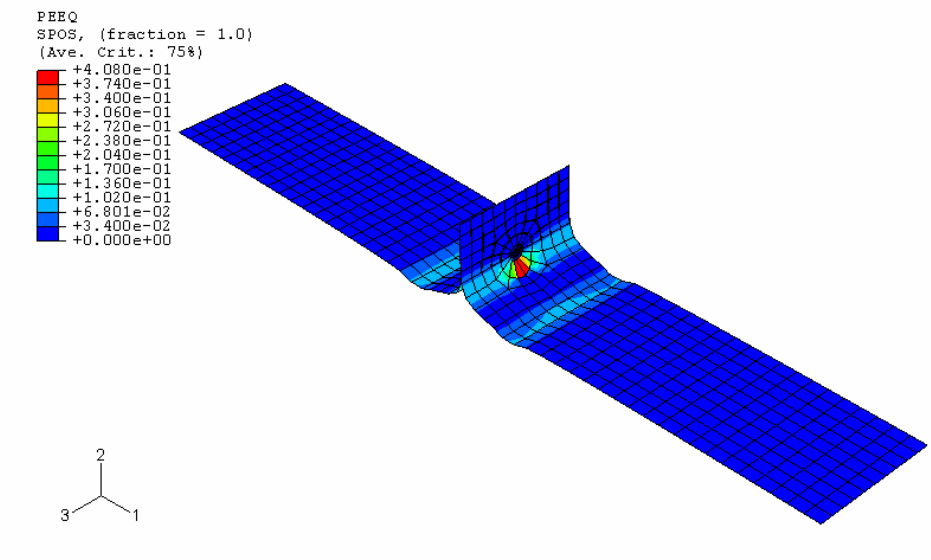

(b)

Fig 7.23: Coach Peel coupon with Parallel Multiple Rigid Beams (PMRB) model for quasi static loading condition analysed with ABAQUS / Standard. (a) Mises equivalent stress distribution (Mpa) (b) Equivalent Strain distribution

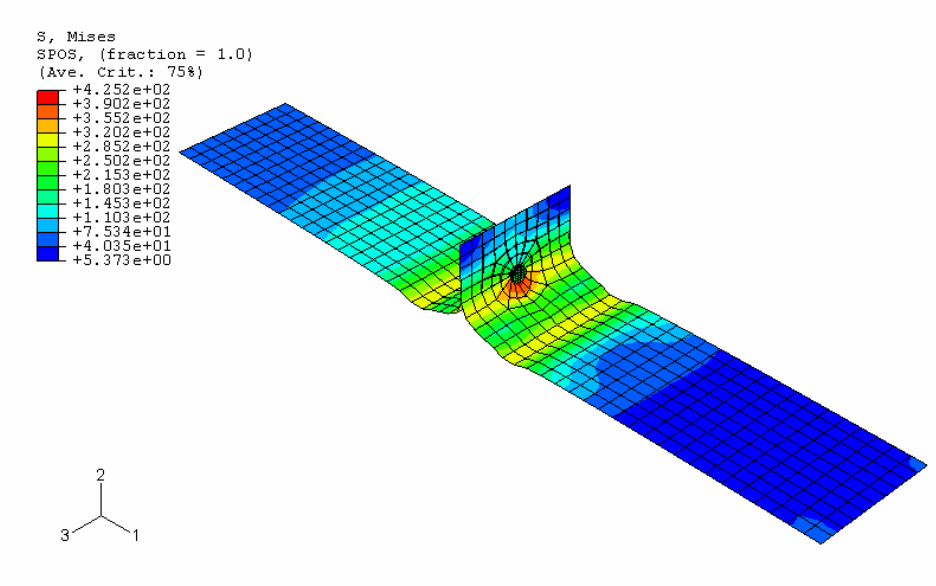

(a)

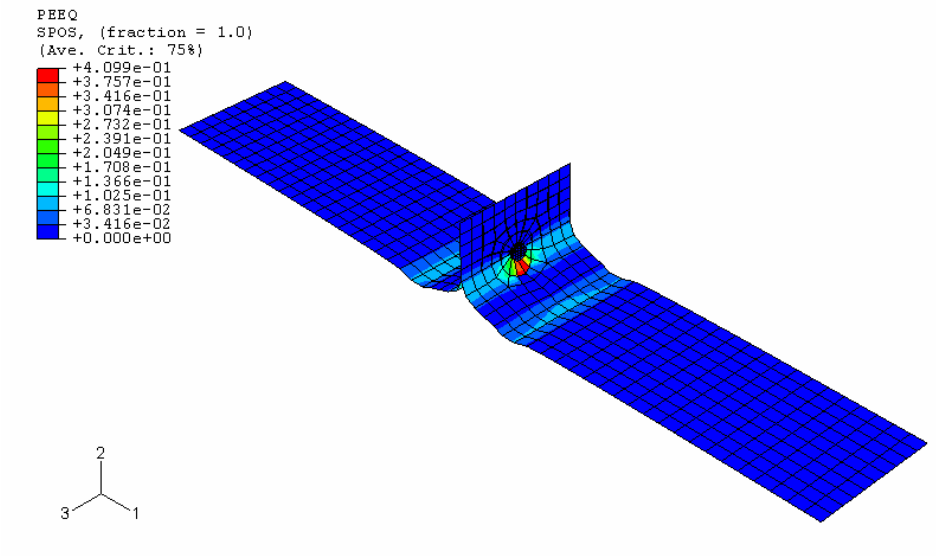

(b)

Fig 7.24: Coach Peel coupon with Solid Element Model (SEM) for quasi static loading condition analysed with ABAQUS / Standard.

(a) Mises equivalent stress distribution (Mpa) (b) Equivalent Strain distribution

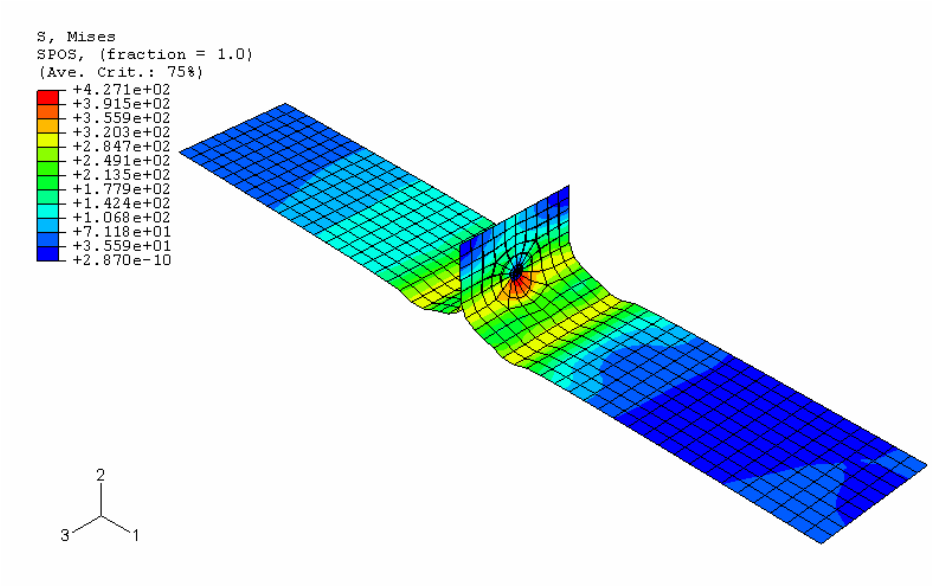

(a)

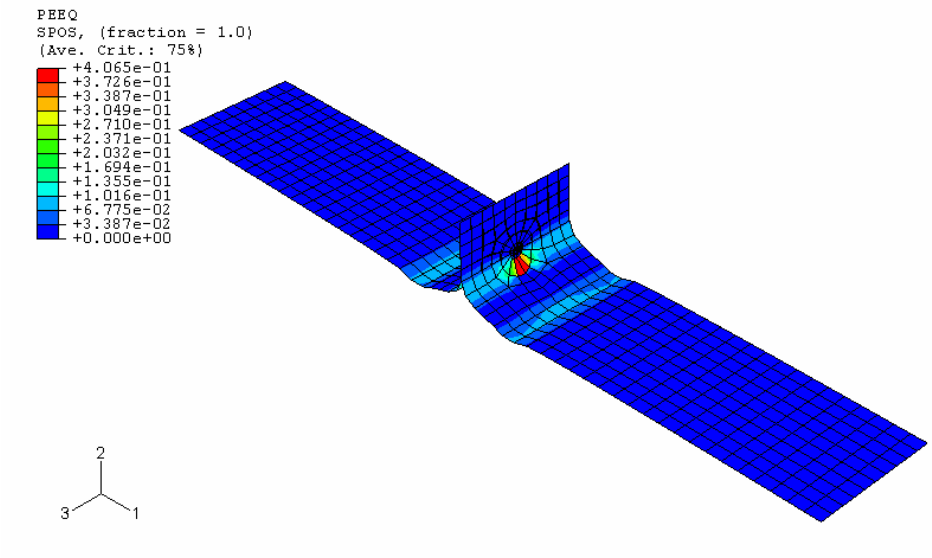

(b)

Fig 7.25: Coach Peel coupon with Spider Configuration - 1 (SC-1) model for quasi static loading condition analysed with ABAQUS / Standard.
(a) Mises equivalent stress distribution (Mpa) (b) Equivalent Strain distribution

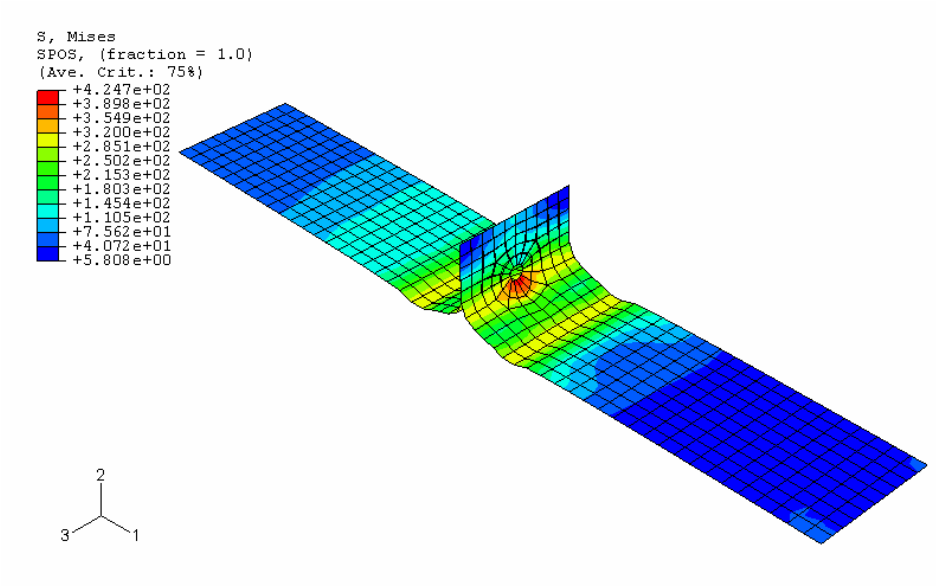

(a)

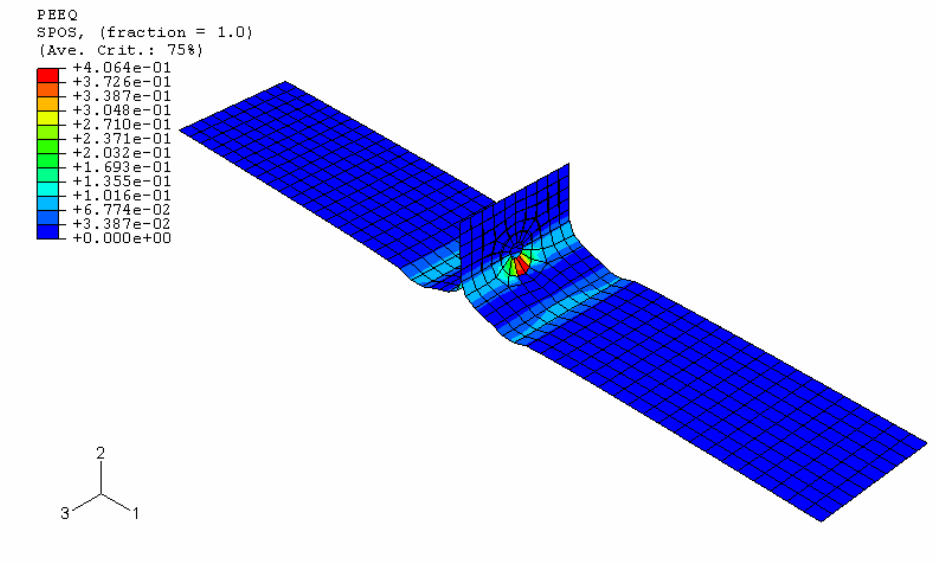

(b)

Fig 7.26: Coach Peel coupon with Spider Configuration - 2 (SC-2) model for quasi static loading condition analysed with ABAQUS / Standard.

(a) Mises equivalent stress distribution (Mpa) (b) Equivalent Strain distribution

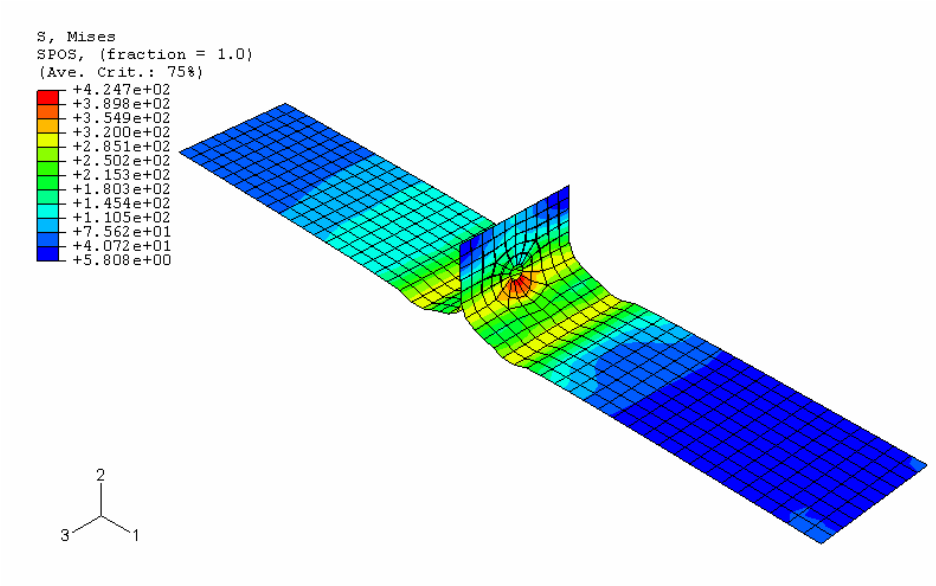

(a)

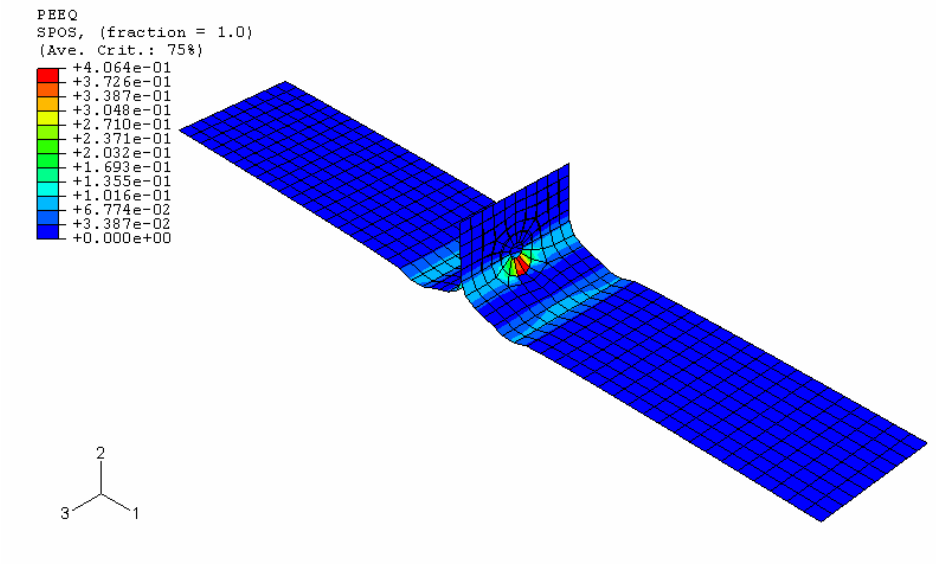

(b)

Fig 7.27: Coach Peel coupon with Spider Configuration - 3 (SC-3) model for quasi static loading condition analysed with ABAQUS / Standard.

(a) Mises equivalent stress distribution (Mpa) (b) Equivalent Strain distribution

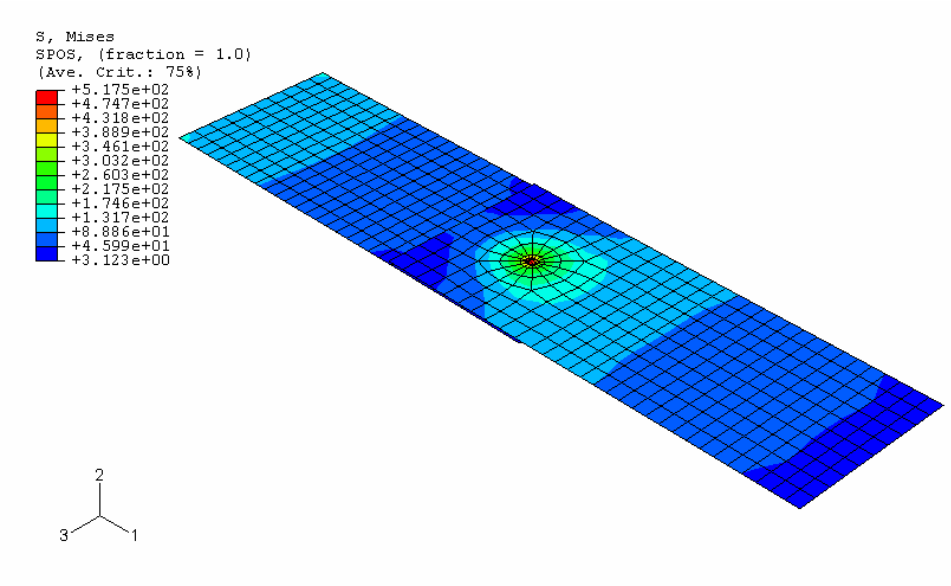

(a)

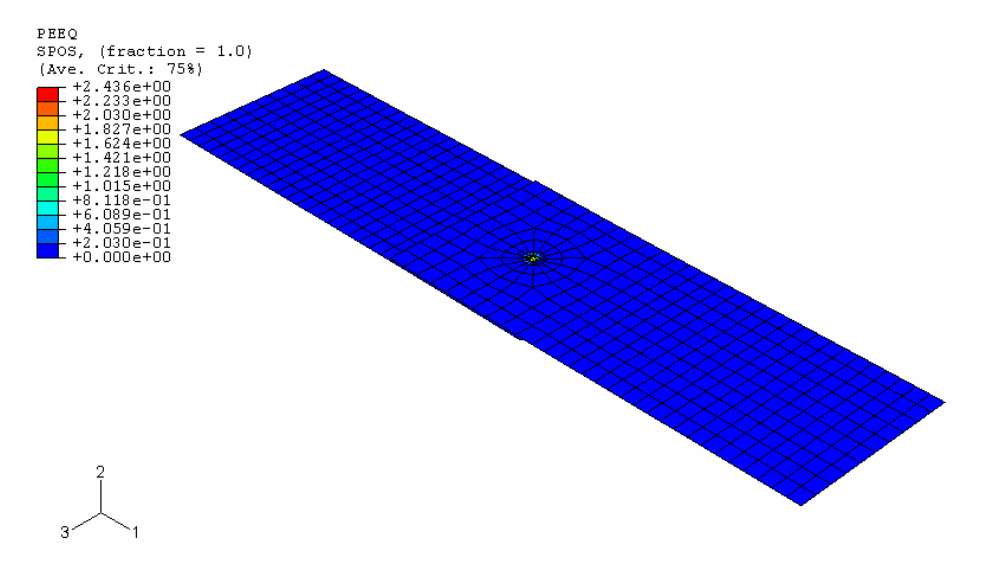

(b)

Fig 7.28: Lap Shear coupon with Individual Rigid Beams (IRB) model for quasi static loading condition analysed with ABAQUS / Standard.

(a) Mises equivalent stress distribution (Mpa) (b) Equivalent Strain distribution

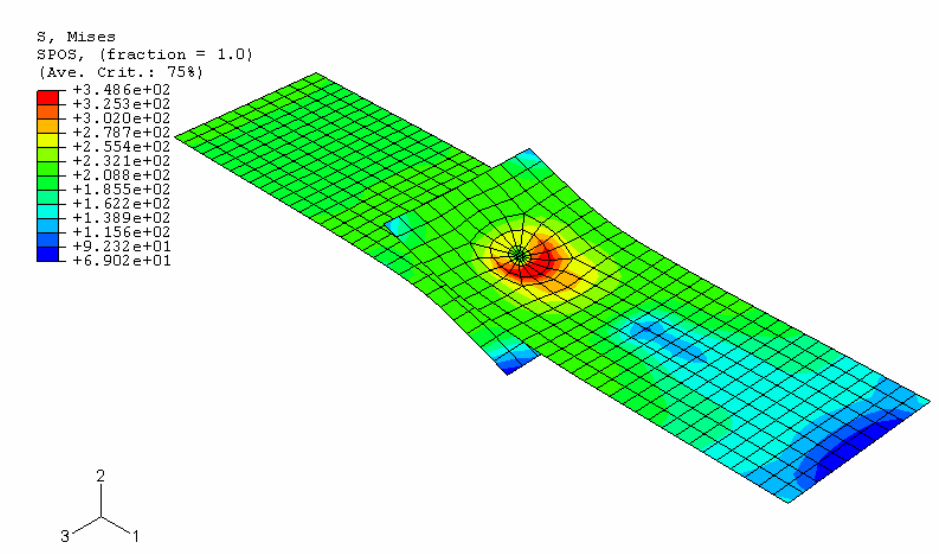

(a)

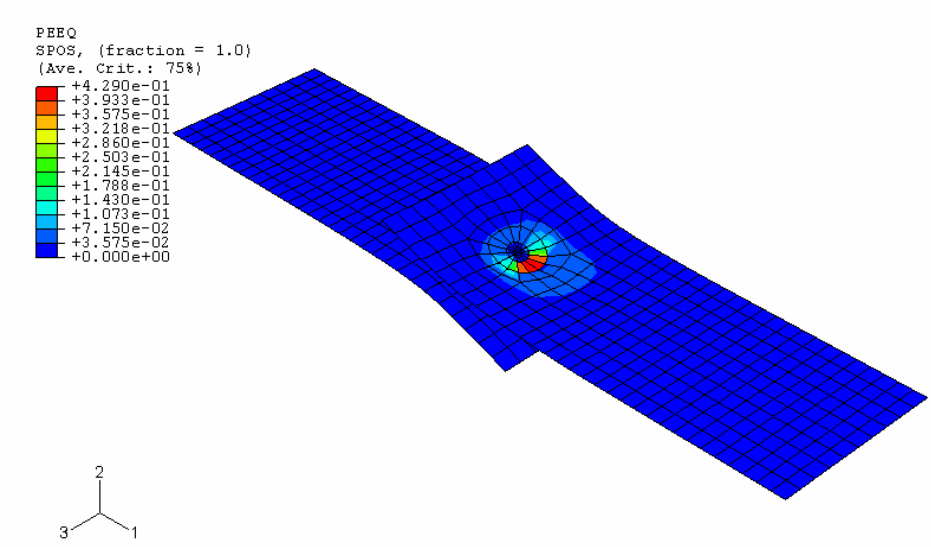

(b)

Fig 7.29: Lap Shear coupon with Parallel Multiple Rigid Beams (PMRB) model for quasi static loading condition analysed with ABAQUS / Standard.

(a) Mises equivalent stress distribution (Mpa) (b) Equivalent Strain distribution

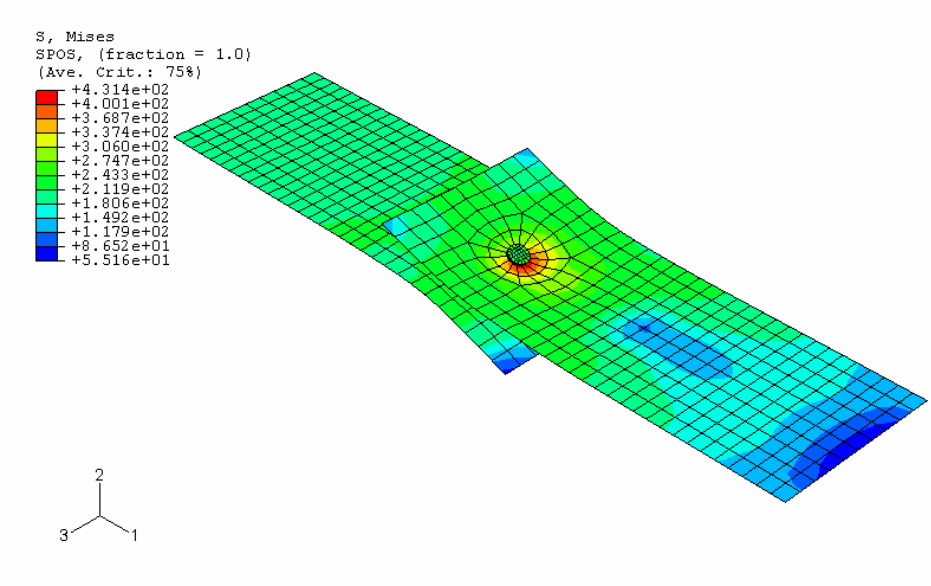

(a)

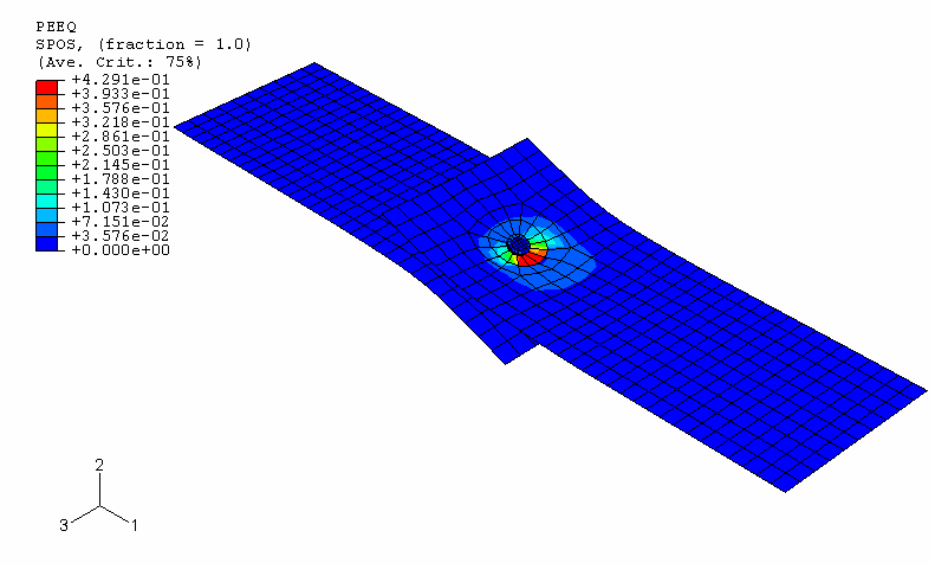

(b)

Fig 7.30: Lap Shear coupon with Solid Element Model (SEM) for quasi static loading condition analysed with ABAQUS / Standard.

(a) Mises equivalent stress distribution (Mpa) (b) Equivalent Strain distribution

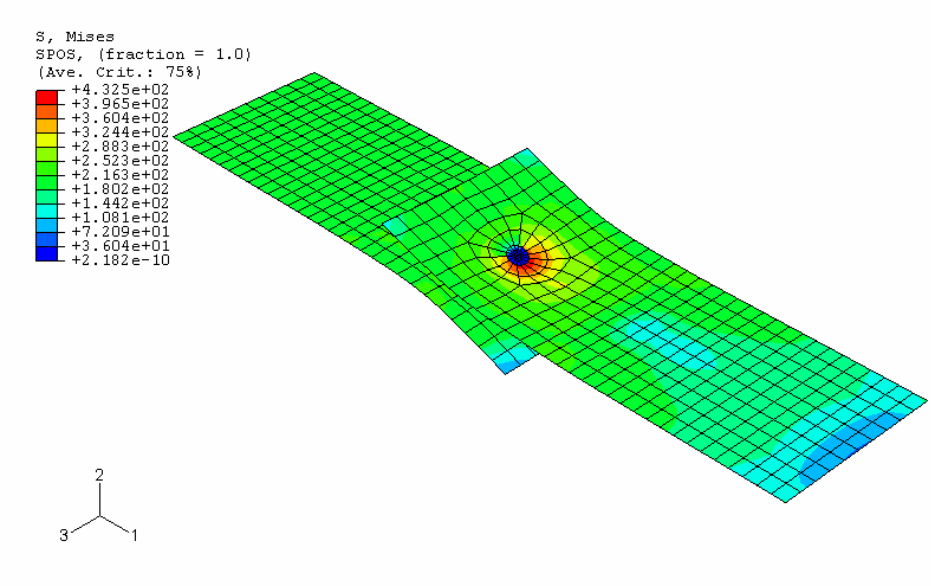

(a)

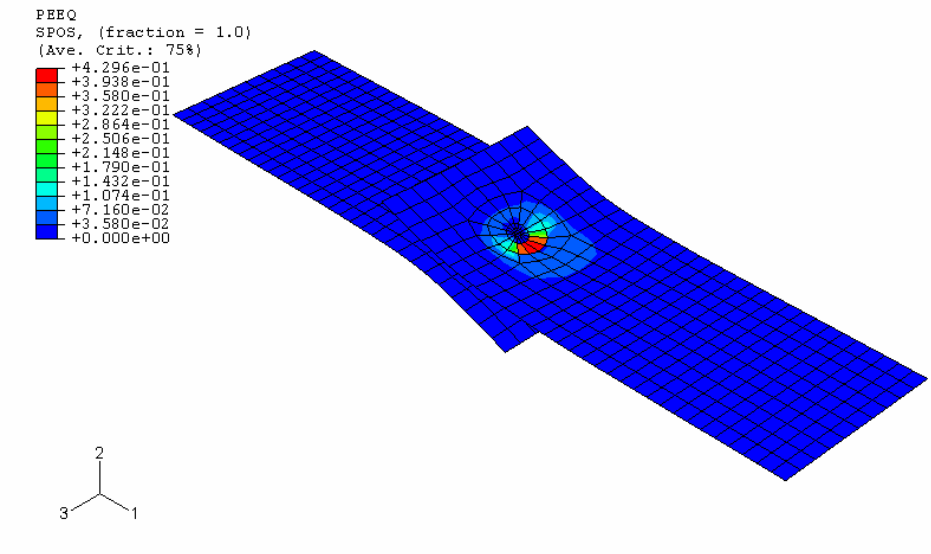

(b)

Fig 7.31: Lap Shear coupon with Spider Configuration - 1 (SC-1) model for quasi static loading condition analysed with ABAQUS / Standard.
(a) Mises equivalent stress distribution (Mpa) (b) Equivalent Strain distribution

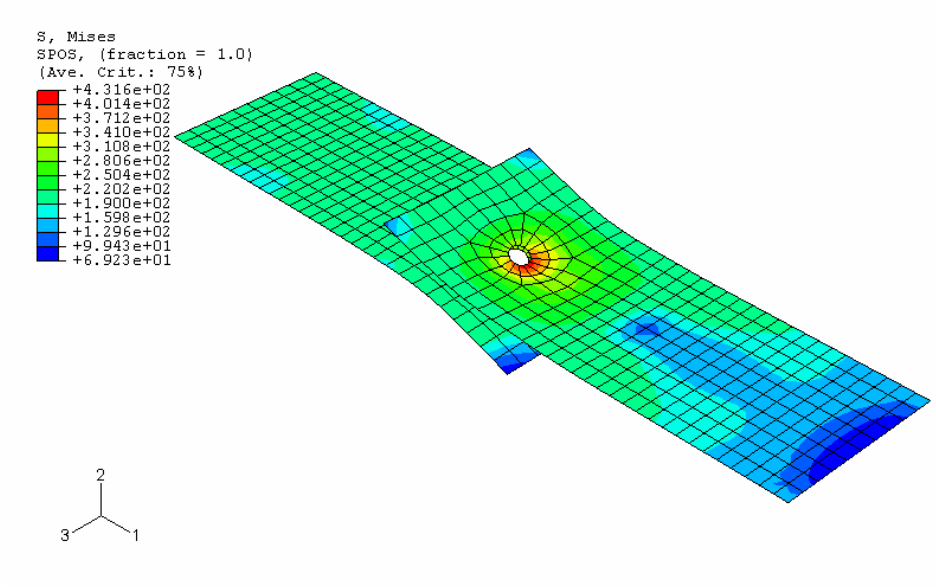

(a)

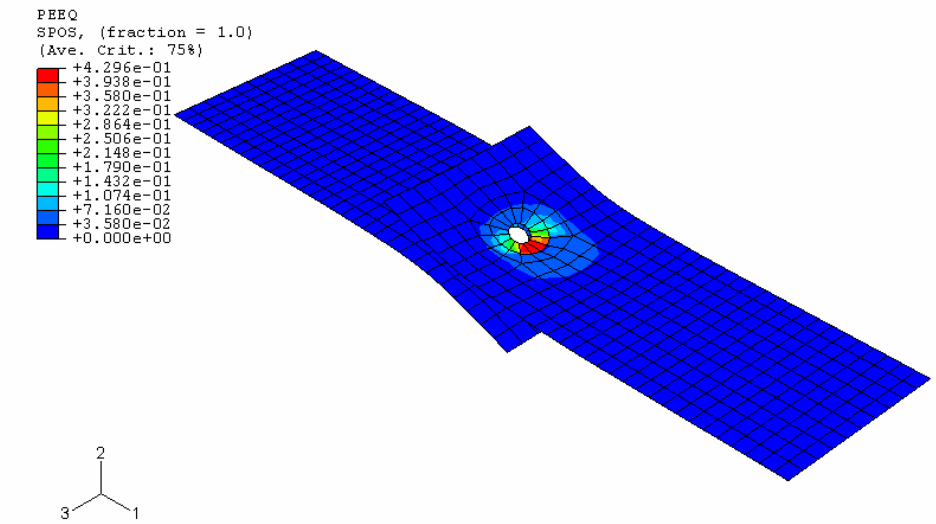

(b)

Fig 7.32: Lap Shear coupon with Spider Configuration - 2 (SC-2) model for quasi static loading condition analysed with ABAQUS / Standard.
(a) Mises equivalent stress distribution (Mpa) (b) Equivalent Strain distribution

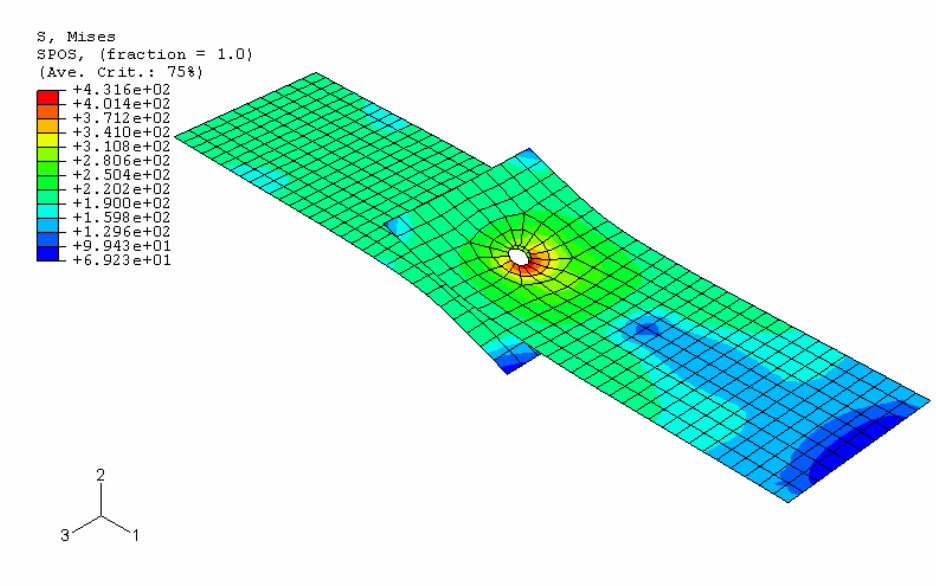

(a)

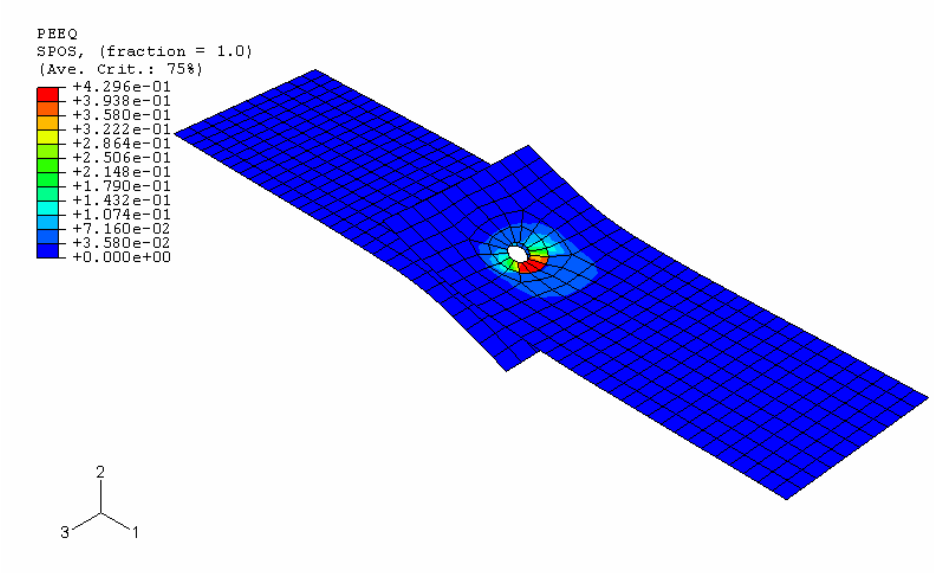

(b)

Fig 7.33: Lap Shear coupon with Spider Configuration - 3 (SC-3) model for quasi static loading condition analysed with ABAQUS / Standard.

(a) Mises equivalent stress distribution (Mpa) (b) Equivalent Strain distribution

7.6 Performance study of the developed models

The comparison of results through the characteristics responses (force displacement curve) elaborates the model performances with respect to the accuracy from a mechanics point of view. But to clarify the complete performances of the developed spot weld models, the computational costs occurring for each model should also be considered.

The computational cost is defined here as the “CPU time” which is the total approximate computation time required by the commercial code for completing the analysis. Other than the CPU time two other parameters were considered for comparison purposes. The first parameter is “Memory Used”. It is defined as the required memory value that enables the commercial code to solve the problem. The other parameter is “Required Disk Space” which is defined as the amount of disk space required for storing the scratch files during the analysis. These scratch files are deleted automatically at the end of the analysis. This is a very important parameter for the implicit analysis procedure. But for the explicit analysis this is not required due to the numerical techniques followed by the analysis procedures. Hence they are not reported here. All the computations were performed on a WINDOWS (X – 86, 32 bit) based platform.

The comparison results are given in the following tables (Table 7.1, 7.2 and 7.3). The computational performance results are given for both the implicit analysis and explicit analysis. As the failure criterion was not appropriately implemented in case of the lap shear coupon and coach peel coupon, the performance results for the explicit procedure is not included in the following table. Similarly as the IRB model did not need to be analysed with the failure criterion, the explicit performance results with this model in the U tension coupon is also not provided.

Table 7.1: Performances of different spot weld models for shear loading condition with lap shear coupon without back plate configuration.

Lap Shear Coupon						
Criteria	Required Disk Space (MB)		Total CPU time (sec)		Memory Used (MB)	
Spot weld models / Analysis techniques	Imp.	Exp.	Imp.	Exp.	Imp.	Exp.
Individual Rigid Beam Model (IRB)	34.11	-	121.30	-	24.27	-
Parallel Multiple Rigid beams Model (PMRB)	33.72	-	108.60	-	24.31	-
Solid Element Model (SEM)	25.38	-	117.1	-	21.54	-
Spider Configuration – 1 (SC – 1)	31.45	-	99.2	-	24.36	-
Spider Configuration – 2 (SC – 2)	20.46	-	88.2	-	20.26	-
Spider Configuration – 3 (SC – 3)	20.59	-	89.8	-	20.594	-

Imp. = Performance for quasi static analysis by ABAQUS / Standard (Implicit Analysis)
Exp. = Performance for failure simulation by ABAQUS / Explicit (Explicit Analysis)

Table 7.2: Performances of different spot weld models for bending loading condition with coach peel coupon.

Coach Peel Coupon						
Criteria	Required Disk Space (MB)		Total CPU time (sec)		Memory Used (MB)	
Spot weld models / Analysis techniques	Imp.	Exp.	Imp.	Exp.	Imp.	Exp.
Individual Rigid Beam Model (IRB)	11.05	-	130.90	-	20.27	-
Parallel Multiple Rigid beams Model (PMRB)	10.95	-	126.30	-	20.27	-
Solid Element Model (SEM)	12.79	-	149.4	-	18.99	-
Spider Configuration – 1 (SC – 1)	10.10	-	109.60	-	20.30	-
Spider Configuration – 2 (SC – 2)	9.99	-	93.10	-	18.65	-
Spider Configuration – 3 (SC – 3)	10.02	-	93.60	-	20.12	-

Imp. = Performance for quasi static analysis by ABAQUS / Standard (Implicit Analysis)
Exp. = Performance for failure simulation by ABAQUS / Explicit (Explicit Analysis)

Table 7.3: Performances of different spot weld models for tensile loading condition with U tension coupon.

U tension Coupon							
Criteria	Required Disk Space (MB)		Total CPU time (sec)		Memory Used (MB)	
Spot weld models / Analysis techniques	Imp.	Exp.	Imp.	Exp.	Imp.	Exp.
Individual Rigid Beam Model (IRB)	4.28	-	56.6	-	16.46	-
Parallel Multiple Rigid beams Model (PMRB)	4.44	-	63.5	5385	16.51	2.4
Solid Element Model (SEM)	6.27	-	88.30	9345	16.73	2.6
Spider Configuration – 1 (SC – 1)	3.92	-	62.90	5531	16.47	2.4
Spider Configuration – 2 (SC – 2)	3.66	-	53.50	1227	16.29	2.6
Spider Configuration – 3 (SC – 3)	3.70	-	55.0	956	16.32	2.2

Imp. = Performance for quasi static analysis by ABAQUS / Standard (Implicit Analysis)
Exp. = Performance for failure simulation by ABAQUS / Explicit (Explicit Analysis)

It can be observed from the data of the following table that in general the Individual Rigid Beam Model (IRB) is incurring more CPU time and disk space than any other models for the implicit analysis. This is due to the fact that this model needs more equilibrium iterations to complete the analysis. In case of the implicit analysis the Spider Configuration – 2 model required coMparatively less CPU time. Hence this model performed better for the implicit analysis.

In case of the explicit analysis the PMRB, SEM and SC-1 model required a huge amount of computation time. This is due to the reason that the element dimension size inside the spot weld nugget region was much smaller than the other elements. It was noticeable that the memory used by the explicit analysis was much less than the required memory in the implicit analysis. It was due to the analysis procedure as described in chapter 5. In case of the explicit analysis the SC -3 model performance was best.

CoMparing the computational performances both for the implicit and explicit analysis and from the force displacement response of the developed spot weld models, the SC-2 and SC-3 model are definitely preferable for the crash analysis procedure.

Chapter – 8

Conclusions and Recommendations

8.1 Conclusions

In this thesis a strategy for developing FEM models of the spot weld joints for dynamic crash analysis and simulations was presented. Six different spot welded joint models were developed and studied for this purpose. A proper meshing strategy around the spot welded joint was also presented. The characteristics of the developed spot weld models were studied for the shear loading condition (with lap shear coupons), tensile loading condition (with U tension coupons) and the bending load condition (with Coach Peel coupons). The developed model performances were evaluated from two perspectives. First with respect to the experimental results (force displacement response) obtained through the spot welded test coupons. Second perspective was with respect to the computational costs incurred by each of the models.

In experimental investigations a simple strategy was followed to design the spot welded test coupons based on the nugget pull out mode of failure. All the test coupons designed according to this strategy failed in the nugget pull out mode irrespective of the applied load rates. The experimental results obtained at the applied rate of 5 mm/min were used to evaluate the load bearing characteristics of the developed models using the implicit FEM code ABAQUS/Standard. On the other hand the experimental results obtained at the applied rate of 500 mm/min were used to evaluate the developed models for spot weld failure situations using the explicit FEM code ABAQUS/Explicit.

For the study of the developed spot weld models with ABAQUS/Standard in all loading situations (shear, tensile and bending) it was found that the individual Rigid Beam (IRB) model (which is the current modelling practice for the spot joint in the automotive industry) could not represent the required stiffness with respect to the experimental results. The IRB model caused severe localized deformation, which caused the early collapse in the force displacement response. The other five models behaved similarly with respect to the load bearing characteristics in all situations. The force displacement response from the developed models for the shear loading situation with the lap shear coupon was found to be unexpectedly higher than the experimental response. The cause of this was due to the particular mesh configuration used for the simulation. To improve this force displacement response from the models the transverse shear effect was attempted to be incorporated into the models. The inclusion of the transverse shear into the models affected the force displacement response at the maximum load bearing point, but this shifted the initial slope of the force displacement curve. This shifting was imposed intentionally to incorporate the transverse shear effect into the plasticity zone of the force displacement response.

The simulation of failure of the spot welded joints was through deleting the elements around the nugget. The failure initiation and propagation criteria used to simulate the failure situation were based upon the damaged material properties according to the state of stress and calibrated plastic equivalent strain with respect to the uni axial tensile test. The force displacement curves for the developed spot weld models in the tensile loading situation with the U tension coupon clearly pointed out the complete failure around the spot weld joint. The Parallel Multiple Rigid Beams (PMRB) model and the Solid Element Model (SEM) predicted a higher load than the experimental results. While the Spider Configuration models (SC – 1, 2 and 3) projected similar force displacement responses which were

similar to the experimental results, the similar failure initiation and propagation criteria did not work properly for the shear load condition (with the lap shear coupon) and the bending load condition (with the Coach Peel coupon). The reason behind the unexpected results in these cases was that the proper state of stresses around the spot weld nugget could not be incorporated in the failure definition of the developed models. This was due to the limited material property data available for the sheet metal used in this study. Further material data of the used sheet metal is required to define the material failure initiation and propagation characteristics.

Regarding the computational performances (according to the incurred computational costs) of the developed models, the Spider Configuration – 2 (SC - 2) model had the best performance for the load bearing characteristics simulations with the implicit code ABAQUS/STANDARD. For the failure simulations with the explicit code ABAQUS/EXPLICIT, the Spider Configuration – 3 (SC-3) model had the best performances. Therefore these two models are recommended as the better spot weld models among the developed models.

8.2 Recommendations

The following is recommended for future studies.

(i) To get the failure initiation and propagation criterion to work properly in the lap shear and Coach Peel coupon configurations, further experimental data of the sheet metal material is required. One of the advanced tests includes the “Erichsen Test”, which is actually an equi - biaxial tensile test of the sheet metal. The three point bending test results may also be included in the failure definition along with the Erichsen test. These are required to define the state of stresses and the strain path which would

effectively define the material characteristic boundary region to which the failure criterion is applicable.

(ii) The change in material properties in the heat affected zones were completely ignored in this study. Now as the better spot weld models have been identified, the effect of the inclusion of the heat affected zone material properties can be properly studied with these models. For this purpose the methods of extracting the material properties of the heat affected zones around the spot weld nugget using indentation techniques proposed by Mignone (2006) may be followed. But this inclusion of the heat affected zones material properties would definitely make the models very complicated and would incur more computational costs.

(iii) The spot weld models were studied in this thesis in test coupon configurations only. Through this study, better spot weld models were identified. The better models were the models with the Spider Configurations (SC – 2 and SC – 3). Now the performances of these models should be studied in a box rail type of structure (single hat structure or double hat structure) along with the proper implementation of the failure initiation and propagation criterion. Moreover the options for the automatic generation of these spider configurations may be pointed out through that study. Specialized pre-processors which have options for automatic spider generation like ANSA or MEDINA may be used for this purpose.

References

Adib, H., Jeong, J., & Pluvinage, G. (2004). Three-Dimensional Finite Element Analysis Of Tensile-Shear Spot-Welded Joints in Tensile and Compressive Loading Conditions. *Strength of Materials, 36*(4), 353-364.

Ahmed, K. (2003). Static failure modes of spot welds-a 3D finite element study. Paper presented at the *International Conference on the Joining of Materials*, Helsingor, Denmark.

Allanki, Y. R., & Kumar, C. A. (2005). Failure load evaluation of resistance spot weld subjected to tensile and shear load. *SAE Technical Paper, 2005-26-045*.

Al-Samhan, A., & Darwish, S. M. H. (2003). Strength prediction of weld-bonded joints. *International Journal of Adhesion and Adhesives, 23*(2003), 23-28.

Anonymous. (1956). *Resistance Welding - Theory and Use*: American Welding Society.

Anonymous. (1980). *Welding Handbook* (7th edition ed. Vol. 3): American Welding Society.

Anonymous. (1991). *Metallic Materials: Tensile testing at ambient temperature* (Vol. AS - 1391): Standards Australia.

Anonymous. (1994). Optimizer locates welds to stiffen structure. *Machine Design, May, 1994,* 18-19.

Anonymous. (2005). *Recommended practices for automotive weld quality - resistance spot welding* (Vol. AWS D8.7M:2005): American Welding Society.

Anonymous. (2005). ABAQUS Documentation. *Version 6.5*.

Birch, R. S., & Alves, M. (2000). Dynamic failure of structural joint systems. *Thin-Walled Structures, 36*, 137-154.

Bouyousfi, B., Sahraoui, T., Guessasma, S., & Chaouch, K. T. (2005). Effect of process parameters on the physical charecteristics of spot weld joints. *Materials and Design, (Article in press)*.

Cavalli, M. N., Thouless, M. D., & Yang, Q. D. (2005). Cohesive-zone modelling of the deformation and fracture of spot-welded joints. *Fatigue Fract Engng Mater Struc, 28*, 861-874.

Chao, Y. J. (2003). Ultimate Strength and Failure Mechanism of Resistance Spot Weld Subjected to Tensile, Shear, or Combined Tensile/Shear Loads. *Journal of Engineering Materials and Technology, 125*(April 2003), 125-132.

Chao, Y. J. (2003). Failure Mode of Spot Welds: Interfacial Versus Pullout. *Science and Technology of Welding and Joining, 8*(2), 133-137.

Chen, W., & Deng, X. (2000). Performance of shell elements in modeling spot-welded joints. *Finite Elements in Analysis and Design, 35*(2000), 41-57.

Combescure, A., Delcroix, F., Caplain, L., Espanol, S., & P.Eliot. (2003). A finite element to simulate the failure of weld points on impact. *International Journal of Impact Engineering, 28*(2003), 783–802.

Darwish, S. M. (2003). Weldbonding strengthens and balances the stresses in spot welded dissimilar thickness joints. *Journal of Materials Processing Technology, 134*(2003), 352-362.

Darwish, S. M., & Al-Samhan, A. M. (2004). Peel and shear strength of spot welded and weld bonded dissimilar bonded joints. *Journal of Materials Processing Technology, 147*(2004), 51-59.

Darwish, S. M. H., & Ghanya, A. (2000). Critical assessment of weld-bonded technologies. *Journal of Materials Processing Technology, 105*(2000), 221-229.

Degermo, E. P., Black, J. T., & Kohser, R. A. (1992). *Materials and processes in manufacturing* (8th edition ed.): Prentice-Hall,Inc.

Deng, X., Chen, W., & Shi, G. (2000). Three-dimensional finite element analysis of the mechanical behavior of spot welds. *Finite Elements in Analysis and Design, 35*(2000), 17-39.

Dincer, S., Cinar, A., Kepenek, D. A., Asureciler, B., Duran, E. T., & Mugan, A. (2006). A comparative study on the finite element models for spot welds and their verification. *SAE Technical Paper, 2006-01-0590*.

Ewing, K. M. W., Cheresh, M., Thompson, R., & Kukuchek, P. (1982). Static and Impact Strengths of Spot Welded HSLA and Low Carbon Steel Joints. *SAE Technical Paper,820281*.

Fang, J., Hoff, C., Holman, B., Muller, F., & Wallerstein, D. (2000). *Weld modeling with MSC Nastran.* Paper presented at the *Second MSC worldwide automotive used conference*, Dearborn, MI, USA.

Fermer, M., McInally, G., & Sandin, G. (1999). *Fatigue life analysis of Volvo S80 Bi fuel.* Paper presented at the *1st worldwide MSC automotive conference*, Munich, Germany.

Fujimoto, M., Mori, N., & Sakuma, S. (1982). Stress Distribution Analysis of Spot Welded Joints under Tension Shear Load. *International Institute of Welding Documents III*, 721-782.

Hahn, O., & Wender, B. (1983). Finite element analysis of a resitance spot welded joint subjected to tensile shear loading using various structural models. *Schweissen und schneiden, 35*(4), 174-178.

Heiser, D., Charging, M., & Sielaft, J. (1999). *High performance process oriented weld spot approach.* Paper presented at the *First MSC worldwide automotive user conference*, Munich, Germany.

Heuschkel, J. (1952). The Expression of Spot Weld Properties. *Welding Journal*(31), 931-943.

Kalpakjian, S. (1992). *Manufacturing Processes for Engineering Materials* (2nd edition ed.).

Lalam, S. H.*Weldability of AHSS*, from www.autosteel.org

Langrand, B., & Comberscure, A. (2004). Nonlinear and failure behaviour of spot welds: a global finite element and experiments in pure and mixed modes I/II. *International Journal of solids and structures, 41*(2004), 6631-6646.

Lardure, P., Lacouture, E., & Blain, E. (2000). *Spot weld modelling technique and performances of finite element models for the vibrational behaviour of automotive structures*.

Lee, H., & Choi, J. (2005). Overload analysis and fatigue life prediction of spot-welded specimens using an effective J-integral. *Mechanics of Materials, 37*, 19-32.

Lee, H., Kim, N., & Lee, T. S. (2005). Overload failure curve and fatigue behaviour of spot-welded specimens. *Engineering Fracture Mechanics, 72*(2005), 1203–1221.

Lemaitre, J., & Chaboche, J. L. (1985). *Mecanique des materiaux solides.* Paris, France: Bordas.

Lin, S.-H., Pan, J., Wu, S., & Tyan, T. (2004). Failure Loads of Spot Weld Specimens under Impact Opening and Shear Loading Conditions. *Experimental Mechanics*, 147-157.

Liu, Y. (2000). *Dynamic Characteristics of welded structure.* MSc. Thesis, University of Alabama, Alabama.

Marya, Manuel, Wang, Kathy, Hector, L. G. Jr.., & Gayden, X. (2006). Tensile shear forces and fracture modes in single and multiple weld specimens in dual phase steels. *Journal of Manufacturing Science and Engineering, Transactions of ASME, 128*(1), 287 - 298.

Mignone, P. J. (2006). *The computational analysis of heat affected zones in spot welds.* B. Eng. Thesis, RMIT University.

Nakano, R. K. (2005). *Strain rate influence in the spot welding joint failure (INFLUENCIA DA TAXA DE DEFORMACAO NA FALHADE UNIOES*

POR SOLDA A PONTO). M.Sc. Thesis, Escola Politecnica da Universidade de Sao Paulo.

Ni, K., & Mahadevan, S. (2003). Probabilistic fatigue crack growth analysis of spot welded joints. *Fatigue Fract Eng Mater struct., 27*, 473-480.

Palmonella, M., Friswell, M. I., Mottershead, J. E., & Lees, A. W. (2004). Guidelines for implementation of CWELD and ACM2 spot weld models in structural dynamics. *Finite Elements in Analysis and Design, 41*(2004), 193-210.

Pollard, B. (1974). Spot Welding Characteristics of HSLA Steel for Automotive Applications. *Welding Journal, Welding Research Suppliment*(August 1974), 343s-350s.

Radaj, D., & Zhang, S. (1995). Geometrically Nonlinear Behaviour Of Spot Welded Joints In Tensile And Compressive Shear Loading. *Engineering Fracture Mechanics, 51*(2), 281-294.

Radaj, D., Zhaoyun, Z., & Mohrmann, W. (1990). Local Stress Parameters at the Weld Spot of Various Specimen. *Engineering Fracture Mechanics, 37*(5), 933-951.

Rathbun, R. W., Matlock, D. K., & Speer, J. G. (2003). Fatigue behavior of spot welded high-strength sheet steels. *Welding Journal, 82*, 207 - 218.

Rui, Y., Borsos, R. S., Gopalakrishnan, R., Agrawal, H. N., & Rivard, C. (1993). The fatigue life prediction method for multi spot welded structures. *SAE Technical Paper, 930571*.

Saleh, N. (2002). *Finite element simulation of crash testing of spot welded peel specimens* (No. IM-2002-004): Swedish Institute for Metals Research.

Sawai, N. P., Ingle, R. B., Patakdar, S. K., & Mahajan, R. S. (2005). *Finite element modelling strategy for spot welds in thin walled sections and its verification.* Paper presented at the ASME International mechanical Engineering Congress and Exposition, Orlando, Florida, USA.

Schneider, F., & Jones, N. (2003). Influence of spot weld failure on crushing of thin walled structural sections. *international Journal of Mechanical Science, 45*, 2061-2081.

Schneider, F., & Jones, N. (2004). Impact of Thin Walled High Strength Steel Structural Sections. *Journal of Automobile Engineering, 218*(2), 131-158.

Sheppard, S. D. (1993). Estimation of Fatigue Propagation Life in Resistance Spot Welds. *Advances in Fatigue Lifetime Predictive Techniques; 2nd Volume, ASTM STP 1211, M R Mitchell and R W Landgraf Eds, American Society for Testing and Materials*, 169-185.

Thronton, P. H., Krause, A. R., & Davis, R. G. (1996). The Aluminium Spot Weld. *Weld Journal, Welding Research Supplement* (75), 101s-108s.

Trigopula, V., Langseth, M., Hopperstad, O. S., & Clausen, A. H. (2006). Axial crushing of thin walled high strength steel section. *International Journal of Impact Engineering, 32*, 847-882.

VandenBossche, D. J. (1977). Ultimate Strength and Failure Mode of Spot Welds in High Strength Steels. *SAE Technical Paper, 770214*.

Wang, J., Xia, Y., Zhou, Q., & Zhang, J. (2006). Simulation of spot weld pullout by modeling failure around nugget. *SAE Technical Paper, 2006-01-0532*.

Westerberg, C. (2002). *Finite element simulation of crash testing of self piercing rivet joints, peel specimen.* MSc. Engineering Thesis, Lund University.

Wung, P. (2000). A Force Based Failure Cruterion for Spot Wed Design. *Experimental Mechanics, 41*(1), 107-113.

Wung, P. (2001). A Method for Spot Welded Structure Analysis. *SAE Technical Paper, 2001-01-0427*.

Wung, P., Walsh, T., Ourchane, A., Stewart, W., & Jie, M. (2001). Failure of Spot Welds under In-plane Static Loading. *Experimental Mechanics, 41*(1), 100-106.

Xiang, Y., Wang, Q., Fan, Z., & Fang, H. (2006). Optimal crashworthiness design of a spot welded thin walled hat section. *Finite Elements in Analysis and Design, 42*, 846-855.

Xu, S., & Deng., X. (2004). An evaluation of simplified finite element models for spot-welded joints. *Finite Elements in Analysis and Design, 40*(2004), 1175-1194.

Yancey, R. N. (2004). Impact Modeling of Spot Welds. *Materials Processing and Design: Modeling, Simulation and Applications: Part Two*, 1215 -1218.

Yoda, S., kumagi, K., Yoshikawa, M., & Tsuji, M. (2006). Development of a method to predict the rapture of spot welds in vehicle crash analysis. *SAE Technical Paper, 2006-01-0533*.

Zhang, H., Zhou, M., & Hu, S. J. (2001). Impact strength measurement of spot welds. *Proc Instn Mech Engrs, IMechE 2001, 215*(Part B), 403-414.

Zhang, S. (2001). Recent Developments in Analysis and Testing of Spot Welds. *SAE Technical Paper, 2001-01-0432*.

Zhang, S. (2005). Simplified spot weld model for NVH simulations. *SAE Technical Paper, 2005-01-0905*.

Zhang, Y., & Taylor, D. (2001). Optimization of spot welded structure. *Finite Elements in Analysis and Design, 37*, 1013-1022.

Zhou, M., H, A., & J, H. S. (1999). Critical Specimen Sizes for Tensile Shear Tests. *Welding Journal, Welding Research Suppliment, 78*(9), 305s-313s.

Zhou, M., Zhang, H., & Hu, S. J. (2003). Relationships between Quality and Attributes of Spot Welds. *Welding Journal, Welding Research Suppliment, April 2003*, 72s-77s.

Zilincik, S. E., DeFrank, W. J., Monroe, E., & Khan, S. (1998). A new approach to evaluating spot welds for automotive durability. *SAE Technical Paper, 982277*.

Zolotarev, B. B. (1960). Distribution of Stress in a Spot Weld under Load. *Welding Production, 3*, 28-33.

Zuniga, S., & Sheppard, S. D. (1997). *Resistance Spot Weld Failure Loads and Modes in Overload Conditions.* Paper presented at the Fatigue and Fracture Mechanics: 27th volume ASTM STP1296,R S Piasick,J C Newman,N E Dowling Eds.

Zuniga, S. M., & Sheppard, S. D. (1995). Determining the constitutive properties of the heat-affected zone in a resistance spot weld. *Modelling Simul. Mater. Sci. Eng., 3*(1995), 391 - 416.

Appendix - A

Chemical Composition of Sheet Metal

The chemical composition of the used sheet metal reported below was taken from the data sheet of CA3SN – G provided by the manufacturer BlueScope Steel Ltd.

GUARANTEED PROPERTIES OF STEEL BASE

MECHANICAL PROPERTIES	GUARANTEED %
Transverse tensile	
Yield strength, MPa	240 max
Tensile strength, MPa	–
Elong on 80 mm, %	
≥ 0.60 < 0.80 mm	35 min
≥ 0.80 mm	36 min
Hardness, HRB	53 max
HR30T	53 max
180° transverse bend (L axis)	0t
Uniform elong, %	–
Plastic strain ratio	
r0	–
r90	–
r45	–

CHEMICAL PROPERTIES	GUARANTEED MAXIMUM %	TYPICAL %
Carbon (C)	0.08	0.04 - 0.06
Phosphorus (P)	0.030	0.005 - 0.020
Manganese (Mn)	0.40	0.20 - 0.26
Sulphur (S)	0.025	0.008 - 0.020
Silicon (Si)	–	0.005 - 0.010
Aluminium (Al)	–	0.04 - 0.06
Nitrogen (N)	–	0.004 - 0.010

FABRICATING PERFORMANCE

Method	Rating
Bending	5
Drawing	4
Pressing	5
Roll-forming	5
Welding	5
Painting (pretreatment)	5

where 1 = limited to 5 = excellent, or
NR = not recommended

Appendix – B

Universal testing machine specifications

(i) MTS machine – Model 810

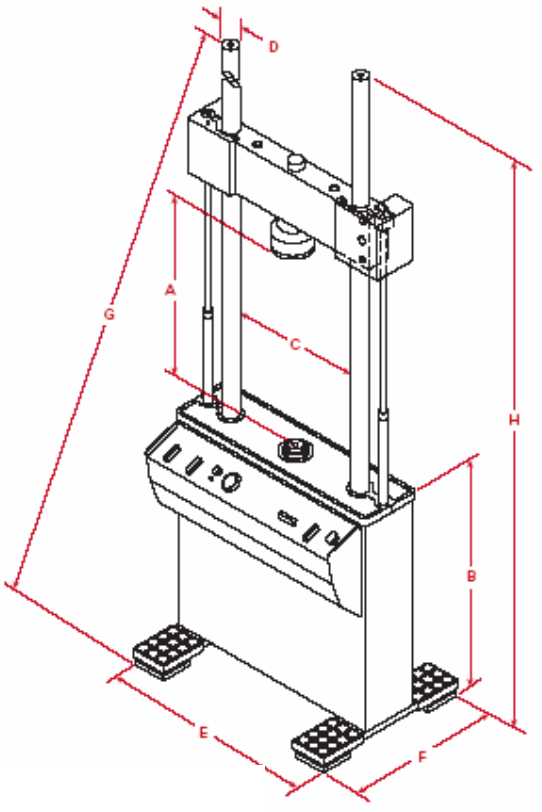

Specifications by Frame Configuration

Load unit specifications

Model	318.10		318.25		318.50	
Force capacity (maximum)	100 kN	(22 kip)	250 kN	(55 kip)	500 kN	(110 kip)
Available actuator ratings	15, 25, 50, 100 kN (3.3, 5.5, 11, 22 kip)		100, 250 kN (22, 55 kip)		250, 500 kN (55, 100 kip)	
Vertical test space* (A)	1308 mm	(51.5 in)	1625 mm	(64 in)	2108 mm	(83 in)
Working height (B)	889 mm	(35 in)	889 mm	(35 in)	889 mm	(35 in)
Column spacing (C)	533 mm	(21 in)	635 mm	(25 in)	762 mm	(30 in)
Column diameter (D)	64 mm	(2.5 in)	76 mm	(3 in)	102 mm	(4 in)
Base width (E)	864 mm	(34 in)	1003 mm	(39.5 in)	1245 mm	(49 in)
Base depth (F)	610 mm	(24 in)	762 mm	(30 in)	914 mm	(36 in)
Diagonal Clearance (G)	2718 mm	(107 in)	3251 mm	(128 in)	3835 mm	(151 in)
Overall Height (H)	2540 mm	(100 in)	3023 mm	(119 in)	3581 mm	(141 in)
Stiffness†	2.6×10^6 N/m	(15×10^6 lb/in)	4.3×10^6 N/m	(2.4×10^6 lb/in)	7.5×10^6 N/m	($4.3 \times 1\ 10^6$ lb/in)
Weight	500 kg	(1100 lb)	910 kg	(2000 lb)	1770 kg	(3900 lb)

*Test space is the maximum distance between the load cell and the actuator with the actuator fully retracted. Optional extended height versions available, add 300 mm (12 inches) to pertinent dimensions.
†Determined at each load unit's full fatigue rating with its crosshead raised 1270 mm (50 in.) above the base plate.

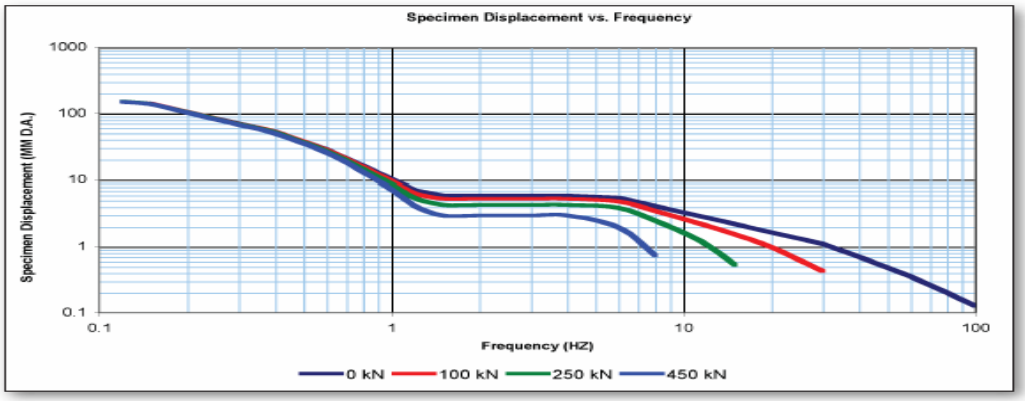

Load Frame Model: *318.50*	500 kN	(110 kip)	**ServoValve(s):** *252.25G x (2)*	114 lpm	(30 gpm)
Actuator Static Force:	500 kN	(110 kip)	**Grip:** *647.50*	148 kg	(326 lbs.)
Actuator Nominal Stroke:	150 mm	(6 inches)	**HPU:** *505.30 60 Hz*	113.5 lpm	(30 gpm)
System Oil Pressure:	210 bar	(3000 psi)			

(ii) Instron machine – Model 5569

Specifications

		Single Column Table Top Models			Twin Column Table Top Models					Floor Standing Models			
		5542	5543	5544	5564	5565	5566	5567	5569	5581	5582	5584	5585H
Load Capacity	kN	0.5	1	2	2	5	10	30	50	50	100	150	250
	kgf	50	100	200	200	500	1000	3000	5000	5000	10000	15000	25000
	lbf	112.5	225	450	450	1125	2250	6750	11250	11250	22500	33750	56200
Maximum Speed	mm/min	1000	1000	1000	2500	1000	500	500	500	1000	500	750	500
	in/min	40	40	40	100	40	20	20	20	40	20	30	20
Minimum Speed	mm/min	0.05	0.05	0.05	0.005	0.001	0.001	0.001	0.001	0.001	0.001	0.001	0.001
	in/min	0.002	0.002	0.002	0.0002	0.00004	0.00004	0.00004	0.00004	0.00004	0.00004	0.00004	0.00004
Maximum Force at Full Speed	kN	0.5	1	2	1	5	10	30	25*	35	75	110	100
	lb	112.5	225	450	225	1125	2250	6750	5620	7870	16860	24730	22500
Maximum Speed at Full Load	mm/min	1000	1000	1000	1000	1000	500	500	250**	500	250	375	200
	in/min	40	40	40	40	40	20	20	10	20	10	15	8
Return Speed	mm/min	1500	1500	1500	2500	1200	600	600	500	1000	600	800	500
	in/min	60	60	60	100	48	24	24	20	40	24	32	20
Position Control Resolution	µm	0.156	0.156	0.208	0.236	0.118	0.057	0.054	0.063	0.100	0.060	0.075	0.060
	µin	6.1	6.1	8.2	9.3	4.6	2.2	2.1	2.5	3.9	2.4	2.9	2.4
Total Crosshead Travel	mm	500	917	917	1135	1135	1135	1135	1135	1235	1235	1180	1180
	in	19.7	36.1	36.1	44.6	44.6	44.6	44.6	44.6	48.6	48.6	46.5	46.5
Total Vertical Test Space [Note 5]	mm	659	1076	1076	1249	1249	1249	1205	1205	1309	1309	1256	1256
	in	25.9	42.4	42.4	49.2	49.2	49.2	47.4	47.4	51.5	51.5	49.4	49.4
Depth Daylight	mm	100	100	100	NA	NA	NA	NA	NA	NA	NA	NA	NA
	in	3.9	3.9	3.9									
Space Between Columns	mm	NA	NA	NA	420	420	420	420	420	575	575	575	575
	in				16.5	16.5	16.5	16.5	16.5	22.6	22.6	22.6	22.6
Height [Note 7]	mm	875	1275	1275	1597	1597	1597	1597	1597	2092	2092	2092	2092
	in	34.4	50.2	50.2	62.9	62.9	62.9	62.9	62.9	82.4	82.4	82.4	82.4
Width	mm	375	375	375	909	909	909	909	909	1300	1300	1300	1300
	in	14.75	14.75	14.75	35.8	35.8	35.8	35.8	35.8	51.2	51.2	51.2	51.2
Depth	mm	500	500	500	700	700	700	700	700	756	756	756	756
	in	19.7	19.7	19.7	27.5	27.5	27.5	27.5	27.5	29.8	29.8	29.8	29.8
Weight	kg	32	37	37	136	136	136	182	240	862	862	952	952
	lb	70	80	80	300	300	300	400	530	1900	1900	2100	2100
Maximum Power Requirement	VA	225	225	400	300	300	300	600	700	1400	1400	2800	2850 VA

Note: Common specifications are on the back page

Appendix – C

Calibration Data for the Extensiometer

INSTRON®

Instron Pty. Ltd.
Australian Head Office ▪ P.O. Box 352 BAYSWATER VIC 3153
Tel: +61 3 9720 3477 ▪ Fax: +61 3 9720 3728 ▪ www.instron.com

NATA

This laboratory is accredited by the National Association of Testing Authorities, Australia. The tests reported herein have been performed in accordance with its terms of accreditation.

Laboratory Accreditation Number 3037

Calibration Report

REPORT NO: Ext217 **ISSUE DATE:** 30/05/2006 **PAGE** 1 **OF** 2

ISSUED TO: RMIT University
Bundoora East Campus
Cnr Plenty Road and McKimmies Lane
Bundoora, VIC 3083

EXTENSOMETER DESCRIPTION:

MAKER:	Instron	**MODEL:** 2603-080	**SERIAL NO:** 1432
GAUGE LENGTH:		25mm	**TRAVEL:** 250mm
READOUT:		**Instron Testing Machine:** 4466H1864 Readout- Smallest increment 0.01%	

LOCATION: Manufacturing Materials Laboratory Building 253
As above

CALIBRATION DATE: 12th May 2006

PRELIMINARY EXAMINATION: The extensometer was in good working order. No adjustments were carried out prior to this calibration.

CALIBRATION PROCEDURE: Calibration was carried out in accordance with AS1545-1976. The extensometer was initially zeroed and spanned using the electronic calibration system of the Instron testing machine. Three sets of readings were taken in an increasing direction with the extensometer mounted in a vertical position.

CONCLUSION: The extensometer performed without fault throughout the calibration and conformed with the Standard for the ranges and grades detailed on page two of this report.

APPROVED SIGNATORY:

The difference is measurable

INSTRON PTY LTD

CONTINUATION OF CALIBRATION REPORT NO: Ext 217 **PAGE** 2 **OF** 2

Extensometer			Range	Calibrated Range		Grade
Load Cell	Ser. No.	Read Out		From	To	
Type 2603-080 GL 25mm Travel 250mm	1432	Front Panel Digital Display; Smallest Increment 0.01 %	Auto	20% 5 mm	1000% 250 mm	D

The mean of three measurements of the extensometer's gauge length was 25.08mm measured with a Mitutoyo digital calliper serial number 0045282.
The repeatability of the extensometer's gauge length was 0.03 mm

The mean ambient temperature during calibration was 22 degrees Celsius.

The values of readability of range, of accuracy and of repeatability of indicated forces do not exceed specification requirements applicable to the tabulated grading.

Uncertainty of Measurement
The uncertainty of measurement of the equipment used for the measurements was 2um.
The uncertainty of measurement stated has been calculated at the 95% level of confidence.
The coverage factor, k, has a value of 2 for this calculation.

NATA Accredited Laboratory Number: 3037
This laboratory is accredited by the National Association of Testing Authorities, Australia. The tests reported herein have been performed in accordance with its terms of accreditation. This document shall not be reproduced except in full.

APPROVED SIGNATORY:
Jimmy Boo

Extensometer Calibration Number: EXT217 **Date:** 12-May-06

Carried Out For: RMIT Univeristy
Bundoora East Campus
Cnr Plenty Road and McKimmies Lane
Bundoora, VIC 3083

Ref: ANNUAL

At: Mfg Materials Lab Bldg 253
As above

Contact: Peter Tkatchyk

Extensometer Description

Manufacturer:	INSTRON	**Model No:**	2603-080	**Serial No:**	1432
Gauge Length Settings:			25 mm	**Travel:**	250 mm
Indicator:	Instron	**Model No:**	4466	**Serial No:**	H1864
Indicator Resolution:			0.01 %		

Standard: AS1545-1976
Method: Extensometer mounted vertically on split specimen in testing machine and tested in an extending direction.

Mean temperature during calibration: 22
Measured Gauge Length: 25.08 25.09 25.06 Mean: 25.08 mm

Applied Extension		Indicated Strain									D Grade Limits			E Grade Limits		
% Strain	mm	Test 1 Strain	mm	Test 2 Strain	mm	Test 3 Strain	mm	Mean	Accuracy	Repeatability	Accuracy µm	Repeat µm	Readability µm	Accuracy µm	Repeat µm	Readability µm
20	5	19.7600	4.94000	19.6700	4.91750	19.6200	4.90500	4.92083	79.2	35.0	102.5	61.5	41	205	123	82
40	10	39.7300	9.93250	39.6400	9.91000	39.6000	9.90000	9.91417	85.8	32.5	202.5	121.5	81	405	243	162
80	20	79.6000	19.90000	79.5200	19.88000	79.5100	19.87750	19.88583	114.2	22.5	402.5	241.5	161	805	483	322
100	25	99.5000	24.87500	99.4400	24.86000	99.4200	24.85500	24.86333	136.7	20.0	502.5	301.5	201	1005	603	402
200	50	199.3000	49.82500	199.2100	49.80250	199.1900	49.79750	49.80833	191.7	27.5	1002.5	601.5	401	2005	1203	802
300	75	299.5000	74.87500	299.4200	74.85500	299.4000	74.85000	74.86000	140.0	25.0	1502.5	901.5	601	3005	1803	1202
400	100	399.2000	99.80000	399.1200	99.78000	399.1100	99.77750	99.78583	214.2	22.5	2002.5	1201.5	801	4005	2403	1602
500	125	499.0000	124.75000	498.9200	124.73000	498.8900	124.72250	124.73417	265.8	27.5	2502.5	1501.5	1001	5005	3003	2002
600	150	599.0000	149.75000	598.9300	149.73250	598.9000	149.72500	149.73583	264.2	25.0	3002.5	1801.5	1201	6005	3603	2402
700	175	698.0000	174.50000	697.9400	174.48500	697.9100	174.47750	174.48750	512.5	22.5	3502.5	2101.5	1401	7005	4203	2802
800	200	798.0000	199.50000	797.9400	199.48500	797.9200	199.48000	199.48833	511.7	20.0	4002.5	2401.5	1601	8005	4803	3202
900	225	898.0000	224.50000	897.9500	224.48750	897.9200	224.48000	224.48917	510.8	20.0	4502.5	2701.5	1801	9005	5403	3602
1000	250	998.0000	249.50000	997.9400	249.48500	997.9100	249.47750	249.48750	512.5	22.5	5002.5	3001.5	2001	10005	6003	4002

Appendix – D

Testing set up and calibration curve for hardness testing

Hardness testing machine specification: Future Tech Hardness Tester, Japan, Model FV – 700 for Vickers hardness testing.

Hardness testing set up:

The basic equation to measure the hardness of any material is as follows.

$$HV = 1.854\left(\frac{F}{d^2}\right)$$

where HV is the hardness value, F is the force in kgf unit and d is the average diagonal distance (average of D_1 and D_2 shown in the figure) of the indentation in mm. The calibrated force is used for measuring the hardness for the chosen material. The distance between the consecutive indentations along the radial directions from the spot weld nugget for the hardness testing was taken as 1mm. (It was recommended to be >4D where D is the average diagonal distance). The testing set up is shown in the following figure.

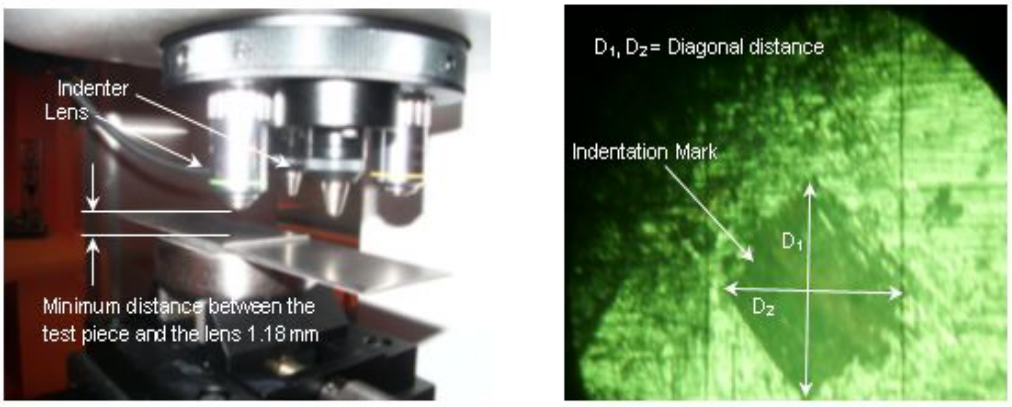

Fig: Hardness testing of spot welded samples (a) Testing set up (b) Indentation mark

Calibration of the force level:

Calibration is carried out based on the hardest and the softest part of the spot weld joint. That is based on the hardness value on the nugget and the base metal. The HAZ is kept out of consideration due to the variable hardness value. The calibrations curves for the choice of the force level are given in the following figures. The choice the force value was 5 kgf.

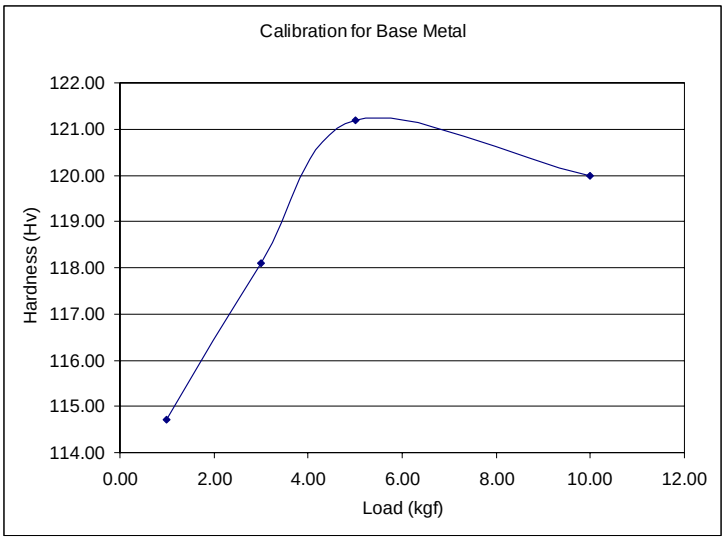

(a)

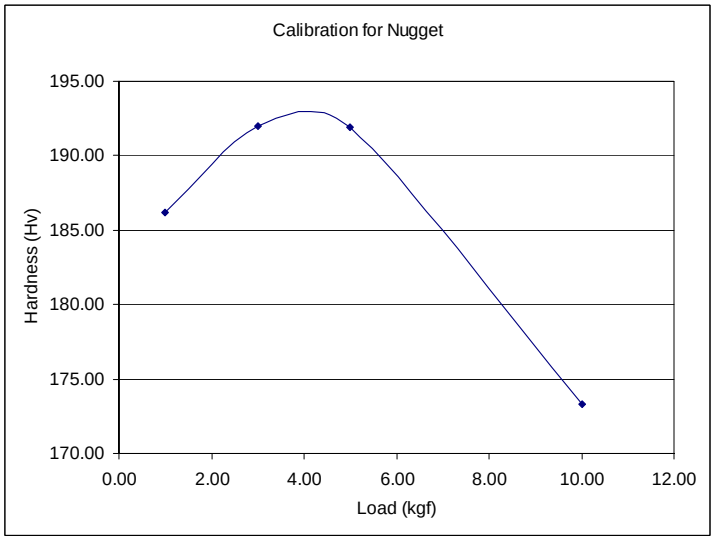

(b)

Fig: Calibration curves for the choice of the force level used to determine the hardness value. (a) Curve for the base metal (b) Curve for the nugget.